Winter 2008

Hypersonic Boundary Layer Receptivity to Acoustic Disturbances Over Cones

Kursat Kara
Old Dominion University

HYPERSONIC BOUNDARY LAYER RECEPTIVITY TO ACOUSTIC DISTURBANCES OVER CONES

by

KURSAT KARA

B.S. June 1999, Istanbul Technical University, Turkey
M.S. May 2003, Istanbul Technical University, Turkey

A Dissertation Submitted to the Faculty of
Old Dominion University in Partial Fulfillment of the
Requirement for the Degree of

DOCTOR OF PHILOSOPHY

AEROSPACE ENGINEERING

OLD DOMINION UNIVERSITY

December 2008

Approved by:

Osama A. Kandil (Director)

Ponnampalam Balakumar (Co-Director)

Oktay Baysal (Member)

Duc T. Nguyen (Member)

ABSTRACT

HYPERSONIC BOUNDARY LAYER RECEPTIVITY TO ACOUSTIC DISTURBANCES OVER CONES

Kursat Kara
Old Dominion University, 2008
Director: Dr. Osama A. Kandil
Co-Director: Dr. Ponnampalam Balakumar

The receptivity mechanisms of hypersonic boundary layers to free stream acoustic disturbances are studied using both linear stability theory (LST) and direct numerical simulations (DNS). A computational code is developed for numerical simulation of steady and unsteady hypersonic flow over cones by combining a fifth-order weighted essentially non-oscillatory (WENO) scheme with third-order total-variation-diminishing (TVD) Runge-Kutta method. Hypersonic boundary layer receptivity to freestream acoustic disturbances in slow and fast modes over 5-degree, half-angle blunt cones and wedges are numerically investigated. The free-stream Mach number is 6.0, and the unit Reynolds number is 7.8×10^6 /ft. Both the steady and unsteady solutions are obtained by solving the full Navier-Stokes equations in two-dimensional and axisymmetric coordinates.

Computations are performed in three steps. After the steady mean flow field is computed, linear stability analysis is performed to find the most amplified frequency and the unstable disturbance modes in different flow regions. Then time accurate computations are performed using slow and fast mode acoustic disturbances, and the

initial generation, interaction and evolution of instability waves inside the boundary layers are studied.

Receptivity computations showed that the acoustic disturbance waves propagated uniformly to downstream, interact with the bow shock, enter the boundary layer, and then generate the initial amplitude of the instability waves in the leading edge region. Effects of the entropy layer due to nose bluntness to the receptivity process are studied. It is found that transition location moves downstream and is delayed by increasing bluntness, and the role of the entropy layer in this process is revealed. Also, the effects of wall cooling to the receptivity process using slow and fast mode acoustic disturbances are studied. The effects of cooling on the first and second mode regions are investigated. It is found that the first mode is stabilized and the second mode is destabilized by wall cooling when the flow is forced by acoustic waves in the slow mode.

To my family for all their love and understanding

Anneme, Babama, Eşime ve Kızıma

ACKNOWLEDGEMENTS

NASA Langley Research Center was the sponsor of this project, and I would like to thank them for making this research possible. I want to express my sincere gratitude and appreciation to my advisor Dr. Osama A. Kandil for his guidance, continued encouragement and support during my dissertation research and course work. Also, I would like to express my most sincere respect for and appreciation to my co-advisor Dr. Ponnampalam Balakumar at NASA Langley Research Center. He always showed great enthusiasm when I was struggling with tough problems. Most of the background material has been derived from the lectures and work of Dr. Balakumar. I am thankful to Dr. Oktay Baysal for encouraging and helping me from my first day at ODU and for offering his time and valuable comments in reviewing this dissertation. I would like to thank Dr. Duc T. Nguyen for his unique way of teaching. His door was always open for all my questions and requests.

I would like to thank my friends Dr. Mehti Koklu, Barbaros Yildirim, Dr. Ilteris Koc, Volkan Kamaci, Bedri Yagiz, Omer San, Isik Ozcer, Dr. Bulent Imamoglu, and K. Kitir for their friendship and support and for making my life fun here in Norfolk. I would like to thank all my professors from Istanbul Technical University for teaching and inspiring me with their knowledge and character.

Last but definitely not least, I want to convey my deepest thanks to my mother, Halime, my father Irfan, my uncle Mustafa, my brother Şamil, and my sisters Neslihan and Hilal. Finally, I want to thank the Kara household – Mualla and Ceyda – who have been patient and understanding while their husband and father was in his ivory tower.

NOMENCLATURE

English Symbols

a	Speed of sound
c	Phase velocity
c_{rj}	Interpolation coefficients
c_{recpt}	Receptivity coefficient
c_v	Specific heat at constant volume
c_p	Specific heat at constant pressure
d_r	Weight coefficients
e	Molecular internal energy
E	Total energy
f	Disturbance frequency
F_0	Non-dimensional disturbance frequency
G_0	Wall to total temperature ratio
F, G	Inviscid fluxes
F_v, G_v	Viscous fluxes
J	Jacobian matrix
k_T	Thermal conductivity coefficient

k	Number of candidate stencils
L	Reference length
M	Mach number
N	N factor
p	Pressure
P_r	Prandtl number
Q	Conservative flow field vector
q	Heat flux
R	Gas constant, Nose radius
R_c	Radius of curvature of bow shock
R_n, r_0	Nose radius
Re	Reynolds number
Re_x	Reynolds number based on distance from leading edge
Re_{r0}	Reynolds number based on nose radius
S	Source term
T	Temperature
t	Time
U	Velocity vector
u_1, u_2, u_3	Velocity in streamwise, spanwise and normal directions

u, v, w	Velocity in streamwise, spanwise and normal directions
w_r	Weight coefficients
x_1, x_2, x_3	Cartesian coordinates
x, y, z	Cartesian coordinates
x, y, θ	Cylindrical coordinates
x_0, z	Distance from leading edge

Greek Symbols

α	Streamwise wave number
β	Spanwise wave number, Shock angle at inviscid limit
β_r	Smoothness indicator
ρ	Density
Π	Stress tensor
μ	Molecular viscosity coefficient, Free stream Mach angle
υ	Kinematic viscosity coefficient
γ	Specific heat coefficient
δ	Boundary layer thickness, Shock standing distance
ξ, η	Curvilinear coordinates
η	Similarity coordinate

ω	Acoustic disturbance frequency
λ	Second viscosity coefficient
λ_k	Maximum eigenvalue
θ	Cone half-angle, Acoustic wave incident angle
τ	Shear stress
σ	Smoothness function
ω	Disturbance frequency

Subscripts

∞	Freestream flow variables
e	Boundary layer edge values
ac	Acoustic disturbance
aw	Variables on adiabatic wall
w	Variables on wall
max	Maximum value
amp	Amplitude of variables
0	Mean flow variables, Stagnation conditions
i	Dummy index, Imaginary part of a complex variable
r	Real part of a complex variable

np	Neutral point
sim	Similarity solution value
tr	Transition values

Superscripts

*	Dimensional variables
`	Acoustic disturbance variables
~	Amplitude of disturbance variables
_	The variables in curvilinear coordinates
^	Numerical flux
+	Split flux with positive eigenvalues
-	Split flux with negative eigenvalues

TABLE OF CONTENTS

LIST OF FIGURES

LIST OF TABLES

CHAPTER I

1. INTRODUCTION

Transition from laminar to turbulent flows in hypersonic boundary layers is crucial for prediction and control of heat transfer, skin friction, separation and other boundary layer parameters. This effect is critical to reentry vehicles and airbreathing hypersonic cruise vehicles, yet the physics of the transition process is not yet well understood enough to be used for predictive purposes[1]. The U.S. National committee on Theoretical and Applied Mechanics reported that "*In hypersonic flight, delaying the transition to turbulence can make the difference between successful reentry from space and the loss of a mission.*" [2] Also, a 1992 National Aerospace Plane review by the Defense Science Board found that further design development and increased confidence in boundary layer transition and scramjet engine performance have paramount importance in the NASP program.

Figure 1.1 shows an example Mach 4.3 transition on a sharp cone near a zero angle of attack, at a freestream Reynolds number of 2.66×10^6 /in.[1] In this figure the cone is travelling from left to right in still air. The lower surface boundary layer is turbulent, and acoustic waves radiated from turbulent eddies can be seen passing downstream at the Mach angle. On the upper surface, the boundary layer is intermittently turbulent, with two turbulent spots being visible in the image, interspersed among laminar regions[1]. Larger waves can be seen in front of the turbulent spots, with smaller levels of acoustic

---

This dissertation is formatted based on *AIAA Journal*.

noise being radiated from the turbulence within the spots. The acoustic noise is not present above the laminar regions[1].

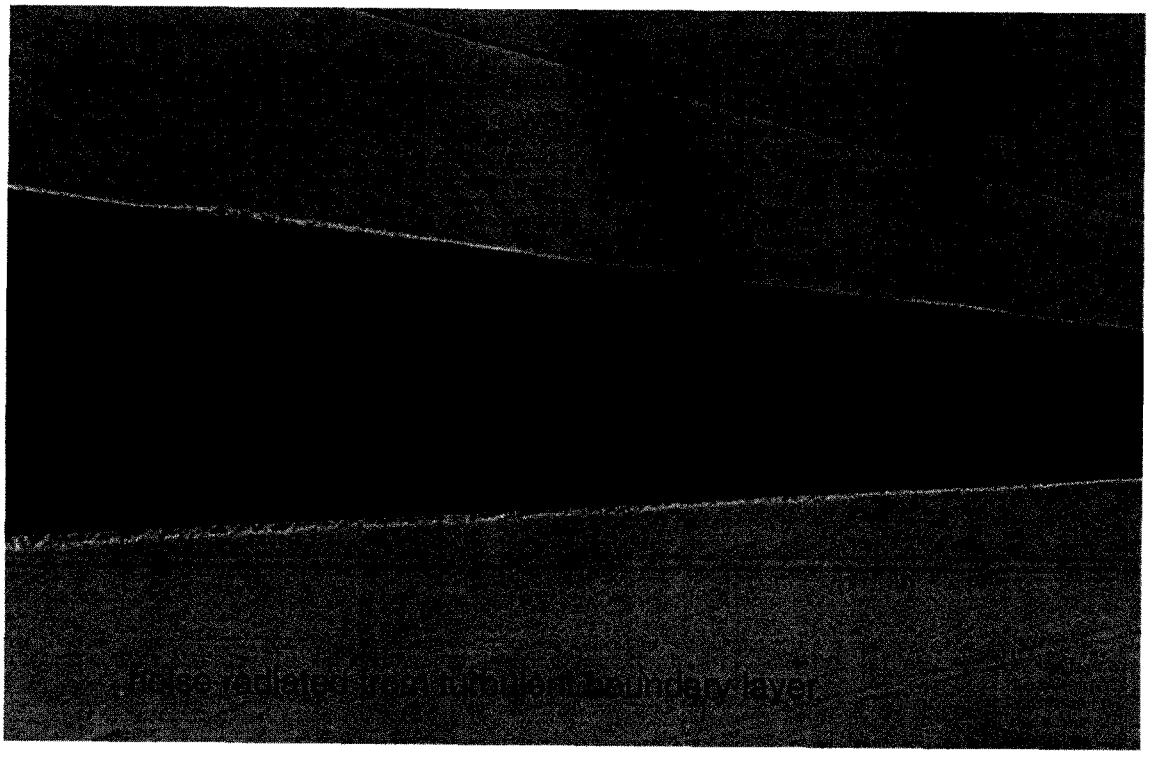

Figure 1.1 Shadowgraph of transition on a sharp cone at Mach 4.31[1].

Laminar to turbulent transition controls are important aerodynamics quantities such as drag and heat transfer. Heating rates generated in the turbulent region may be three to eight times higher than that of the laminar region as shown in Figure 1.2 which presents computations and measurements of the surface heat transfer during the reentry-F test of ballistic RV. Here, the symbols show the flight data and the computations were done using a variable-entropy boundary layer code. According to Hamilton, who conducted the simulations, the typical accuracies are 20-25% for the turbulent boundary layer and 15-20% for the laminar layer; error bars are sketched on the figure based on these estimates. Transition onset causes the rise in heating at z/L=0.65. Current computational capabilities for laminar and turbulent heating in attached flows are fairly

good; the uncertainty in prediction of the overall heating is often dominated by the uncertainty in predicting the location of transition[1].

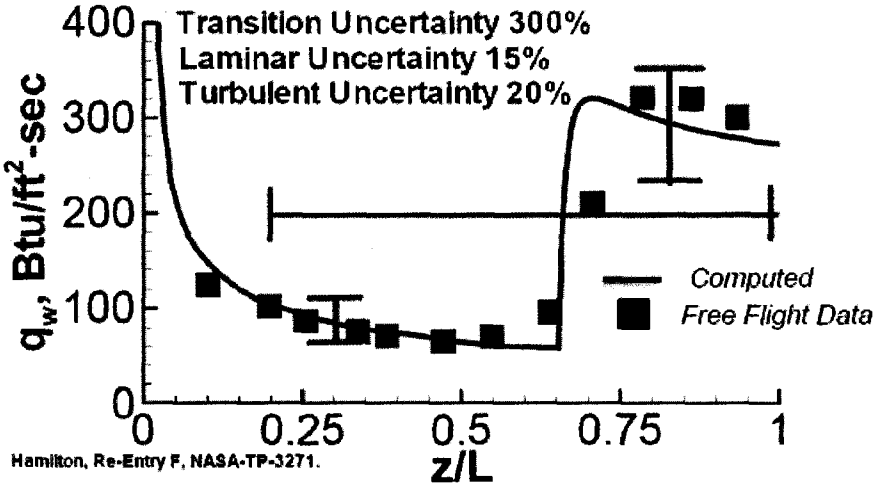

Figure 1.2 Heating-rate distribution along cone for reentry-F[1].

1.1 Hypersonic Flow over a Blunt Cone

In hypersonic flow, blunt leading edge is necessary to control the heating of the leading edge region. The effect of bluntness can be experienced by the flow hundreds of

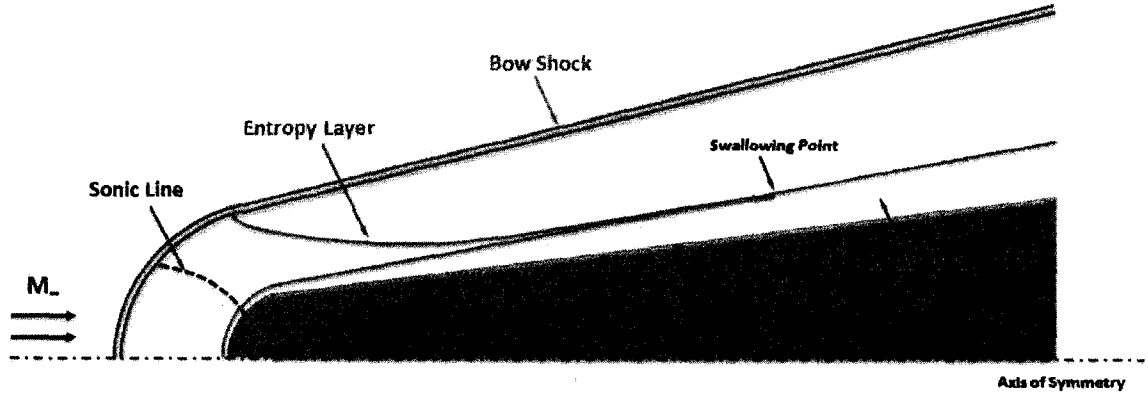

Figure 1.3 Schematic view of hypersonic flow over a blunt cone.

nosetip radii downstream. The actual distance that the effects seem to propagate is dependent on the bluntness and the free stream conditions[3].

Figure 1.3 shows a schematic view of hypersonic flow over a blunt cone. Hypersonic flow comes from the left and generates a strong bow shock at the downstream of the nose region. The bow shock creates a layer of high specific entropy and strong entropy gradients in the gas outside the boundary layer, commonly referred to as an entropy layer. The thickness of this layer is a function of the bluntness on the leading edge of the cone. The entropy layer is "swallowed" by the growing boundary layer at a certain downstream location of the cone called a swallowing point.

1.2 Hypersonic Boundary Layer Transition and Receptivity

The physical mechanism of transition from laminar to turbulent flow has long been investigated since Reynolds' famous experiment in 1883. At the present time, no mathematical model exists that can predict the transition Reynolds number on a flat plate[4]. One obvious reason for this is the variety of influences such as free stream turbulence, surface roughness, sound, etc. that are incompletely understood. Periodically the state of our knowledge is reviewed by Dryden[5], Tani[6], Morkovin[7], Reshotko[8-11], Morkovin and Reshotko[12], Bayley[13], Arnal[14], Saric[4, 15-17], and Reed[18, 19].

The process of transition for boundary layers in external flows can be qualitatively described using Figure 1.4 and following a scenario based on one of the different roadmaps to turbulence developed over the years[4, 20]. In Figure 1.4, the initial amplitude increases systematically from left to right. Initially, these disturbances may be too small to measure, and they are observed only after the onset of instability.

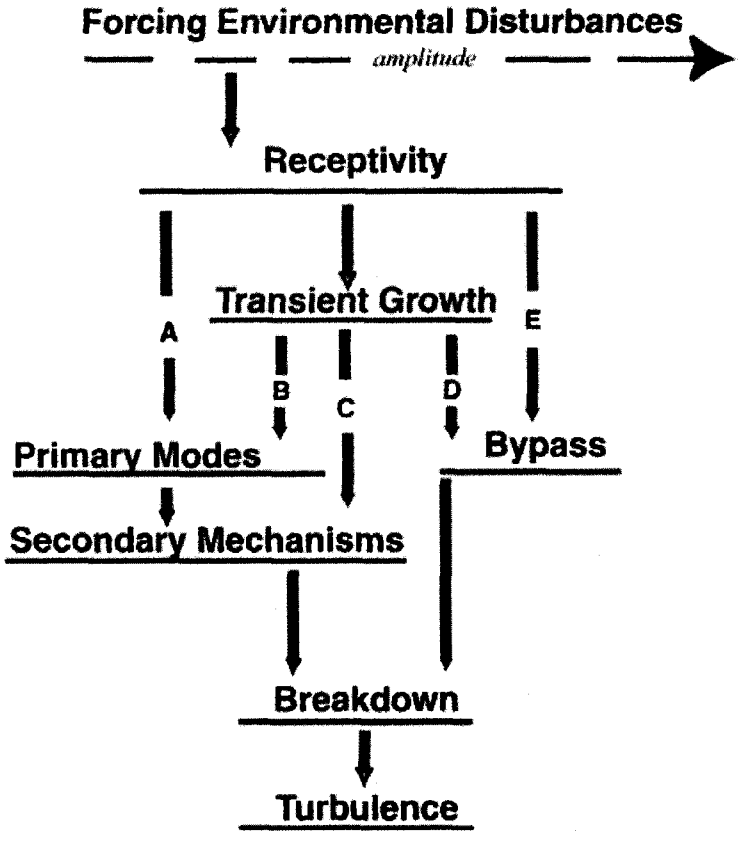

Figure 1.4 The paths from receptivity to transition[4].

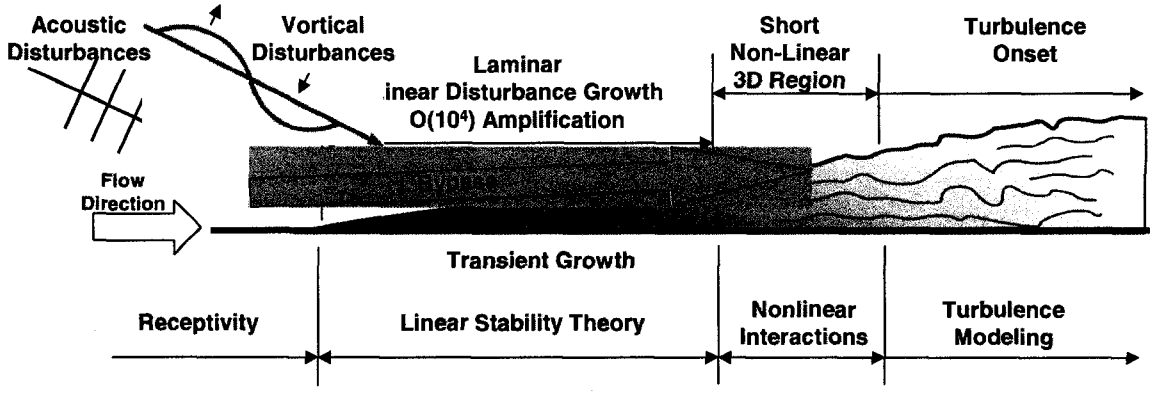

Figure 1.5 Schematic view of transition process. (from Saric)

A number of different instabilities can occur independently or together, and the appearance of any particular type of instability depends on the Reynolds number, wall curvature, sweep, roughness, and initial conditions.

Though there are several mechanisms and routes to go from a laminar to turbulent state, most generally follow these fundamental processes[21]:

1. Receptivity
2. Linear instability
3. Nonlinear instability and saturation
4. Secondary instability and breakdown to turbulence.

In the receptivity process (see Morkovin[7], and Reshotko[8]) external disturbances such as free stream (acoustic, vortical and thermal perturbations) and/or wall induced (vibrations, periodic suction/blowing, surface heating, roughness, and geometry) enter the boundary layer and generate initial amplitude, frequency and phase of instability waves.

In the second step, the amplitudes of these instability waves grow exponentially downstream and this process is governed by the linearized Navier-Stokes equations. Further downstream, the amplitudes of the disturbances become large, and the nonlinear effects inhibit the exponential growth and the amplitude of the waves eventually saturate. Then these finite amplitude saturated disturbances become unstable to two- and/or three-dimensional disturbances. This is called secondary instability. Beyond this stage the spectrum broadens due to complex interactions and further instabilities, and the flow becomes turbulent in a short distance downstream[21, 22].

1.3 Outline of Present Research

The main objective of the present research is to study hypersonic boundary layer receptivity to free stream acoustic disturbances by direct numerical simulation (DNS) over cones. Figure 1.6 shows the schematic view of the cone geometry and computational

domain in axisymmetric coordinates. By DNS we refer to the numerical simulation of the full nonlinear, time-dependent Navier-Stokes equations without any empirical closure assumptions.

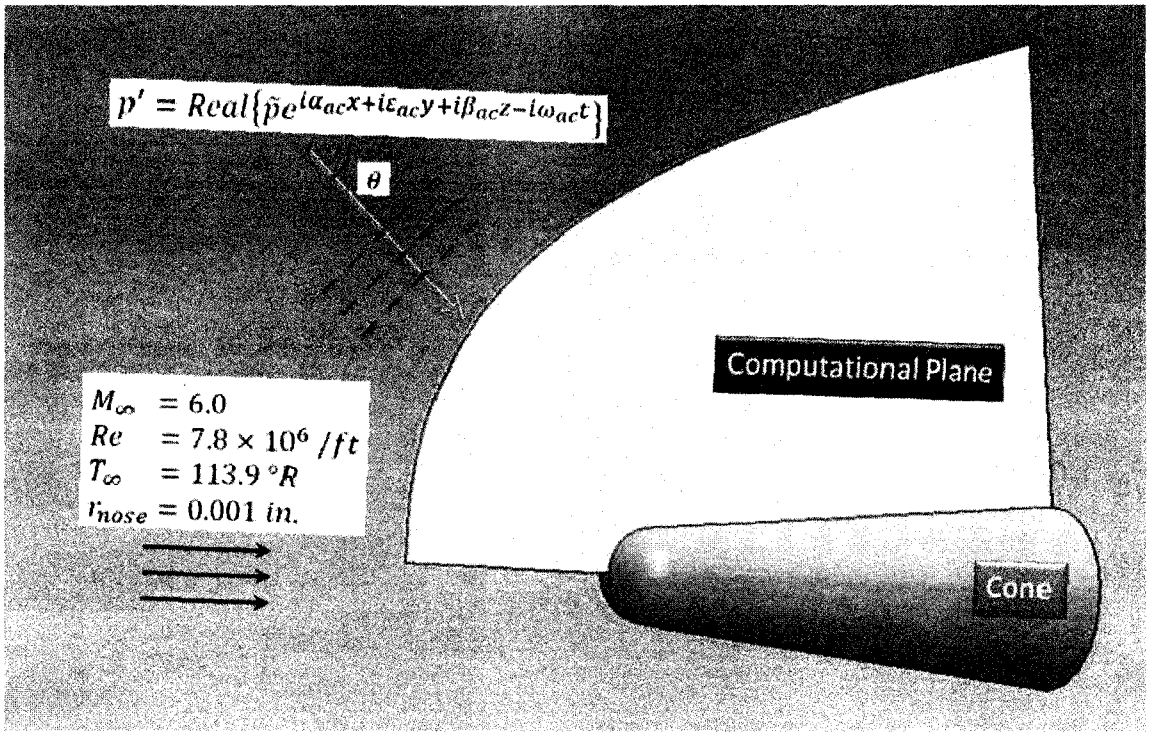

Figure 1.6 Sketch of cone geometry and computational domain.

This approach can provide a complete space-time history of the flow field and permit precise parametric study. It is the most accurate and appropriate method for laminar to turbulence transition study. However, linear stability and PSE results are also used in the present work. This dissertation includes the following chapters.

In chapter 2, the governing equations, numerical methods, computational grid and solution algorithm for two-dimensional and axisymmetric geometries are presented.

In chapter 3, validation results of the axisymmetric flow solver are presented.

In chapter 4, the transition process induced by the interaction of acoustic disturbances in the free stream with boundary layers over a 5-degree straight cone and wedge with blunt nose is numerically investigated at free stream Mach number 6.0.

In chapter 5, effects of nose bluntness on hypersonic boundary layer receptivity are investigated using DNS, and steady and unsteady simulation results are presented.

In chapter 6, effects of wall cooling on hypersonic boundary layer receptivity are investigated using DNS, and steady and unsteady simulation results are presented.

In chapter 7, conclusions of the present research and recommendations for future research are presented.

CHAPTER II

2. GOVERNING EQUATIONS AND SOLUTION METHOD

In this study, the main objective is to investigate hypersonic boundary layer receptivity to free-stream acoustic disturbances over cone and wedge using direct numerical simulation (DNS). In this chapter, we will first give a derivation of Navier-Stokes equations in two-dimensional and axisymmetric coordinates and numerical schemes to solve these equations

2.1 General Form of Governing Equations

Unsteady, compressible three-dimensional Navier-Stokes equations in the vector notation in Cartesian coordinate system can be expressed in the following equations where the superscript '*' denotes the dimensional variables.

$$\frac{\partial \rho^*}{\partial t^*} + \nabla \cdot \rho^* \mathbf{V}^* = 0 \tag{2.1}$$

$$\rho^* \left(\frac{\partial \mathbf{V}^*}{\partial t^*} + \mathbf{V}^* \cdot \nabla \mathbf{V}^* \right) = \nabla \cdot \Pi^* \tag{2.2}$$

$$\rho^* c_V \left(\frac{\partial T^*}{\partial t^*} + \mathbf{V}^* \cdot \nabla T^* \right) = \nabla \cdot k_T^* \nabla T^* + \Phi^* \tag{2.3}$$

$$p^* = \rho^* R T^* \tag{2.4}$$

Equations (2.1)-(2.4) represent continuity, momentum, energy, and state equation respectively. The gas is assumed to be thermally and calorically perfect, Π represents stress tensor and its components τ_{ij} are expressed in Equation (2.5) where Stokes' hypothesis $\lambda^* = -\frac{2}{3}\mu^*$ is enforced.

$$\tau_{ij}^* = -p^*\delta_{ij} + \mu^*\left(\frac{\partial u_i^*}{\partial x_j^*} + \frac{\partial u_j^*}{\partial x_i^*} - \frac{2}{3}\delta_{ij}\frac{\partial u_k^*}{\partial x_k^*}\right) \tag{2.5}$$

The dissipation term, Φ, in energy Equation (2.3) can be expressed as follows

$$\Phi^* = \tau_{ij}^* e_{ij}^* \tag{2.6}$$

where

$$e_{ij}^* = \frac{1}{2}\left(\frac{\partial u_i^*}{\partial x_j^*} + \frac{\partial u_j^*}{\partial x_i^*}\right) \tag{2.7}$$

Molecular viscosity coefficient (μ^*) is calculated using Sutherland's law.

$$\mu^* = \frac{c_1 T^{*\frac{3}{2}}}{c_2 + T^*} \tag{2.8}$$

where $c_1 = 7.30246 \cdot 10^{-7}, c_2 = 198.7°\text{R}$.

The thermal conductivity coefficient (k_T^*) is given in terms of the Prandtl number (P_r).

$$k_T^* = \frac{\gamma}{\gamma - 1}\frac{\mu^*}{P_r} \tag{2.9}$$

where γ is the specific heat coefficient, $\gamma = 1.4$ and $P_r = 0.7$

2.2 Nondimensionalization of Navier-Stokes Equations

Before proceeding, to the computation model governing equations are nondimensionalized using characteristic quantities for convenience. The density, ρ^*, temperature, T^*, pressure, p^*, and velocities, u_i^*, are nondimensionalized using their corresponding upstream reference values, $\rho_\infty^*, T_\infty^*, p_\infty^*$, and U_{ref}^*, respectively. The reference values for length and velocity are computed by

$$L_{ref}^* = \sqrt{\frac{\nu_\infty^* x_0^*}{U_\infty^*}}, \qquad U_{ref}^* = \sqrt{RT_\infty^*} \tag{2.10}$$

where, x_0^* is the location of the beginning of the computational domain in the streamwise direction.

Using the above characteristic quantities, nondimensional variables can be written in the following form.

$$x_i = \frac{x_i^*}{L_{ref}^*}, \qquad t = \frac{t^*}{L_{ref}^* / U_{ref}^*}, \qquad u_i = \frac{u_i^*}{U_{ref}^*},$$

$$\rho_i = \frac{\rho^*}{\rho_\infty^*}, \qquad T = \frac{T^*}{T_\infty^*}, \qquad p = \frac{p^*}{p_\infty^*},$$

$$\mu_i = \frac{\mu_i^*}{\mu_\infty^*}, \qquad Re = \frac{\rho_\infty^* U_{ref}^* L_{ref}^*}{\mu_\infty^*}, \qquad Pr = \frac{\mu_\infty^* c_p}{k_\infty^*}$$

The nondimensionalized Navier-Stokes equations in two-dimensional and axisymmetric coordinate systems are given in the following sections.

2.3 Two-dimensional Navier-Stokes Equations

After nondimensionalization using the above reference quantities, two-dimensional, unsteady, compressible Navier-Stokes equations can be written from equations (2.1)-(2.4) in conservative flux vector form as follows.

$$\frac{\partial Q}{\partial t}+\frac{\partial F}{\partial x}+\frac{\partial G}{\partial y}=\frac{\partial F_v}{\partial x}+\frac{\partial G_v}{\partial y} \tag{2.11}$$

where Q is the solution flow field vector, F and G are the streamwise- and wall normal-direction inviscid flux vectors given by

$$Q=\begin{bmatrix}\rho\\ \rho u\\ \rho v\\ \rho E\end{bmatrix} \qquad F=\begin{bmatrix}\rho u\\ \rho u^2+p\\ \rho uv\\ (\rho E+p)u\end{bmatrix} \qquad G=\begin{bmatrix}\rho v\\ \rho vu\\ \rho v^2+p\\ (\rho E+p)v\end{bmatrix} \tag{2.12}$$

and F_v and G_v are the streamwise- and wall normal-direction viscous flux vectors given by

$$F_v=\begin{bmatrix}0\\ \tau_{xx}\\ \tau_{xy}\\ u\tau_{xx}+v\tau_{xy}-q_x\end{bmatrix} \qquad G_v=\begin{bmatrix}0\\ \tau_{yx}\\ \tau_{yy}\\ u\tau_{yx}+v\tau_{yy}-q_y\end{bmatrix} \tag{2.13}$$

Shear stresses (2.14) and heat fluxes (2.15) have the following form.

$$\begin{aligned}\tau_{xx}&=\frac{2}{3}\frac{\mu}{Re}\left(2\frac{\partial u}{\partial x}-\frac{\partial v}{\partial y}\right)\\ \tau_{xy}=\tau_{yx}&=\frac{\mu}{Re}\left(\frac{\partial u}{\partial y}+\frac{\partial v}{\partial x}\right)\\ \tau_{yy}&=\frac{2}{3}\frac{\mu}{Re}\left(2\frac{\partial v}{\partial y}-\frac{\partial u}{\partial x}\right)\end{aligned} \tag{2.14}$$

$$q_x = -\frac{\gamma}{(\gamma-1)PrRe}\frac{\partial T}{\partial x}$$
$$q_y = -\frac{\gamma}{(\gamma-1)PrRe}\frac{\partial T}{\partial y} \tag{2.15}$$

Here (x, y) are the two-dimensional Cartesian coordinates, and (u, v) are the corresponding velocity components. ρ is the density, and p is the pressure. E is the total energy given by

$$E = e + \frac{u^2+v^2}{2}$$
$$e = c_v T \tag{2.16}$$
$$p = \rho RT$$

Here e is the molecular internal energy, and T is the temperature.

2.4 Navier-Stokes Equations in Axisymmetric Coordinates

For governing equations of an axisymmetric flow field, the vector form of Navier-Stokes Equations (2.1)-(2.4) are written in cylindrical coordinates (x, y, θ). Then, these equations are nondimensionalized using reference quantities given in Section 2.2. In axisymmetric flow it is assumed that there is no flow in the circumferential (θ) direction and the derivatives in this direction are also zero.

$$[\ ]_\theta = 0, \qquad \frac{\partial(\ )}{\partial\theta} = 0 \tag{2.17}$$

The axisymmetric flow assumptions in Equation (2.17) are applied to nondimensionalized equations and the resulting axisymmetric, unsteady, compressible

Navier-Stokes equations in conservative flux vector form are expressed in the following form.

$$\frac{\partial Q}{\partial t}+\frac{\partial F}{\partial x}+\frac{\partial G}{\partial y}=\frac{\partial F_v}{\partial x}+\frac{\partial G_v}{\partial y}+S \tag{2.18}$$

where Q is the solution flow field vector, F and G are the axial- and radial- direction inviscid flux vectors given by

$$Q=\begin{bmatrix}\rho\\ \rho u\\ \rho v\\ \rho E\end{bmatrix} \qquad F=\begin{bmatrix}\rho u\\ \rho u^2+p\\ \rho uv\\ (\rho E+p)u\end{bmatrix} \qquad G=\begin{bmatrix}\rho v\\ \rho vu\\ \rho v^2+p\\ (\rho E+p)v\end{bmatrix} \tag{2.19}$$

and F_v and G_v are the axial- and radial- direction viscous flux vectors given by

$$F_v=\begin{bmatrix}0\\ \tau_{xx}\\ \tau_{xy}\\ u\tau_{xx}+v\tau_{xy}-q_x\end{bmatrix} \qquad G_v=\begin{bmatrix}0\\ \tau_{yx}\\ \tau_{yy}\\ u\tau_{yx}+v\tau_{yy}-q_y\end{bmatrix} \tag{2.20}$$

The vector S contains viscous and inviscid fluxes of the source term associated with the axisymmetric geometry. The source term Equation (2.21), shear stresses Equation (2.22) and heat fluxes Equation (2.23) in the axisymmetric formulation have the following form.

$$S=\frac{1}{y}\left\{\begin{bmatrix}0\\ \tau_{yx}\\ \tau_{yy}-\tau_{\theta\theta}\\ u\tau_{yx}+v\tau_{yy}-q_y\end{bmatrix}-\begin{bmatrix}\rho v\\ \rho uv\\ \rho v^2\\ (\rho E+p)v\end{bmatrix}\right\} \tag{2.21}$$

$$\begin{aligned}
\tau_{xx} &= \frac{2}{3}\frac{\mu}{Re}\left(2\frac{\partial u}{\partial x} - \frac{\partial v}{\partial y} - \frac{v}{y}\right) \\
\tau_{xy} = \tau_{yx} &= \frac{\mu}{Re}\left(\frac{\partial u}{\partial y} + \frac{\partial v}{\partial x}\right) \\
\tau_{yy} &= \frac{2}{3}\frac{\mu}{Re}\left(2\frac{\partial v}{\partial y} - \frac{\partial u}{\partial x} - \frac{v}{y}\right) \\
\tau_{\theta\theta} &= \frac{2}{3}\frac{\mu}{Re}\left(2\frac{v}{y} - \frac{\partial u}{\partial x} - \frac{\partial v}{\partial y}\right)
\end{aligned} \tag{2.22}$$

$$\begin{aligned}
q_x &= -\frac{\gamma}{(\gamma-1)PrRe}\frac{\partial T}{\partial x} \\
q_y &= -\frac{\gamma}{(\gamma-1)PrRe}\frac{\partial T}{\partial y}
\end{aligned} \tag{2.23}$$

There exists a singularity along the axis of symmetry, $y=0$. To remove the singularity we apply l'Hopital rule to the source term and take the limit of the resulting equation as $y \to 0$ using symmetry conditions given in Equation (2.24). The source term along the axis of symmetry becomes;

$$\begin{aligned}
\left.\frac{\partial \rho}{\partial y}\right|_{y=0} &= 0 \\
\left.\frac{\partial u}{\partial y}\right|_{y=0} &= 0 \\
\left.\frac{\partial p}{\partial y}\right|_{y=0} &= 0 \\
\left.\frac{\partial T}{\partial y}\right|_{y=0} &= 0 \\
v|_{y=0} &= 0
\end{aligned} \tag{2.24}$$

$$S=\begin{bmatrix} \rho\left.\dfrac{\partial v}{\partial y}\right|_{y=0} \\ \rho u_{y=0}\left.\dfrac{\partial v}{\partial y}\right|_{y=0}-\dfrac{\mu}{\mathrm{Re}}\left[\dfrac{\partial}{\partial y}\left(\left.\dfrac{\partial u}{\partial y}\right|_{y=0}+\left.\dfrac{\partial v}{\partial x}\right|_{y=0}\right)\right] \\ -\dfrac{\mu}{\mathrm{Re}}\dfrac{\partial}{\partial y}\left(\left.\dfrac{\partial v}{\partial y}\right|_{y=0}\right) \\ \begin{bmatrix} (\rho e+p)\left.\dfrac{\partial v}{\partial y}\right|_{y=0} \\ -u_{y=0}\dfrac{\mu}{\mathrm{Re}}\left[\dfrac{\partial}{\partial y}\left(\left.\dfrac{\partial u}{\partial y}\right|_{y=0}+\left.\dfrac{\partial v}{\partial x}\right|_{y=0}\right)\right] \\ -\left.\dfrac{\partial v}{\partial y}\right|_{y=0}\dfrac{2}{3}\dfrac{\mu}{\mathrm{Re}}\left(\left.\dfrac{\partial v}{\partial y}\right|_{y=0}-\left.\dfrac{\partial u}{\partial x}\right|_{y=0}\right) \\ -\dfrac{\gamma}{(\gamma-1)\mathrm{Pr}\,\mathrm{Re}}\dfrac{\partial}{\partial y}\left(\left.\dfrac{\partial T}{\partial y}\right|_{y=0}\right) \end{bmatrix} \end{bmatrix} \tag{2.25}$$

Applying the same procedure to shear stresses and heat fluxes we get new terms without singularity in them along the symmetry axis ($y=0$).

$$\begin{aligned} \tau_{xx} &= \frac{4}{3}\frac{\mu}{Re}\left(\frac{\partial u}{\partial x}-\frac{\partial v}{\partial y}\right)\Bigg|_{y=0} \\ \tau_{yy} &= \frac{2}{3}\frac{\mu}{Re}\left(\frac{\partial v}{\partial y}-\frac{\partial u}{\partial x}\right)\Bigg|_{y=0} \\ \tau_{\theta\theta} &= \tau_{yy} \\ \tau_{xy} &= 0 \\ \tau_{yx} &= 0 \end{aligned} \tag{2.26}$$

$$\begin{aligned} q_x &= -\frac{\gamma}{(\gamma-1)PrRe}\left.\frac{\partial T}{\partial x}\right|_{y=0} \\ q_y &= 0 \end{aligned} \tag{2.27}$$

Here (x, y) are the axisymmetric coordinates, and (u, v) are the corresponding velocity components. ρ is the density, and p is the pressure. E is the total energy given in Equation (2.16).

2.5 Coordinate Transformation

For convenience of computation, the equations are transformed from physical coordinates (x, y) to the computational coordinate system (ξ, η) in a conservative manner such that the general form of the equations is unchanged.

$$\frac{\partial \bar{Q}}{\partial t}+\frac{\partial \bar{F}}{\partial \xi}+\frac{\partial \bar{G}}{\partial \eta}=\frac{\partial \bar{F}_v}{\partial \xi}+\frac{\partial \bar{G}_v}{\partial \eta}+\bar{S} \tag{2.28}$$

where

$$\xi=\xi(x,y), \qquad \eta=\eta(x,y) \tag{2.29}$$

The metrics are expressed as the following.

$$\begin{aligned} \xi_x &= |J| y_\eta & \eta_x &= -|J| y_\xi \\ \xi_y &= -|J| x_\eta & \eta_y &= |J| x_\xi \end{aligned} \tag{2.30}$$

where J is the Jacobian given by

$$J=\begin{bmatrix} \xi_x & \xi_y \\ \eta_x & \eta_y \end{bmatrix} \tag{2.31}$$

The components of the flux in the computational domain are related to the flux in the physical domain by

$$\bar{Q} = \frac{Q}{|J|} \qquad \bar{S} = \frac{S}{|J|}$$
$$\bar{F} = \frac{(\xi_x F + \xi_y G)}{|J|} \qquad \bar{G} = \frac{(\eta_x F + \eta_y G)}{|J|} \tag{2.32}$$
$$\bar{F}_v = \frac{(\xi_x F_v + \xi_y G_v)}{|J|} \qquad \bar{G}_v = \frac{(\eta_x F_v + \eta_y G_v)}{|J|}$$

2.6 Computational Methods

The governing equations are solved using the 5th order weighted essentially non-oscillatory (WENO) scheme for space discretization and the 3rd order total variation diminishing (TVD) Runge-Kutta scheme for time integration. These methods are suitable in flows with discontinuities or high gradient regions and solve the governing equations discretely in a uniform structured computational domain in which flow properties are known at grid points.

The WENO scheme approximates the spatial derivatives in a given direction to a higher order at the nodes, using neighboring nodal values in that direction. The TVD-RK scheme integrates the resulting equations in time to get the point values as a function of time. Since the spatial derivatives are independent of the coordinate directions, the method can easily add other dimensions. It is well known that approximating a discontinuous function by a higher order (two or more) polynomial generally introduces oscillatory behavior near the discontinuity, and this oscillation increases with the order of the approximation (Figure 2.1).

The essentially non-oscillatory (ENO) and the improvement of these WENO methods are developed to keep the higher order approximations in the smooth regions and to eliminate or suppress the oscillatory behavior near the discontinuities.

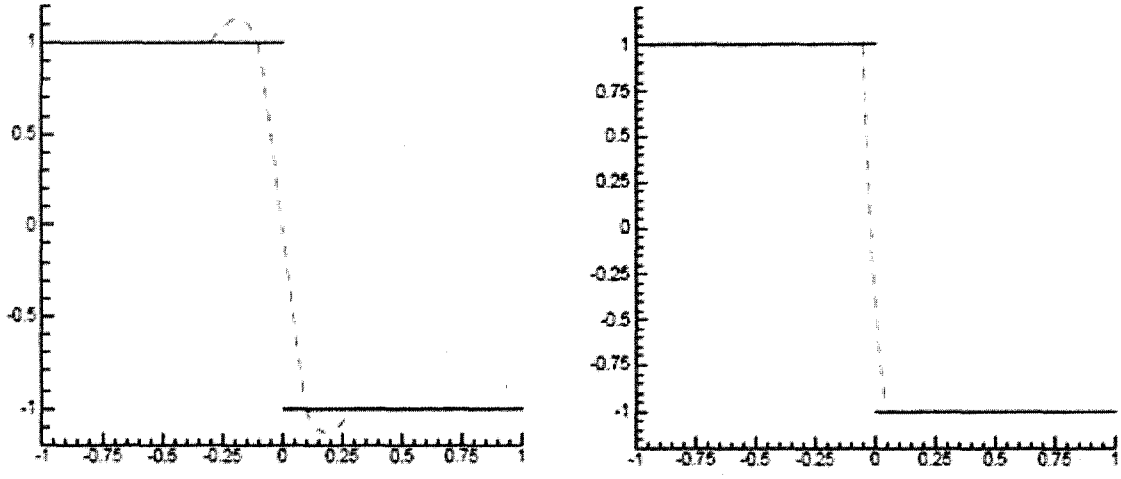

Figure 2.1 Fixed central stencil cubic interpolation (left) and ENO cubic interpolation (right) for the step function. Solid: exact function; Dashed: interpolation polynomials.[23]

They are achieved by systematically adopting or selecting the stencils based on the smoothness of the function being approximated. Shu[23] explains the construction, analysis and application of ENO, WENO and TVD-RK methods and the formulas for hyperbolic conservation laws. Atkins[24] gives the application of ENO method to the laminar three-dimensional Navier - Stokes equations. Balakumar et al.[25] describe in detail the application of WENO and TVD-RK schemes to three-dimensional Navier-Stokes equations.

2.7 Essentially Non-Oscillatory (ENO) Scheme

The ENO idea was proposed in the classic paper of Harten, Engquist, Osher and Chakravarthy[26] in 1987. It seemed to be the first successful attempt to obtain a self-

similar (i.e. no mesh size dependent parameter), uniformly high order accurate, yet essentially non-oscillatory interpolation for piecewise smooth functions. The generic solution for hyperbolic conservation laws is in the class of piecewise smooth functions. The ENO scheme is based on point values and TVD-RK discretization, which can save computational costs significantly in multi-dimensions are developed later[27, 28]. In the ENO and WENO methods the spatial derivatives with respect to a given direction are approximated by expansions in that direction only. Hence, a one-dimensional description is trivially extended to multi space dimensions. Here we considered application of the ENO scheme to the following one-dimensional equation.

$$\frac{\partial q}{\partial t} = -\frac{\partial f}{\partial x} \tag{2.33}$$

The spatial derivative at a point is calculated using difference of numerical fluxes; Equation (2.34) is similar to the approach of finite-volume methods.

$$\frac{\partial f(x_i)}{\partial x} = \frac{\hat{f}(x_{i+\frac{1}{2}}) - \hat{f}(x_{i-\frac{1}{2}})}{\Delta x_i} + O(\Delta x_i^{\,k}) \tag{2.34}$$

where x_i represents the coordinate at the i^{th} grid point and k stands for the order of accuracy.

The numerical flux is determined from linear combination of flux values at neighboring nodes from Equation (2.35).

$$\hat{f}_{x_{(i+1/2)}} = \sum_{j=0}^{k-1} c_{rj} f_{x_{(i-r+j)}}, \quad r = 0,\ldots,k-1 \tag{2.35}$$

where c_{rj} are the interpolation coefficients for the rth interpolation cell. Equation (2.36) gives the interpolation coefficient formula for uniform grids, and Table 2.1 gives the values of c_{rj} for $k=3$ and 5.

$$c_{rj} = \sum_{m=j+1}^{k} \frac{\sum_{l=0 \atop l\neq m}^{k} \prod_{q=0 \atop q\neq m,l}^{k} (r-q+1)}{\prod_{l=0 \atop l\neq m}^{k} (m-l)} \tag{2.36}$$

Table 2.1 The interpolation constants c_{rj}.

k	r	j=0	j=1	j=2	j=3	j=4
3	-1	11/6	-7/6	1/3		
	0	1/3	5/6	-1/6		
	1	-1/6	5/6	1/3		
	2	1/3	-7/6	11/6		
5	-1	137/60	-163/60	137/60	-21/20	1/5
	0	1/5	77/60	-43/60	17/60	-1/20
	1	-1/20	9/20	47/60	-13/60	1/30
	2	1/30	-13/60	47/60	9/20	-1/20
	3	-1/20	17/60	-43/60	77/60	1/5
	4	1/5	-21/20	137/60	-163/30	137/60

Figure 2.2 shows the physical and numerical fluxes defined in Equation (2.35) on a one-dimensional grid.

The ENO scheme uses an adaptive procedure to search for the smoothest stencil relative to the specified reference point. Therefore, a good resolution at the discontinuity can be achieved. The basic idea of ENO is to construct a stencil that does not include a cell which contains discontinuity. For example, if we want to construct a third order interpolation function at point $x_{i+1/2}$, three candidate stencils can be used: (x_i, x_{i+1}, x_{i+2}),

(x_{i-1}, x_i, x_{i+1}), and (x_{i-2}, x_{i-1}, x_i). Among these stencils, shown in Figure 2.3, some may contain a discontinuous cell or cells. These stencils are not desired in the numerical flux reconstruction and have to be removed from the reconstruction process.

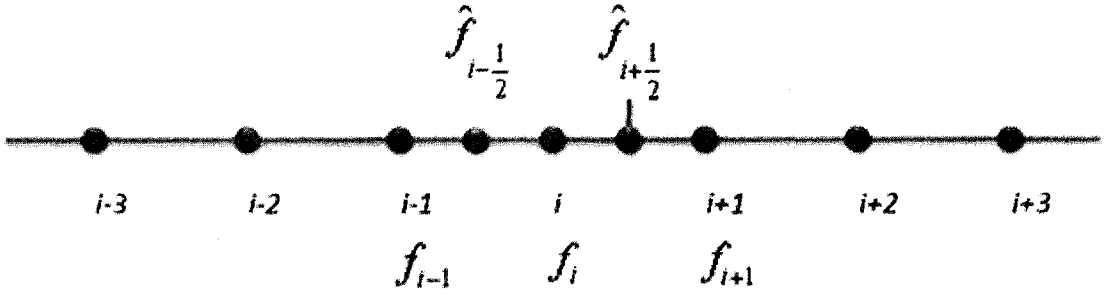

Figure 2.2 Physical and numerical fluxes on one-dimensional grid.

The selection procedure of the interpolation stencil has been described by Shu[23] in *Procedure 2.1 1D ENO reconstruction.* Using this procedure, one can get an interpolation stencil of k^{th} order, which is the smoothest one among all other computed stencils at the interpolation point

2.8 Weighted Essentially Non-Oscillatory (WENO) Scheme

In the ENO scheme one first calculates fluxes from k candidate stencils covering the *(2k-1)* cell during the stencil selection process and then uses only the smoothest stencil and obtains k^{th} order accuracy. However, if all of the *(2k-1)* cells in the potential stencils are used, one could get $(2k-1)^{th}$ order accuracy in smooth regions. This is the reason for the development of the WENO scheme.

As an example for three candidate stencils *(k=3)* five cells are considered *(2*3-1=5),* and the smoothest stencil is used to form the numerical flux and 3rd order accuracy gained in the ENO scheme. In contrast, the WENO scheme uses three stencils *(k=3)*

covering *(2*3-1=5)* cells then combines the stencils to form the numerical flux, resulting in 5^{th} order accuracy.

The basic idea of the WENO scheme is that instead of using only one of the candidate stencils to form the reconstruction, one can use a convex combination of all of them. Numerical fluxes can be calculated for each stencil shown in Figure 2.3 as follows.

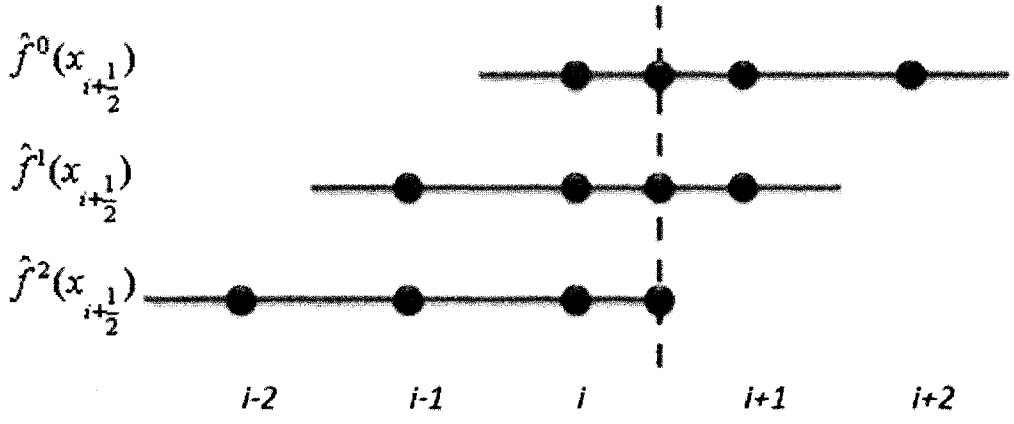

Figure 2.3 Numerical flux components in WENO scheme.

$$\hat{f}^r_{(x_{i+1/2})} = \sum_{j=0}^{k-1} c_{rj} f_{(x_{i-r+j})}, \quad r = 0,...,k-1 \tag{2.37}$$

In the next step, convex combination of the numerical fluxes from all the stencils can be computed using the following formula.

$$\hat{f}_{(x_{i+1/2})} = \sum_{r=0}^{k-1} \omega_r \hat{f}^r_{(x_{i+1/2})}, \quad r = 0,...,k-1 \tag{2.38}$$

Apparently, key to the success of the WENO scheme is the choice of the weights ω_r. For stability and consistency, the following conditions are required.

$$\omega_r \geq 0, \qquad \sum_{r=0}^{k-1} \omega_r = 1 \tag{2.39}$$

When the function f has discontinuity in one or more of the stencils, it is required that the corresponding weights, ω_r, should be essentially zero to emulate successful ENO ideas. Another consideration is that the weights should be smooth functions of the cell averages involved. Also, the weights should be computationally efficient. All of these considerations lead to the following form given in *Section 2.2.2 Weno approximation* of Shu[23]

$$\omega_r = \frac{\alpha_r}{\sum_{s=0}^{k-1} \alpha_s}, \quad r = 0,..,k-1 \tag{2.40}$$

where

$$\alpha_r = \frac{d_r}{(\varepsilon + \beta_r)^2} \tag{2.41}$$

Here $\varepsilon > 0$ is introduced to prevent the denominator from becoming zero, and we take $\varepsilon = 10^{-6}$ in our numerical computations. The d_r is the weight coefficient for the r^{th} interpolation stencil when $f_{(x)}$ is smooth in all of the candidate stencils. We can see that d_r must satisfy

$$d_r \geq 0 \qquad \sum_{r=0}^{k-1} d_r = 1 \tag{2.42}$$

For the 5th order WENO scheme which employs three candidate stencils covering five cells, the weight coefficients are

$$d_0 = \frac{3}{10}, \qquad d_1 = \frac{6}{10}, \qquad d_2 = \frac{1}{10} \tag{2.43}$$

Smoothness indicators, β_r, for the r^{th} stencil are

$$\beta_0 = \frac{13}{12}(\rho_i - 2\rho_{i+1} + \rho_{i+2})^2 + \frac{1}{4}(3\rho_i - 4\rho_{i+1} + \rho_{i+2})^2$$
$$\beta_1 = \frac{13}{12}(\rho_{i-1} - 2\rho_i + \rho_{i+1})^2 + \frac{1}{4}(\rho_{i-1} - \rho_{i+1})^2 \quad (2.44)$$
$$\beta_2 = \frac{13}{12}(\rho_{i-2} - 2\rho_{i-1} + \rho_i)^2 + \frac{1}{4}(\rho_{i-2} - 4\rho_{i-1} + 3\rho_i)^2$$

2.9 Flux Splitting

The inviscid and viscous terms of Navier-Stokes equations represent fundamentally different properties and require different numerical treatments[24]. The inviscid terms characteristically describe wave phenomena. The ideal approach would be to decompose the inviscid flux vector into characteristic components and treat each wave with an appropriate scalar operator. However, within the WENO framework, such an approach requires the creation of a characteristic subset at each grid point, which greatly increases the computational cost and storage requirements. A computationally efficient alternative is a local flux-splitting approach[24]. For each coordinate direction, k, the inviscid flux is split into two components: one with all positive eigenvalues and the other with all negative eigenvalues.

$$f_k = f_k^+ + f_k^- \quad (2.45)$$

$$f_k^{\mp} = f_k \mp \sigma_k q \quad (2.46)$$

$$\sigma_k = \sigma_{(\lambda_k)} \geq |\lambda_k| \quad (2.47)$$

where $\lambda_k = maximum\ eigenvalue\ of\ \left|\frac{\partial f_k}{\partial q}\right|$

More elaborate means of flux splitting exist, but this simple approach is inexpensive and works well. The only formal restriction on the splitting is that split fluxes must be smooth functions of q. This is necessary to ensure that higher order derivatives exist when evaluating the numerical flux, in addition to the usual need to prohibit expansion shocks. For the present splitting technique, the splitting flux will be smooth if the function σ is smooth. In the present implementation it is selected as

$$\sigma_{(\lambda)} = \sqrt{\varepsilon_1^2 + \lambda^2} \tag{2.48}$$

where ε_1 is a small number taken as 0.05 in this computation[25].

The viscous terms are diffusive and dissipative in nature and should be treated symmetrically. Therefore, the viscous flux is divided into two parts equally, and each part is added to the positive and negative component of the inviscid flux respectively. The WENO scheme is then applied to each component of the combined flux according to the wave propagation direction.

2.10 Total Variation Diminishing (TVD) Runge-Kutta Integration

A class of total variation diminishing (TVD) high order Runge-Kutta methods is developed by Shu and Osher[27], and Gottlieb and Shu[29]. Figure 2.4 shows the result of the TVD Runge-Kutta method and non-TVD method for a shock propagation problem. We can clearly see that the non-TVD result is oscillatory (there is an overshoot). Such oscillations may cause difficulties when physical problems are solved, such as the appearance of negative density and pressure Euler equations of gas dynamics. On the other hand, the TVD Runge-Kutta method guarantees that each middle stage solution is

also TVD, and this result convinces us that it is much safer to use a TVD Runge-Kutta method for solving hyperbolic problems[23].

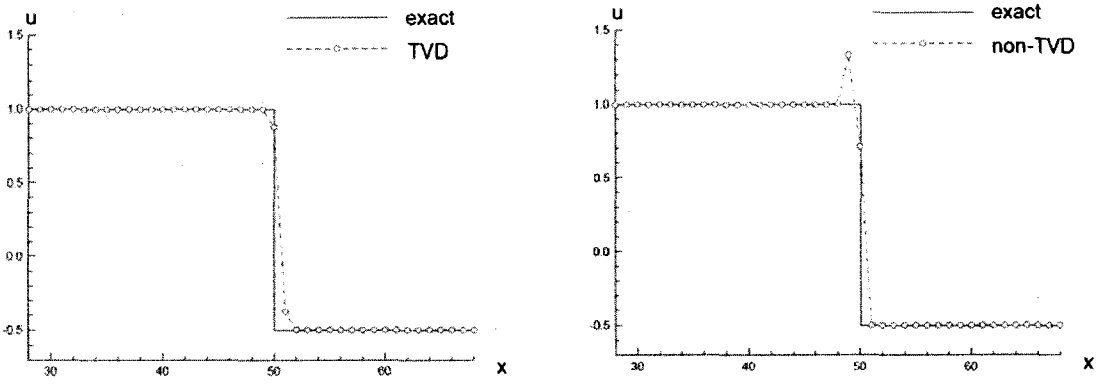

TVD time discretization Non-TVD time discretization

Figure 2.4 Comparison of second order TVD MUSCL spatial discretization[23].

Although higher order TVD Runge-Kutta methods are available, the third-order method was chosen on the basis of storage considerations. The optimal third-order method is given by:

$$
\begin{aligned}
q^{(1)} &= q^n + \Delta t L_{(q^n)} \\
q^{(2)} &= \frac{3}{4} q^n + \frac{1}{4} q^{(1)} + \frac{1}{4} \Delta t L_{(q^{(1)})} \\
q^{n+1} &= \frac{1}{3} q^n + \frac{2}{3} q^{(2)} + \frac{2}{3} \Delta t L_{(q^{(2)})}
\end{aligned}
\tag{2.49}
$$

where $L_{(q)}$ is the WENO approximation to the spatial derivative of flux vectors. The time step Δt is determined on the basis of an inviscid CFL number,

$$
CFL = \frac{\Delta t}{|J|} \sum_{k=1}^{3} |\lambda_k| \tag{2.50}
$$

where λ_k are the eigenvalues of the Jacobian matrix.

2.11 Boundary Conditions

The equations of motions require boundary conditions on all sides of the domain in which the solution is to be obtained. In CFD methods the boundary conditions (solid wall, symmetry, inflow, outflow, etc.) must be applied at each edge of the computational blocks. This section describes the boundary conditions used in steady and unsteady flow computations. Figure 2.5 shows the computational setup.

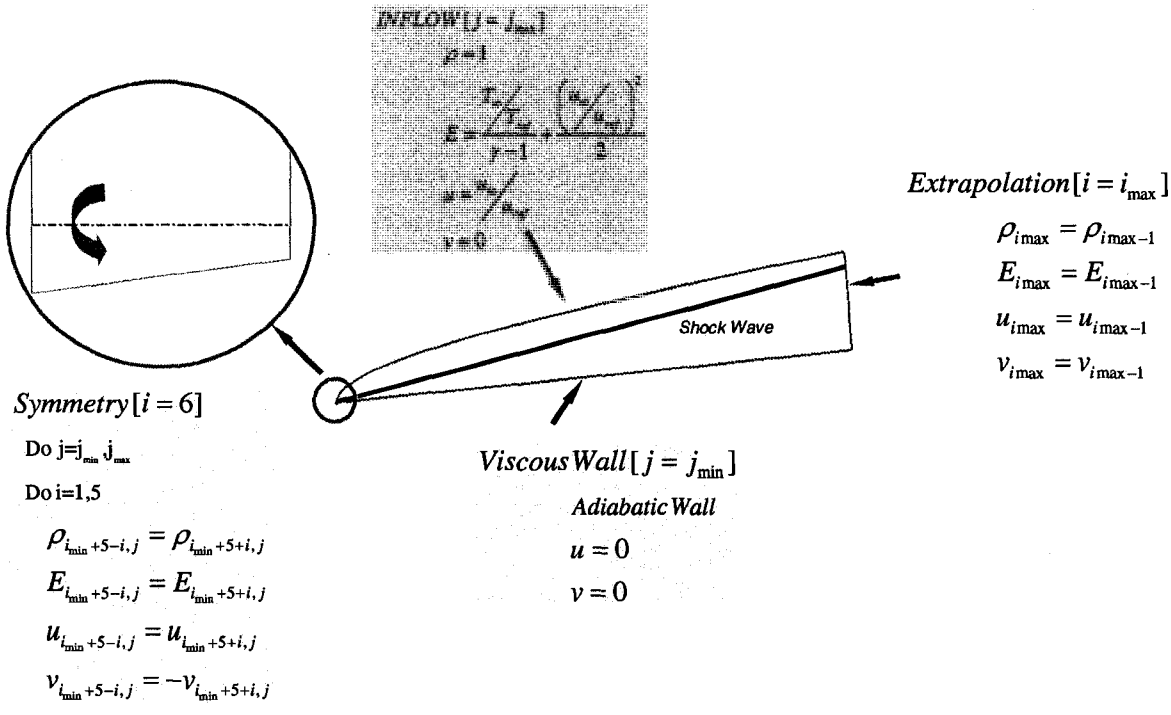

Figure 2.5 Computational domain and boundary conditions.

At the outflow boundary, the extrapolation boundary condition is used. At the wall, viscous conditions for the velocities and adiabatic or isothermal condition for the temperature are used. The density is computed from the continuity equation. The cone and wedge are assumed to align with the free stream, and the symmetry condition is applied to the axis of symmetry of cone and wedge. In the mean flow computations, the simulation prescribes the free stream values at the outer boundary, which lies outside of

the bow shock. In the unsteady computations, it superimposes the acoustic perturbations on the uniform mean flow at the outer edge.

Acoustic disturbance waves are obtained from the linearized Euler equations in a uniform mean flow as follows

$$\begin{aligned}
&\frac{\partial \rho}{\partial t}+U_0\frac{\partial \rho}{\partial x}+\rho_0\frac{\partial u}{\partial x}+\rho_0\frac{\partial v}{\partial y}=0\\
&\rho_0\frac{\partial u}{\partial t}+\rho_0 U_0\frac{\partial u}{\partial x}=-\frac{\partial p}{\partial x}\\
&\rho_0\frac{\partial v}{\partial t}+\rho_0 U_0\frac{\partial v}{\partial x}=-\frac{\partial p}{\partial y}\\
&\rho_0\frac{\partial w}{\partial t}+\rho_0 U_0\frac{\partial w}{\partial x}=-\frac{\partial p}{\partial z}\\
&\rho_0 c_p\frac{\partial T}{\partial t}+\rho_0 U_0 c_p\frac{\partial T}{\partial x}=\frac{\partial p}{\partial t}+U_0\frac{\partial p}{\partial x}\\
&P_0=\rho_0 R T_0\\
&p=\rho_0 R T+\rho R T_0
\end{aligned} \tag{2.51}$$

The solution of this system can be written as

$$\begin{Bmatrix}\rho\\ u\\ v\\ w\\ T\end{Bmatrix}=\begin{Bmatrix}1/a_0^2\\ -\alpha_{ac}/\left(\rho_0\left(\alpha_{ac}U_0-\omega\right)\right)\\ -\varepsilon_{ac}/\left(\rho_0\left(\alpha_{ac}U_0-\omega\right)\right)\\ -\beta_{ac}/\left(\rho_0\left(\alpha_{ac}U_0-\omega\right)\right)\\ (\gamma-1)T_0/\rho_0 a_0^2\end{Bmatrix}p \tag{2.52}$$

Here the pressure p is in the form

$$p=p_{amp}e^{i(\alpha_{ac}x+\varepsilon_{ac}y+\beta_{ac}z-\omega t)} \tag{2.53}$$

The dispersion relation among the wave numbers $\alpha_{ac}, \varepsilon_{ac}, \beta_{ac}$ and the frequency ω is given by

$$(\alpha_{ac}U_0 - \omega)^2 = (\alpha_{ac}{}^2 + \varepsilon_{ac}{}^2 + \beta_{ac}{}^2)a_0{}^2 \tag{2.54}$$

For acoustic disturbances with zero sweep (i.e. $\beta_{ac} = 0$), and zero incident angle (i.e. $\theta = \tan^{-1}\frac{\varepsilon_{ac}}{\alpha_{ac}} = 0$), the x-wave number α_{ac} can be expressed as

$$\alpha_{ac} = \frac{\omega}{(U_0 \pm a_0)} \tag{2.55}$$

The plus sign corresponds to the fast moving wave, and the minus sign corresponds to the slow moving wave. The corresponding phase speeds are $c = U_0 \pm a_0$. The wave number of the fast moving wave is $\alpha_{ac} < \frac{\omega}{U_0+a_0}$ and for the slow moving wave is $\alpha_{ac} > \frac{\omega}{U_0-a_0}$. For free stream Mach number *M=6.0* and nondimensional frequency $F=1.2x10^{-4}$, wave numbers and wave lengths of the slow and fast waves are given in Table 2.2.

Table 2.2. Wave number and wave length for the slow and fast acoustic waves. F=1.2x10-4(f = 467.79 kHz)

	α_{ac}	λ (in.)
Slow wave	0.0821	0.0671
Fast wave	0.0586	0.0940

2.12 Computational Grid

The grid is generated using analytical formulae. The grid stretches in the η direction close to the wall and is uniform outside of the boundary layer. In the ξ direction, the grid is symmetric about the leading edge and very fine near the nose and is uniform in the flat region. Figure 2.6 shows that every 10^{th} grid line of the computational grid near the leading edge region.

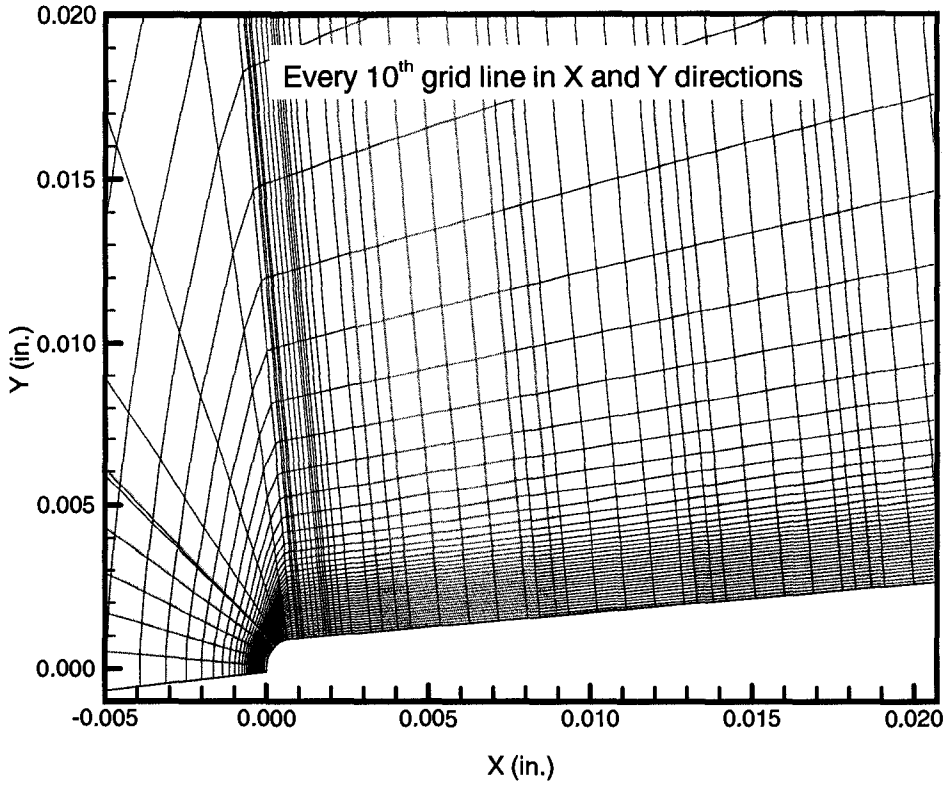

Figure 2.6 The computational grid near nose region.

The outer boundary that lies outside the shock follows a parabola so that the boundary layer growth could be captured accurately. The computational domain extends from x = *-0.015* to *20.0* in. in the axial direction. The length of the computational domain is determined using neutral stability analysis. After obtaining mean flow results, linear stability analysis is performed to find the most amplified frequencies, an N-Factor curve is computed for this frequency, and the location of transition onset determined. The grid distribution in the ξ direction on the flat part of the cone is determined from the wavelength (Table 2.2) of acoustic disturbance. To capture the disturbance propagation one wavelength is represented by 20 points that give *dx=0.003* in. on the flat part.

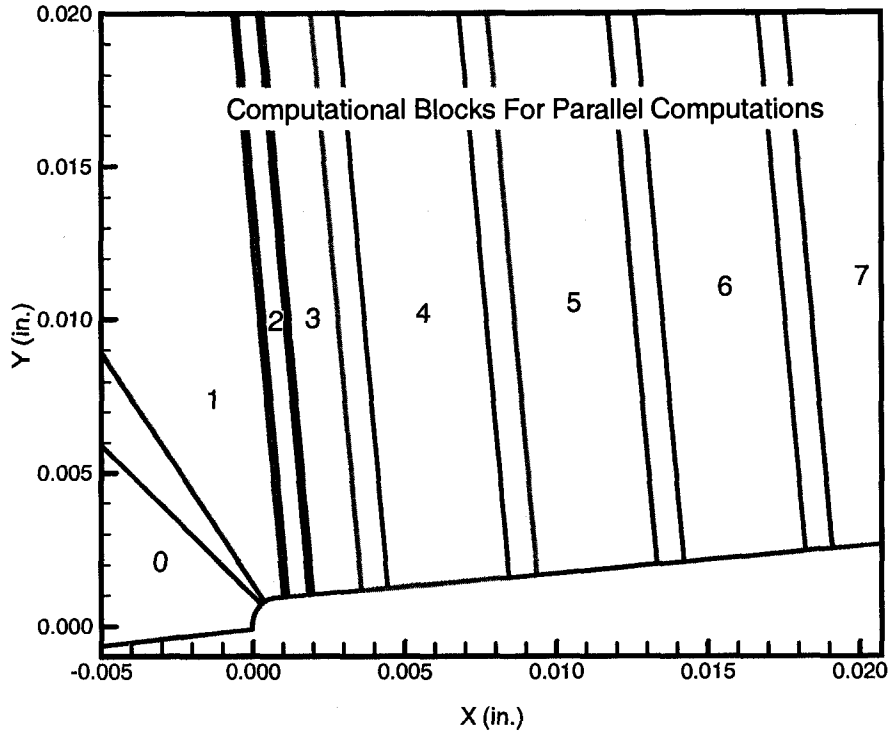

Figure 2.7 Computational blocks for parallel computation.

Calculations were performed using a grid that has 32 blocks; each block has *127x425* grid points. The computational domain has approximately 2 million grid points. Due to the very fine grid requirement near the nose, the allowable time step is very small and the computations become very expensive to simulate the unsteady computations in the entire domain.

Figure 2.7 shows the streamwise partitioning of the computational domain in the nose region. In the computation, blocks are numbered from 0 to 31. Although the code is running on 32 processors it can be scalable to any number. Data exchange at the interfaces is done using MPI routines. Each block sends and receives data from a block on the left and on the right. These sending and receiving functions are executed at each step of the Runge-Kutta time iteration. The master node sends the flow parameters to every block and organizes the work between the blocks.

2.13 Solution Algorithm

This section summarizes the solution procedure of this work. The governing equations are solved using a 5^{th} order accurate, Weighted Essentially Non-Oscillatory (WENO) scheme for space discretization and a 3^{rd} order total-variation-diminishing (TVD) Runge-Kutta scheme for time integration. Computations are performed for hypersonic flow at free stream Mach number 6.0 over a 5-degree, half-angle cone with different nose bluntness and wall temperature conditions. Also, cone results are compared with wedge results.

In the first step steady mean flow is computed by performing unsteady computations using a variable time step until the maximum residual reaches a small value, $\sim 10^{-11}$. These computations use a CFL number of 0.2 for the adiabatic case and 0.1 for isothermal cases. Mean flow density and temperature profiles are compared to similarity profiles to validate the results. Also, bow shock standing distance and shock shape are compared with the available formulas. Using mean flow results, linear stability analysis is then performed to find the stability characteristic of the mean flow. Neutral stability diagrams and N-Factor curves are calculated, and the most amplified frequency is found. In the next step unsteady disturbances with the most amplified frequency are introduced at the upper boundary of the computational domain and time accurate computations are performed to investigate the interaction and evolution of these disturbances to downstream. Since a very fine spatial grid is used to resolve the leading edge region, these computations require a very small time step that is taken as the minimum time step allowable for the CFL number given in Equation (2.50).

The acoustic field that impinges on the outer boundary is taken to be in the following form.

$$p' = Real\left\{\tilde{p}e^{i\alpha_{ac}x \pm i\varepsilon_{ac}y - i\omega t}\right\} \tag{2.56}$$

Here α_{ac}, ε_{ac} are the x, y wave numbers, respectively, of the acoustic wave, and ω is the corresponding frequency of the acoustic disturbance. The incident angle θ of the acoustic wave is defined as

$$\theta = \tan^{-1}\frac{\varepsilon_{ac}}{\alpha_{ac}} \tag{2.57}$$

and in this study computations are performed for zero incidence angles.

2.14 Summary

In this chapter, we have discussed the governing equations, numerical algorithms and boundary conditions for direct numerical simulation of Navier-Stokes equations in two-dimensional and axisymmetric coordinates. In the next few chapters, we will apply these theories and numerical methods to analyze hypersonic boundary layer receptivity due to free stream acoustic disturbances over blunt cones and wedges. First, developed code is validated with available experimental data. Then a DNS was performed to study evolution of two-dimensional acoustic disturbances over cone and wedge, and receptivity characteristics were compared. Finally, nose bluntness and wall cooling effects on the hypersonic boundary layer stability and receptivity are investigated. DNS results were checked using linear stability theory (LST) and parabolized stability equations (PSE).

CHAPTER III

3. CODE VALIDATION

In this study our objective is to solve hypersonic steady and unsteady flow around circular cones and wedges to study hypersonic boundary layer receptivity and transition problems. For this reason, a 5^{th} order accurate flow solver is developed. In this chapter, to validate the axisymmetric solver a series of comparisons with the data available in the literature was performed.

3.1 Comparison with Mair's Experiment

Mair[30] performed experiments on blunt-nosed bodies in supersonic flow and some of his results were included in Van Dyke's[31] famous An Album of Fluid Motion. In this section supersonic flow field around hemisphere-cone is computed and results are compared with Mair's[30] experiment. Table 3.1 gives the flow parameters, and Figure 3.1 shows the comparison of the flow field.

Table 3.1 Flow parameters for Mair's[30] wind tunnel model.

Free stream		
Mach number	M_∞ =	1.96
Reynolds number	Re_∞ =	1.3×10^7 / m
Density	ρ_∞ =	0.2922 kg / m^3
Velocity	U_∞ =	511.76 m / s
Reservoir Pressure	P_0 =	14230.9 N / m^2
Reservoir Temperature	T_0 =	169.65 °K
Wall temperature	Adiabatic condition	
Prandtl number	Pr =	0.70
Ratio of specific heats	γ =	1.4
Length scale (x_0=0.5m)	$\sqrt{\nu_\infty x_0 / U_\infty}$ =	6.5×10^{-3} m

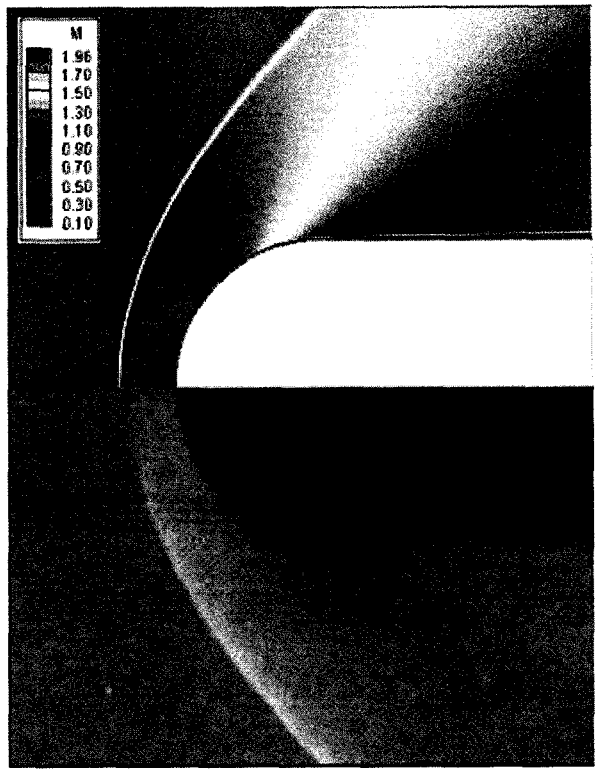

Figure 3.1 Comparison of Mach contours with Mair's[30] experiment.

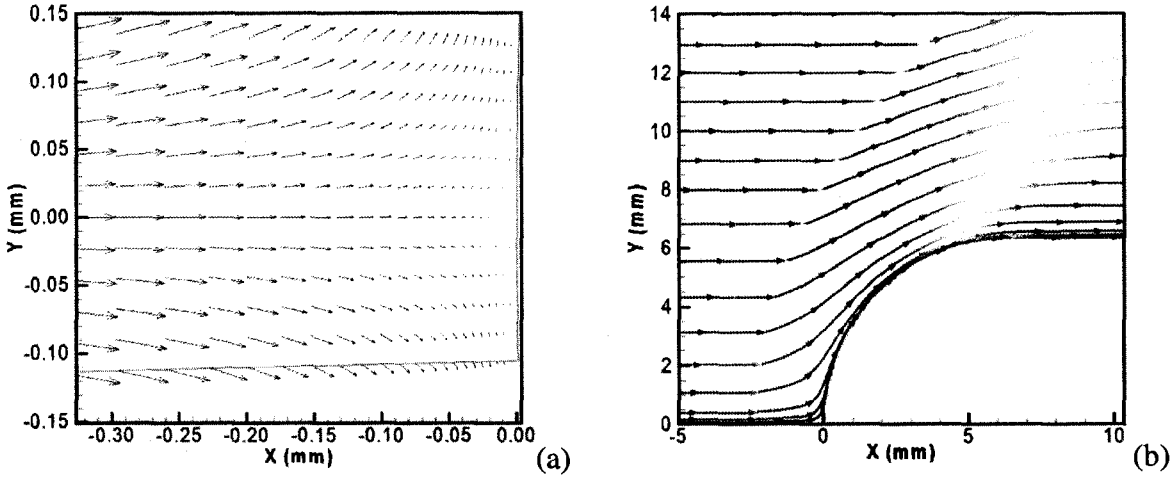

Figure 3.2 (a) Velocity vectors near the stagnation point. (b) Streamlines colored by Mach contours near the leading edge.

Figure 3.1 clearly shows that the shock shape, bow shock standing distance matched perfectly. Velocity vectors near the stagnation point are shown in Figure 3.2 (a). From this figure one can easily see that flow is decelerating and stops on the stagnation streamline. Also, Figure 3.2 (b) shows the streamlines near the leading edge colored by Mach contours. In this figure uniform flow comes from left parallel to the x-axis and sees the bow shock and changes its direction.

3.2 Comparison of Bow Shock Shape and Standoff Distance

Bow shock shape and standoff distance are flow features that are reasonably easy to measure in experiments using optical techniques such as Schlieren imaging and shadowgraphs[32]. The position and shape of the shock is strongly dependent on flow physics and will not be correctly predicted by a CFD solver with an improper implementation of the Navier-Stokes or Euler equations[33]. In this section we will consider bow shock standing distance and shock shapes.

Ambrosio and Wortman[34] developed a correlation for shock standoff distances as a function of Mach number. The correlations are given as follows

$$\frac{\delta}{R} = 0.143 e^{\frac{3.24}{M_\infty^2}} \tag{3.1}$$

$$\frac{\delta}{R} = 0.386 e^{\frac{4.67}{M_\infty^2}} \tag{3.2}$$

for sphere-cones and cylinder-wedges, respectively. Bow shock standoff distance is denoted by δ, and R is the nose radius of the body. Simulations performed for Mach numbers ranges from 1.5 to 6.0. Table 3.2 shows the computational parameters used in

these simulations. The nose part is modeled as a sphere and cylinder for cone and wedge respectively, and nose radius is 0.03125 in. for both. The length of the model is 0.2 in. and the flat part has a 5-degree, half-angle. Computations were performed using two-dimensional and axisymmetric WENO codes on a 721 x 321 cell grid.

Table 3.2 Flow parameters for Horvarth's[35] experiment.

Free stream		
Mach number	M_∞ =	6.0
Reynolds number	Re_∞ =	7.8×10^6 / ft
Density	ρ_∞ =	7.059×10^{-3} lbm / ft^3
Velocity	U_∞ =	3140.21 ft / s
Reservoir Pressure	P_0 =	475 psi
Reservoir Temperature	T_0 =	475 °F
Wall temperature	Adiabatic condition	
Prandtl number	Pr =	0.72
Ratio of specific heats	γ =	1.4
Length scale (x_0=0.05in)	$\sqrt{\nu_\infty x_0 / U_\infty}$ =	7.308×10^{-3} ft

Simulated standoff distances are presented in Figure 3.3, together with the curves of Equations (3.1) and (3.2). Very good agreement is observed for both cone and wedge geometries at high Mach numbers, with results diverging slightly at lower speeds. This happened due to the same grid, which is used for all simulations.

Additionally, some empirical correlations for shock shape based on experimental results are given by Billig[36] and summarized by Anderson[37, 38] as follows

$$x = R + \delta - R_c \cot^2 \beta \left[\left(1 + \frac{y^2 \tan^2 \beta}{R_c^2} \right)^{1/2} - 1 \right] \tag{3.3}$$

$$\frac{R_c}{R} = 1.143 e^{\frac{0.54}{(M_\infty - 1)^{1.2}}} \qquad sphere - cone \tag{3.4}$$

$$\frac{R_c}{R} = 1.386 e^{\frac{1.8}{(M_\infty - 1)^{0.75}}} \qquad cylinder - wedge \tag{3.5}$$

Equation (3.3) gives the shock shape in Cartesian coordinates. Here R is the radius of the nose. R_c is the radius of curvature of the shock wave at the vertex of the hyperbola, δ is the shock standoff distance, x and y are Cartesian coordinates, and β is the wave angle for an attached shock wave in the inviscid limit[37, 38].

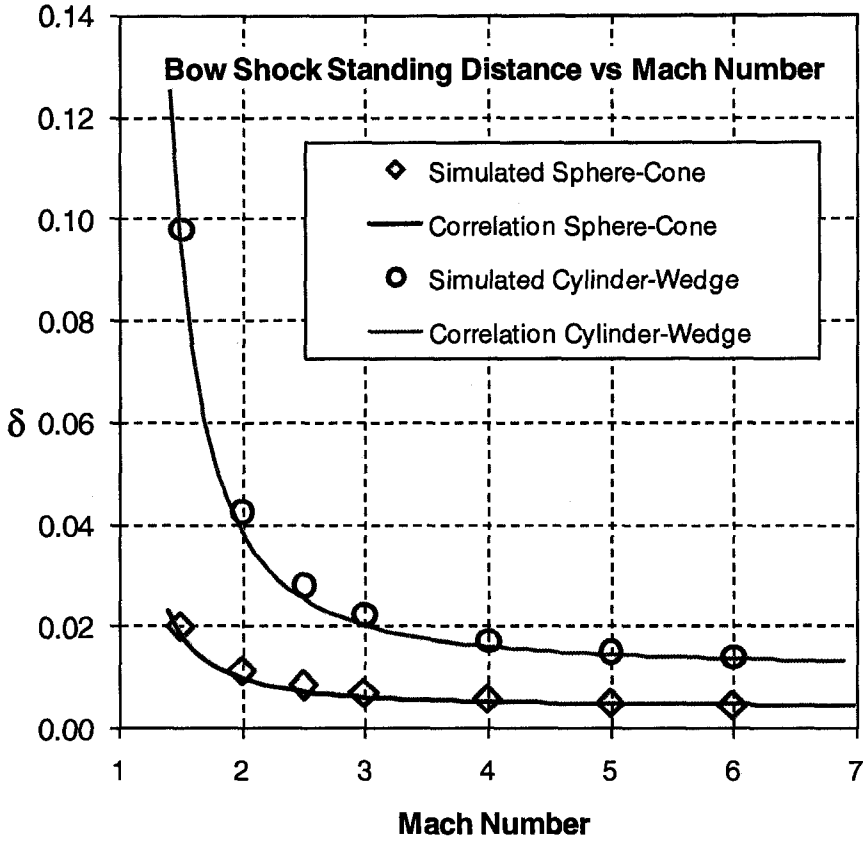

Figure 3.3 Bow shock standoff distances obtained by simulation compared with the predictions from the correlations of Ambrosio and Wortman[34].

Here shock shape is constrained to a hyperbolic curve fit which asymptotes to the freestream Mach angle[37, 38], μ, given by

$$\mu = \arcsin\left(\frac{1}{M}\right) \tag{3.6}$$

In addition to code validation, shock shape is also used to help the grid generation process. To enforce the inflow boundary condition on the $j=j_{max}$ line shock shape needs to be known and upper boundary, which lies outside the bow shock is, created based on this information.

Figures 3.4 and 3.5 show the comparison of bow shock shape obtained by numerical simulation with the predictions from the correlations of Billig[36] for sphere-cone and cylinder-wedge, respectively. The figures show Mach contours. The white dotted lines are obtained from Equation (3.3) and show the empirical results.

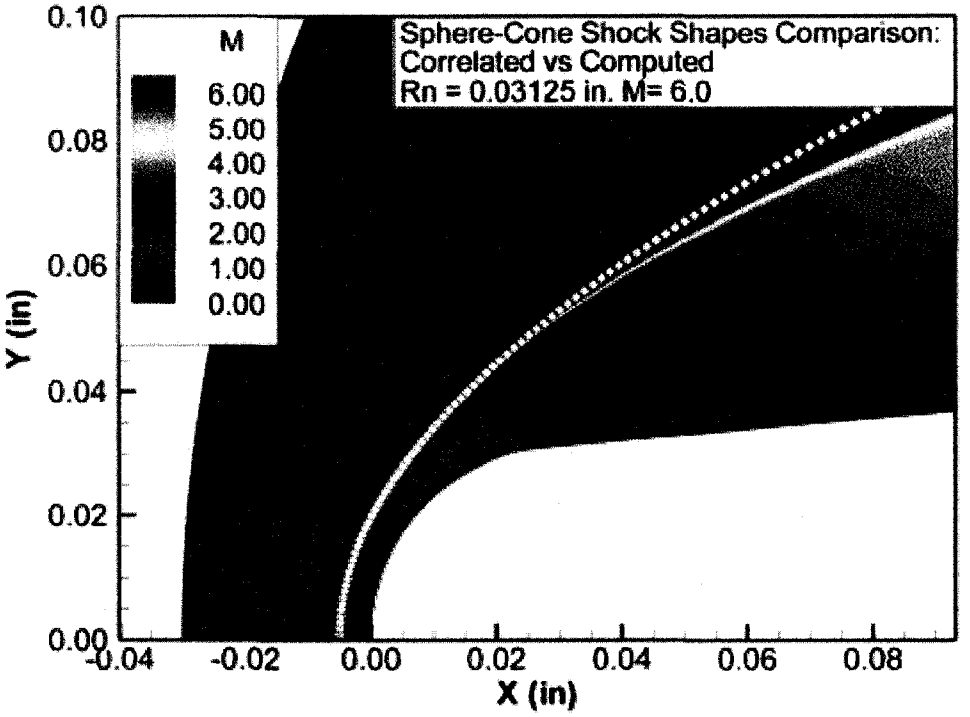

Figure 3.4 Bow shock obtained by simulation for cone compared with the predictions from the correlations of Billig[36].

In the nose region simulated and correlated shock shapes are matched very well but away from the leading edge they separated from each other. Since the correlations are

based on a number of experimental results containing scatter, perfect agreement is not expected.

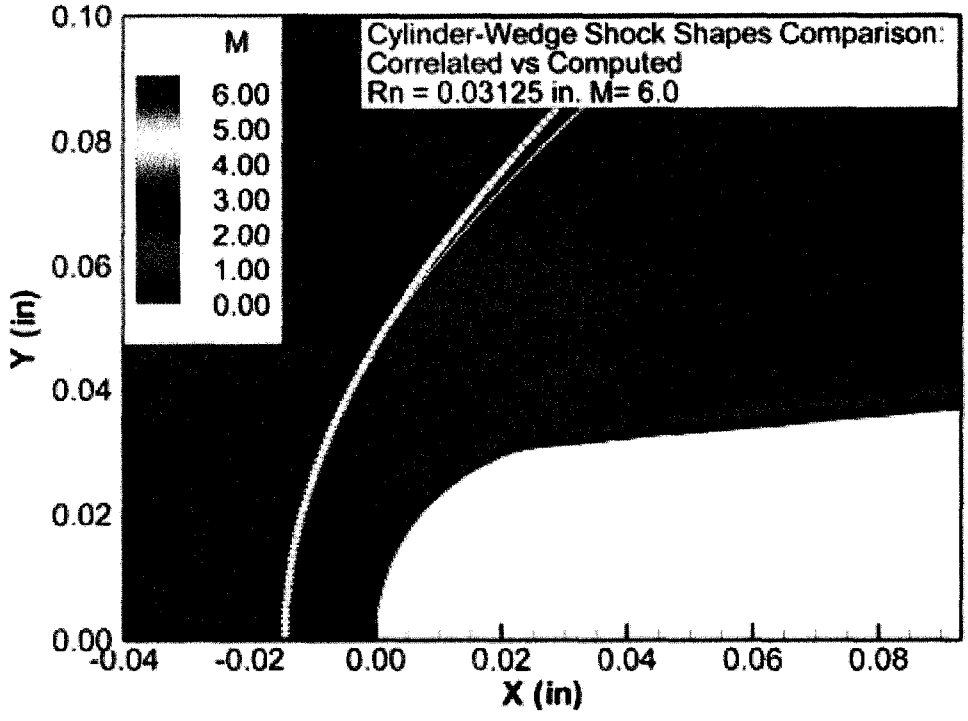

Figure 3.5 Bow shock obtained by simulation for wedge compared with the predictions from the correlations of Billig[36].

3.3 Comparison of Wall to Total Temperature Ratios

Horvath et al.[35] investigated the effect of bluntness on the transition onset at Mach 6.0 for 5-degree, half-angle cones. Figure 3.6 shows the schematic diagram of the experimental model. They measured wall to total temperature ratio to see the effect of bluntness on boundary layer transition. In this section computations were performed for three different nose bluntness that are used in the experiment[35], and wall to total temperature ratios in the laminar part are compared. Computational parameters are the same as the parameters given in Table 3.2, but the length of computational domain and

grid resolution is different for each case where nose radii are 0.0625, 0.3125, and 0.001 in.

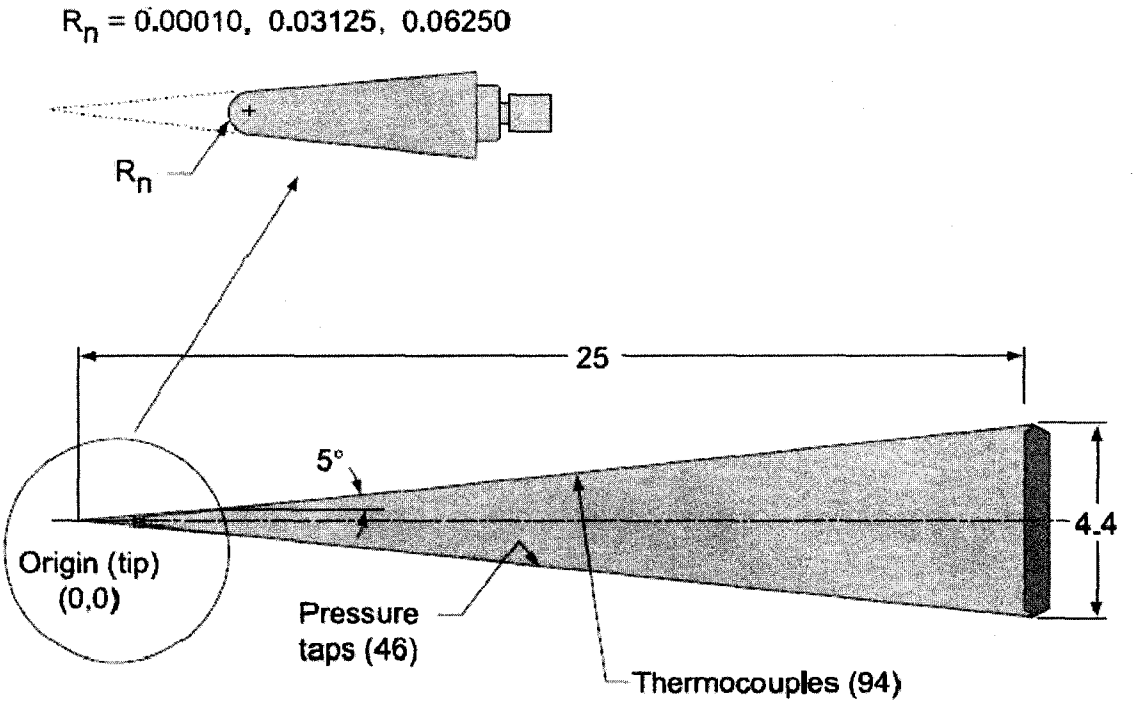

Figure 3.6 Schematic diagram of the experimental model[35].
M_∞=6.0, Re=7.8x10^6 /ft, T_0=475 °F, P_0=475psi

Figure 3.7 shows the comparison of simulated wall to total temperature ratio with conventional wind tunnel data[35] 5-degree straight cone of tree different nose radii, 0.0625, 0.03125, and 0.001 in. Adiabatic wall to total temperature ratio is 0.86 for all cases. In Figure 3.7 red lines show the simulation results, which match perfectly with the experimental results shown by a dotted black line. The transition location is observed at x=11 in. for Rn=0.0625 in. From leading edge to this point, flow is laminar, and it becomes turbulent after x=15 in. Between these regions is called as transition region. Good agreement is obtained in all three simulations until the transition onset point.

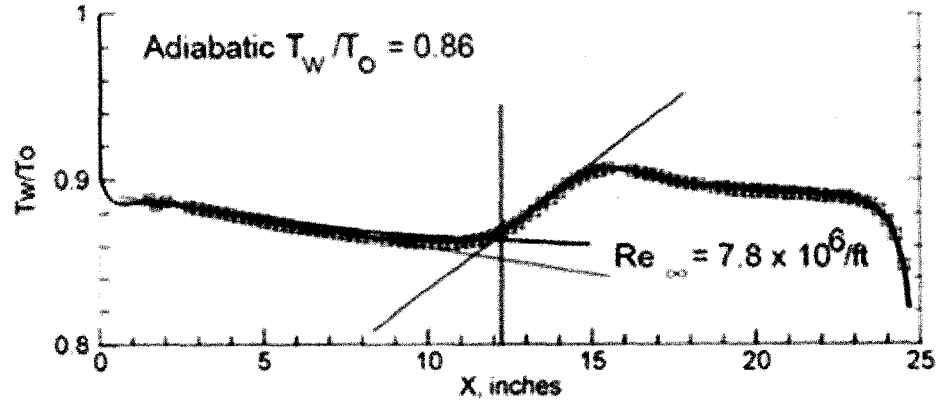

a) Rn=0.0625 in

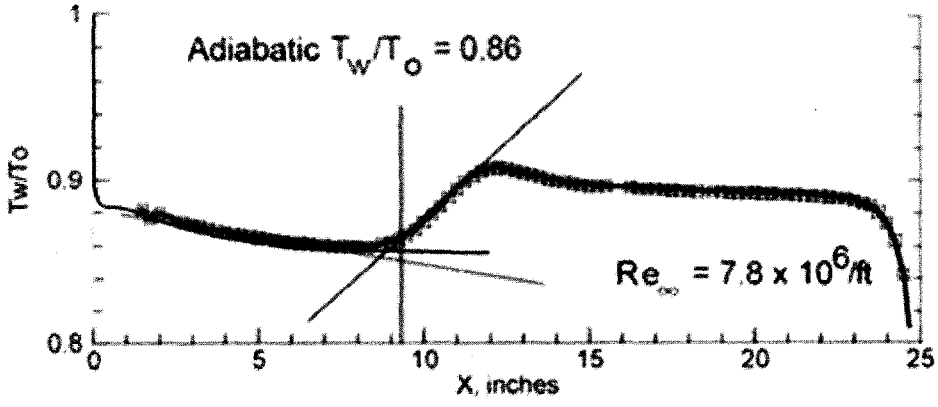

b) Rn=0.03125 in

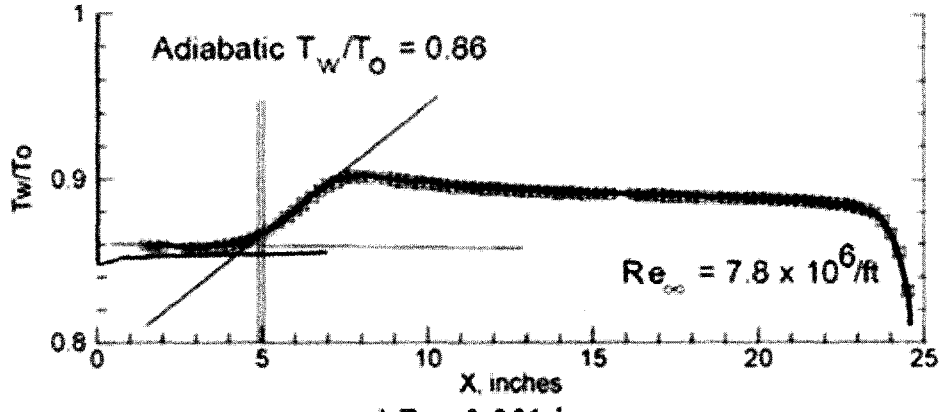

c) Rn=0.001 in

Figure 3.7 Comparison of simulated wall to total temperature ratio with conventional wind tunnel data[35] for different nose radii of 5-degree, half-angle straight cone (a) Rn=0.0623 in. (b) Rn=0.03125 in. (c) Rn=0.001 in.

Since we are interested in receptivity and boundary layer transition problems that occur in the leading edge and the laminar part of the flow, the comparison is done only for the laminar region.

3.4 Comparison with Similarity Solutions

Preceding sections of this chapter showed that axisymmetric and two-dimensional solvers produce good results. In addition to these validation cases, for every mean flow simulation we also compared the mean flow density and/or temperature profiles over the body at different axial locations with similarity solutions. Similarity profiles are obtained by solving boundary layer momentum and energy equations given as

$$\frac{d}{d\eta}\left(\frac{\rho\mu}{\rho_\infty\mu_\infty}f''\right)+ff''=0 \tag{3.7}$$

$$\frac{d}{d\eta}\left(\frac{\rho\mu}{\rho_\infty\mu_\infty}\frac{g'}{\mathrm{Pr}}\right)+fg'+(\gamma-1)M_\infty^2\left(\frac{\rho\mu}{\rho_\infty\mu_\infty}\right)f''^2=0 \tag{3.8}$$

The boundary conditions for these equations are

$$\begin{aligned} &f_{(\eta=0)}=f'_{(\eta=0)}=0\\ &f_{(\eta\to\infty)}=g_{(\eta\to\infty)}=1\\ &g'_{(\eta=0)}=\begin{cases}0 & Adiabatic\,Wall\\ \dfrac{T_w}{T_\infty} & Isothermal\,Wall\end{cases}\end{aligned} \tag{3.9}$$

Equations (3.7) and (3.8) are solved using a 4^{th} order Runge-Kutta scheme with the given boundary conditions.

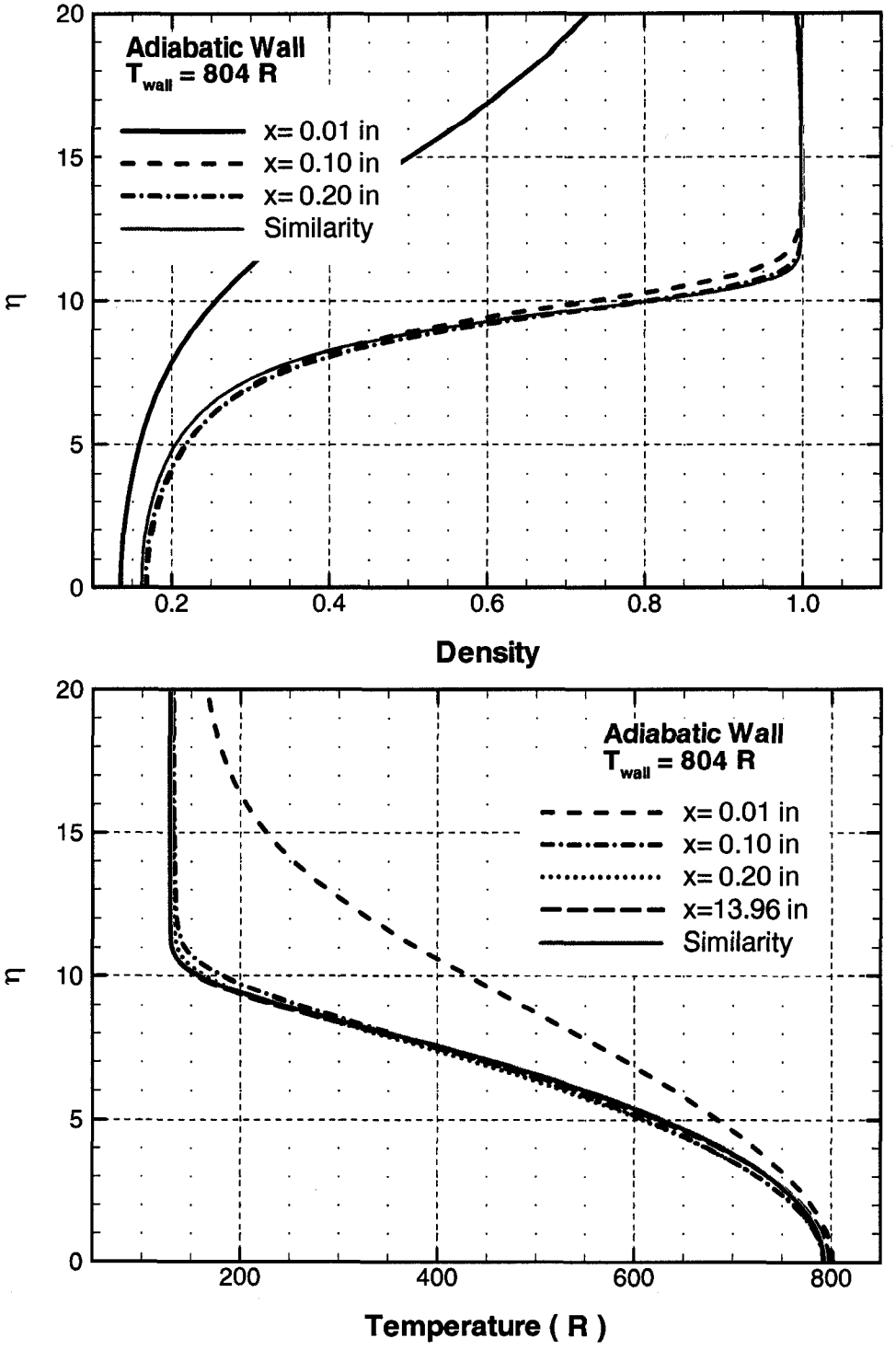

Figure 3.8 Comparison of mean flow (a) density and (b) temperature profiles at different axial locations in similarity coordinates with similarity solutions. Rn=0.001 in. M=6.0

3.5 Summary

In this chapter, we have shown the validation studies of axisymmetric code. Results are compared with available experimental data, empirical formulation and analytical methods. Very good agreements are obtained in the comparisons. In addition to these results for the following chapters, mean flow profiles compared with similarity solutions and unsteady computations are performed after validating the steady mean flow results. Also, mean flow pressure distribution along the surface, boundary layer edge Mach number and temperature are checked. Oblique shock converged to inviscid shock angle for cone and wedge. Results of this chapter were published by the author[39, 40]. In the next few chapters, we will apply these theories and numerical methods to analyze hypersonic boundary layer receptivity due to free stream acoustic disturbances over blunt cones and wedges. First we will compare the receptivity of hypersonic boundary layers due to small acoustic disturbances over cone and wedge.

CHAPTER IV

4. RECEPTIVITY OF BLUNT CONE AND WEDGE

4.1 Introduction

In this chapter the transition process induced by the interaction of acoustic disturbances in the free-stream with boundary layers over a 5-degree straight cone and a wedge with a blunt nose is numerically investigated at a free-stream Mach number of 6.0. To compute the shock and the interaction of shock with the instability waves, the Navier-Stokes equations are solved in two-dimensional and axisymmetric coordinates. The governing equations are solved using the 5^{th} order accurate, Weighted Essentially Non-Oscillatory (WENO) scheme for space discretization and using 3^{rd} order Total-Variation-Diminishing (TVD) Runge-Kutta scheme for time integration.

After the mean flow field is computed, acoustic disturbances are introduced at the outer boundary of the computational domain, and unsteady simulations are performed.

Generation and evolution of instability waves and the receptivity of boundary layer to slow and fast acoustic waves are investigated. The mean flow data are compared with the experimental results and similarity solutions. The results show that the instability waves are generated near the leading edge, and the non-parallel effects are stronger near the nose region for the flow over the cone than that over a wedge. It is also found that the boundary layer is much more receptive to the slow acoustic wave (by almost a factor of 67) as compared to the fast wave.

4.2 Literature Review

There have been a number of investigations conducted on the interaction of acoustic waves with supersonic boundary layers. The interactions of acoustic waves with a supersonic boundary layer using inhomogeneous stability equations were investigated by Mack[41] and Gaponov[42]. One important finding was that due to the interaction, the acoustic waves excite disturbances inside the boundary-layer, which is much larger than that in the free stream. The interaction of stream acoustic waves with a non-parallel boundary layer was studied by Gaponov and Smorodsky[43]. The analysis and the calculations showed that the disturbances inside the boundary layer reach values significantly higher compared to that in the free-stream. It was also observed that there exists a critical Reynolds number where this excitation is the highest.

For a supersonic boundary layer with sufficiently high Mach number to allow both first and second Mack modes[44], Fedorov and Khokhlov[45] considered boundary layer response to both the fast and slow acoustic waves. The boundary layer modes excited near the leading edge by the two acoustic waves can be referred to as Mode F and Mode S, for convenience. The work of Fedorov and Khokhlov[46] and Fedorov[47] identified two receptivity mechanisms in this Mach number regime: (1) leading-edge receptivity and (2) inter-modal exchange between Mode F and Mode S. For the adiabatic wall, Federov[47] found that receptivity to slow acoustic waves could be as much as 50 times the receptivity via the fast acoustic waves. Thus, the leading edge receptivity via the slow mode excitation is much stronger than in the case of inter-modal exchange. According to Fedorov[47], this receptivity mechanism may gain significance in the highly cooled boundary layers.

Ma and Zhong[48-50] performed direct numerical simulation for a Mach 4.5 flat-plate boundary layer to investigate receptivity to fast and slow acoustic waves and the mechanisms of inter-modal exchange. They employed a fifth-order accurate shock fitting method to solve the governing equations. Egorov, Fedorov and Soudakov[51] investigated a similar problem at a Mach number of 6.0 whereby simulation of receptivity to slow and fast acoustic waves and the effect of incidence angle on the receptivity were studied.

The transition process induced by the interaction of acoustic disturbances in the free stream was numerically investigated for a boundary layer over a flat plate with a blunted leading edge at a free stream Mach number of 3.5 by Balakumar[22]. The governing equations are solved using 5^{th} –order accurate Weighted Essentially Non-Oscillatory (WENO) scheme for space discretization and 3^{rd} –order TVD Runge-Kutta scheme for time integration. Balakumar[21] also investigated the receptivity of boundary layers over blunt flat plates and wedges at a free stream Mach number of 3.5 and at a high Reynolds number of 10^6 /in. The linear stability result of his work showed that the bluntness has a strong stabilizing effect on the stability of two dimensional boundary layers. It was also revealed that the boundary layers on blunt wedges are far more stable than on blunt flat plates. Malik and Balakumar[52] investigated the receptivity of supersonic boundary layers to acoustic disturbances at a free stream Mach number of 4.5. The results showed that the instability waves are generated near the leading edge region and that the boundary layer is much more receptive to slow acoustic waves by almost a factor of 20 compared to fast acoustic waves. The effect of the acoustic wave incidence angle was also investigated, and it was found that the receptivity of the boundary layer on the wind ward side decreases when the incidence angle is increased.

An experimental investigation was conducted on a 5-degree, half-angle cone in a conventional Mach 6 wind tunnel by Horvath et al[35] to examine the effects of facility noise on boundary layer transition. They checked the influence of tunnel noise on the transition onset points by comparing transition locations determined from their test to those previously obtained in a Mach 6 low disturbance quiet tunnel.

Here, we employ a fifth order weighted essentially non-oscillatory (WENO) scheme for spatial discretization and use a third order total variation diminishing (TVD) Runge-Kutta scheme for time integration to solve for the hypersonic boundary layer receptivity problem.

The objectives of this chapter are to understand the receptivity process near the leading edge of a cone and to estimate the receptivity coefficient of the instability waves generated near the leading edge. Computations are performed to determine whether the slow or the fast acoustic waves are more efficient in generating the instability waves. Also, comparisons of computed shock standoff distances with the experimental results are shown. To compare the receptivity process between the axisymmetric and two-dimensional geometries, computations are performed for the hypersonic flows over a cone and a wedge.

4.3 Mean Flow Results

For this study, we have selected the following flow conditions (Table 3.2), geometry (Figure 3.6) used by Horvath et al.[35] and computational set up (Figure 2.5). The cone has a small nose radius (Rn=0.001 in.), and the flow around the leading edge is resolved by using a sufficiently dense grid. We assume adiabatic wall conditions for

steady flow computations. Boundary conditions, computational grid and the solution algorithm used in this chapter to obtain steady mean flow are given in Sections 2.11-2.13, respectively. Flow conditions at the boundary layer edge for the cone and wedge are given in Table 4.1.

Table 4.1 Conditions at the edge of the boundary layer.

$(Var.)_{edge} / (Var.)_{\infty}$	Cone	Wedge
Mach Number	0.932	0.885
Pressure Ratio	1.560	2.069
Density Ratio	1.372	1.663
Temperature Ratio	1.137	1.244

Figure 4.1 illustrates the mean flow data for the cone and the wedge computed using the WENO code. The figures on the left show the contours for the cone and the figures on the right show the results for the wedge. Figures 4.1 (a) and (b) show the mean flow density contours for the entire domain obtained by the Navier-Stokes computations. As expected, the bow shock for the cone is narrower than that for the wedge because of the relieving effect of axisymmetry.

Figures 4.1 (c), (d) show the density contours and (e), (f) show the Mach contours near the leading edge for the cone and wedge respectively. The bow shock for the cone is located at $\delta_{cone}=2.4\text{x}10^{-4}$ in. upstream of the leading edge, and for the wedge it is at $\delta_{wedge}=5.6\text{x}10^{-4}$ in. Beyond the expansion fan the shock angles approach an inviscid shock angle of 10.6 degrees for the cone and 13.1 degrees for the wedge. Figures 4.2 (a) and (b) show the streamline patterns colored by Mach contours. Figure 4.2 (b) clearly shows that the boundary layer is thicker, and deflection of the flow due to bow shock is larger for the wedge.

The density profiles at x = 0.01, 0.03, 0.05, 8.94 in. ($\sqrt{Re_x}$= 87, 151, 196, 2615) are plotted in Figure 4.3 (a) and (b) in similarity coordinate for the cone and the wedge. The compressible Blasius similarity profile is also included for comparison. The density profiles approach the similarity solutions close to x=0.1-in. for the cone. However, the density profile of the wedge is away from the similarity solution even at the end of the computational domain x = 9 in. This implies that the bluntness effects are stronger and persist for a longer distance for flow over wedges compared to flow over cones. Figures 4.4 (a) and (b) depict the same mean density profiles in physical coordinates. These figures clearly show that the flow becomes self similar for the cone after it passes the nose part, but for the wedge non-parallel effects are dominant even at the end of the flat part.

Figure 4.5 (a) shows the mean flow wall pressure distribution along the surface for the cone and the wedge, and Figure 4.5 (b) shows the variation of the boundary layer edge Mach number. Figure 4.5 (b) also illustrates that there is a strong bow shock located very close to the leading edge, and the associated compression is followed by an expansion over the leading edge. Then the shock approaches the inviscid solution for the cone and the wedge at x=8.9 in., M_e=5.57 and T_e=129.61°R and M_e=5.29 and T_e=141.79°R for cone and wedge respectively.

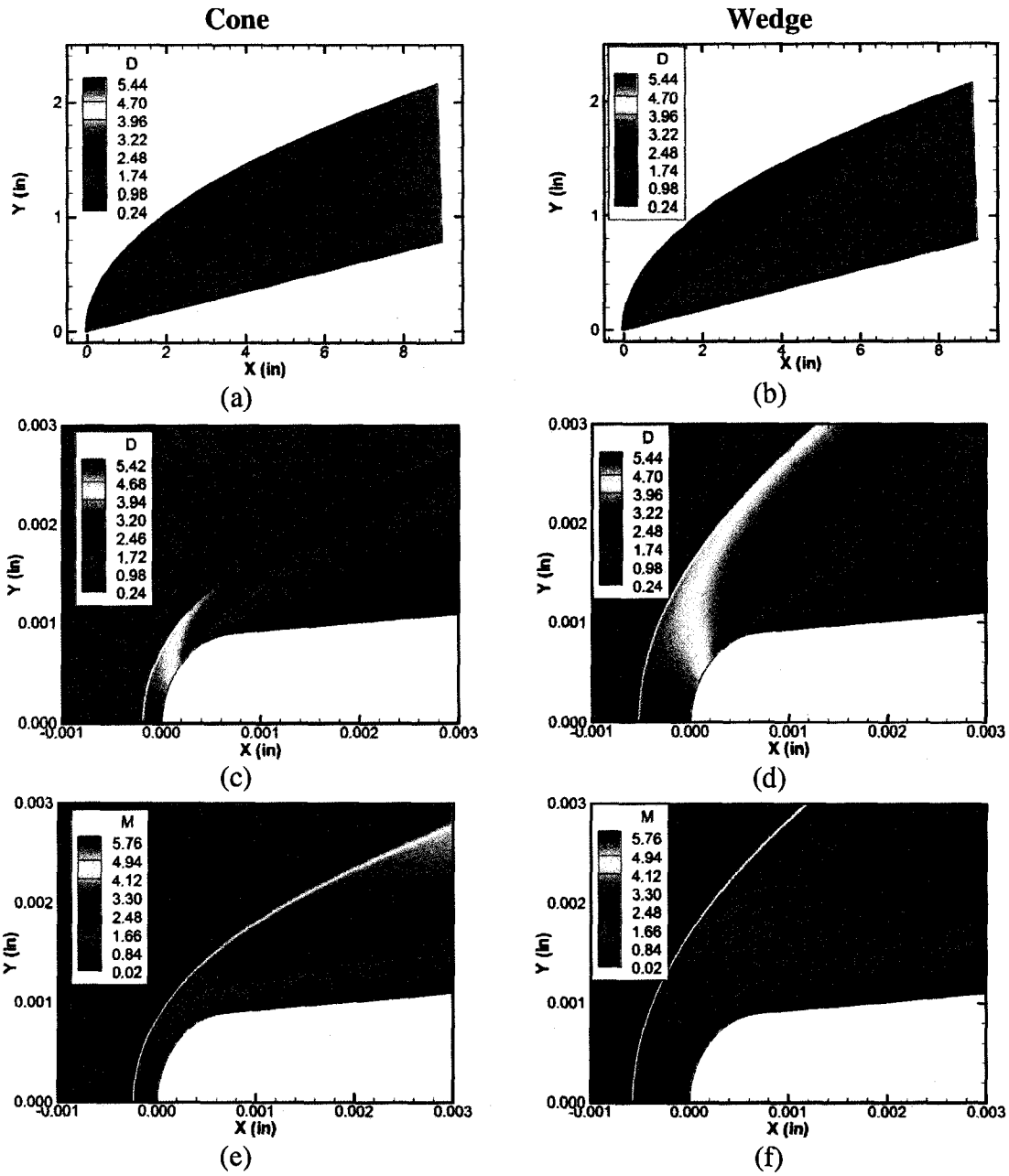

Figure 4.1 Comparison of mean flow density and Mach contours for cone and wedge at freestream Mach number 6.0. Cone results are on the left and wedge results are on the right. (a) and (b) show density contours in the whole domain; (c) and (d) show density contours at the leading edge; (e) and (f) show Mach contours at the leading edge region.

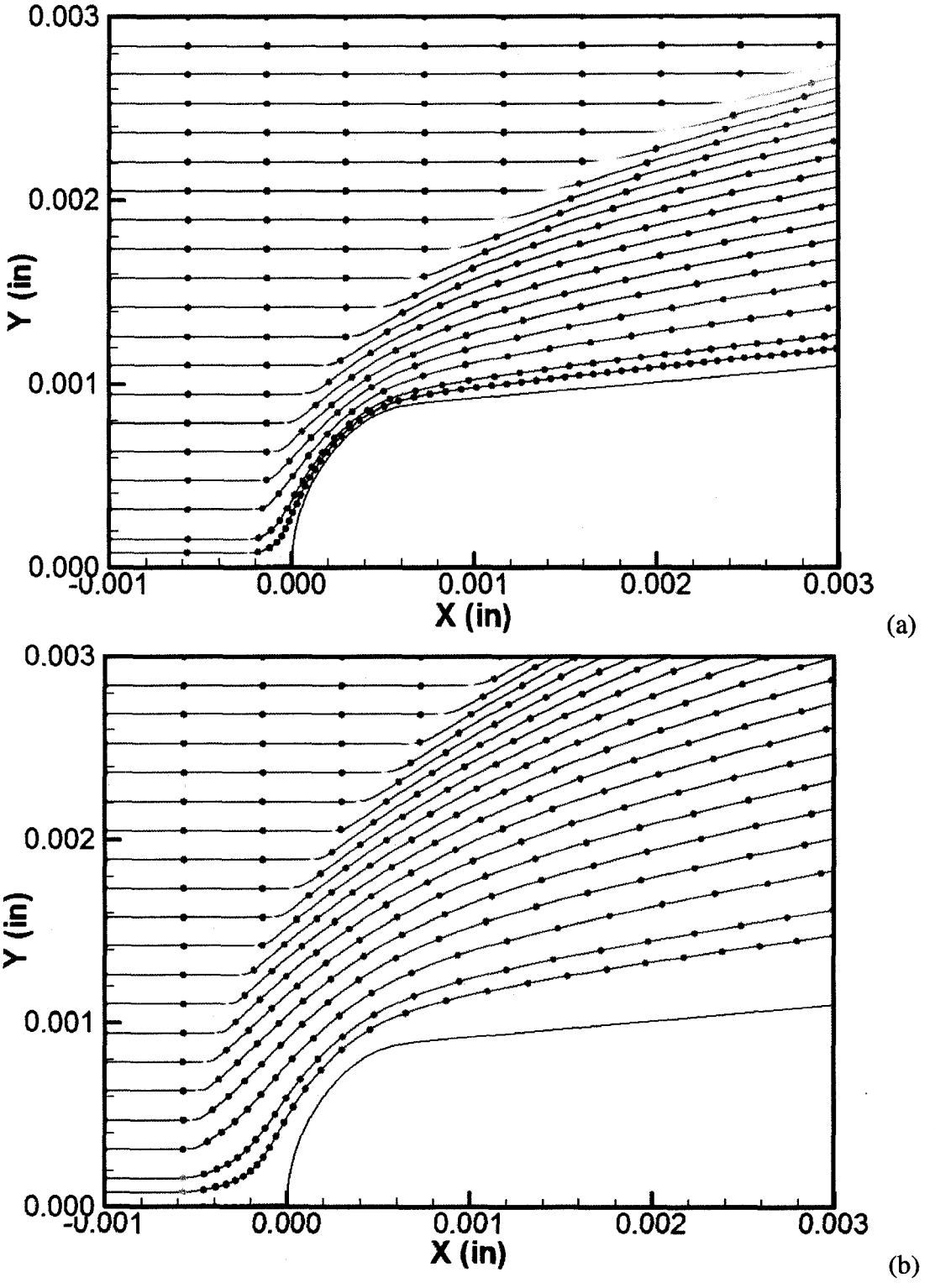

Figure 4.2 Mean flow streamlines colored by Mach contours in the leading edge region. (a) Cone, (b) Wedge.

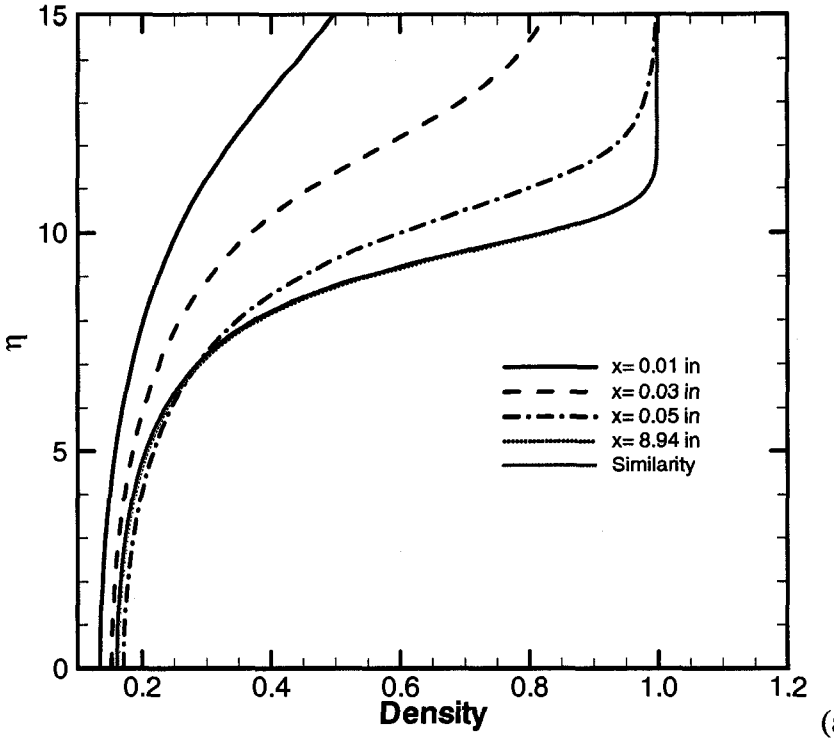

(a)

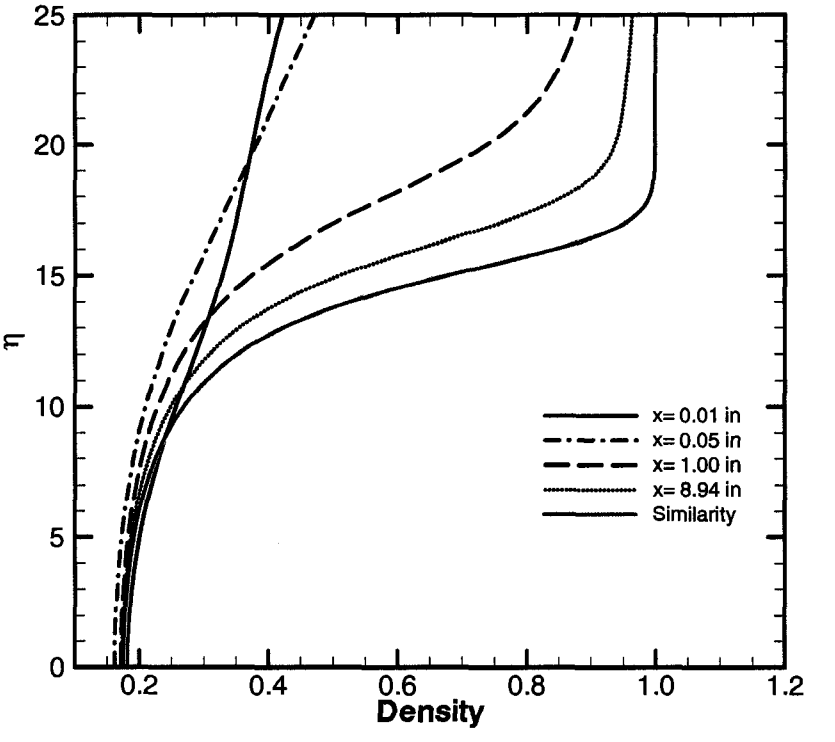

(b)

Figure 4.3 Mean flow density profiles at different axial locations for (a) cone and (b) wedge compared with similarity profiles.

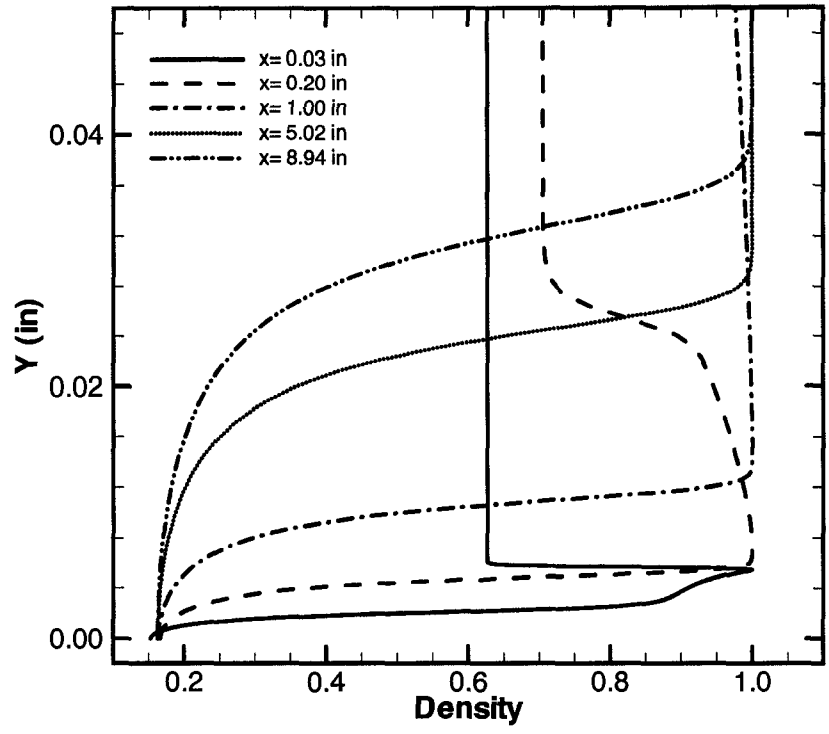

(a)

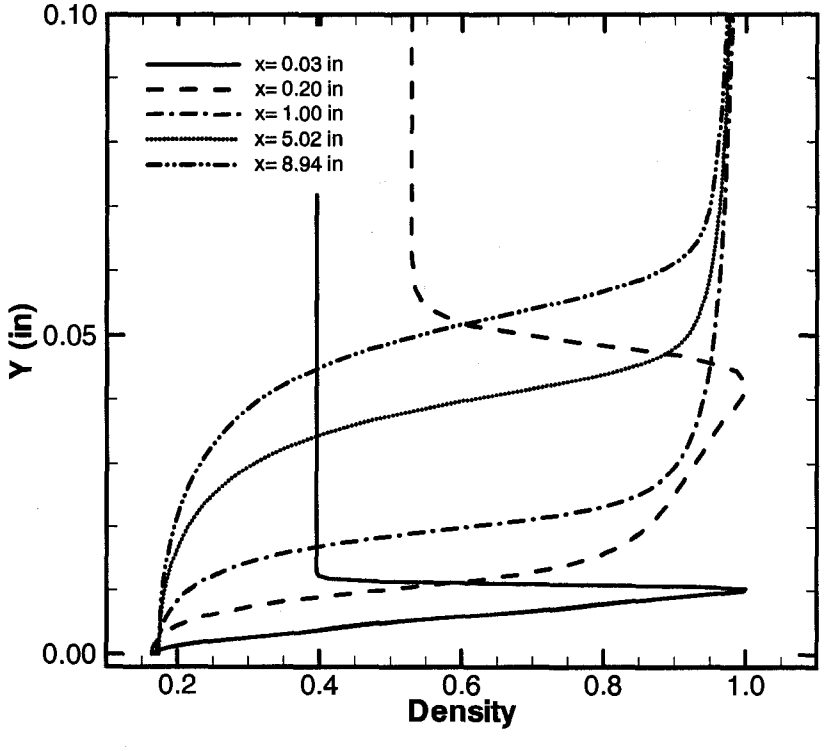

(b)

Figure 4.4 Mean flow density profiles at different axial locations for (a) cone and (b) wedge in physical coordinates.

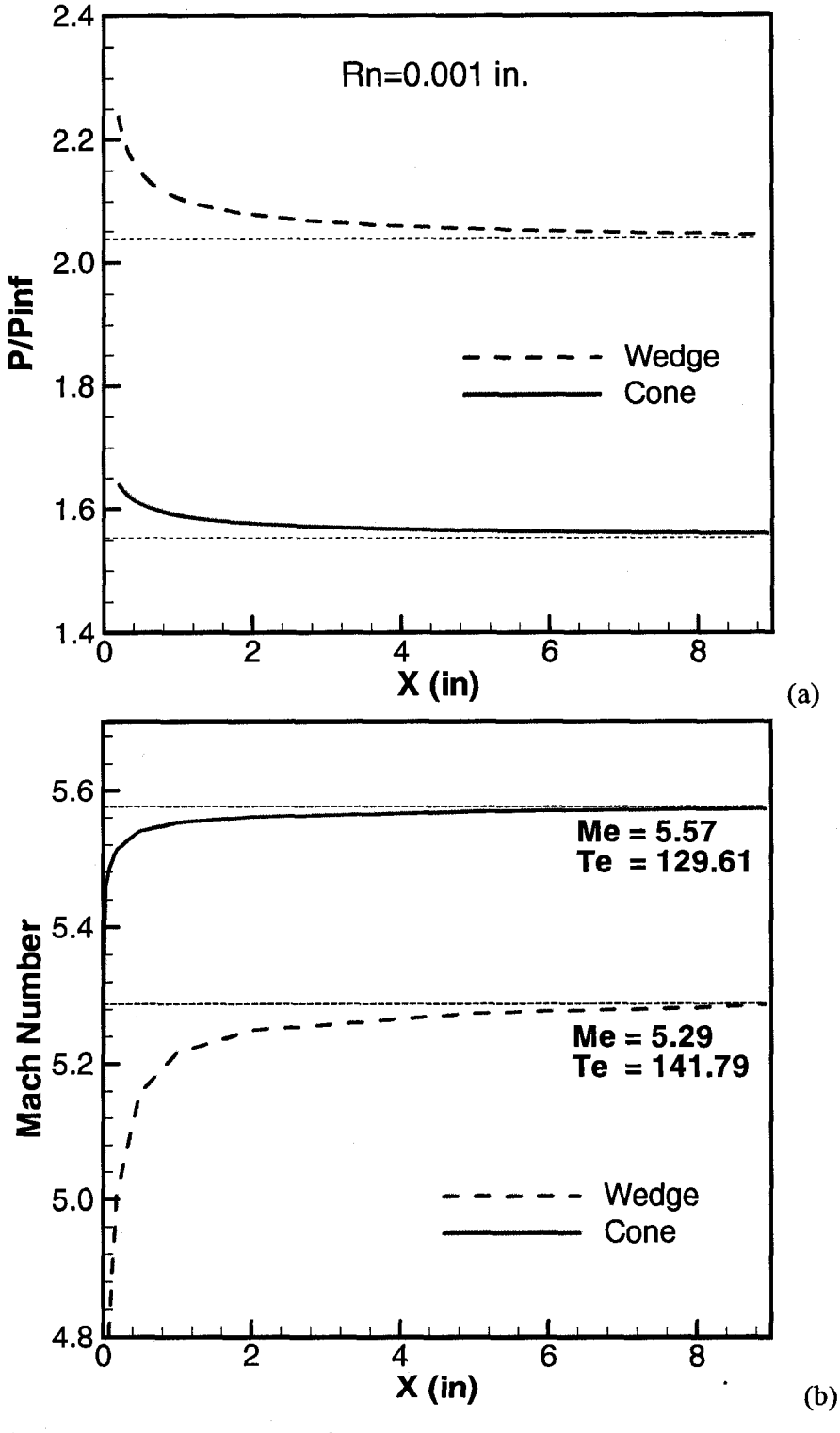

Figure 4.5 (a) Comparison of mean flow wall pressure distribution. (b) Comparison of Mach number distribution at the edge of the boundary layer for cone and wedge.

4.4 Linear Stability Analysis

Derivation of linear stability equations and the numerical scheme to solve are given in the appendix. Linear stability results for the similarity boundary layer over a cone and a wedge for the inviscid conditions at the surfaces are presented in Figure 4.6. Figures 4.6 (a) and (b) show the neutral stability diagram in (Re, F) plane for two-dimensional disturbances. The figures show the first and second mode unstable regions and the variation of the wave number with the Reynolds number. Figures 4.7(a) and (b) show the N-Factor curves for different frequencies. Here the variables are non-dimensionalized by the variables at the edge of the boundary layer. To obtain the variables non-dimensionalized by the free stream values as given in Table 3.2, the variables in this section should be multiplied by the appropriate factors from Table 4.1. The non-dimensional frequency F has to be multiplied by 1.174 to obtain the values in terms of free stream values.

In Figures 4.6 (a) and (b) the neutral stability curve clearly shows the unstable first and second mode regions for the boundary layers over the cone and wedge at a free stream Mach number of 6.0. The first mode and the second mode neutral stability curves merge at a Reynolds number of Re=1600 for the cone, and they do not merge for the wedge case for these parameters. The most amplified frequencies are higher for the cone boundary layers than for the wedge. The transition Reynolds numbers based on an N-Factor of 9 are about 3500 for the cone and about 5200 for the wedge. The most amplified frequencies are 0.85×10^{-4} and 0.34×10^{-4} for the cone and the wedge respectively.

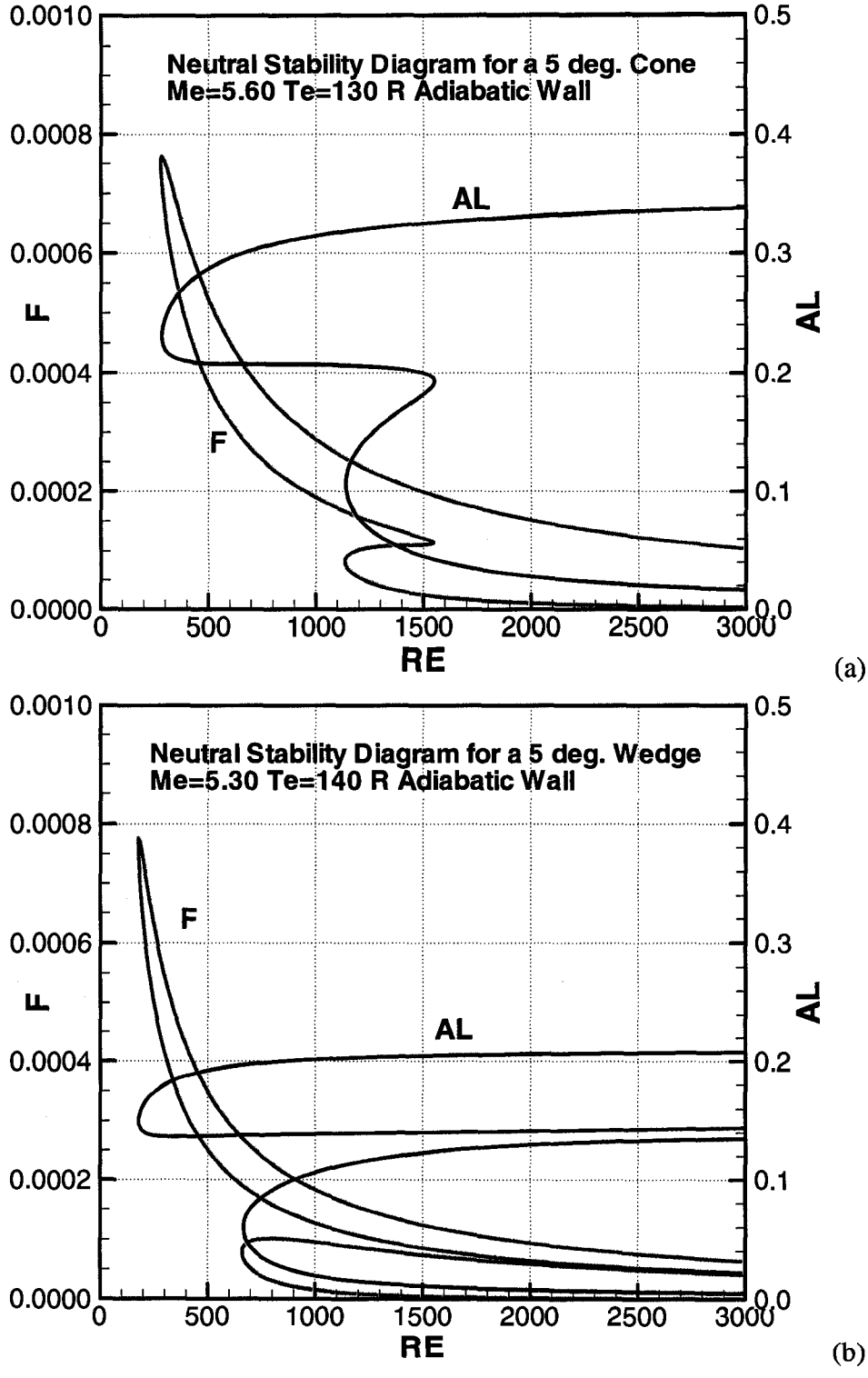

Figure 4.6 Neutral stability diagram and variation of wave number with Reynolds number. (a) Cone and (b) Wedge.

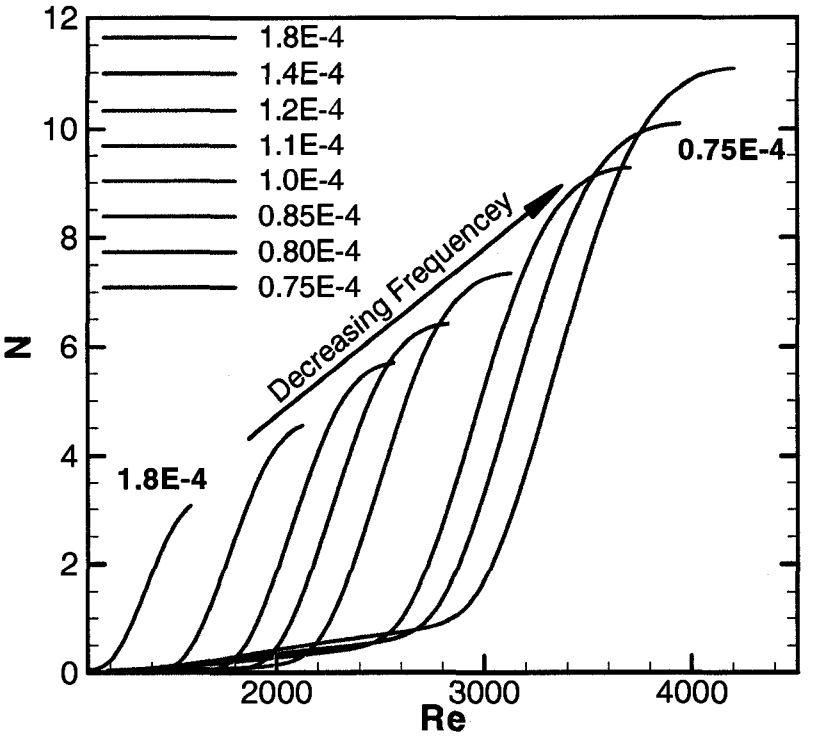

(a)

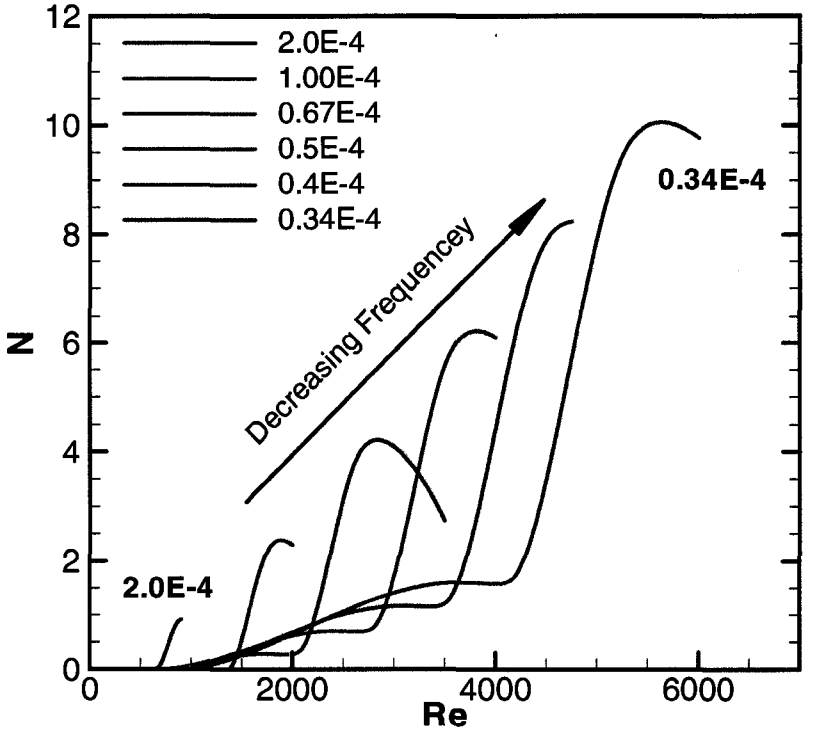

(b)

Figure 4.7 N-Factor curves for increasing frequency for (a) Cone and (b) Wedge.

4.5 Interactions of Acoustic Disturbances with Boundary Layer

After the steady mean flow is computed, two dimensional slow and fast acoustic disturbances are separately introduced at the outer computational boundary as explained in Section 2.11, and the time accurate simulations are performed. Unsteady simulations are performed using the frequencies F=1.2 $x10^{-4}$ and 1.4 x 10^{-4} for the cone case and using the frequency F=0.85 x10-4 for the wedge. These frequencies give maximum amplifications within the computational domain of x=9 in. For the freestream these frequencies correspond to 331, 467 and 546 kHz respectively. To remain in the linear regime, the amplitude of the forcing freestream acoustic waves is given a small value of $P_{ac}/P_{\infty}=2x10^{-5}$. Even with this small amplitude, nonlinearity starts to develop near the end of the computational domain for the frequency F=1.2 $x10^{-4}$.

Figure 4.8 shows the evolution of unsteady density fluctuations obtained from the simulations for the slow acoustic wave at a fixed time for the cone case with F=1.2 $x10^{-4}$. To obtain fluctuation plots, mean flow results are subtracted from unsteady simulation results. Figure 4.8(a) shows the contours of the density fluctuations in the entire domain, and Figure 4.8(b) depicts the same results inside the boundary layer. In Figure 4.8(b) the surface of the cone is plotted along the x-axis to show the clear growth of instability waves inside the boundary layer.

In Figure 4.8(a) the perturbation field can be divided into four regions. One region is the area outside the shock where the acoustic waves uniformly propagate to downstream. The second region is the shock layer across which the acoustic waves are transmitted. The third region is the area between the shock and the boundary layer. This region consists of the transmitted external acoustic field and the disturbances that are

radiated from the boundary layer. The fourth region is the boundary layer where the instability waves evolve.

Figures 4.8 (a) and (b) noticeably show that the disturbances inside the boundary layer are generated near the nose region. Figure 4.8 (b) also shows the evolution of the first mode up to x~4.5 in. and the gradual transformation of the first mode to the second mode in downstream. Another interesting observation is that the region between the boundary layer and the shock layer is quieter compared to the acoustic waves outside the shock layer. This implies that the acoustic waves are weakly transmitted through the shock. This was also observed in the flat plate simulation of Malik and Balakumar[52] where, as the acoustic wave incidence angle is increased, disturbances become quieter in the windward side.

Figure 4.9 shows the contours of the density fluctuations inside the boundary layer at different streamwise locations to illustrate the structure and the evolution of the instability waves inside the boundary layer. The contours show that the disturbances are concentrated near the edge of the boundary layer and in downstream the disturbances exhibit the classical "rope"-like structures associated with the second mode.

Figures 4.10 and 4.11 show the evolution of the wall pressure fluctuations for the cone and the wedge case. Figures 4.10 (a) and (b) show the pressure fluctuations induced by the slow and the fast acoustic waves for the frequency $F=1.2 \times 10^{-4}$ for the cone case, and Figure 4.11(a) shows the results induced by the slow acoustic wave for the frequency $F=1.4 \times 10^{-4}$. Figure 4.11(b) shows the pressure fluctuation induced by the slow wave for the frequency $F=0.85 \times 10^{-4}$ for the wedge case. It should be noted that different scales are used in Figure 4.10 due to a difference in amplification in the slow and the fast mode

cases. For the frequency F=1.2 $x10^{-4}$, the maximum amplitude in the slow mode case is about 0.16 and is about 0.0025 in the fast mode case. This implies that the slow mode is more efficient (by about 67 times) in generating the instability wave inside the boundary layer compared to the fast wave. This agrees qualitatively with other simulations and analysis[21, 22, 52, 53].

One other observation is the amplification of the first mode near the leading edge region. The parallel linear computations revealed that the first mode is stable up to x~3 in. for this frequency. However, the simulation shows that the first mode disturbances are growing starting from the leading edge. Hence, the non-parallel effects are stronger in the cone case compared to the flat plate case, and this yields a higher amplification ratio (about 67) between the induced flow field by the slow and the fast modes in the cone case compared to the flat plate case (about 20). Figure 4.11(b) shows that the amplification of the disturbances are small for the wedge case for this frequency F=0.85$x10^{-4}$. The maximum amplitude attained is about $2x10^{-4}$ compared to 0.16 in the cone case. The first mode region in the wedge case is stable in contrast to the cone case.

Figures 4.12 and 4.13 show the amplitude of the pressure fluctuations along the wall in a log scale. This figure also includes results from the parabolized stability equations (PSE) computations obtained for the same mean boundary layer profiles. The growth of the disturbances agrees very well with the PSE results. The figures clearly show the initial generation and the eventual exponential growth of the instability waves inside the boundary layer. The slow wave whose wavelength is closer to the wavelength of the instability wave transforms into an instability wave smoothly. The fast mode, as was in the flat plate case, initially generated the instability mode corresponding to the fast

acoustic wave and then switched to the unstable second mode close to x = 4.5 in. As discussed earlier, Figure 4.12(a) shows that the first mode is growing due to the non-parallel effect. Due to the growth of the first mode starting from the nose region, it is difficult to define a receptivity coefficient in the cone case. We selected the amplitude near the nose region x~1.0 in. to compute the receptivity coefficient defined by the ratio between the initial amplitude of the pressure fluctuations at the wall near x~1.0 in., and the free stream acoustic pressure can be evaluated.

For the wedge case (Figure 4.13 (b)), the first mode is decaying and a well defined neutral point is discerned. The receptivity coefficient is the ratio of the amplitude of wall pressure fluctuations at the neutral point to the initial amplitude of pressure waves and is given by Equation (4.1). Table 4.2 gives the respective receptivity coefficients for the different cases. The receptivity coefficient for the cone cases is about 4.569 and 0.068 for the slow and the fast acoustic modes, and it is about 0.77 for the slow acoustic mode for the wedge case.

$$C_{recpt,p_{wall}} = \frac{(p_{wall})_{np}}{p_{ac}} \tag{4.1}$$

Table 4.2 Variation of receptivity coefficient for different X locations.

	Cone		Cone		Wedge
$F\,(\text{x}10^{-4})$	1.2		1.4		0.85
$x(in.)$	1.0	1.5	1.0	1.5	Neutral Point. (x=3.6)
$C_{recpt,p_{wall},Slow}$	3.826	4.569	3.91	4.89	0.77
$C_{recpt,p_{wall},Fast}$	0.057	0.068			
$\frac{C_{recpt,p_{wall},Slow}}{C_{recpt,p_{wall},Fast}}$	67.12	67.19			

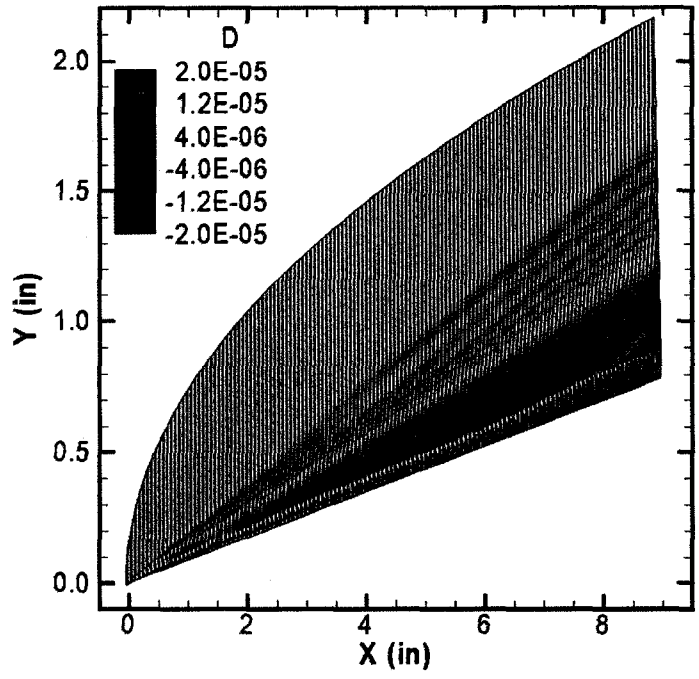

(a)

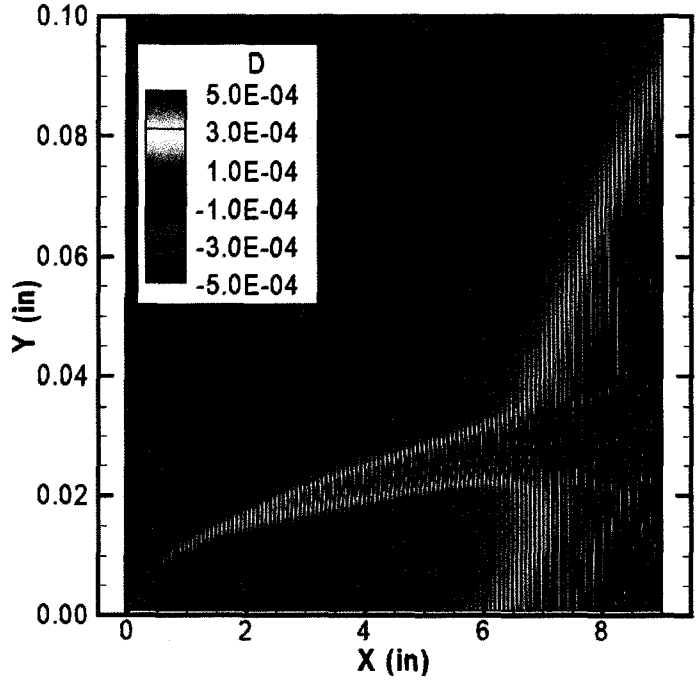

(b)

Figure 4.8 Contours of the unsteady density fluctuations due to the interaction of slow acoustic waves over a blunt cone. $F=1.2\times10^{-4}$. (a) Whole domain (b) Fluctuations inside the boundary layer. Computational domain rotated 5-degree clockwise to show the density fluctuations clearly.

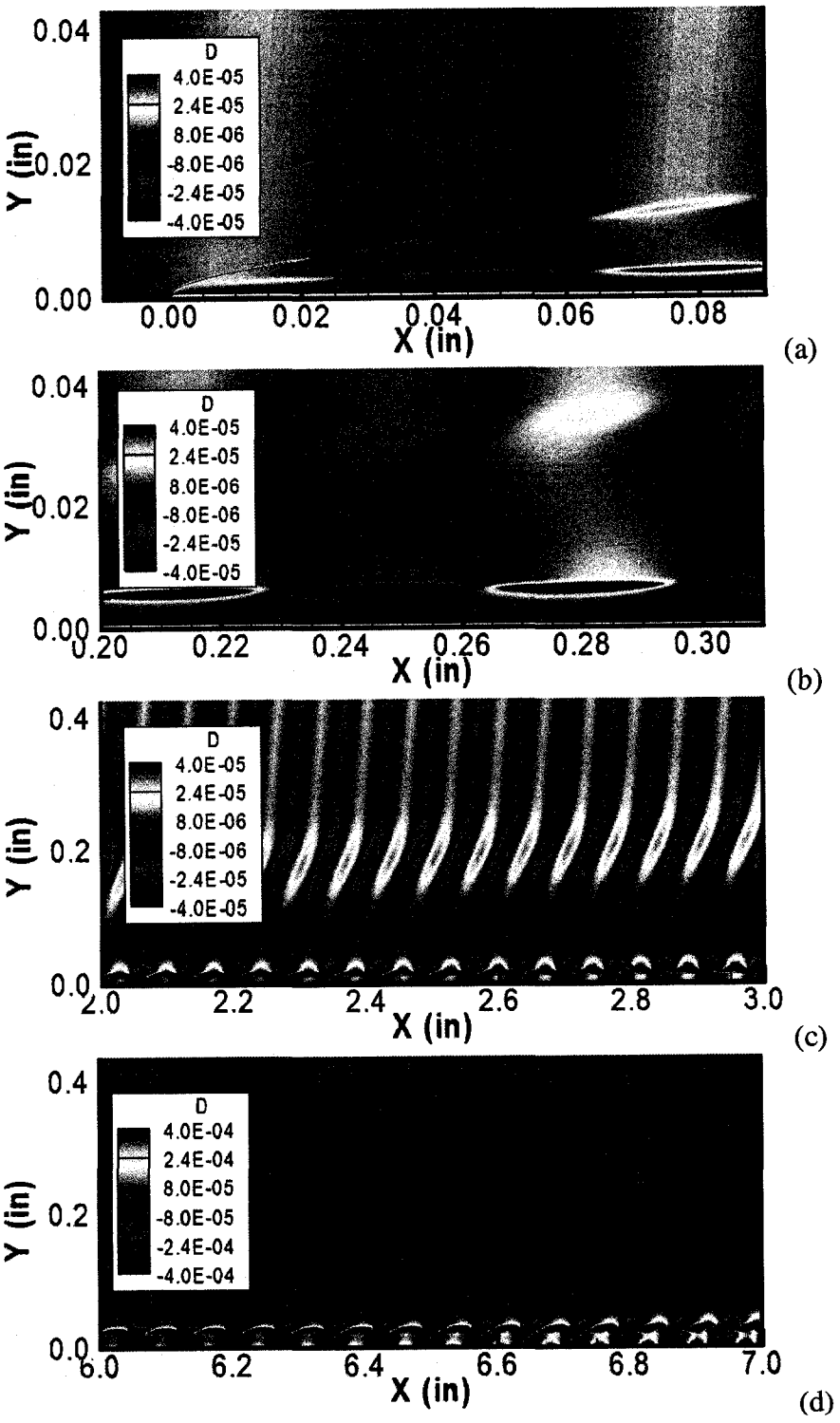

Figure 4.9 Contours of unsteady density fluctuations inside the boundary layer along the cone surface. F=1.2x10^{-4}, Slow acoustic wave, and Rotated 5-degree clockwise.

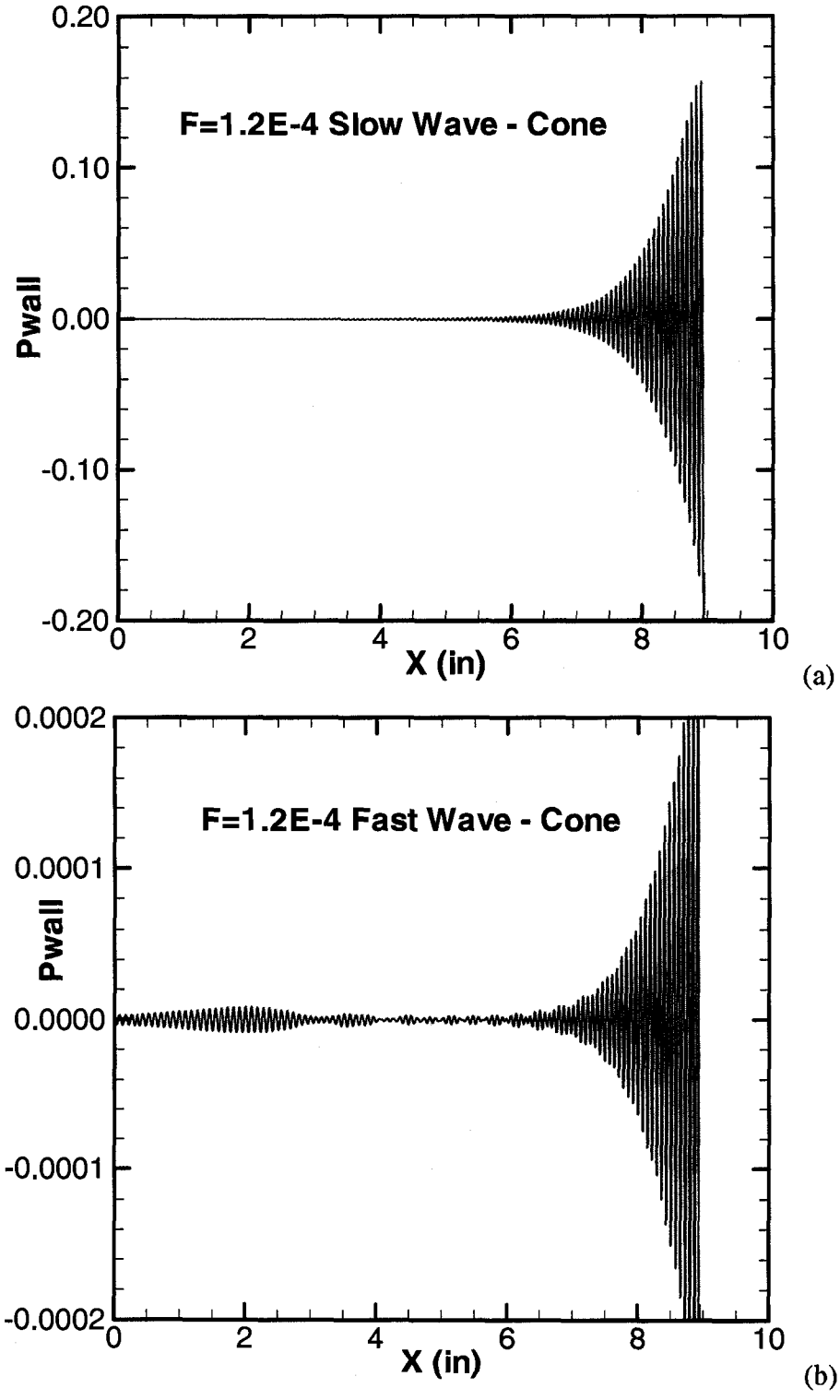

Figure 4.10. Wall pressure fluctuations generated by slow and fast acoustic modes for non-dimensional frequency $F=1.2\times10^{-4}$. (a) Slow mode and (b) Fast mode.

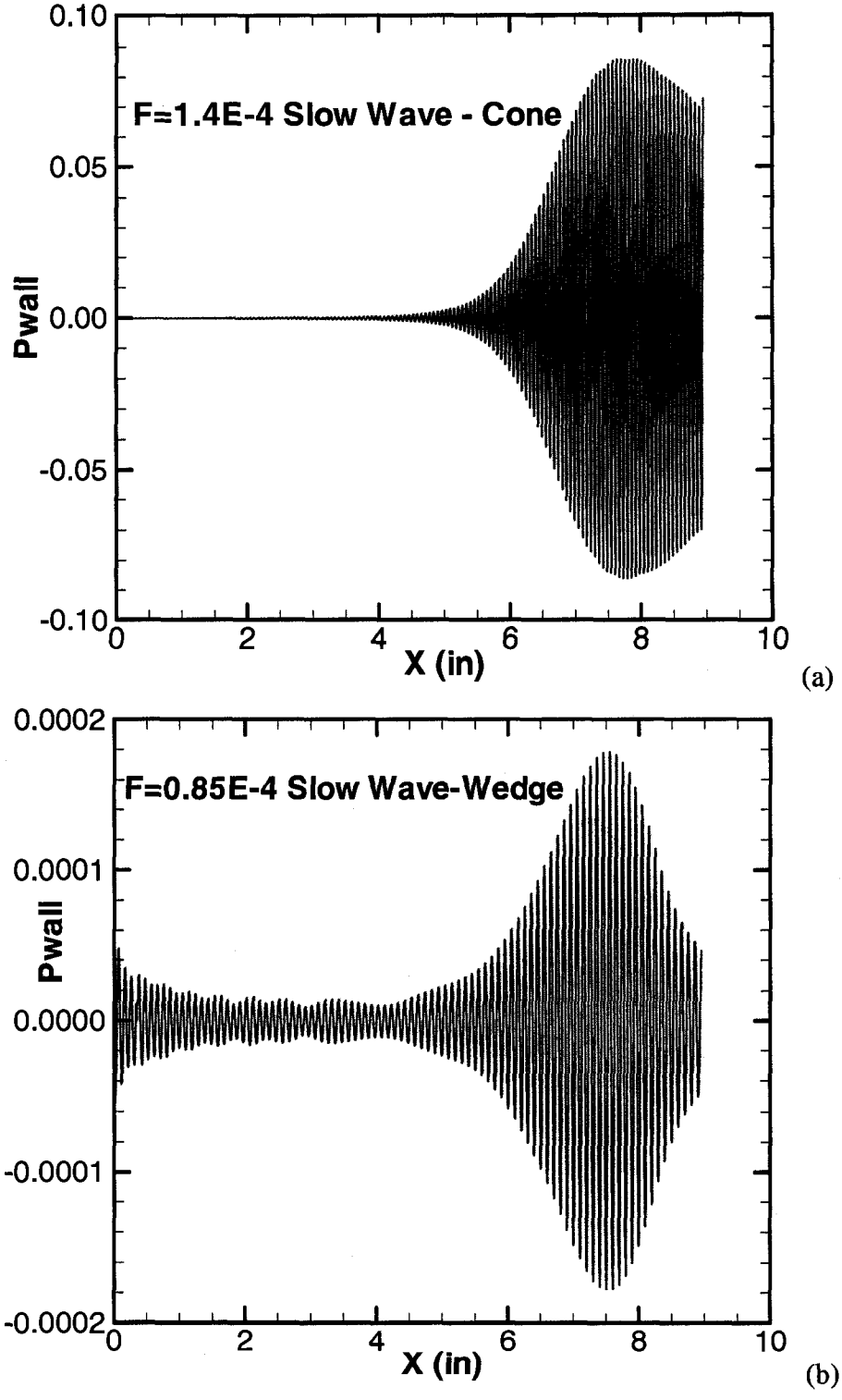

Figure 4.11. Wall pressure fluctuations generated by slow acoustic modes for (a) Cone, $F=1.2\times10^{-4}$ and (b) Wedge, $F=0.85\times10^{-4}$.

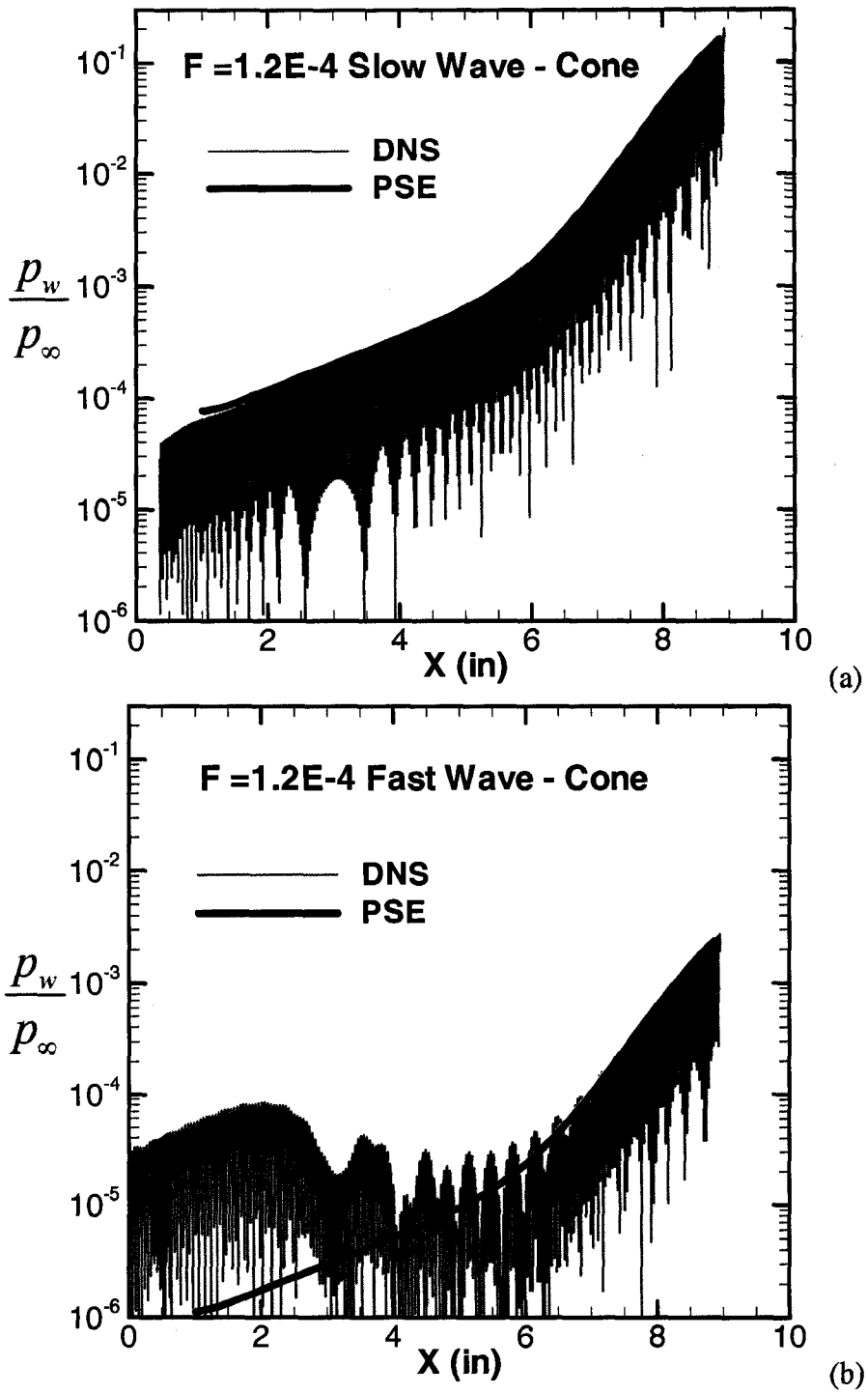

Figure 4.12. Wall pressure fluctuations generated by slow and fast acoustic modes for non-dimensional frequency F=1.2x10^{-4} in log scale are compared with PSE (a) Slow mode and (b) Fast mode.

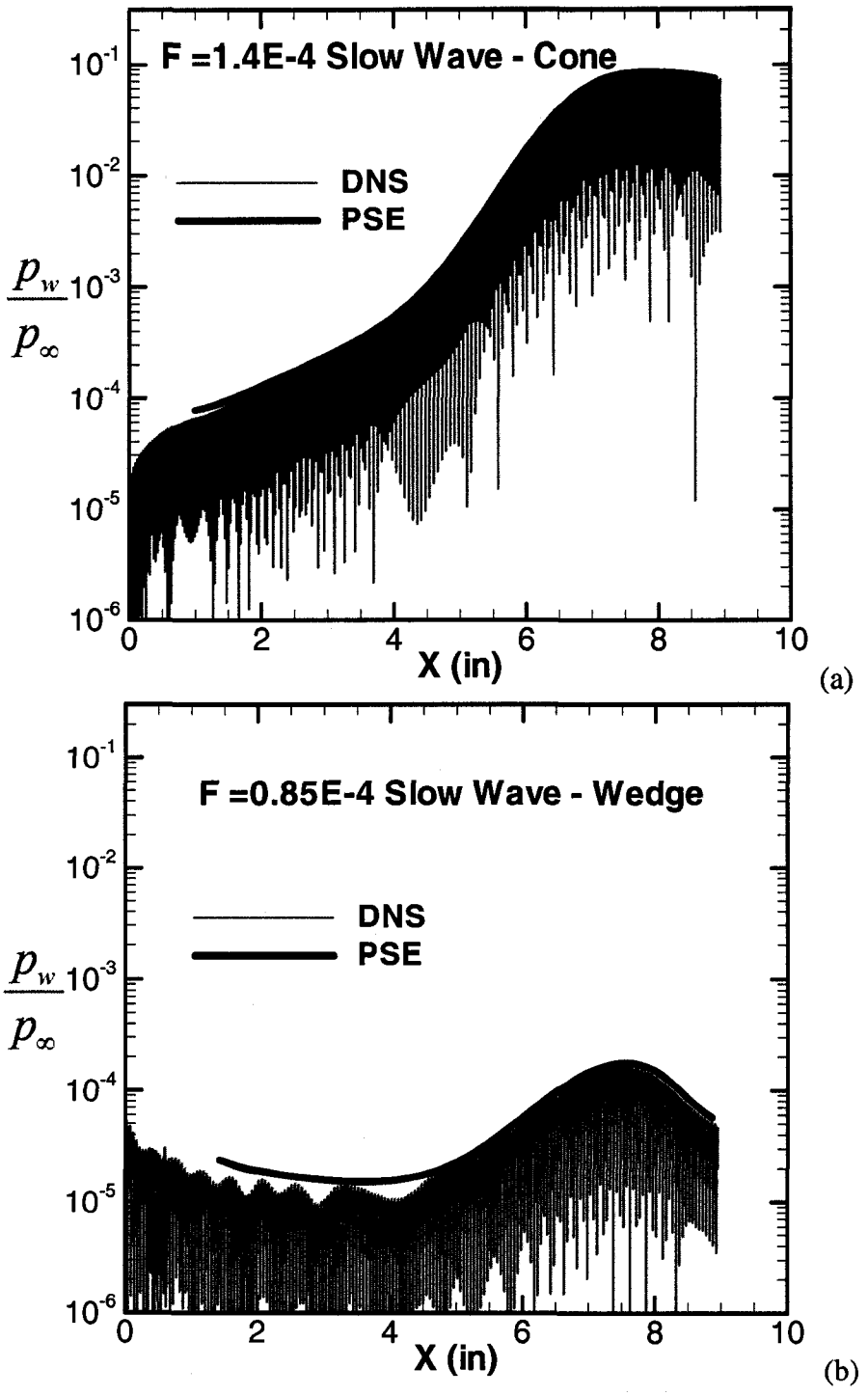

Figure 4.13. Wall pressure fluctuations generated by slow acoustic waves in log scale are compared with PSE (a) Cone, F=1.2x10^{-4} and (b) Wedge, F=0.85x10^{-4}.

4.6 Discussion and Conclusion

In this chapter the receptivity and stability of hypersonic boundary layers due to the interaction of two-dimensional slow and fast acoustic waves over a 5-degree, half-angle cone and wedge with nose bluntness 0.001 in. are numerically investigated at a free stream Mach number of 6.0 and at a Reynolds number of 7.8×10^6/ft. Both steady and unsteady solutions are obtained by solving compressible Navier-Stokes equations in two-dimensional and cylindrical coordinates using the 5^{th} order accurate Weighted Essentially Non-Oscillatory (WENO) scheme for space discretization and using a third-order Total-Variation-Diminishing (TVD) Runge-Kutta scheme for time integration.

The unsteady simulations showed that the instability waves are generated very close to the leading edge region. The simulations for the cone showed that the first mode starts to grow starting from the leading edge due to the nonparallel effects before they grow strongly due to the unstable second mode. In the wedge case, the first mode disturbances decay first, before they start to grow, due to the second mode. The receptivity coefficient of the instability waves generated by the slow acoustic wave is about 4 times the amplitude of the free stream acoustic wave.

It is also found that the amplitude of the instability waves generated by the slow acoustic waves is about 67 times larger than that for the case of fast acoustic waves. Therefore, forcing the flow by slow acoustic wave is much more relevant in the transition process involved in hypersonic boundary layers.

The receptivity coefficient in the wedge case is about 0.8 which is about 5 times smaller than that in the cone case. This is due to the initial growth of the first mode in the

cone case compared to the decay in the wedge case and also due to the strong stabilization effect of the bluntness in the wedge case. The receptivity coefficient for a flat plate boundary layer with a bluntness of 0.0001 in.[52] at a free stream Mach number of 4.5 is about 9, and the slow mode is about 20 times more efficient than the fast mode in generating the instability waves. This shows that the slow mode is much more efficient in flows over axisymmetric bodies than in two-dimensional flows.

CHAPTER V

5. NOSE BLUNTNESS EFFECTS ON RECEPTIVITY

In this chapter receptivity and stability of hypersonic boundary layers are numerically investigated for boundary layer flows over a 5-degree straight cone at a free-stream Mach number of 6.0 to find out the effects of nose bluntness on the receptivity process. To compute the shock and the interaction of shock with the instability waves, we solve the Navier-Stokes equations in axisymmetric coordinates. The governing equations are solved using the 5^{th} –order accurate Weighted Essentially Non-Oscillatory (WENO) scheme for space discretization and using the 3^{rd} –order Total-Variation-Diminishing (TVD) Runge-Kutta scheme for time integration.

After the mean flow field is computed, disturbances are introduced at the upstream end of the computational domain. Our objectives in this chapter are to estimate the stabilizing effects of nose bluntness on the hypersonic boundary layers over cones, to calculate the transition Reynolds numbers based on e^N criteria, and to compute the receptivity coefficients of the instability waves generated inside the boundary layer. Also, generation of instability waves from the leading edge region and receptivity of the boundary layer to slow acoustic waves are investigated.

The objectives of this work are to estimate the stabilizing effect of bluntness on the hypersonic boundary layers over blunt cones and to estimate the transition Reynolds number based on the e^N criteria and to compute the receptivity coefficient of the instability waves generated inside the boundary layer.

To investigate the effect of the Reynolds number based on nose bluntness, simulations are performed at different leading edge radii r_0 = 0.001, 0.05 and 0.10 in. at a unit Reynolds number of 7.8×10^6/ft for a 5-degree, half-angle cone. To differentiate the unit Reynolds number effect from the nose Reynolds number effect, one simulation is performed at a higher unit Reynolds number of 15.6×10^6/ft with a bluntness of 0.05 in. These parameters yield the Reynolds number based on the nose radius to vary from 650 to 130,000 and listed in Table 5.1. The results consist of: (1) mean flow profiles, linear stability and transition onset Reynolds numbers at different bluntness, and (2) receptivity coefficients for different bluntness.

Table 5.1 Computational parameters for nose bluntness study

Nose radius, r_0 (in.)	$Re_{unit} \times 10^6$ /ft	Re_{r0}
0.001	7.80	650
0.050	7.80	32,500
0.100	7.80	65,000
0.050	15.6	65,000
0.100	15.6	130,000

5.1 Introduction

The transition onset mainly depends on the boundary layer characteristics and on the frequency, wave number distributions, and the amplitudes of the disturbances that enter the boundary layer. The boundary layer profiles depend on the flow parameters such as Mach number, Reynolds number, wall temperature, and model geometry. In supersonic and hypersonic boundary layers, one important geometrical parameter is nose bluntness. The effects of bluntness on transition have been studied experimentally and

numerically by many researchers[54-60]. It was found that the bluntness generally stabilizes the boundary layer. The critical Reynolds numbers for blunt cones are much higher compared to those for sharp cones. However, the transition Reynolds number increased only by a factor of two compared to the sharp cones.

It was identified that the entropy layer that is formed near the bow shock region persists for a long distance downstream as shown in Figure 5.1 and makes the boundary layer more stable compared to the sharp cone case.

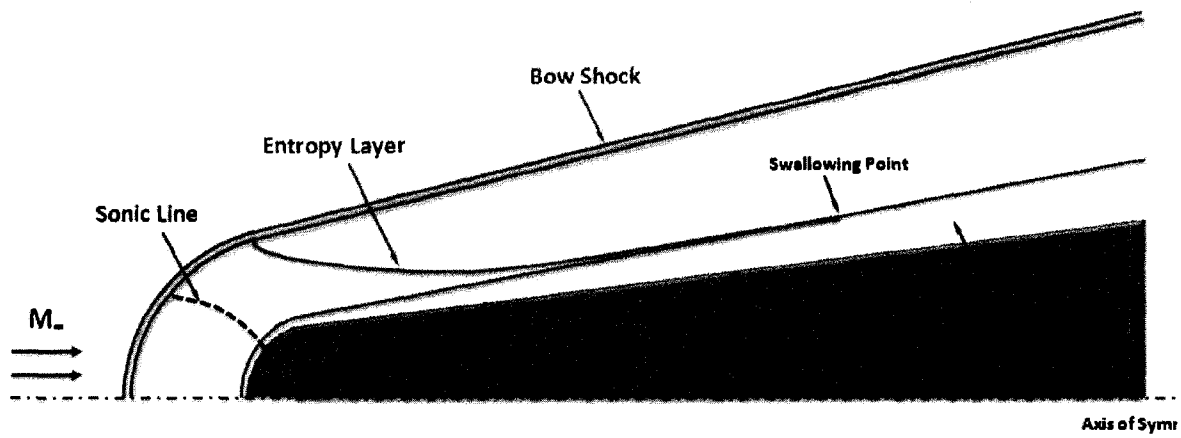

Figure 5.1 Hypersonic flow field over a blunt cone

After the entropy layer and the boundary layer that is developing along the surface merge together, the boundary layer becomes unstable. It was also found that in addition to the first and second mode instability waves, other inviscid type disturbances grow inside the entropy layer. It is also observed that with increasing bluntness the stabilizing trend is reversed in axisymmetric boundary layers. Another influence of the bluntness is in the generation of instability waves near the leading edge region.

5.2 Literature Review

Stetson[60] carried out boundary layer experiments to investigate the effects of nose tip bluntness on an 8-degree, half-angle cone containing two rays of thermocouples in AEDC Tunnel F at Mach 6. The location of the boundary layer transition was obtained from heat transfer measurements. It was found that the small nose tip bluntness had a stabilizing effect upon the boundary layer when transition occurred at locations where the entropy layer was nearly swallowed.

Also, Stetson et al.[54] experimentally investigated the stability of the laminar boundary layer on a blunt, 7-degree, half-angle cone at Mach 8 and identified disturbances growing in the entropy layer indicating the existence of an inviscid instability.

Recently, Maslov et al.[61, 62] conducted stability experiments on sharp and blunt cones at Mach 5.92. Rufer and Schneider[63] measured mass flux profiles over 7-degree, half-angle sharp and blunt (0.020 in. radius) cones to study the amplitude and growth of instability waves. Also, Schneider[64] published additional experimental stability results of Stetson's[54] experiment.

An experimental investigation was conducted by Horvath et al.[35] on a 5-degree, half-angle cone in a conventional Mach 6 wind tunnel to examine the effects of facility noise on boundary layer transition. In addition, the model nose tip radius was varied from 0.0001 in. to 0.0625 in. to examine the effect of bluntness on transition onset.

Malik et al.[56] computed the effect of nose bluntness on boundary layer instability for Mach 8 flow past a 7-degree, half-angle cone. They included the entropy-layer effect

using Parabolized Navier-Stokes equations. It is concluded that nose bluntness stabilizes the boundary layer, and the effect of unit the Reynolds number in the aeroballistic range data of Potter[65] was a nose bluntness effect.

Rosenboom et al.[66] and Zhong[67] did further study on the effect of nose bluntness on the linear stability of hypersonic flow over Stetson's[54] blunt cone and focused on the transition reversal phenomenon. However, no instability reversal was observed as the nose radius increased in both studies. Their results indicated that to understand the cause of the transition reversal phenomenon it is necessary to conduct further studies on nose bluntness.

Balakumar[22] performed computations for a blunt flat plate with thicknesses from 0.0001 to 0.01 in. and a wedge of 10-degree, half-angle with different leading edge radii 0.001 and 0.01 in. to find out the effect of nose bluntness on the stability of two dimensional boundary layers. He found that bluntness has a strong stabilizing effect on the stability of two dimensional boundary layers, and the boundary layers on wedges are far more stable than on blunt flat plates.

Here, we employ the fifth order Weighted Essentially Non-Oscillatory (WENO) scheme for spatial discretization and use the third order Total Variation Diminishing (TVD) Runge-Kutta scheme for time integration to solve for the hypersonic boundary layer receptivity problem.

5.3 Mean Flow Results

For this study, we have selected the following flow conditions (Table 3.2 and Table 5.1), geometry (Figure 3.6) used by Horvath et al.[35], and computational setup

(Figure 2.5). The nose radii are varied from r_0 = 0.001 to 0.010 in. and the flow around the leading edge is resolved by using a sufficiently dense grid. We assume adiabatic wall conditions for steady flow computations. Boundary conditions, the computational grid and the solution algorithm used in this chapter are summarized in Sections 2.11 – 2.13.

Figures 5.2 and 5.3 show the mean flow density contours computed using the WENO code. Figures 5.2 (a), (b) and 5.3 (a), (b) show the results for the 5-degree, half-angle cone at different nose radii r_0= 0.001, 0.05, 0.10 and 0.10 in. (at two-times the unit Reynolds number). Smaller nose radii cases r_0= 0.001, 0.05 and 0.10 in. are performed at a unit Reynolds number of 7.8×10^6 /ft. This yields Reynolds numbers based on the nose radius of 650 to 65,000 (Table 5.1). Figure 5.3(b) shows the results obtained at a higher unit Reynolds number of 15.6×10^6 /ft with r_0= 0.10 in., which yields the Reynolds number based on the nose radius of 130,000. All of these figures show the density contours near the nose region.

One interesting observation is that the inviscid density contours and the shock locations are the same between Figures 5.3 (a) and (b), which are obtained with the same bluntness, r_0= 0.10 in., but at different unit Reynolds numbers 7.8 and 15.6 $*10^6$ /ft. The leading edge shocks are located at approximately 0.0002, 0.008 and 0.016 in. upstream of the leading edge.

The density profiles at different axial locations are plotted in Figures 5.4 (a) - (d) for the different bluntness cases r_0=0.001, 0.05, 0.05(Re_∞=15.6×10^6 /ft) and 0.10 in. in the similarity coordinates. The compressible Blasius similarity profile is also included for comparison, and Figures 5.4 (e) and (f) show the density profiles for r_0= 0.05 and 0.10 in. in the physical coordinates. For the small bluntness case the density profiles matched

perfectly immediately beyond the nose region, as shown in Figure 5.4 (a). However, the difference between the density profiles and the similarity profiles increased proportionally with increasing nose bluntness of the cone. Even at the end of the computational domain bluntness effects are observed on the density profiles in Figures 5.4 (b)-(d).

Figures 5.5 and 5.6 depict the entropy contours for different bluntness cases r_0= 0.001, 0.05, 0.10 and 0.10 (Re_∞=15.6x10^6) in. For the small bluntness case r_0= 0.001, only the boundary layer appears near the nose region, and the entropy layer is not discernable in the outer part of the boundary layer as shown in Figure 5.5 (a). For the higher bluntness cases the entropy layer that is visible near the nose region persists downstream and eventually merges with the boundary layer.

Figures 5.7 and 5.8 show the entropy profiles at different axial locations for different bluntness cases. Figure 5.7 (a) shows that the entropy layer is not discernable for the small bluntness case as was observed in the entropy contours (Figure 5.5 (a)). For the bluntness case r_0= 0.05, two layers are clearly seen in the profiles at x= 0.50 and 1.0 in. One layer is very close to the wall with a large gradient, and the other is away from the wall with a small gradient. The outside entropy layer merges with the boundary layer near the wall close to x= 2.0 in.

Figure 5.8 shows more blunt cases where the boundary and entropy layers are more evident and merging occurs at larger axial distances from the nose. Figure 5.8 (a) illustrates that the two layers merge around x=6.0 in. for r_0=0.10 in. with Re_∞=7.8x10^6 /ft, and Figure 5.8 (b) shows the merging point for two times the unit Reynolds number at

x=6.0 in., which is equivalent to 12.0 in. when it is converted to the same unit Reynolds number.

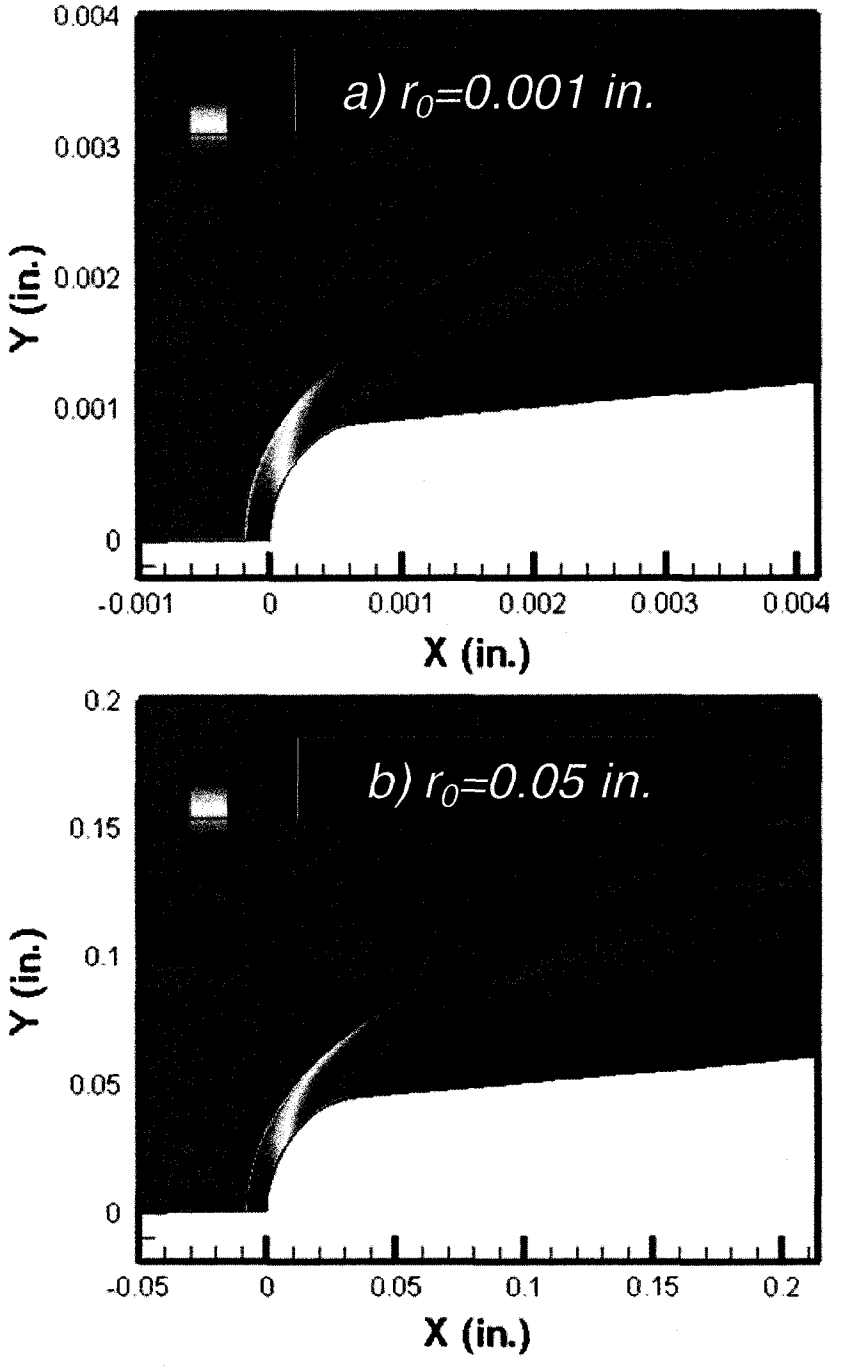

Figure 5.2 Density contours for different nose bluntness (a) r_0=0.001 in, (b) r_0=0.05 in. at M=6.0 and Re=7.8x10^6 /ft.

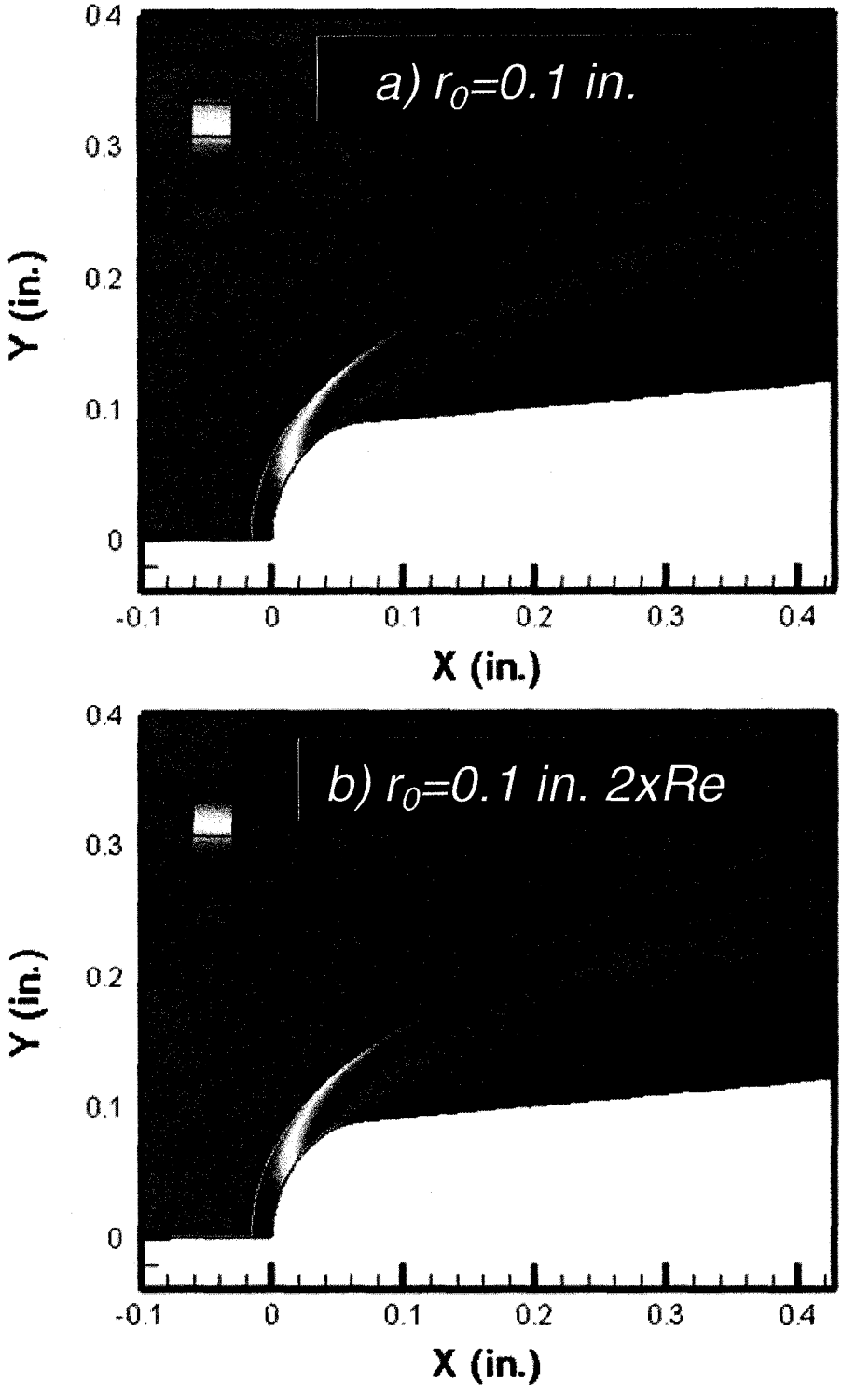

Figure 5.3 Density contours for different Reynolds numbers (a) Re=7.8x10^6 /ft, (b) Re=15.6x10^6 /ft at M=6.0 and r_0=0.10 in.

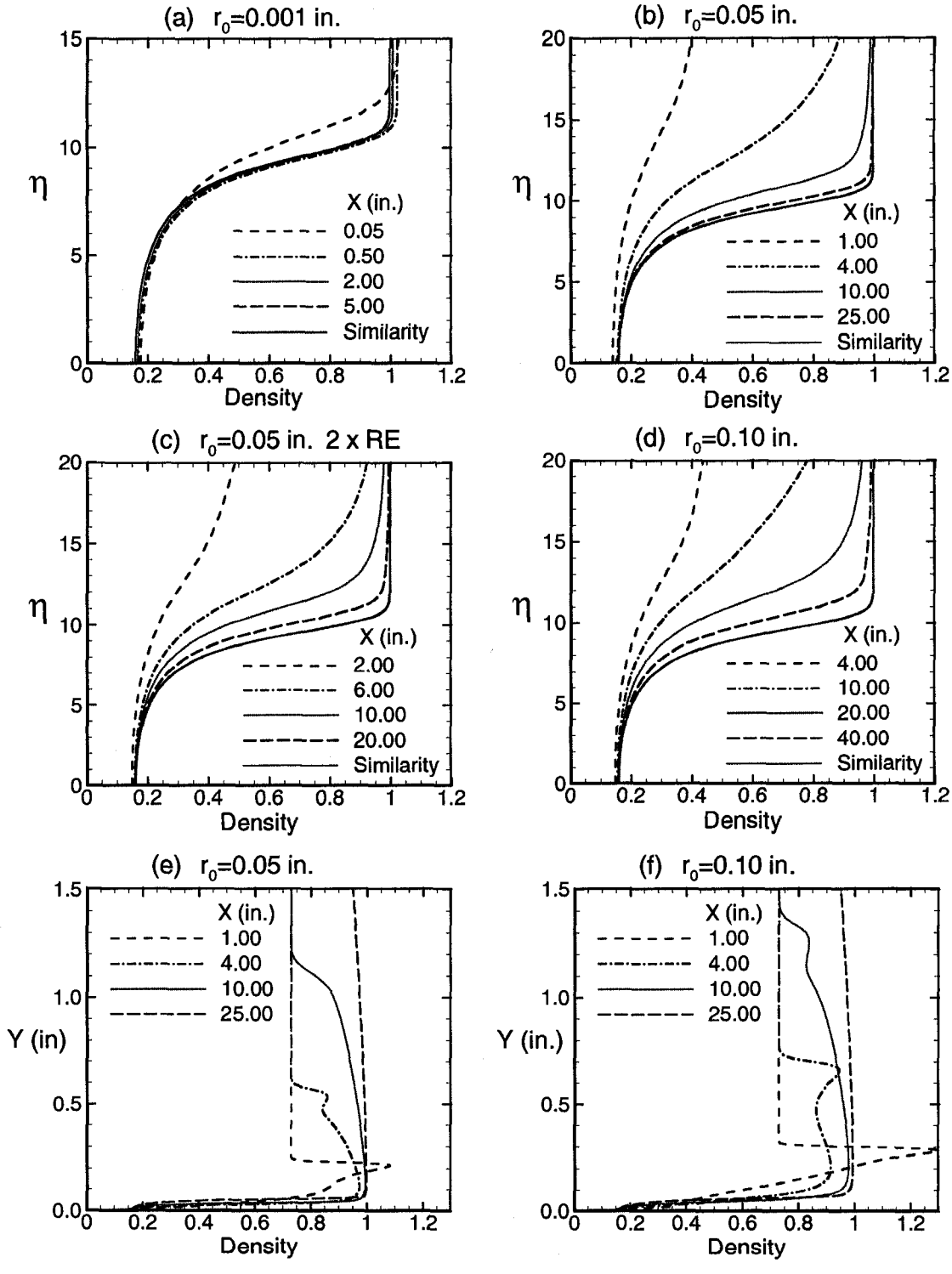

Figure 5.4 Mean flow density profiles at different axial locations compared with similarity solutions for (a) r_0=0.001 in. Re=7.8x10^6, (b) r_0=0.05 in., (c) r_0=0.05 in., (d) r_0=0.10 in. Density profiles in physical coordinates for (e) r_0=0.05 in., (f) r_0=0.10 in.

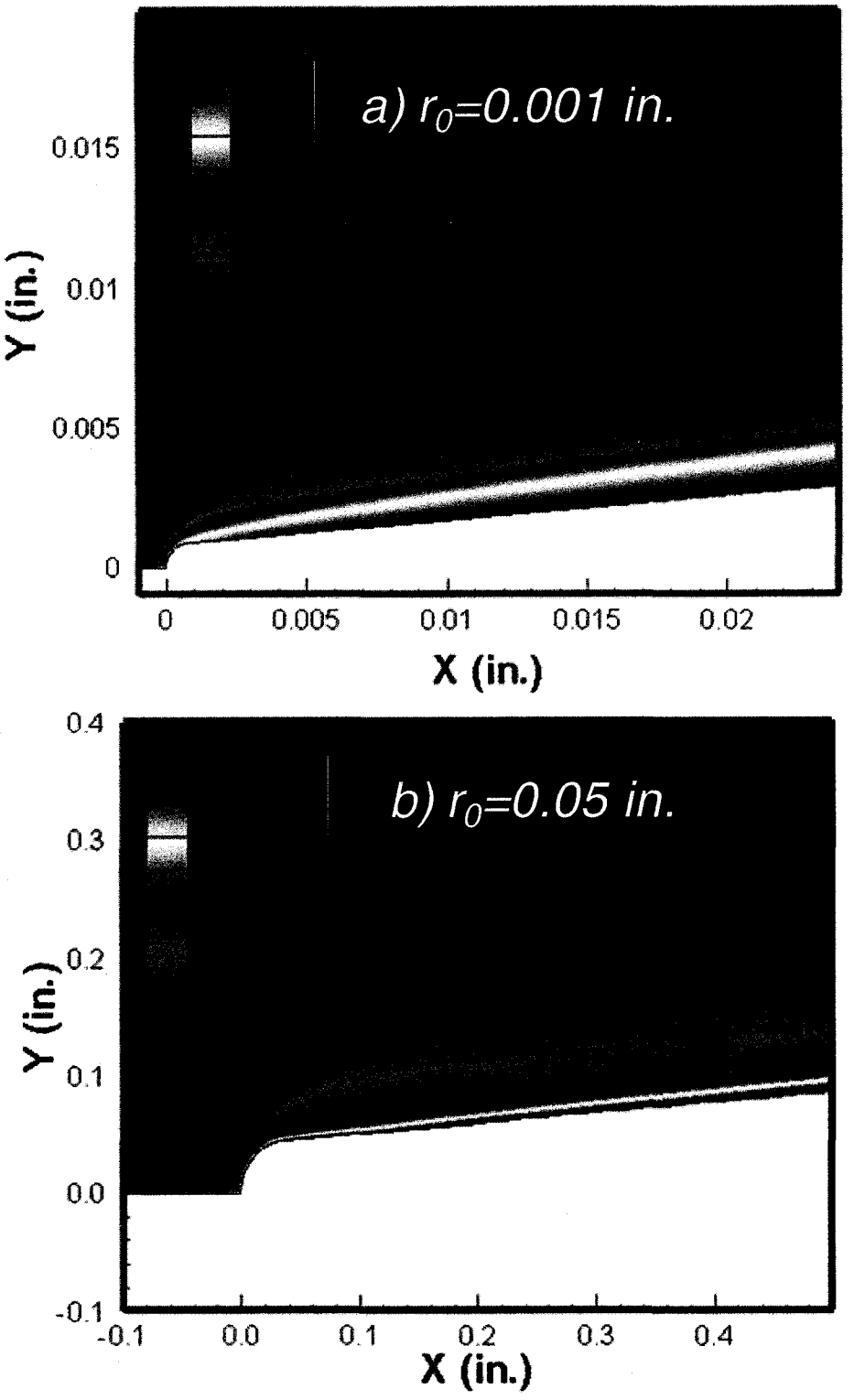

Figure 5.5 Entropy contours for different nose bluntness (a) r_0=0.001 in, (b) r_0=0.05 in. at M=6.0 and Re=7.8x10^6 /ft.

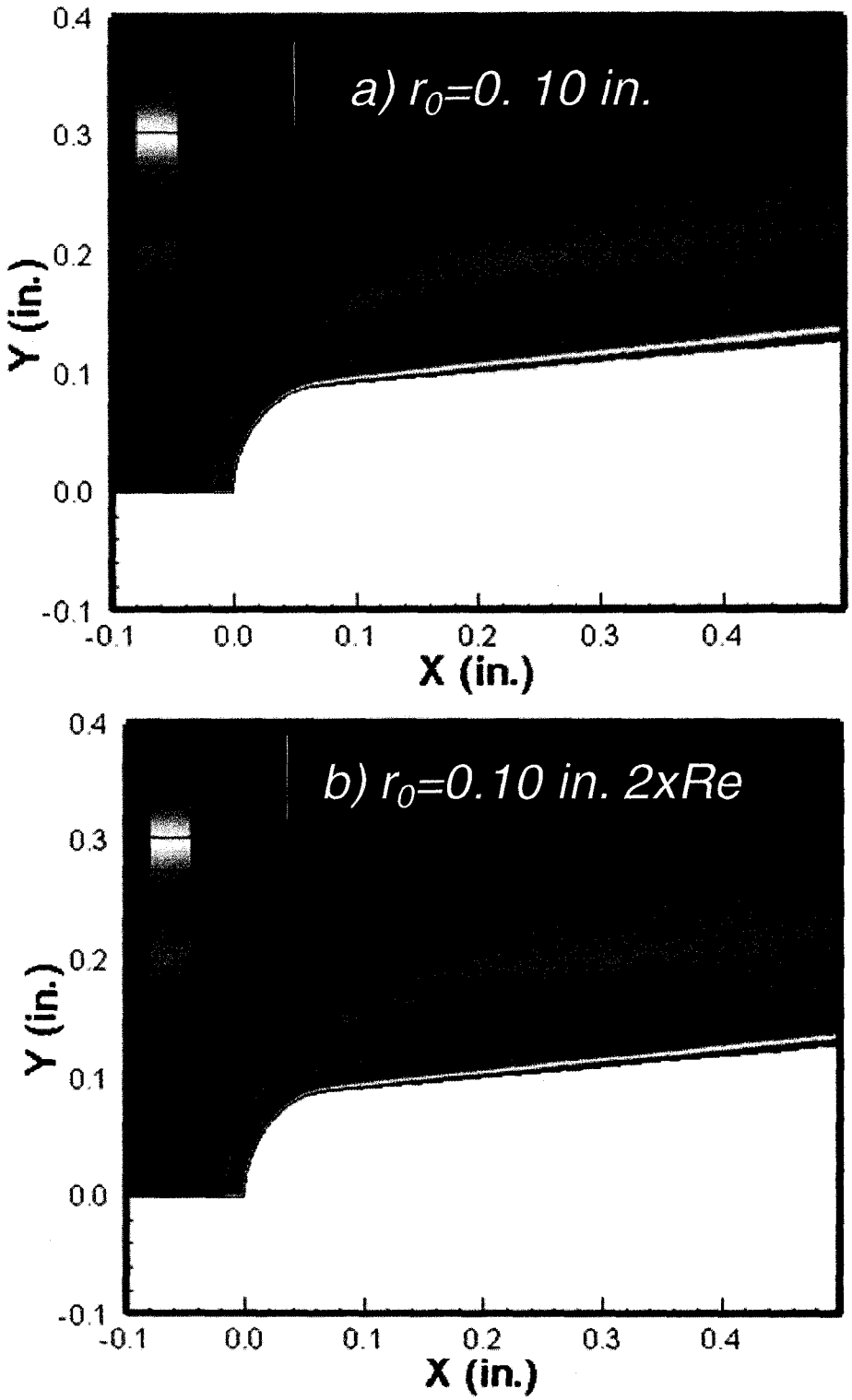

Figure 5.6 Entropy contours for different Reynolds numbers (a) Re=7.8x10^6 /ft, (b) Re=15.6x10^6 /ft at M=6.0 and r_0=0.10 in.

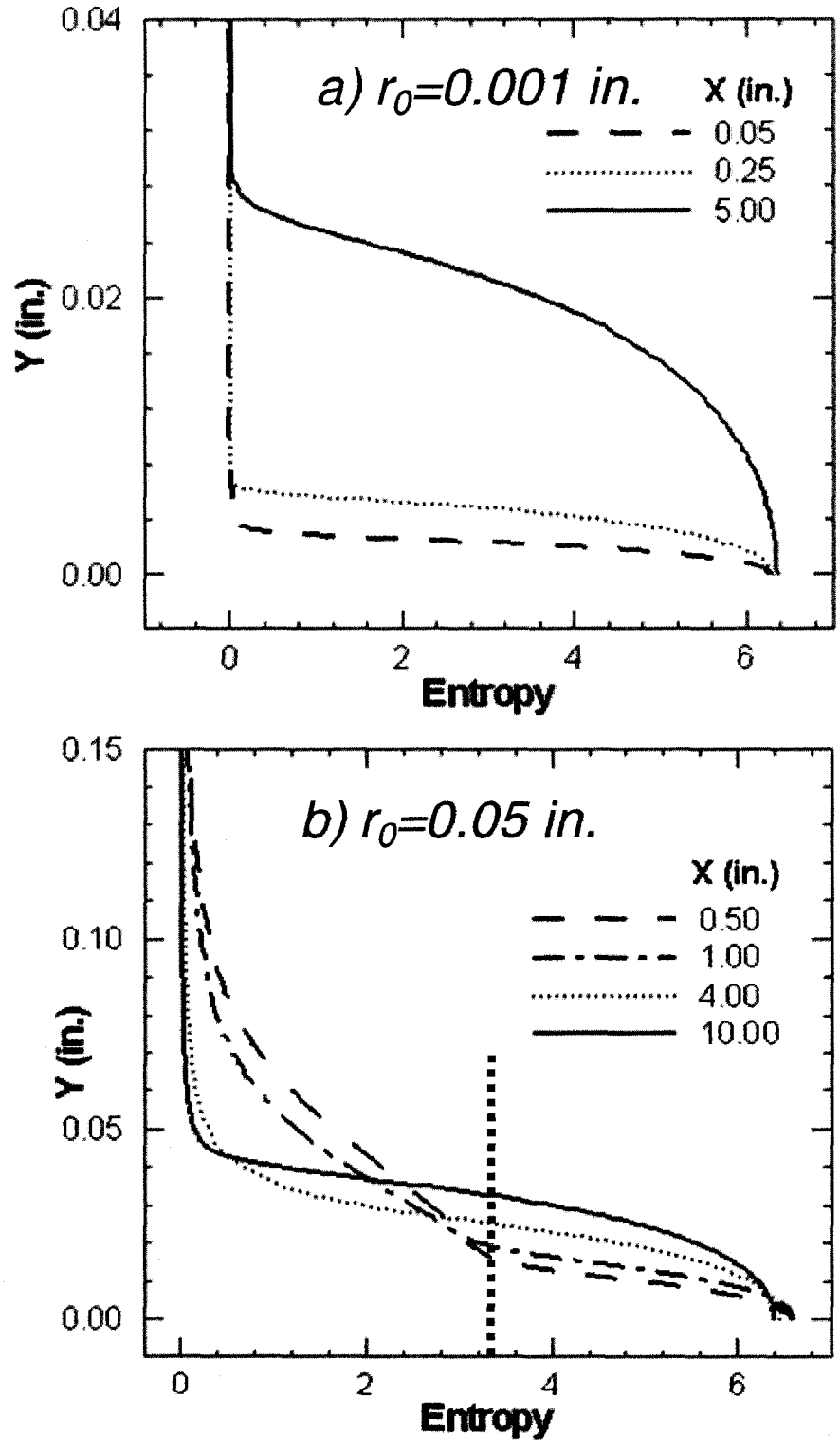

Figure 5.7 Entropy profiles at axial locations for different nose bluntness (a) r_0=0.001 in, (b) r_0=0.05 in. at M=6.0 and Re=7.8x10^6 /ft.

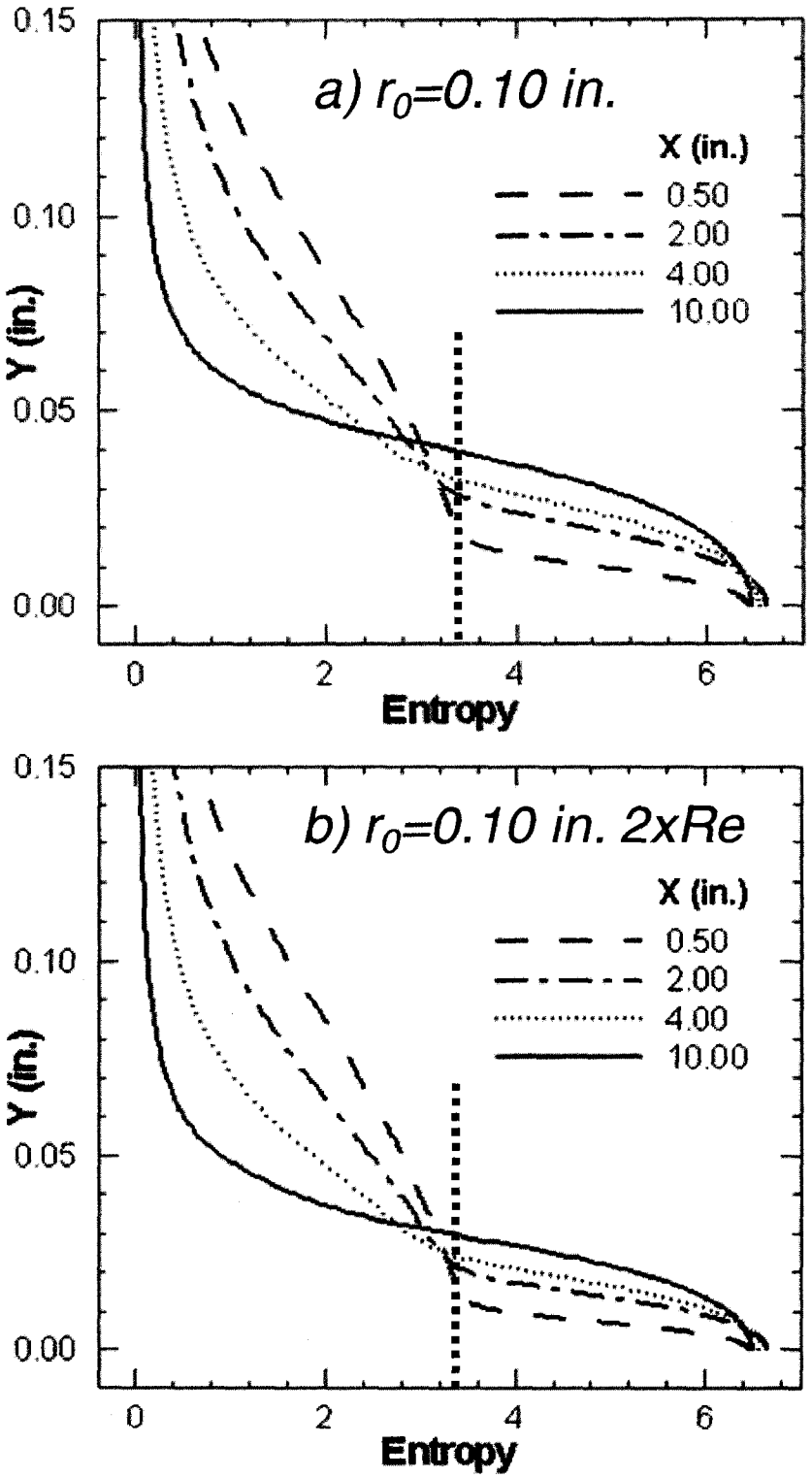

Figure 5.8 Entropy profiles at axial locations for different Reynolds numbers (a) Re=7.8x10^6 /ft, (b) Re=15.6x10^6 /ft at M=6.0 and r_0=0.10 in.

5.4 Linear Stability Analysis

Derivation of linear stability equations and the numerical scheme to solve are given in the appendix. In this section, Figures 5.9 (a) and (b) show the N-Factors and the growth rates for the most amplified disturbances computed using the mean profiles obtained from the numerical simulation for different bluntness r_0= 0.001, 0.05, 0.10 with the unit Reynolds number of 7.8×10^6/ft and for r_0= 0.05, 0.10 with the higher unit Reynolds number of 15.6×10^6/ft. For comparison, the results for the Blasius similarity profiles, which model a sharp leading edge, are also shown in the figures.

The frequency for the most amplified wave is about F= 0.90×10^{-4} for the similarity profiles. There is significant difference both for the mean flow and the stability results with increasing bluntness. The growth rates become smaller and the N-Factor curves move downstream. For the smaller bluntness, r_0= 0.001 in., the N-Factor curve remains closer to the similarity curve. For the larger bluntness cases the growth rates become smaller, and the N-Factor curves move further to the right. The most amplified frequencies are (0.85×10^{-4}, 0.75×10^{-4}, 0.60×10^{-4}, 0.425×10^{-4}) for r_0= 0.001, 0.05, 0.10 and 0.10 in. (with two times the unit Reynolds number) respectively. This shows that the frequencies of the most amplified disturbances become smaller with increasing bluntness. The growth rate curves are similar to the Blasius profile for all the cases.

The transition Reynolds numbers obtained using the N-factor of 10 for different bluntness cases are summarized in Table 5.2 and plotted in Figure 5.10. The ratio between the transition Reynolds number with respect to nose bluntness and the transition Reynolds number for the similarity profile, $(Re_{tr})_{r0}$ / $(Re_{tr})_{Similarity}$, is about 1.10, 1.27, 1.82, 3.33, respectively for Re_{r0} = 650, 32500, 65000 and 130000. To differentiate

between the effects of the free stream unit Reynolds number and the nose Reynolds number one simulation is performed for the bluntness case r_0= 0.05 in. at twice the unit Reynolds number of 2x7.8x10^6/ft. The expectation is that the results from this simulation should be close to the results obtained for the case with r_0= 0.10 in. at a unit Reynolds number of 7.8x10^6/ft. It is interesting to see in Figure 5.9 that the growth rates and the N-Factor curves are very close to each other, and the most amplified non-dimensional frequencies are also the same, F=0.60x10^{-4}. The transition Reynolds numbers are 21.90x10^6 and 23.70x10^6 for the cases r_0 = 0.10 in. and 0.05 in. (higher unit Reynolds number) respectively.

Table 5.2 Transition Reynolds numbers with respect to nose bluntness.

r_0 (in.)	Re_{r0}	x_{tr} (in.)	Re_{tr} x10^6	$(Re_{tr})_{r0}/(Re_{tr})_{Sim}$
0.0	0	18.55	12.06	1.00
0.001	650	20.50	13.32	1.10
0.050	32,500	23.50	15.30	1.27
0.100	65,000	33.70	21.90	1.82
0.10 (2xRe)	130,000	61.88	40.22	3.33
0.05 (2xRe)	65,000	36.44	23.70	1.96

The transition Reynolds number for this case is also included in Figure 5.10. This implies that the stability and the transition over blunt bodies are determined by the nose Reynolds number. Previous experiments[54] and the stability calculations[56] showed that the transition Reynolds number for a blunt cone at a Mach number of 8 with nose Reynolds numbers of 30,000 increased by a factor of 1.7~2.0 compared to a sharp cone. Potter[65] found from a series of aeroballistic range experiments on nominally sharp cones that the transition Reynolds number increases with the free stream unit Reynolds number as a power of 0.63. A line with the slope of 0.60 is included in Figure 6.10 for comparison. The prediction from the present calculations follows this slope closely.

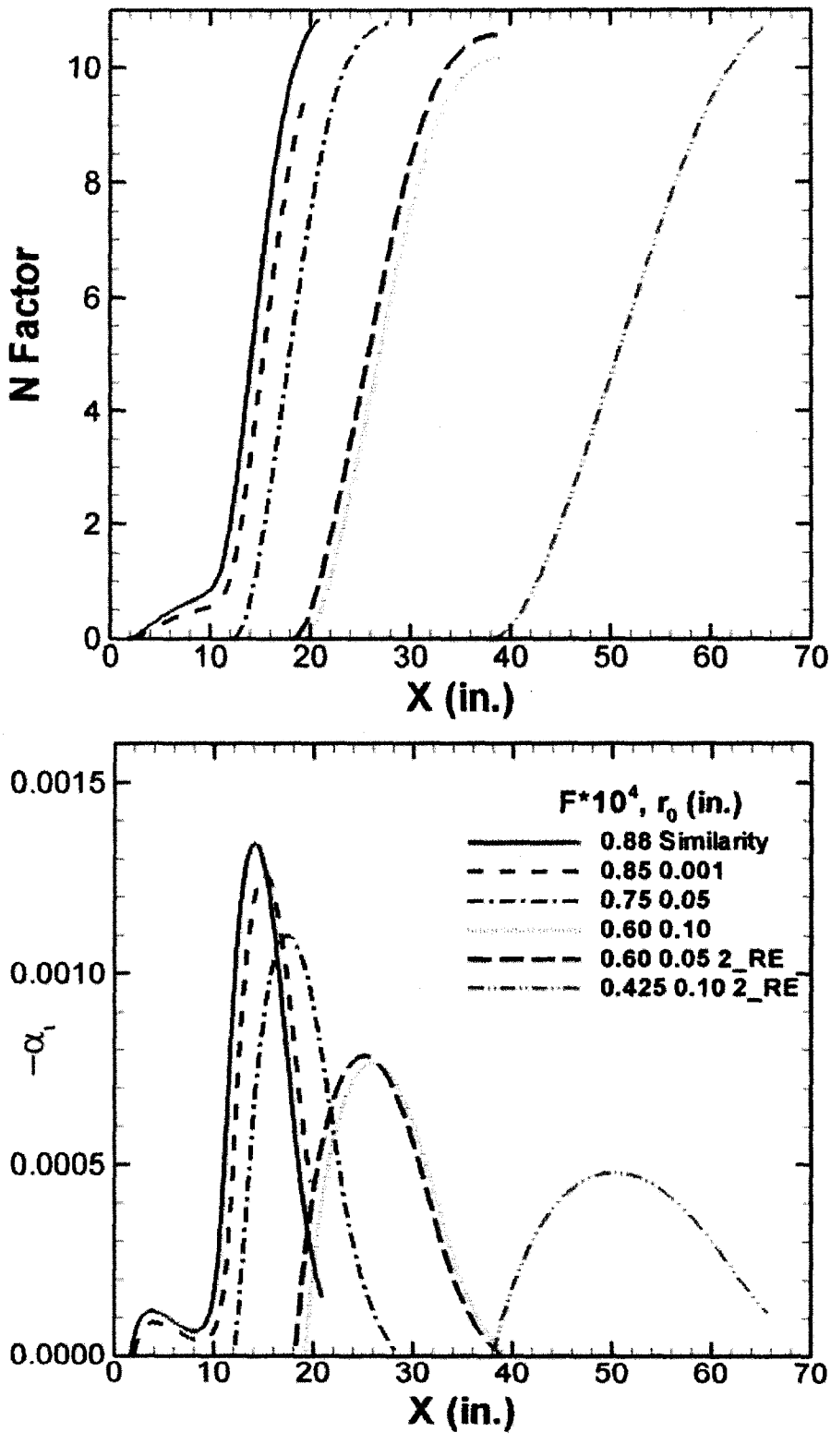

Figure 5.9 N-Factor and growth rate curves for different nose bluntness cases.

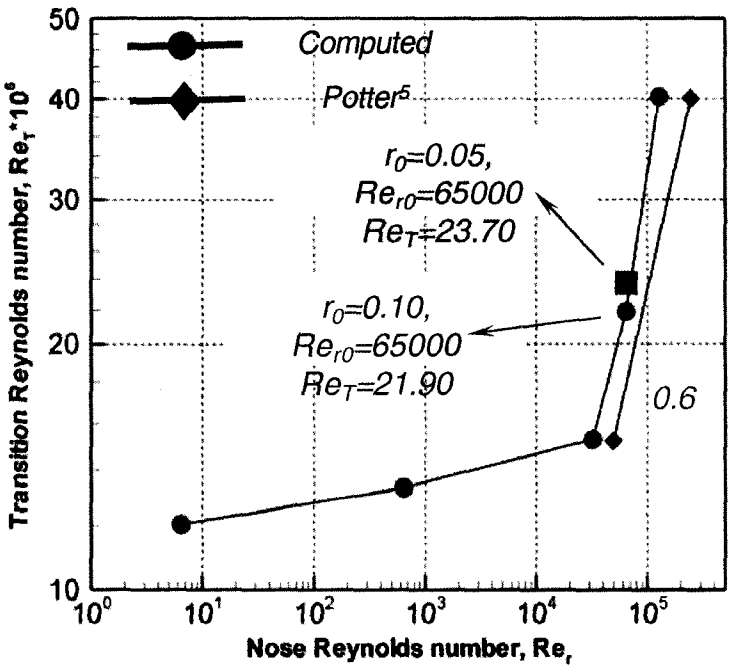

Figure 5.10 The transition Reynolds numbers for different bluntness.

5.5 Interactions of Acoustic Disturbances with Boundary Layer

After the mean flow is computed two dimensional slow acoustic disturbances are introduced at the outer computational boundary as described in Section 2.13, and the time accurate simulations are performed. Unsteady simulation results are presented for the cases r_0= 0.001, 0.05, 0.05(2xRe_∞), 0.10 in. at the most amplified frequencies F=0.80 x10^{-4}, 0.75x10^{-4}, 0.60 x10^{-4} and 0.60x10^{-4} respectively. These frequencies correspond to 304, 285, 228 and 556 kHz respectively for this unit Reynolds number.

To remain in the linear region, the amplitude of the forcing freestream acoustic waves is given a small value of P_{ac}/P_∞=2x10^{-6}. Even with this small amplitude, nonlinearity starts to develop near the end of the computational domain for the small bluntness case, r_0=0.001 in., with the frequency F=0.80 x10^{-4}.

Figure 5.11 shows the results for the evolution of unsteady fluctuations obtained from the simulations for the slow wave at a fixed time for the case where r_0=0.05 in. and F=0.75 x10^{-4}. Figure 5.11 (a) shows the contours of the density fluctuations near the nose region up to x ~ 6.0 in. and Figure 5.11 (b) depicts the results near the end of the computational domain x=15~25 in.

Figures 5.12 (a)-(d) display the expanded view of the density contours near the wall along the axial direction. The perturbation field can be divided into four regions. One region is the area outside the shock where the acoustic waves propagate uniformly. The second region is the shock layer across which the acoustic waves are transmitted. The third region is the area between the shock and the boundary layer. This region consists of a transmitted external acoustic field and the disturbances that are radiated from the boundary layer.

Figures 5.12 (a)-(d) also show that the flow field between the shock and the wall exhibit four different regions of excitations. One is the region directly below the shock where small wave diffraction occurs; the second is the region below this diffraction zone and above the entropy layer where the disturbances are quieter; the third is the entropy layer and the boundary layer edge region where large perturbations exist; and the fourth is the region near the wall.

The first important observation is that near the nose region (Figures 5.11 (a) and 5.12 (a)) the acoustic disturbances propagate across the leading edge bow shock and perturb the entropy layer. These disturbances as they evolve downstream remain inside the entropy layer and get into the boundary layer further downstream. Figures 5.12 (b)-

(d) clearly show that these disturbances remain near the edge of the boundary layer for a long distance before they become the highly unstable second mode.

Another interesting observation is that the region between the boundary layer and the shock layer is quieter compared to the acoustic waves outside the shock layer. This quiet region originates from the leading edge region (Figures 5.11 (a) and 5.12(a)) where the bow shock and the oblique shock meet. This implies that the acoustic waves are weakly transmitted through the shock and do not directly interact with the boundary layer further downstream. This was also observed in the flat plate simulation[52] whereas when the acoustic wave incidence angle is increased disturbances become quiet on the windward side.

Figure 5.13 shows the evolution of the wall pressure fluctuations for different cases. Figures 5.13 (a), (c), (e), and (g) show the amplitude of the pressure fluctuations along the wall in a linear scale, while Figures 5.13 (b), (d), (f) and (h) depict the same results in a log scale and include the results from the Parabolized Stability Equations (PSE) computations obtained for the same mean flow boundary layer profiles. The growth of the disturbances agrees very well with the PSE results. The figures clearly show the generation and the eventual exponential growth of the instability waves inside the boundary layer.

The first observation is that there are large differences in the amplitude levels of the disturbances attained between the small bluntness case and the large bluntness cases. In all the cases the amplitude of the free stream acoustic pressure is the same. For the small bluntness case r_0=0.001 in. in Figures. 5.13 (a) and (b), the disturbances grow from the leading edge and reach large amplitude levels of 0.50 near the predicted transition

onset point. The slow wave whose wavelength is closer to the wavelength of the instability wave smoothly transforms into an instability wave near the nose region. The parallel linear computations show that the first mode amplifies weakly up to x~10 in. for this frequency and yields an N-Factor of 1.0 near x~10 in. However, the simulation shows that the first mode disturbances are growing much stronger near the leading edge and yield an N-Factor of 3.0 near x~10 in. Hence, the non-parallel effects are stronger in the small bluntness case near the nose region.

The maximum amplitudes obtained for the large bluntness cases r_0=0.05 in., 0.05 in. ($2xRe_\infty$), 0.10 in. (Figures 5.13 (c-d), (e-f), (g-h)) are very small in the range of ~10^{-4}. The reason for this is the disappearance of the amplification of the first modes in the early part of the evolution. The disturbances not only grow but decay by two orders in magnitude before they start to grow due to the instability of the second modes. This may be due to the thickening of the boundary layer due to the entropy layer.

Following the PSE results up to the neutral point, the initial amplitude of the instability waves at the neutral point can be estimated. From these values the receptivity coefficients defined by the amplitude of the pressure fluctuations at the wall at the neutral point non-dimensionalized by the free-stream acoustic pressure can be evaluated using Equation (4.1).

Table 5.3 shows the amplitude of the pressure fluctuations at the neutral point $(P_{wall})_{np}$ and the receptivity coefficients for different nose radii. The amplitudes are $8.5x10^{-6}$ for the small bluntness case, and they are on the order of 10^{-9} for the large bluntness cases. This is reflected in the magnitude of the receptivity coefficients. The

receptivity coefficients are 4.23, 1.85×10^{-3} and 4.75×10^{-3} for the cases where r_0=0.001, 0.05 and 0.10 in.

Also interesting is the comparison of the amplitudes and the receptivity coefficients for the two cases where r_0=0.10 in. and r_0=0.05 in. ($2 \times Re_\infty$). The amplitudes and the receptivity coefficients are almost the same for these two cases. Hence, not only the instability properties but also the receptivity coefficients depend only on the nose Reynolds number. This implies that the unit Reynolds number effect is a direct consequence of the variation in the nose Reynolds numbers.

Table 5.3 Receptivity coefficients for different nose readii.

r_0 (in.)	Re_{r0}	F ($\times 10^{-4}$)	$(P_{wall})_{np}$	$C_{recpt.Slow}$
0.001	650	0.80	8.5×10^{-6}	4.23
0.050	32500	0.75	3.7×10^{-6}	1.85×10^{-3}
0.100	65000	0.60	9.5×10^{-9}	4.75×10^{-3}
0.050 ($2Re_\infty$)	65000	0.60	10.0×10^{-9}	5.0×10^{-3}

Figure 5.14 shows the density fluctuations inside the boundary layer near the nose region for a small r_0=0.001 in. and a large r_0=0.10 in. case. This clearly shows the effect of bluntness in the generation of disturbances near the nose region. As discussed previously, in the small bluntness case there is no entropy layer, and the disturbances excite the boundary layer up to the wall. However, in the large bluntness case, the disturbances are seen only away from the wall inside the entropy region.

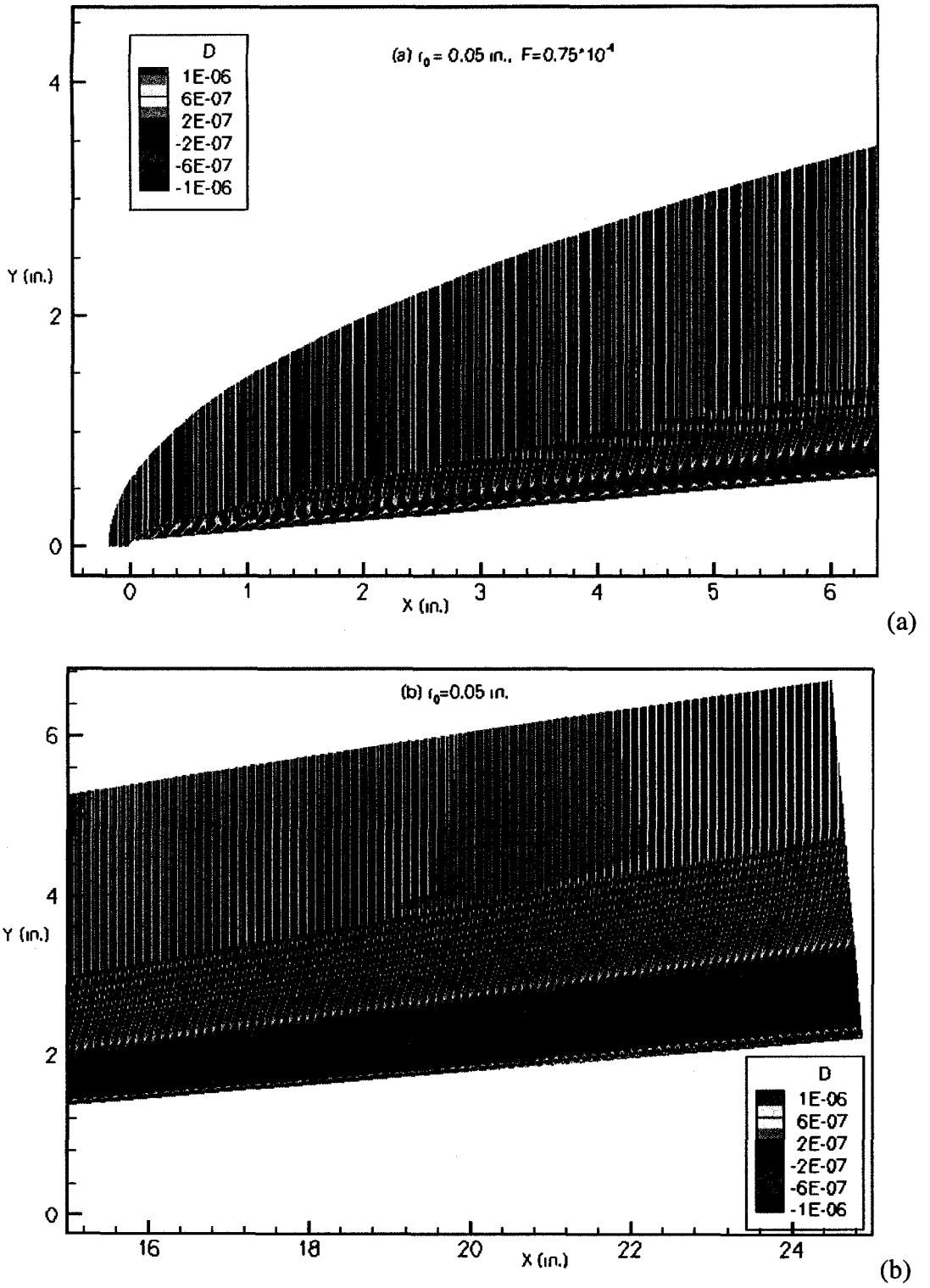

Figure 5.11 Contours of the unsteady density fluctuations due to the interaction of slow acoustic wave with a blunt cone: F=0.75x10-4. (a) Nose part. (b) Flat end.

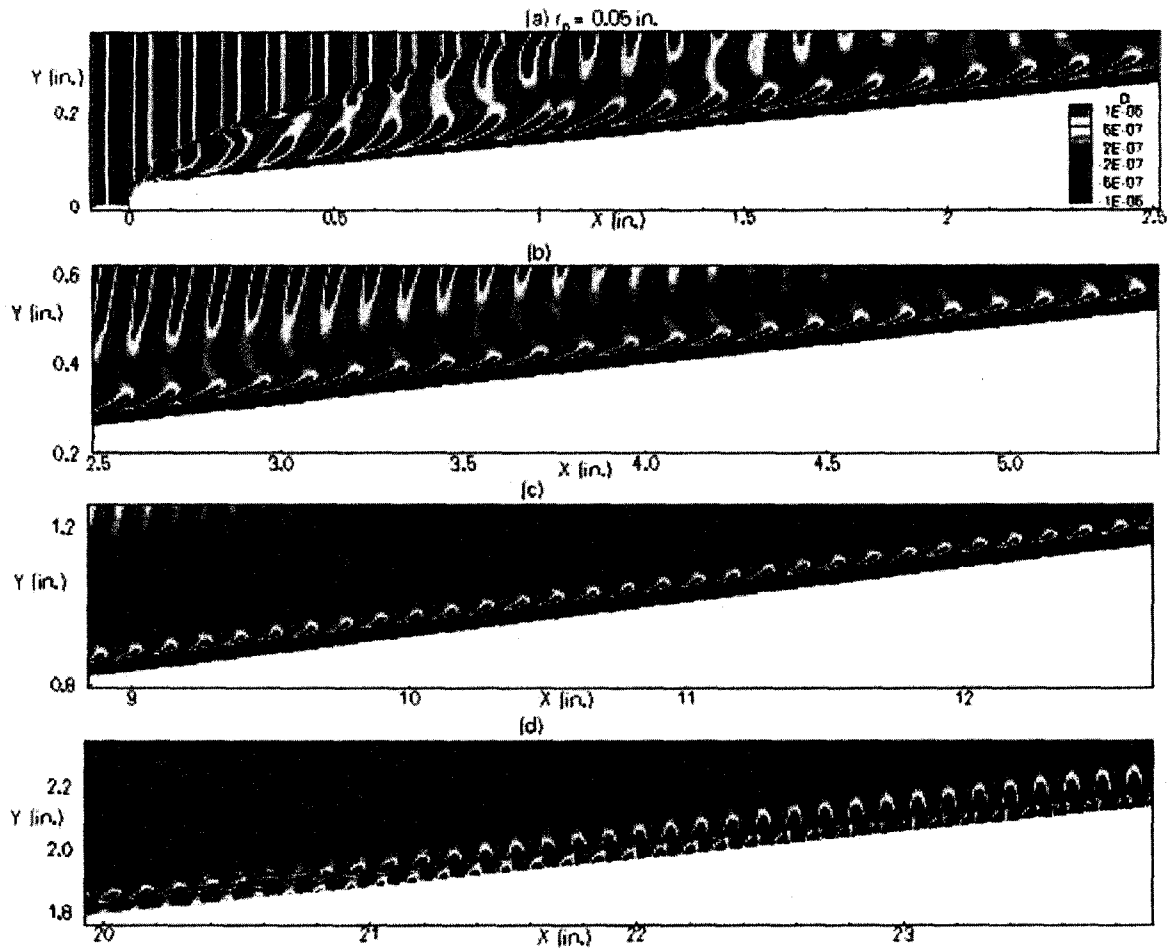

Figure 5.12 Expanded view of the contours of unsteady density fluctuations near the wall along the axial direction

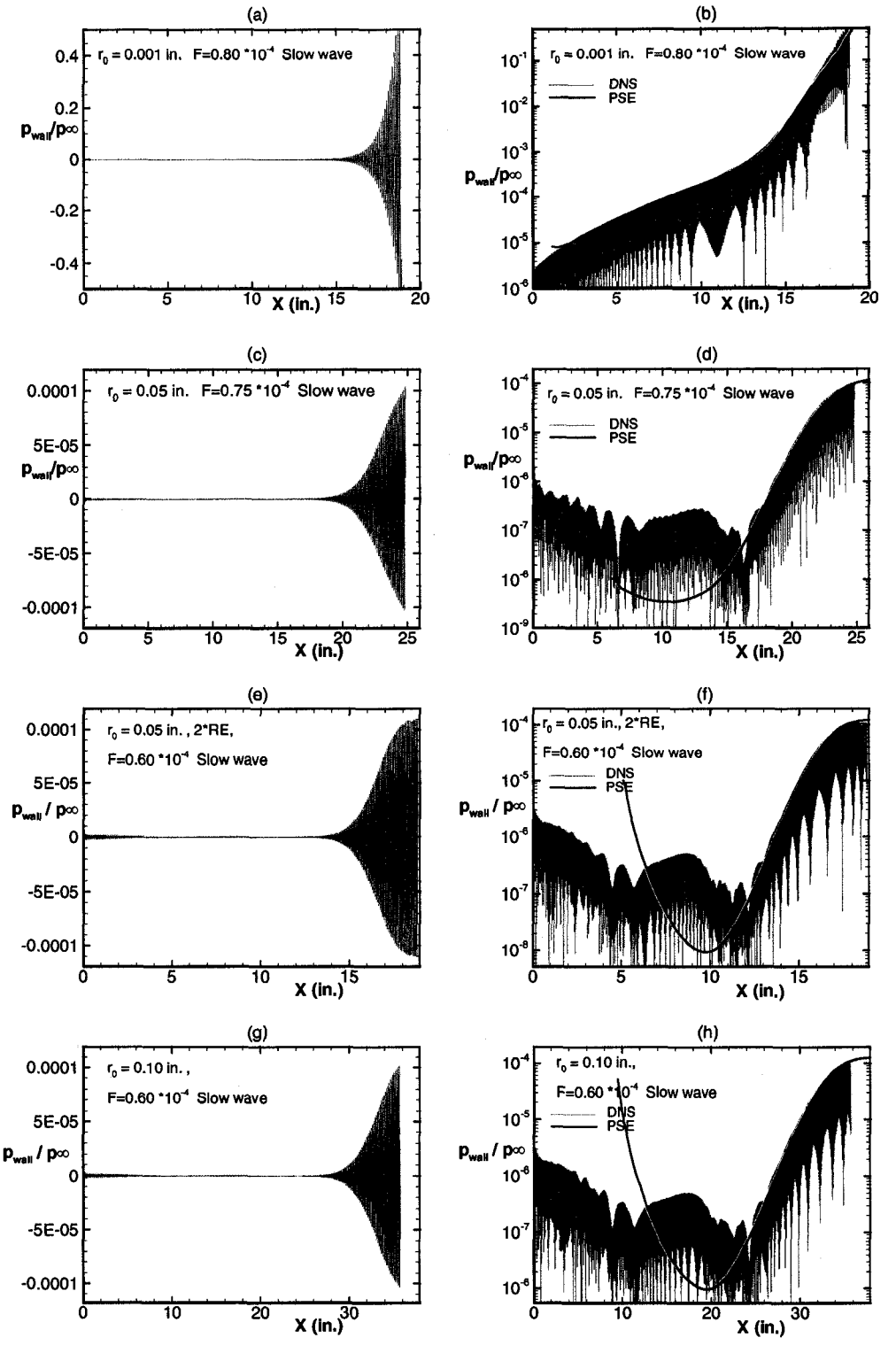

Figure 5.13 Amplitude of the pressure fluctuation on the wall (a), (c), (e), (g), and comparison with the PSE (b), (d), (f), (g).

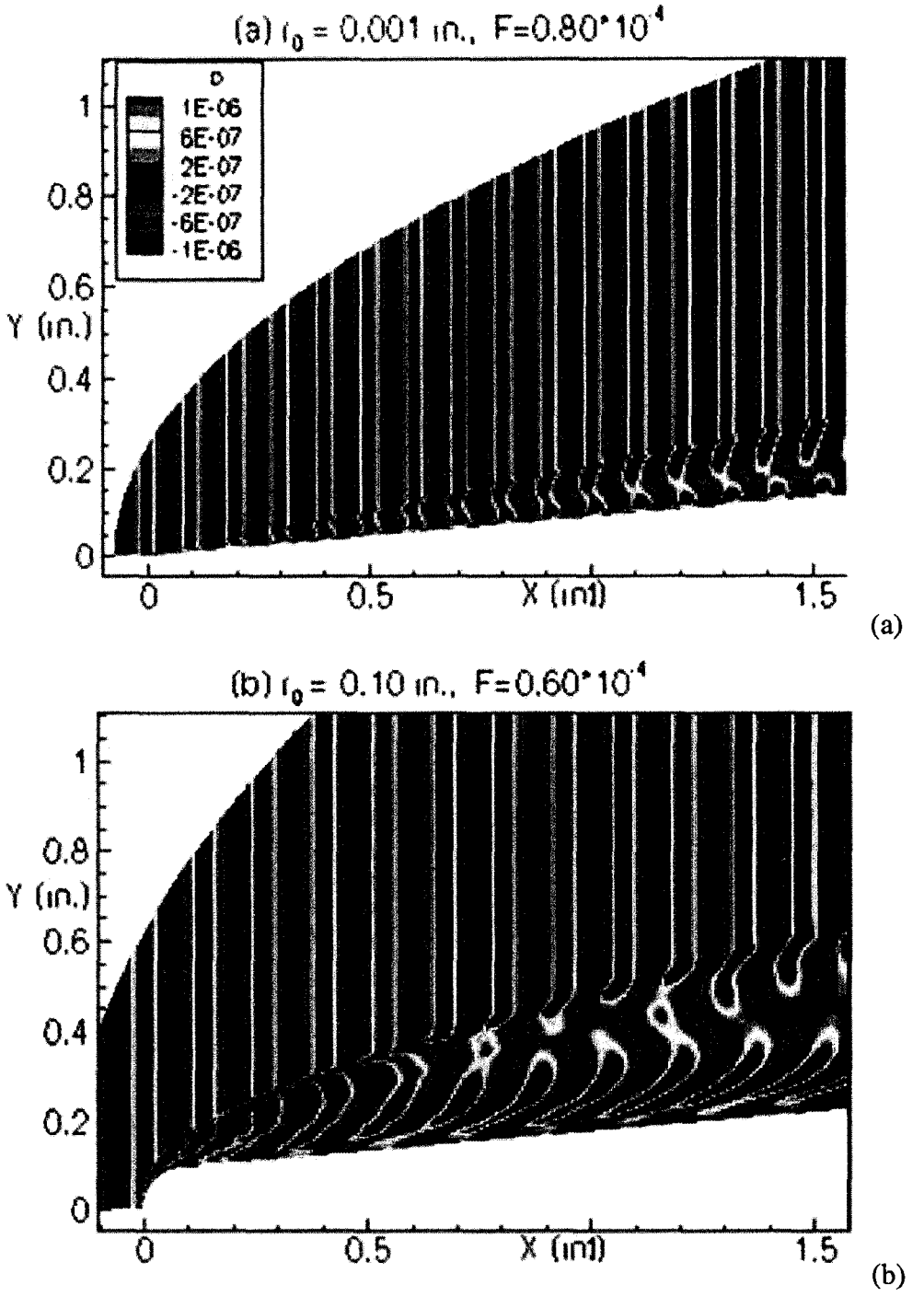

Figure 5.14 Contours of unsteady density fluctuations inside the boundary layer near the nose region for two bluntness cases (a) r0=0.001, F=0.80x10-4 and (b) r0=0.10, F=0.60x10-4.

5.6 Discussion and Conclusion

In this chapter the effect of nose bluntness on the receptivity and stability of hypersonic boundary layers over a blunt cone with a 5 degree half-angle are numerically investigated at a free stream Mach number of 6.0 and at a unit Reynolds number of 7.8×10^6 /ft. Both steady and unsteady solutions are obtained by solving compressible Navier-Stokes equations using the 5^{th} order accurate Weighted Essentially Non-Oscillatory (WENO) scheme for space discretization and using a third-order Total-Variation-Diminishing (TVD) Runge-Kutta scheme for time integration. Computations are performed for different nose radii r_0= 0.001, 0.05, 0.05 ($2xRe_\infty$), 0.10, 0.10 in. ($2xRe_\infty$), which yield nose Reynolds numbers of 650, 32500, 65000, 65000, 130000.

The results show that bluntness has a strong stabilizing effect on the stability of the boundary layers. The transition Reynolds number increases slowly up to a nose Reynolds number of 30,000 and then increases sharply at higher nose Reynolds numbers. The transition Reynolds number for a cone at a nose Reynolds number of 65,000 is about 1.8 times larger than that for the Blasius boundary layer. This is due to the entropy layers that are generated near the leading edges. These layers persist for longer distances with increasing bluntness. There may be other unstable modes in the entropy layer as were observed in the experiments[54] other than the first-mode type instabilities that were considered in this work. Whether they exist and what role these waves play in the transition process still has to be investigated.

In the small bluntness case, the disturbances grow starting from the nose region and reach very large values of ~0.50 near the transition point. The growth of the first mode is much stronger for this case due to the non-parallel effects. The amplitude levels

of the disturbances are much smaller in the order of 10^{-4} in the larger bluntness cases. There are no unstable first modes observed in the large bluntness cases, and the disturbances decay by two orders before they start to grow due to the second mode instability. The receptivity coefficient of small bluntness, r_0=0.001 in., case is about 4.23, and it becomes much smaller, in the order of ~ 10^{-3}, for the larger bluntness cases. This raises some questions about the transition process over blunt bodies. If the receptivity coefficients are very small for the second modes as was found in this chapter, how can the amplitude of the disturbances attain high values? One possibility is that the N-Factors are larger, about 15~16, in these cases. This will increase the transition Reynolds number further than is computed in this work. Another possibility is that the receptivity coefficients at non-zero acoustic incident angles may be larger than is obtained at zero incident angles. These computations have to be carried out to find the largest receptivity coefficients.

CHAPTER VI

6. WALL COOLING EFFECTS ON RECEPTIVITY

6.1 Introduction

In this chapter the effects of wall cooling on the receptivity process induced by the interaction of slow and fast acoustic disturbances in the free-stream are numerically investigated for a boundary layer flow over a 5-degree straight cone. The free-stream Mach number is 6.0, and the Reynolds number is 7.8×10^6 /ft. Both the steady and unsteady solutions are obtained by solving the full Navier-Stokes equations using the 5^{th} order accurate weighted essentially non-oscillatory (WENO) scheme for space discretization and using the 3^{rd} order total variation diminishing (TVD) Runge-Kutta scheme for time integration.

Computations are performed for a cone with nose radius of 0.001 in. for adiabatic wall temperature (T_{aw}), $0.75 \times T_{aw}$, $0.5 \times T_{aw}$, $0.40 \times T_{aw}$, $0.30 \times T_{aw}$, and $0.20 \times T_{aw}$. Once the mean flow field is computed, disturbances are introduced at the upstream end of the computational domain.

Generation of instability waves from the leading edge region and receptivity of the boundary layer to slow acoustic waves are investigated. Computations showed that wall cooling has a strong stabilization effect on the first mode disturbances as was observed in the experiments. Transition location moved upstream when wall cooling was

applied. It was also found that the boundary layer is much more receptive to the fast acoustic wave (by almost a factor of 50).

6.2 Literature Review

The transition process from laminar to turbulent flow is still an important challenge even after years of research. Accurate prediction of the transition location is vital for the design of hypersonic vehicles. Because transition controls important quantities such as aerodynamic drag, heat transfer and other boundary layer parameters. In hypersonic boundary layers one important parameter is the wall temperature. Wall cooling would be expected to stabilize first mode disturbances while destabilizing the second mode. The effects of cooling on transition have been studied experimentally and numerically by many researchers.

Lees[68] predicted that cooling the surface would stabilize the boundary layer. Later, Mack's[69] results showed that the first mode was stabilized by cooling; however, the higher modes were destabilized by this process. Experiments of Demetriades[70] and Lysenko[71] confirmed that cooling the wall increased the growth rates of the second mode disturbances and reduced the transition Reynolds number. Stetson[72] investigated the effects of surface temperature on the stability of the laminar boundary layer experimentally, and the results also verified the linear stability theory. Balakumar and Malik[73] computed the parametric effects of the pressure gradient and wall cooling on the stability of the flow over the cone using the quasi-parallel, compressible linear stability e^{Malik} code.

Receptivity[7] is a process by which free-stream or wall-induced disturbances enter the laminar boundary layer and generate unstable waves[8]. The receptivity process is poorly understood at hypersonic speeds. The understanding of this phenomenon is of great importance because receptivity connects the amplitude of the free-stream disturbances and initial amplitude of the unstable waves[61]. Recent experimental,[3, 61, 63, 74, 75] theoretical[46, 47, 76-79] and computational[22, 40, 48-53, 58, 67, 80-85] studies increased our understanding about the receptivity mechanism. However, it still remains a challenging problem with practical importance.

The objectives of this chapter are to estimate the destabilizing effects of wall cooling on the hypersonic boundary layers over a blunt cone and to calculate the receptivity coefficient of the instability waves generated near the leading edge.

6.3 Mean Flow Results

Computations are performed for hypersonic flow at a free stream Mach number of 6.0 over a 5-degree, half-angle cone with blunt leading edge, R_n=0.001 in., for different wall temperatures to investigate the effects of wall cooling on hypersonic boundary layer receptivity due to acoustic disturbances in slow and fast modes. For this study we used the following flow conditions (Table 3.2 with adiabatic and isothermal wall temperature conditions), geometry (Figure 3.6) used by Horvath et al.[35], and computational setup (Figure 2.5). Boundary layer edge conditions for a sharp cone are given in Table 4.1. The nose region of the cone is modeled as a circle. Simulations are performed for wall temperatures T_w= Adiabatic wall (T_{aw}), 0.75xT_{aw}, 0.50xT_{aw}, 0.40xT_{aw}, 0.30xT_{aw}, and 0.20xT_{aw}. Different cases are summarized in Table 6.3. This table shows wall

temperature ratios to adiabatic wall temperature (804 °R) and freestream temperature (113.98 °R) and corresponding bow shock standoff distances. According to the data in Table 6.1 the standoff distance (in column 4) decreased proportionally to the applied wall temperature from 2.50×10^{-4} to 2.13×10^{-4}.

Table 6.1 Wall temperatures and bow shock standing distances.

$T_{wall}/T_{Ad.wall}$	$G_0 = T_{wall}/T_\infty$	T_{wall}(°R)	δ ($\times 10^{-4} in.$)
1.00	7.052	804	2.50
0.75	5.289	603	2.39
0.50	3.526	402	2.28
0.40	2.8208	322	2.21
0.30	2.1156	241	2.15
0.20	1.4104	161	2.13

$T_\infty = 113.98$ °R.

Validation studies of axisymmetric code are given in Chapter 3 and presented by the author[39, 40]. Figures 6.1 and 6.2 show the mean flow temperature contours computed using the WENO code. Figures 6.1 (a), (b) and 6.2 (a), (b) show the results for the 5-degree, half-angle cone at different wall temperatures T_w=Adiabatic wall (T_{aw}), $0.75xT_{aw}$, $0.50xT_{aw}$, and $0.20xT_{aw}$. In the adiabatic wall case bow shock generated a high temperature region. This region convected to downstream over the cone wall. For cooled wall cases the high temperature region is trapped between the bow shock and nose part of the cone. Bow shock standing distance decreased 15% when wall temperature decreased to $0.20xT_{aw}$ (Table 6.1).

Figures 6.3 (a) and (b) depict the mean flow density contours over the adiabatic cone and cooled cone (T_w=$0.20xT_{aw}$) cases. Maximum non-dimensional density occurred on the stagnation point for adiabatic and cooled conditions are 6 and 33 respectively. Over the flat part of the cone density contours look similar. The high density region is

increased when is cooling applied, but it does not extend to the flat part. Figure 6.4 compares the Mach contours of the aforementioned wall conditions. Wall cooling decreased the oblique shock angle and compressed the Mach layers to the wall.

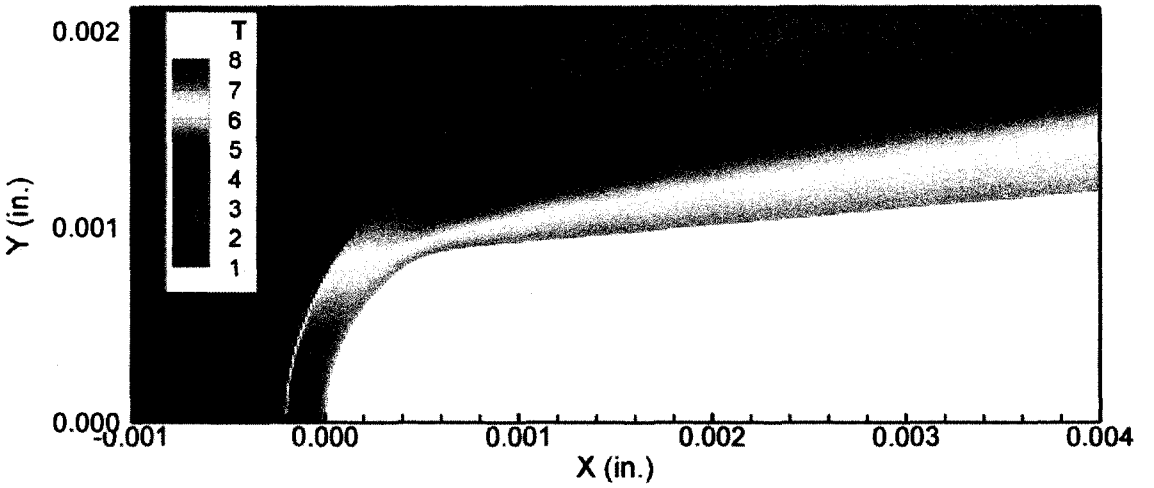

(a) Adiabatic wall (T_{aw})

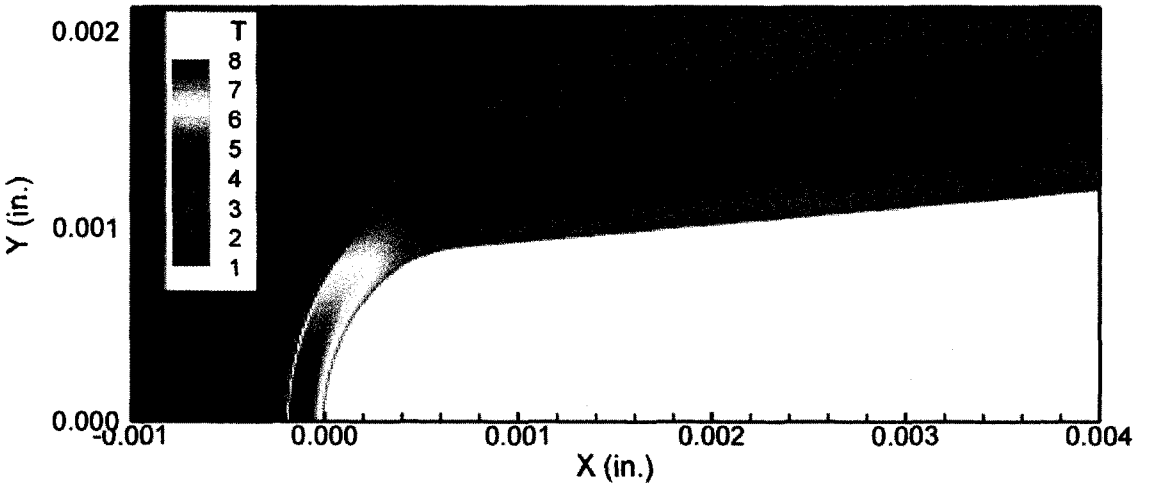

(b) $T_w=T_{aw}x0.75$.

Figure 6.1 Mean flow temperature contours for different wall temperature conditions (a) Adiabatic wall (T_{aw}), (b) $T_w=T_{aw}x0.75$.

Figure 6.5 (a) shows the wall to free stream temperature ratio, G_0, along the cone surface for different wall cooling conditions, and Figure 6.5 (b) shows the variation of the

boundary layer edge Mach number, M_e, along the cone surface. The boundary layer edge Mach number and temperature for the adiabatic case at x=13.96 in. are M_e=5.57 and T_e=129.53 °R, and for the 80% cooled case at x=19.58 in., are M_e=5.58 and T_e=129.2 °R.

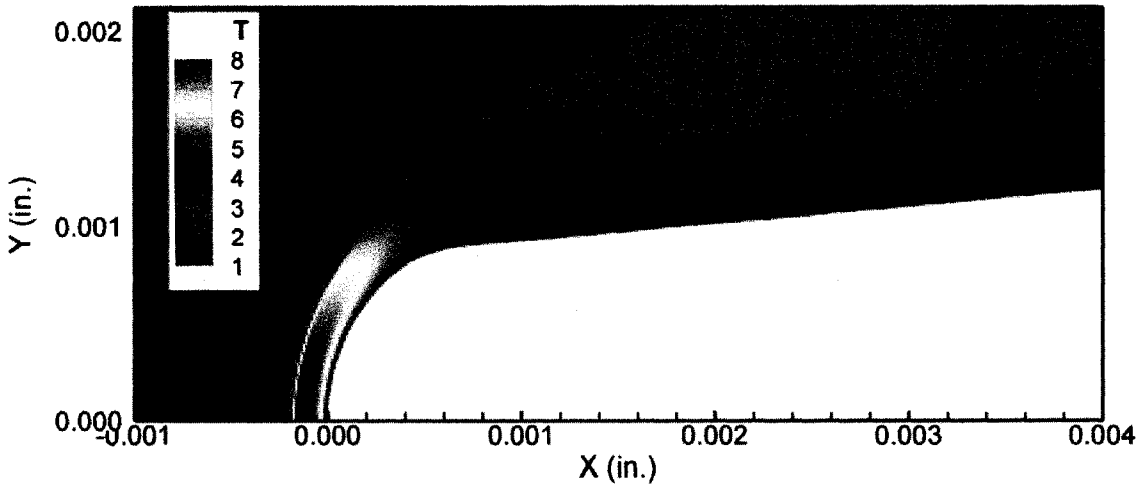

(a) $T_w=T_{aw}$x0.50

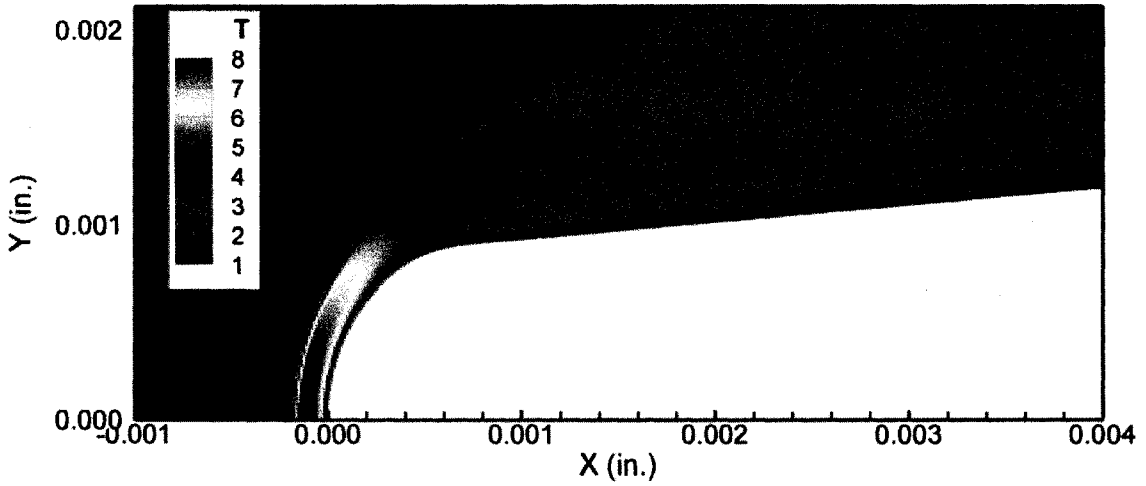

(b) $T_w=T_{aw}$x0.20

Figure 6.2 Mean flow temperature contours for different wall temperature conditions (a) $T_w=T_{aw}$x0.50, (b) $T_w=T_{aw}$x0.20.

Steady mean flow density profiles at different axial locations are plotted in Figures 6.6 and 6.7 in similarity coordinates for adiabatic wall and cooled walls

($0.50xT_{aw}$, $0.30xT_{aw}$, and $0.20xT_{aw}$). In Figure 6.6 (a) mean flow density profiles converge to a certain profile at x=0.2 in., which stays the same until the end of the computational domain for adiabatic wall conditions.

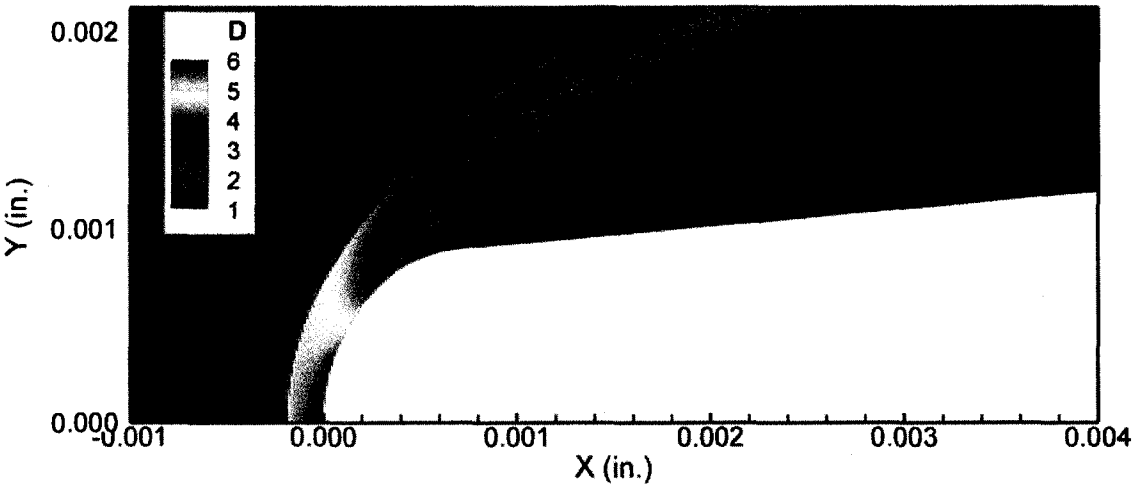

(a) Adiabatic wall (T_{aw})

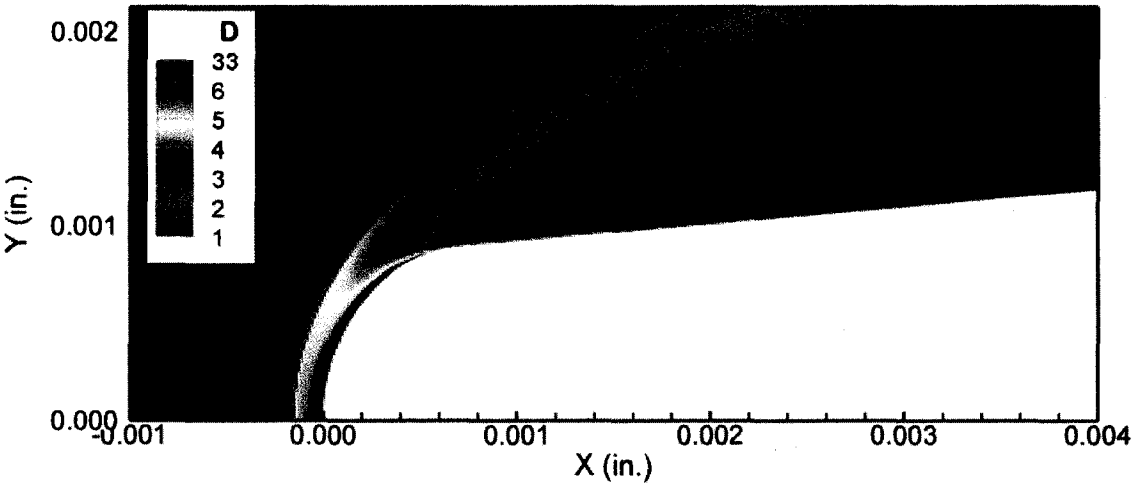

(b) $T_w=T_{aw}x0.20$

Figure 6.3 Mean flow density contours for different wall temperature conditions (a) Adiabatic wall (T_{aw}), (b) $T_w=T_{aw}x0.20$.

Figures 6.6 (a) and 6.7 (b) show that wall cooling decreased boundary layer thickness from $\eta=14.6$ ($T_w=T_{aw}$) to $\eta=8.19$ ($T_w=0.20xT_{aw}$) and also increased the non-

dimensional density on the wall from ρ=0.16 (T_w=T_{aw}) to ρ=0.80 (T_w=0.20xT_{aw}). The density increase on the wall changed the characteristic of density profiles. In the adiabatic case, the minimum value of the density occurred on the cone wall and steadily increased away from it.

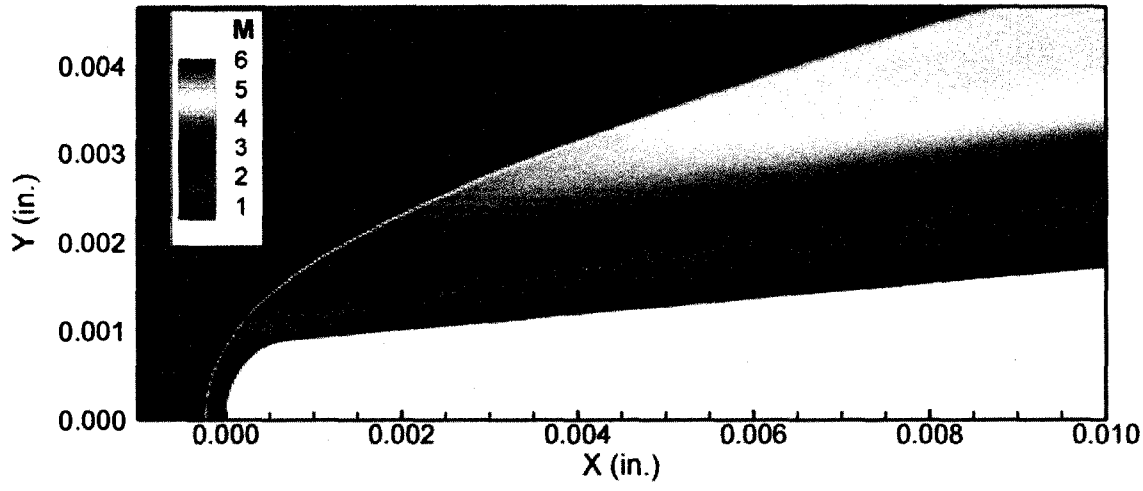

(a) Adiabatic wall (T_{aw})

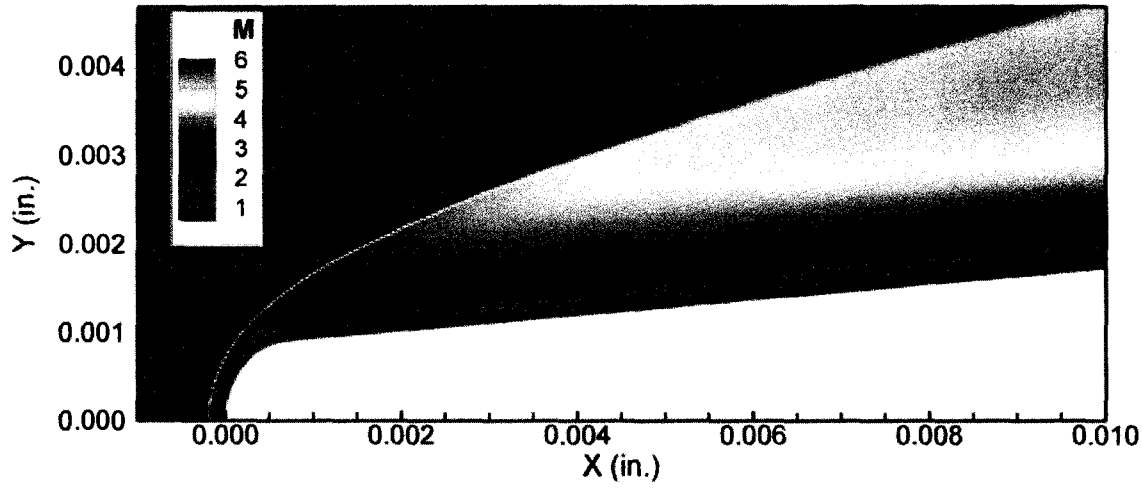

(b) T_w=T_{aw}x0.20.

Figure 6.4 Mean flow Mach contours for different wall temperature conditions (a) Adiabatic wall (T_{aw}), (b) T_w=T_{aw}x0.20.

However, for the cooled wall case (T_w=0.20xT_{aw}) the density on the wall ($\rho_{\eta=0}$=0.80) first started to decrease away from the wall until η=2 ($\rho_{\eta=2}$=0.42). After

making a minimum at this point the density changed its character and increased as in the adiabatic wall case. Even these density profiles seem to have a low density region. Their minimum density, at $\eta=2$ ($\rho_{\eta=2}=0.42$), is 2.6 times larger than the minimum density value of adiabatic case ($\rho_{\eta=0}=0.16$). As a result, we can say that wall cooling reduced the boundary layer thickness and increased the density inside it.

Figures 6.8-10 show the temperature profiles at axial locations for different cooling cases. The compressible Blasius similarity profiles are also included for comparison. In the adiabatic wall case even at x=0.2 in. calculated mean flow temperature profiles perfectly matched with the similarity solution as shown in Figure 6.8 (a). As was observed in the density graphs, temperature profiles also converged to the same profile at x=0.2 in. and stayed the same until the end of the computational domain. Wall cooling decreased thermal boundary layer thickness also.

For the highest cooling case ($T_w=0.20xT_{aw}$), as shown in Figure 6.10 (b), the wall temperature was 161 °R, and it increased away from the wall until $\eta=2$ ($T_{\eta=2}=305$ °R). After maxing out at this point the temperature of the mean flow decreased, as was seen in the adiabatic case, to 129.26 °R. The difference between the similarity profiles and simulation results originates with the leading edge bluntness.

Figures 6.11 (a) and (b) show the mean flow density profiles at different axial locations in physical coordinates for the adiabatic ($T_w=804$ °R) and highest wall cooling case ($T_w=161$ °R) respectively. The minimum value of mean flow nondimensional density is 0.43 at y=0.01 in. normal to the wall, and boundary layer thickness is 0.04 in. for highly cooled wall simulation. Figure 6.11 also shows that wall cooling decreased the

boundary layer thickness two times from 0.08 in. to 0.04 in. Non-parallel effects are stronger for the cooled wall at x=1.01 in. as compared to the adiabatic case.

Figures 6.12 (a) and (b) depict the mean flow temperature profiles at different axial locations in physical coordinates for adiabatic (T_w=804 °R) and cooled wall (T_w=161 °R) conditions.

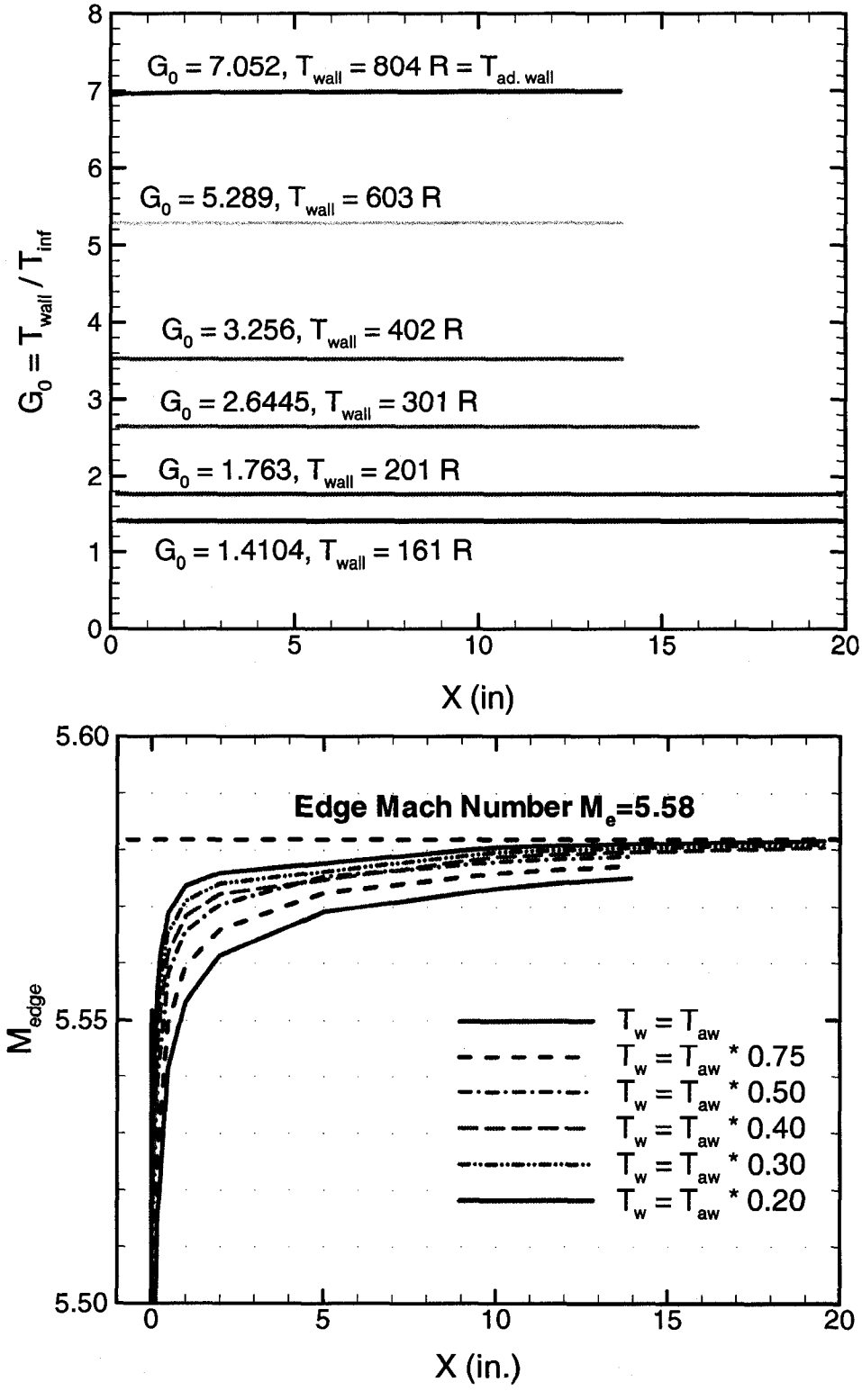

Figure 6.5 (a) Wall to free stream temperature ratio along the cone surface for different simulations. (b) Effect of wall cooling on the boundary layer edge Mach number.

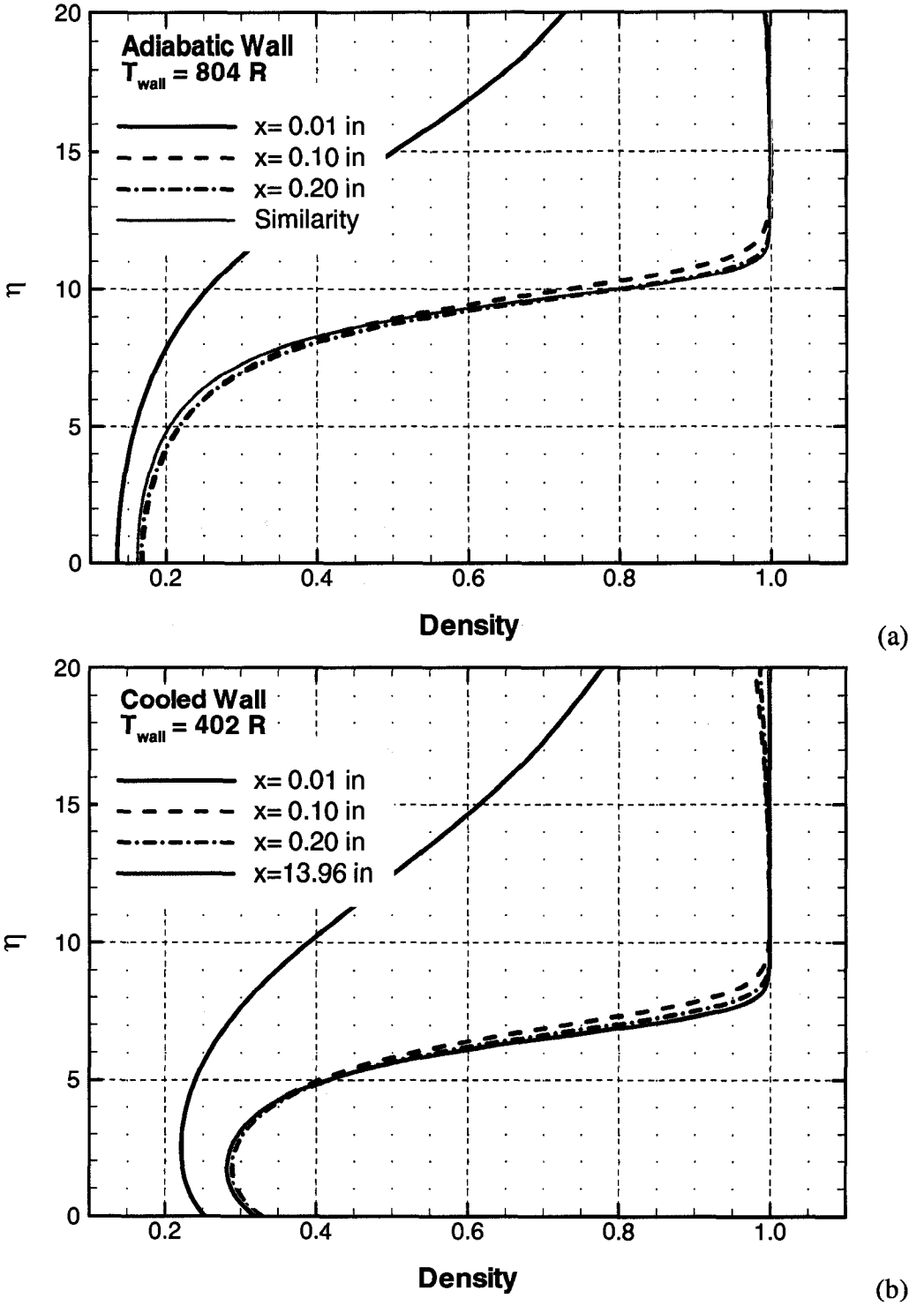

Figure 6.6 Mean flow density profiles at different axial locations in similarity coordinates for different wall temperatures. (a) Adiabatic wall (T_{aw}), (b) $T_w=T_{aw}*0.50$

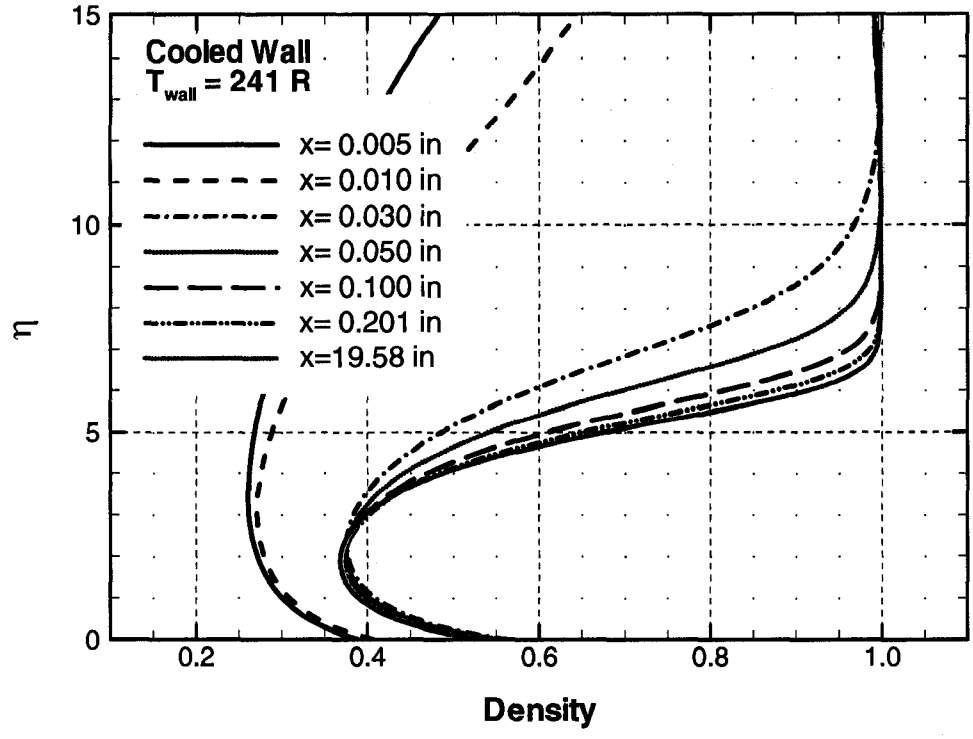

Figure 6.7 Mean flow density profiles at different axial locations in similarity coordinates for different wall temperatures. (a) $T_w=T_{aw}x0.30$, (b) $T_w=T_{aw}x0.20$

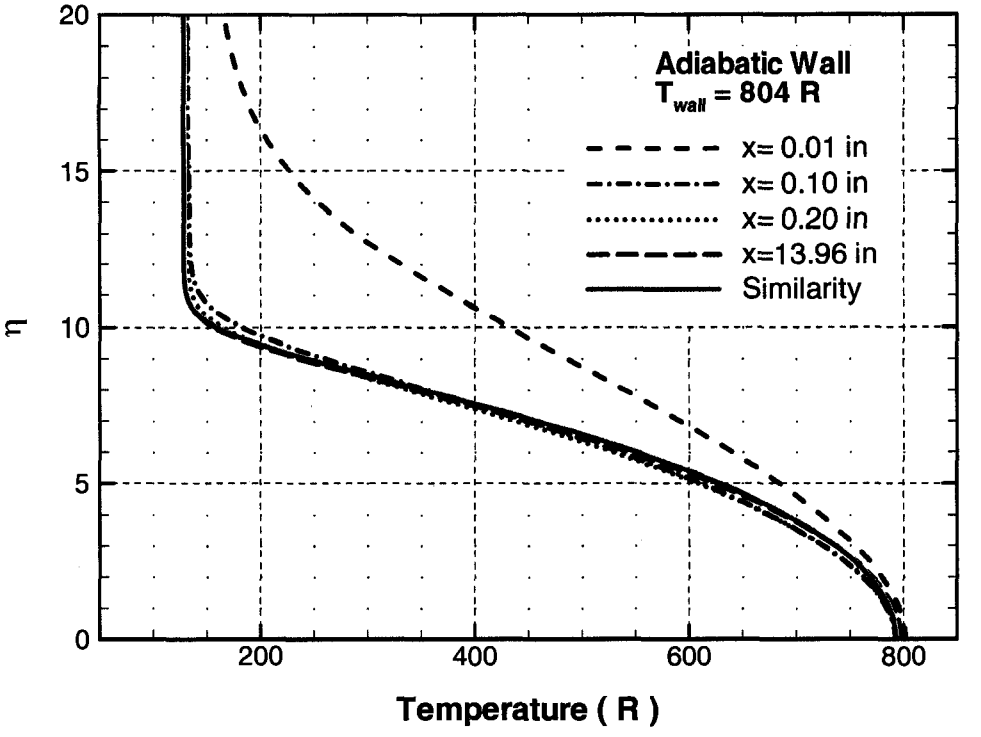

(a)

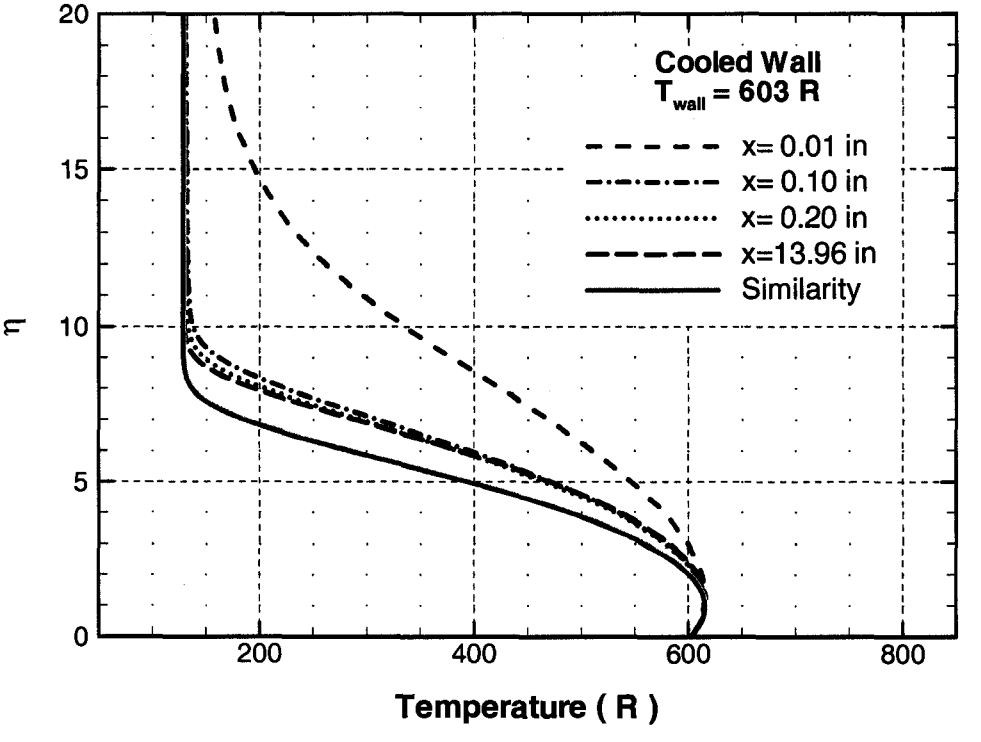

(b)

Figure 6.8 Mean flow temperature profiles at different axial locations in similarity coordinates for different wall temperatures. (a) Adiabatic wall (T_w), (b) $T_w=T_{aw}$x0.75.

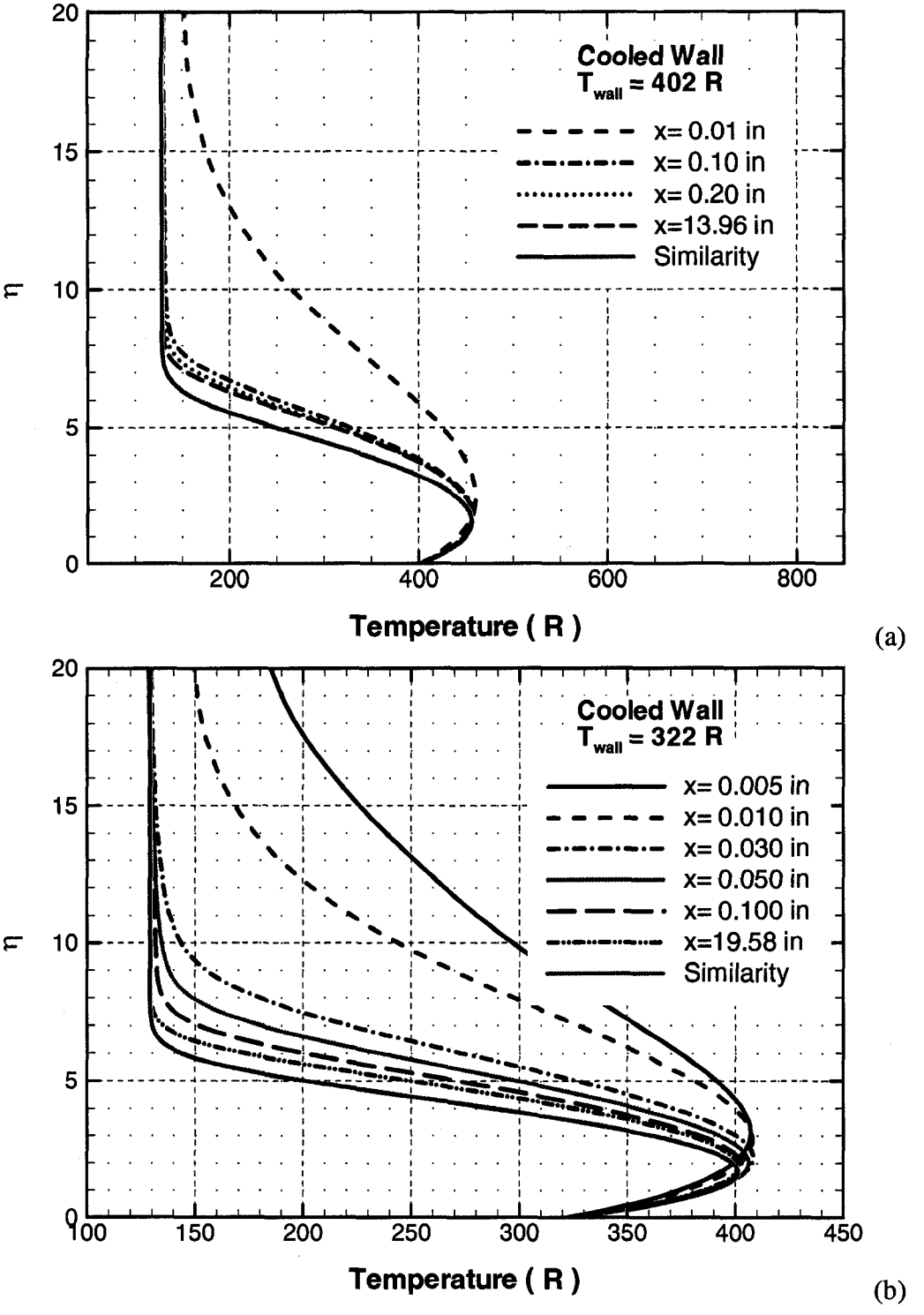

Figure 6.9 Mean flow temperature profiles at different axial locations in similarity coordinates for different wall temperatures. (a) $T_w=T_{aw}x0.50$, (b) $T_w=T_{aw}x0.40$.

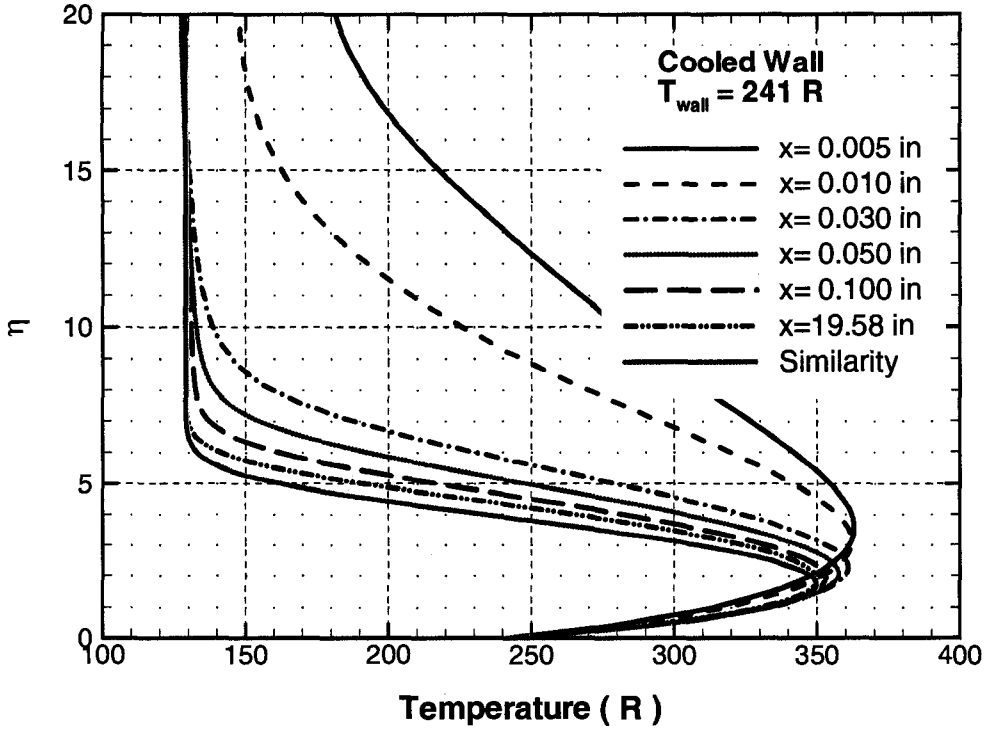

(a)

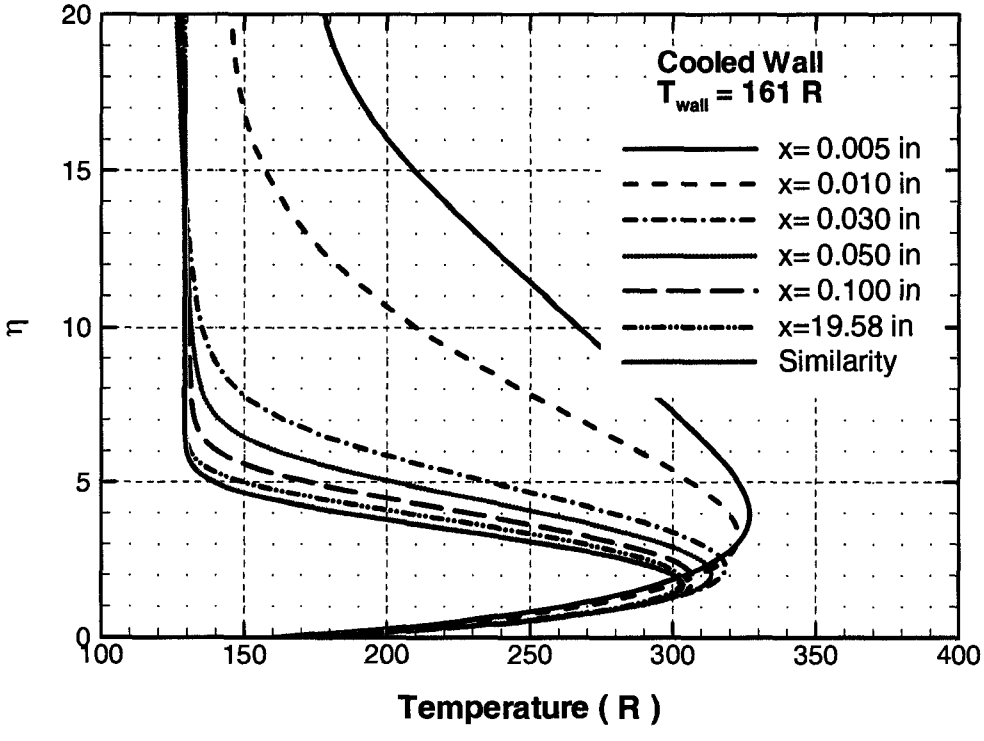

(b)

Figure 6.10 Mean flow temperature profiles at different axial locations in similarity coordinates for different wall temperatures. (a) $T_w=T_{aw}x0.30$, (b) $T_w=T_{aw}x0.20$.

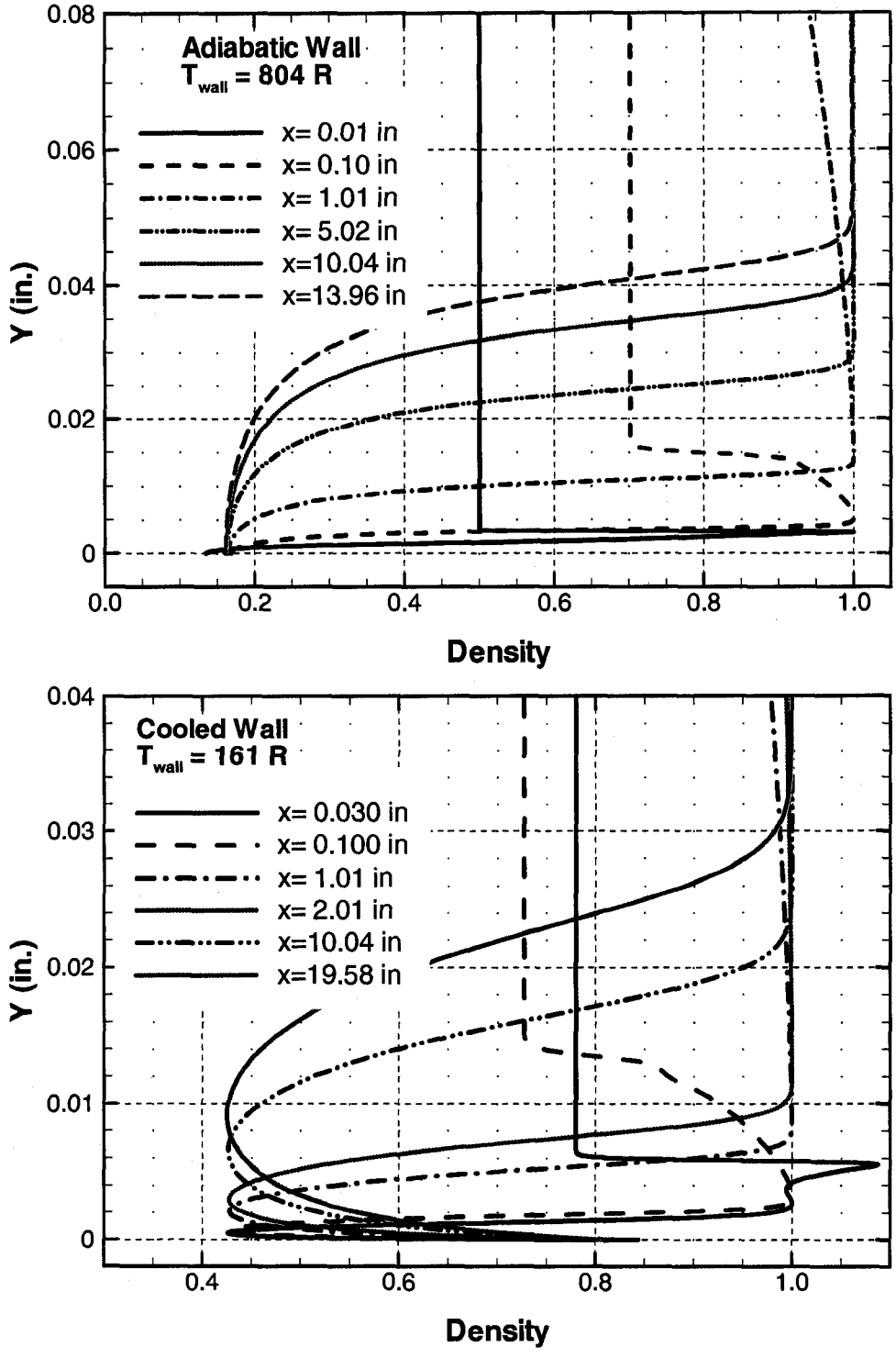

Figure 6.11 Mean flow density profiles at different axial locations in physical coordinates for different wall temperatures. (a) T_w Adiabatic wall (T_{aw}), and (b) T_w=T_{aw}*0.20.

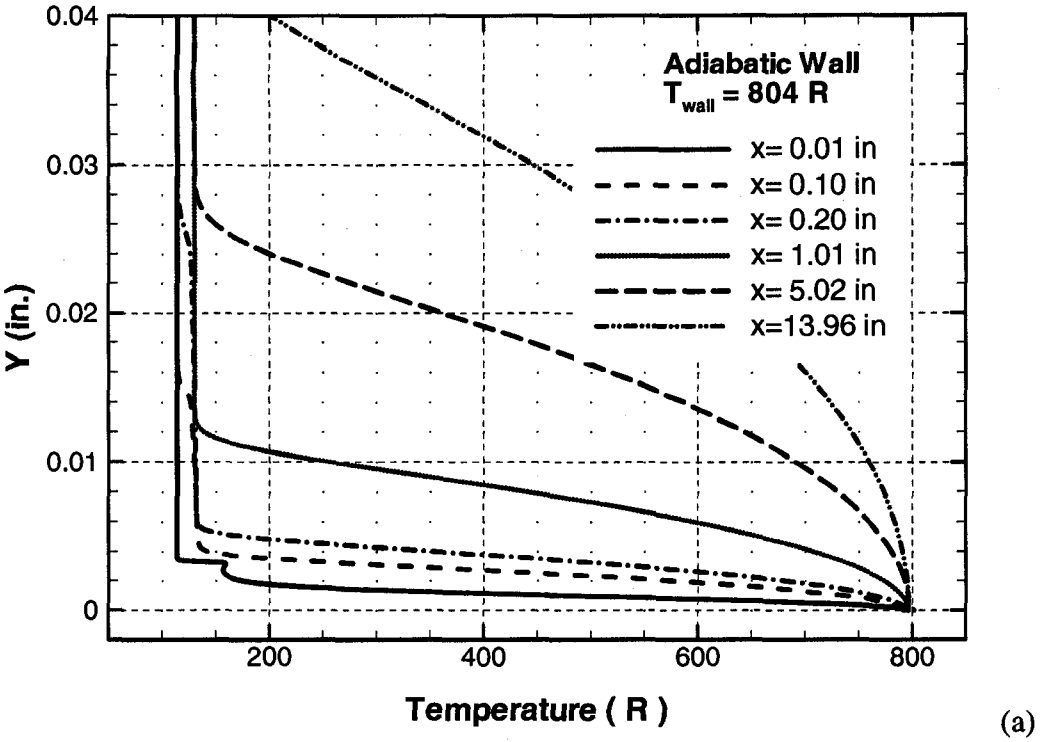

(a)

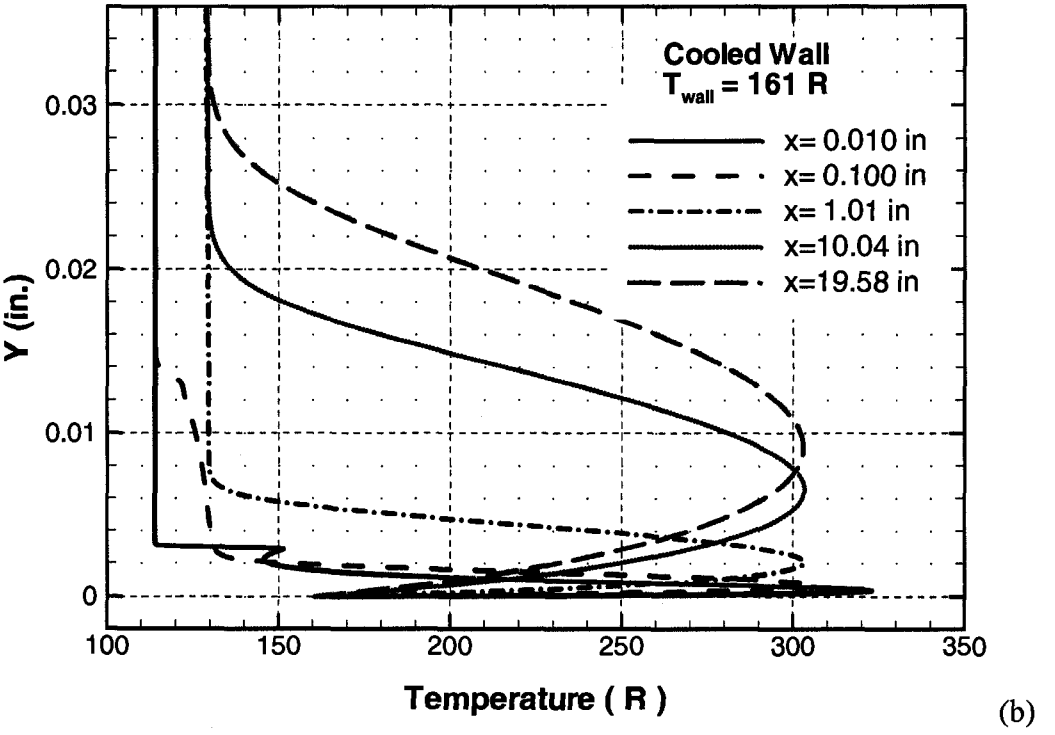

(b)

Figure 6.12 Mean flow temperature profiles at different axial locations in physical coordinates for (a) T_w Adiabatic wall (T_{aw}), and (b) T_w=T_{aw}*0.20.

6.4 Linear Stability Analysis

Linear stability computations are done for flow over an axisymmetric cone at a free stream Mach number of 6 at different wall temperature conditions T_w/T_{aw}=1.0, 0.50 and 0.20. The derivation of the linear stability equations and the numerical scheme to solve are given in the appendix. Figures 6.13 and 14 depict the results in the (Re, F), (Re, α) and (Re, C_r) planes for two-dimensional disturbances respectively.

Figure 6.13 shows the neutral stability diagram for the steady mean flow over a 5-degree straight cone. This figure clearly shows the first and second mode unstable regions for adiabatic wall temperature conditions, but when wall cooling is applied the unstable first mode region disappears. The first and second modes of the neutral stability curves merge at a Reynolds number of Re=1600 for the cone. From this figure we can say that wall cooling stabilized the first mode and increased the unstable frequencies.

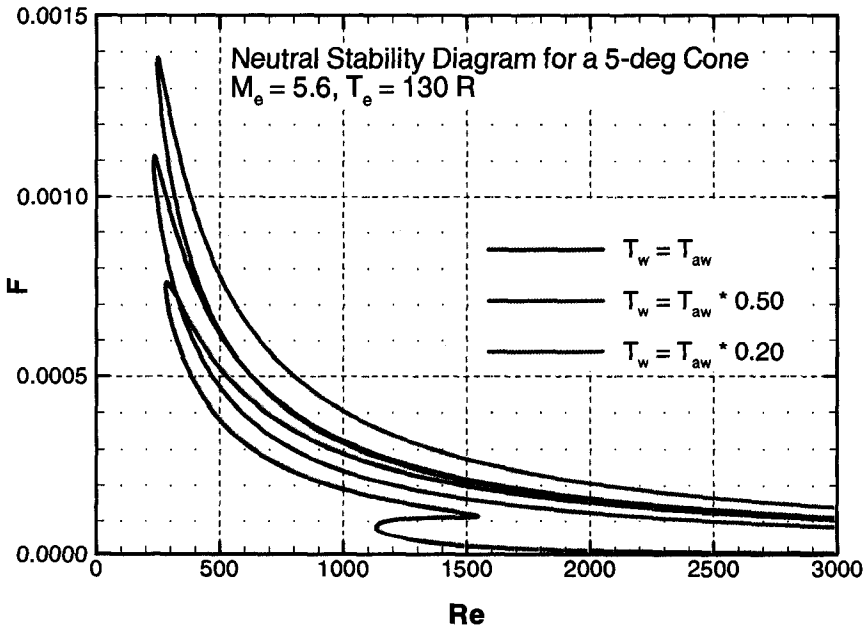

Figure 6.13 Neutral stability diagrams for a 5-degree cone at different wall temperature conditions in Re-F plane.

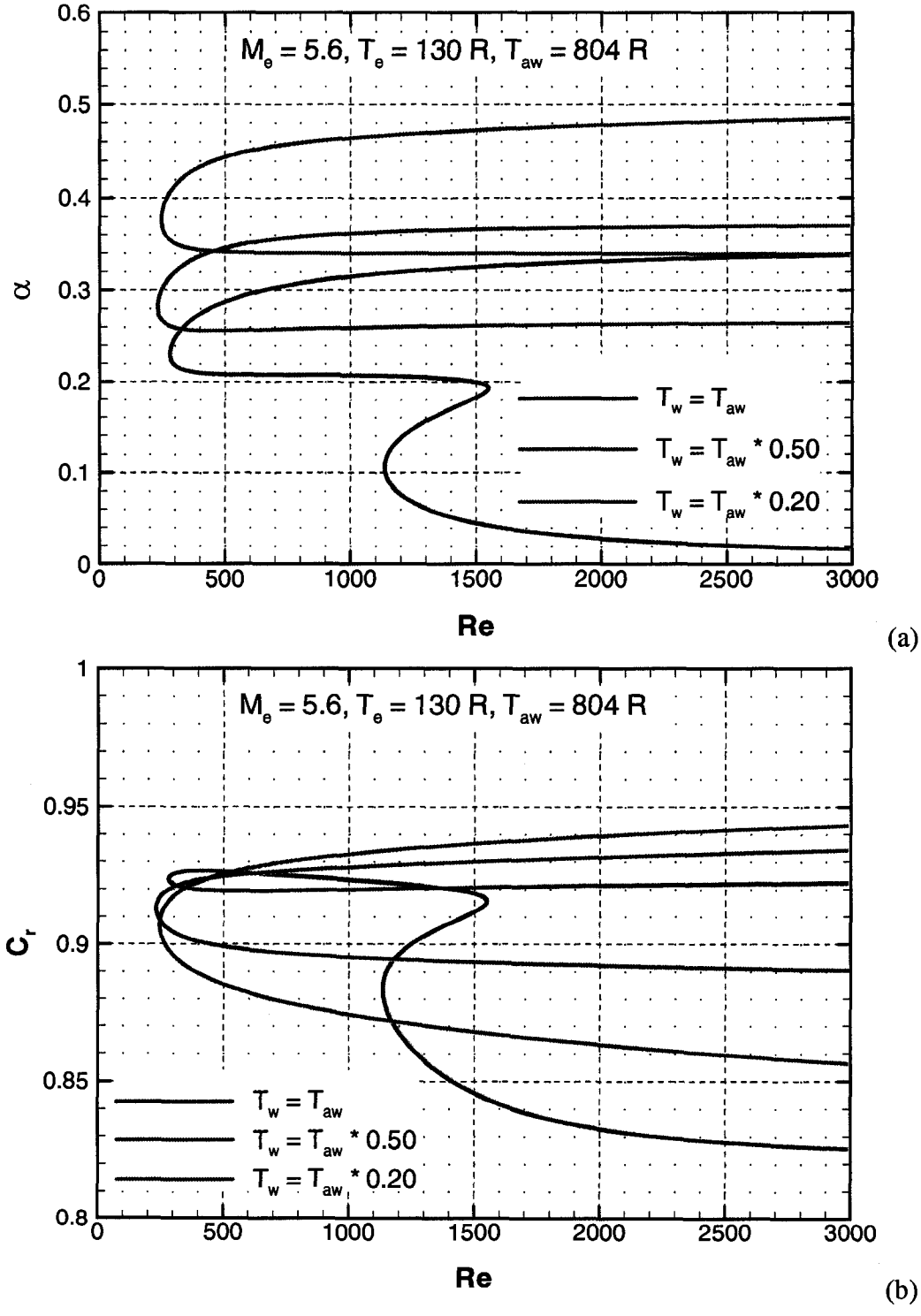

Figure 6.14 Neutral stability diagrams for a 5-degree cone at different wall temperature conditions in (a) Re-α plane, (b) Re-C_r plane.

Figure 6.14 shows the neutral stability diagram for the same conditions in the (Re, α) and (Re, C_r) planes. Figure 6.14 (a) also shows the first and second mode unstable regions for adiabatic wall temperature conditions. As expected, when wall cooling is applied the unstable first mode region disappears. Also, the unsteady wave number increased with wall cooling. The range of wave speeds of the unstable waves narrows with wall cooling as shown in Figure 6.14 (b).

Figures 6.15 and 16 show the N-Factor curves for decreasing frequencies at different wall temperature conditions. The most amplified frequencies for wall temperatures T_w/T_{aw}=1.0, 0.75, 0.50 and 0.20 are found as $0.8x10^{-4}$, $0.9x\ x10^{-4}$, $1.1\ x10^{-4}$, and $1.7\ x10^{-4}$ for N=10. These values clearly show that the most amplified frequency is increased more than two times with wall cooling. Here, the variables are non-dimensionalized by the variables at the edge of boundary layer. To obtain the variables non-dimensionalized by the free stream values as given in Table 3.2, the variables in this section should be multiplied by the appropriate factors from Table 4.1. The frequency variable F has to be multiplied by 1.174 to obtain the values in terms of free stream values.

Figure 6.15 (a) shows the N-Factor curves for the frequencies ranging from $0.70x10^{-4}$ to $1.0x10^{-4}$ at adiabatic wall conditions. In this figure the curves start from zero and increase linearly until a certain value in the first mode unstable region then change its characteristic and grow exponentially in the second mode unstable region. Since there is no first mode unstable region in cooled cases, the linear growth is not observed in Figures 6.15 (b), 6.16 (a), and 6.16 (b). The second mode is destabilized and estimated transition location moved upstream with increased wall cooling.

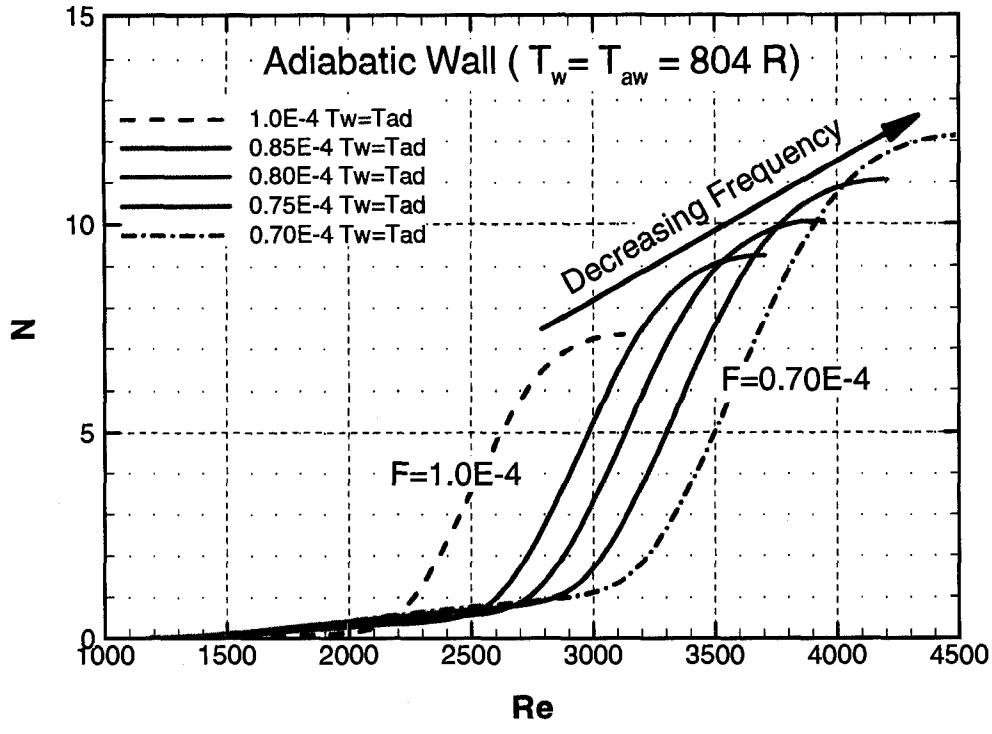

(a)

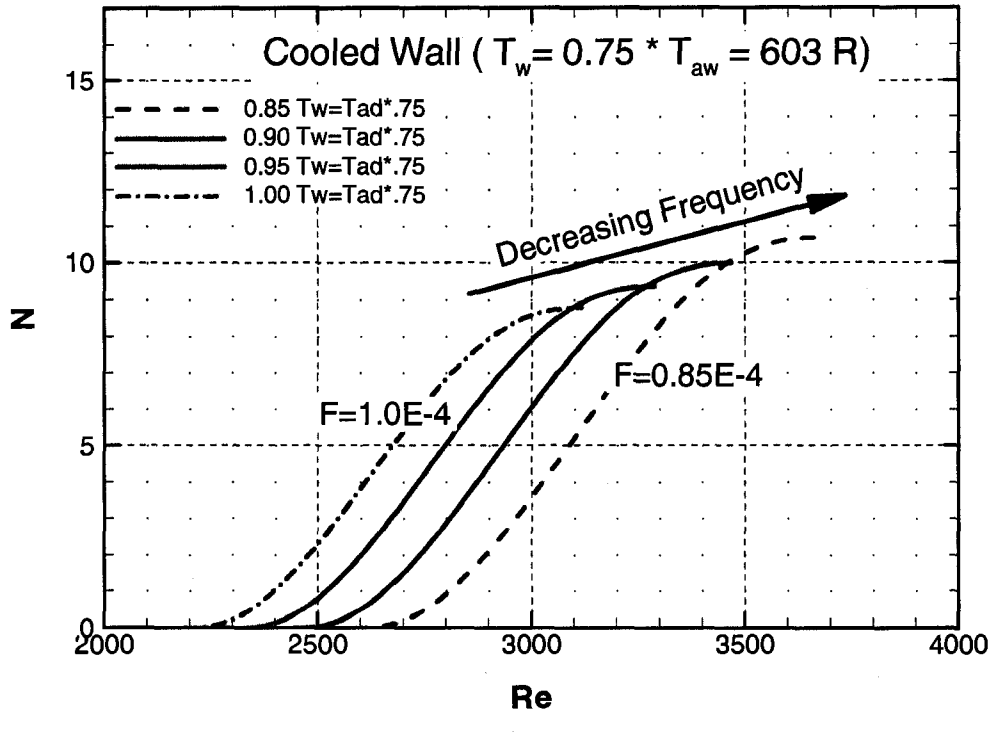

(b)

Figure 6.15 N-Factor curves for decreasing frequencies for a blunt cone (r_n=0.001 in.) at different wall temperature conditions. (a) Adiabatic wall (T_{aw}), (b) T_w=T_{aw}x0.75.

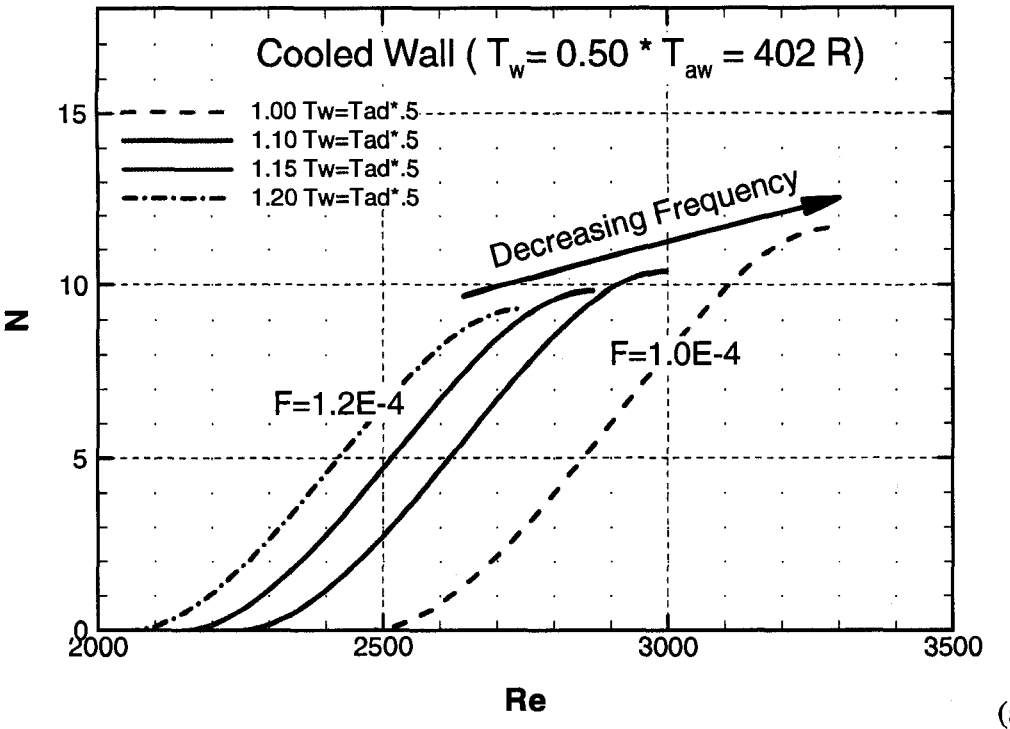

(a)

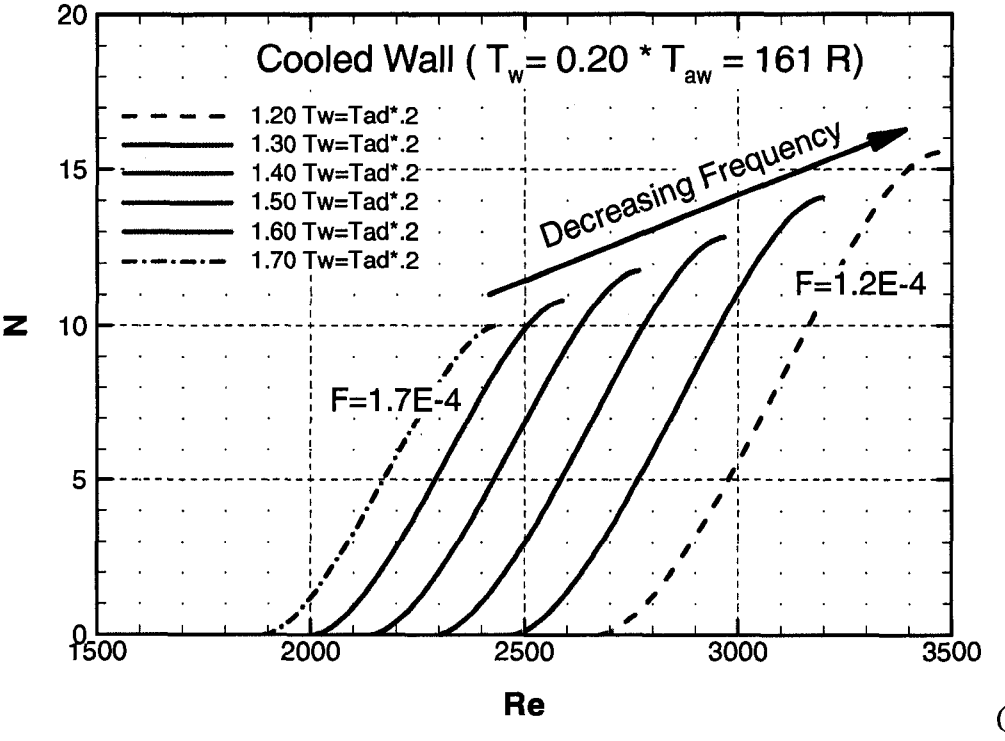

(b)

Figure 6.16 N-Factor curves for decreasing frequencies for a blunt cone (r_n=0.001 in.) at different wall temperature conditions. (a) T_w=T_{aw}x0.50, (b) T_w=T_{aw}x0.20.

6.5 Interactions of Acoustic Disturbances with Boundary Layer

After the mean flow is computed two dimensional slow acoustic disturbances are introduced at the outer computational boundary, and the time accurate simulations are performed. Unsteady simulation results are presented for the cases $T_w=T_{aw}$, $0.75xT_{aw}$, $0.50xT_{aw}$, and $0.20xT_{aw}$ (slow and fast acoustic waves) at the most amplified frequencies $0.96x10^{-4}$, $1.08\ x10^{-4}$, $1.32\ x10^{-4}$, and $2.0\ x10^{-4}$. These frequencies correspond to 375, 421, 515, and 780 kHz respectively. These frequencies give maximum amplification within the computational domain. To remain in the linear region, the amplitude of the forcing freestream acoustic waves is given a small value of $2x10^{-5}$ for the first three simulations and $2x10^{-6}$ for $0.20xT_{aw}$ simulation. Even with these small amplitudes, nonlinearity starts to develop near the end of the computational domain for the adiabatic case.

Figures 6.17 and 18 show the evolution of the wall pressure fluctuations for the aforementioned cases in a linear scale while Figures 6.19 and 20 depict the same results in a log scale. The figures clearly show the generation and the eventual exponential growth of the instability waves inside the boundary layer for adiabatic and cooled wall conditions.

For adiabatic wall conditions, Figure 6.17 (a) and Figure 6.19 (a), the disturbances grow from the leading edge and reach large amplitude levels of 0.50 near the predicted transition onset point at x=19in. The slow wave whose wavelength is closer to the wavelength of the instability wave transforms smoothly into an instability wave near the nose region. The parallel linear computations show that the first mode amplifies starting from the leading edge weakly up to x~15 in. for this frequency.

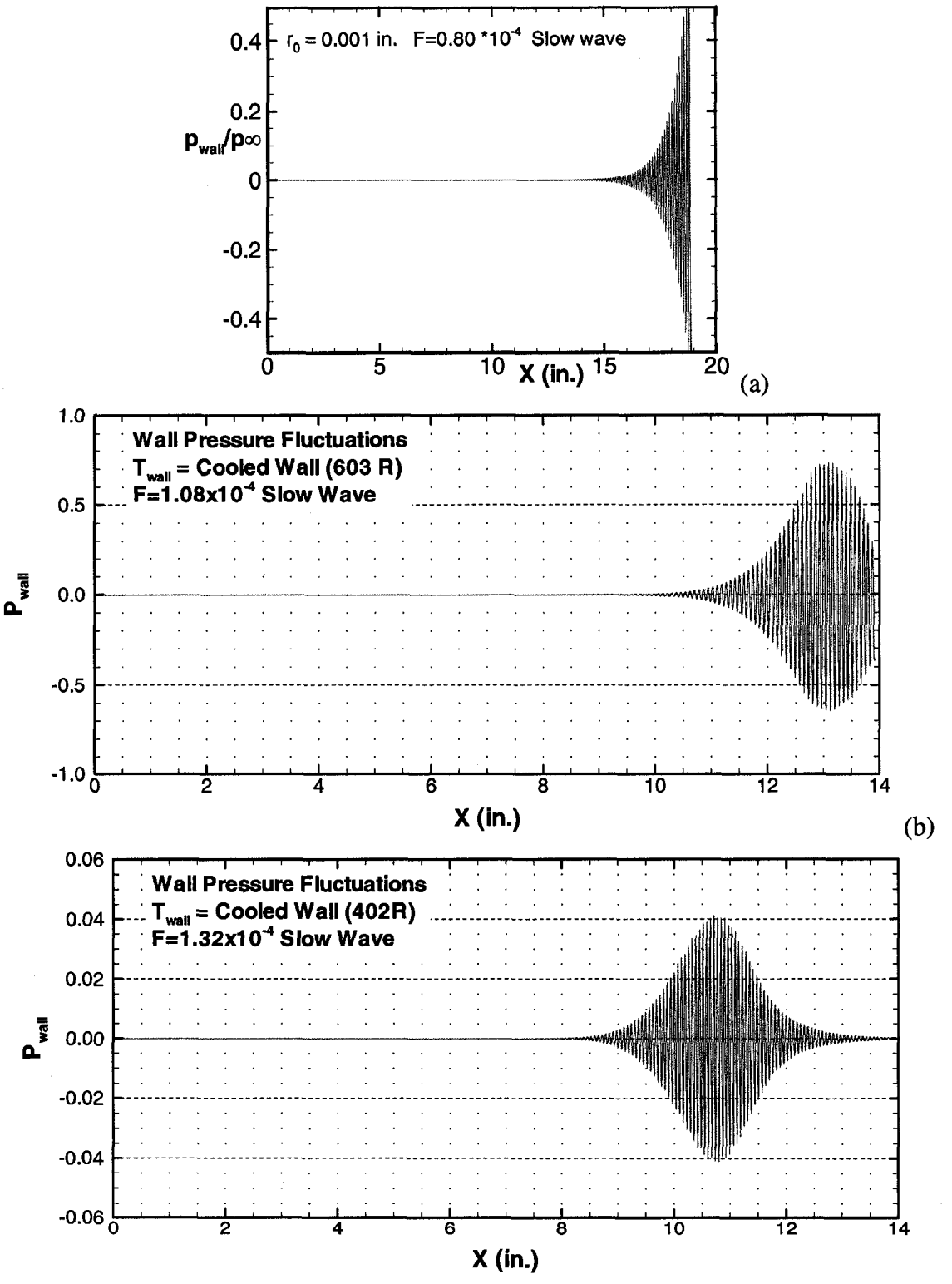

Figure 6.17 Unsteady pressure fluctuations on the wall, (a) Adiabatic wall (T_{aw}), (b) $T_w=T_{aw}$x0.75, (c) $T_w=T_{aw}$x0.50.

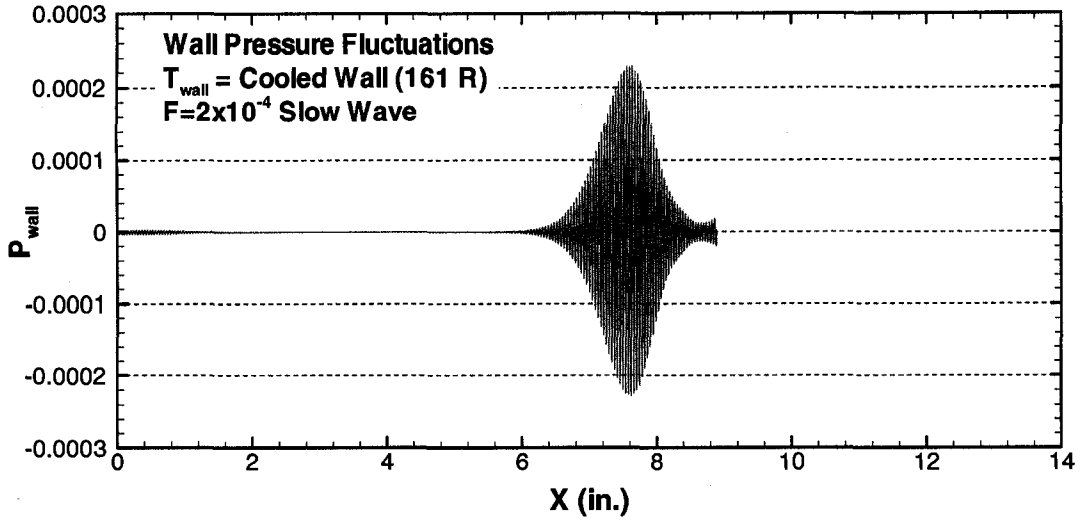

(a)

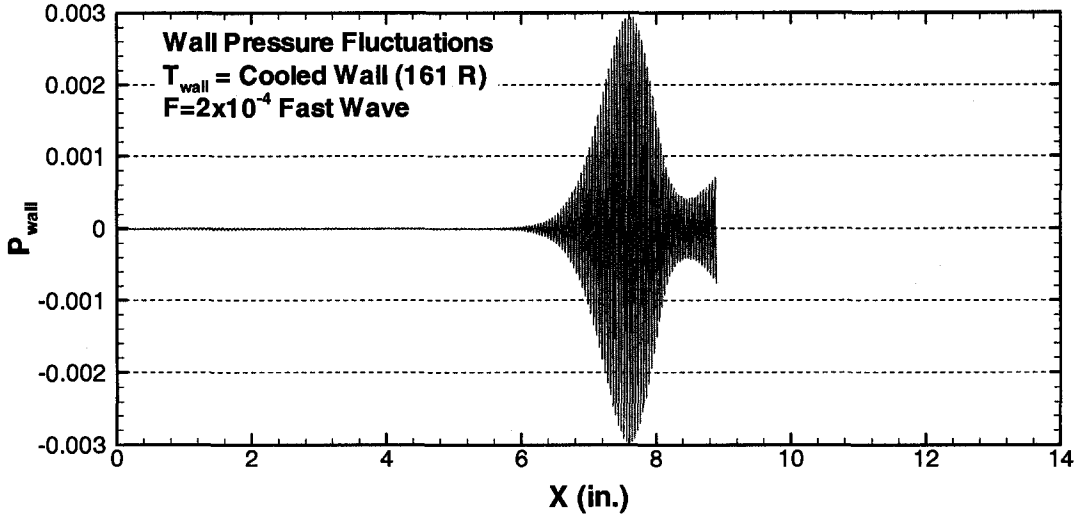

(b)

Figure 6.18 Unsteady pressure fluctuations on the wall (a) $T_w=T_{aw}x0.20$ (Slow Wave), (b) $T_w=T_{aw}x0.20$ (Fast Wave).

Figure 6.19 (b) shows the pressure fluctuations for $T_w=0.75xT_{aw}$ in log scale. It is evident that wall cooling reduced the growth of the first mode until x=6 in. then growth of the second mode is observed. Maximum amplitude only reached to 0.734 because of the wall cooling and it is in the same order of adiabatic case. When more wall cooling ($T_w=0.50xT_{aw}$) is applied stabilization of the first mode becomes obvious.

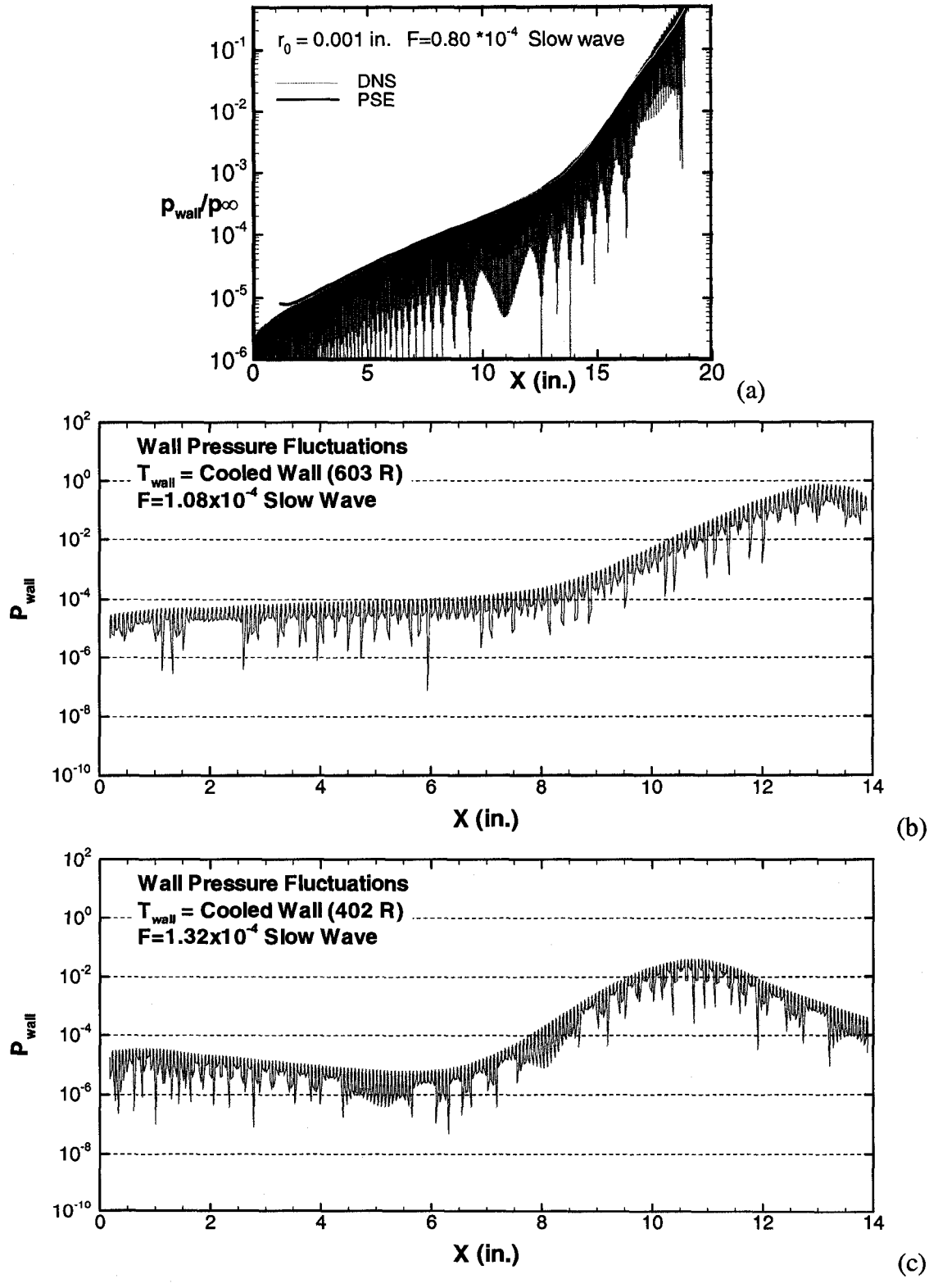

Figure 6.19 Unsteady pressure fluctuations on the wall in log scale, (a) Adiabatic wall (T_{aw}), (b) T_w=T_{aw}x0.75, (c) T_w=T_{aw}x0.50.

In Figure 6.19 (c) the neutral point appeared at x=5.55 in. with an amplitude of $6.18x10^{-6}$. Maximum amplitude for this case is 0.041 at x=10.73 in. The neutral points are not discernable for the adiabatic case and $T_w=0.75xT_{aw}$, but it appeared for $T_w=0.50xT_{aw}$ and stayed in the picture for cooler cases.

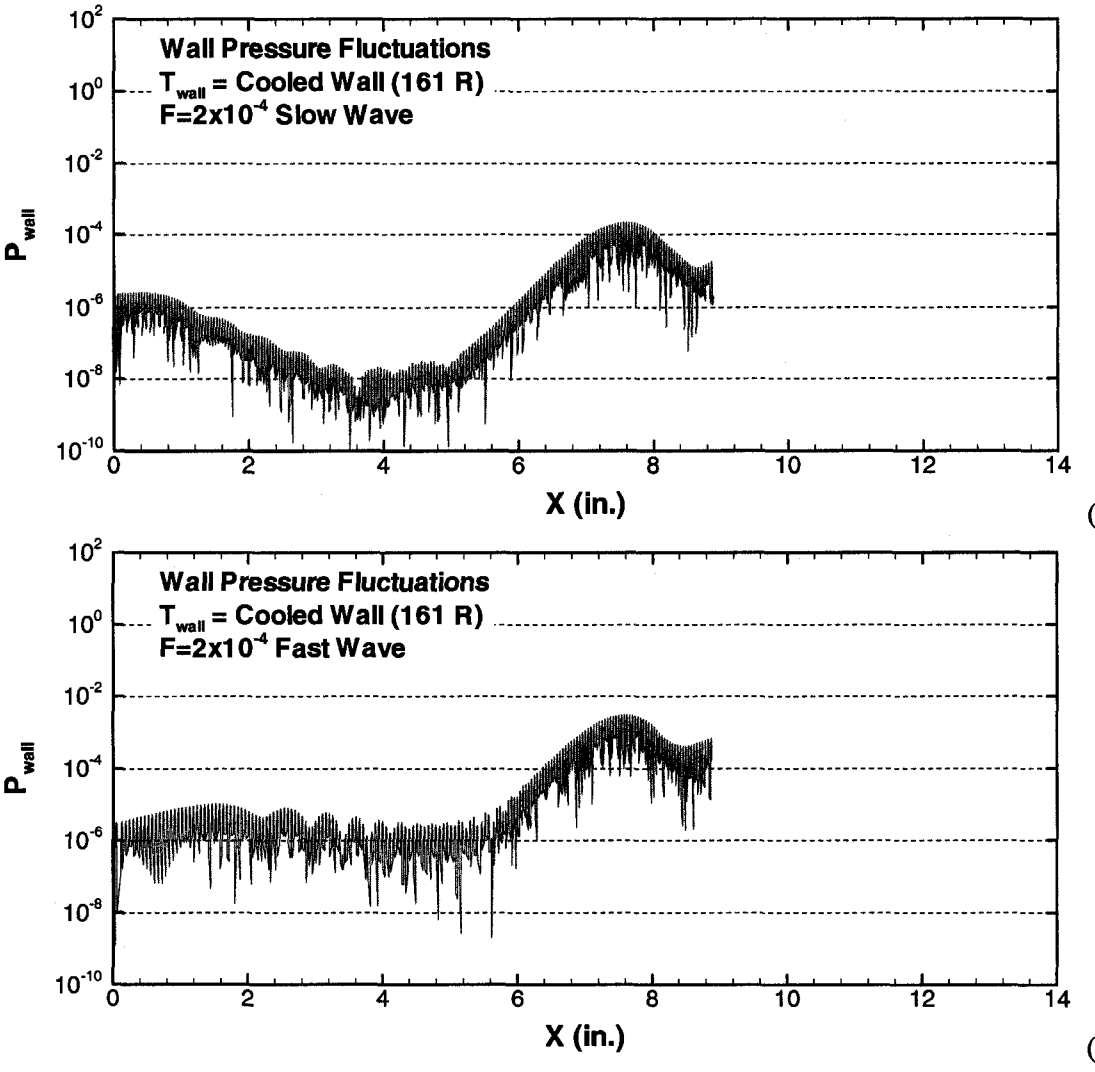

Figure 6.20 Unsteady pressure fluctuations on the wall in log scale (a) $T_w=T_{aw}x0.20$ (Slow Wave), (b) $T_w=T_{aw}x0.20$ (Fast Wave).

Figures 6.20 (a) and (b) show the wall pressure fluctuations for slow and fast acoustic disturbance waves respectively at $T_w=0.20xT_{aw}$. In these figures the neutral points are located at 4.94 in. (Slow Wave) and 5.62 in. (Fast Wave) with amplitudes of

$2x10^{-8}$ and $1x10^{-6}$ respectively. Maximum wall pressure amplitudes of 0.00023 for slow a wave and 0.0029 for a fast wave are observed at x=7.6 in for both cases. Because of the difference in the initial amplitude of the acoustic disturbances the maximum amplitudes for $T_w=T_{aw}$, $0.75xT_{aw}$ and $0.50xT_{aw}$ need to be divided by 10, and they become 0.05, 0.0734, and 0.0041 respectively. The maximum amplitude of $T_w=0.20xT_{aw}$ simulation is 0.00023 for slow acoustic waves, and it is in the same order for fast acoustic waves. On the other hand it is almost 20 times less than the $0.50xT_{aw}$ simulation.

Also, it is interesting to observe that the first mode is not stabilized for fast acoustic wave simulation in Figure 6.20 (b) while Figures 6.19 and 6.20(a) clearly show the stabilization effect of wall cooling on the first mode for slow acoustic wave simulations. The transition locations obtained from these simulations for $T_w=T_{aw}$, $0.75xT_{aw}$, $0.50xT_{aw}$, and $0.20xT_{aw}$ (slow and fast) wall temperature conditions are 19, 13, 10.7, and 7.6 in. respectively. From these results one can conclude that wall cooling is destabilizing the boundary layer and estimated transition points are moving upstream.

Another set of simulations were run for $T_w=T_{aw}$, $0.75xT_{aw}$, $0.50xT_{aw}$, $0.40xT_{aw}$, $0.30xT_{aw}$, and $0.20xT_{aw}$ using the same forcing disturbance frequency, $F=1.2x10^{-4}$, in slow wave mode to observe the effects of wall cooling on development of instability waves in the same disturbance environment. Figures 6.21 and 6.22 show the unsteady wall pressure fluctuations for the aforementioned simulations.

Figure 6.22 (b) shows the pressure fluctuations for $T_w=0.50xT_{aw}$ in log scale. It is evident that wall cooling reduced the growth of the first mode until x=6.96 in. where the amplitude is $6.5x10^{-6}$; then growth of the second mode started. In this case maximum amplitude only reached 0.0035 because of the wall cooling. It is 35 times less than of the

adiabatic case. Stabilization of the first mode became apparent with wall cooling as was seen in the neutral stability diagrams (Figure 6.13). An exponential decrease of amplitude of wall pressure fluctuations for the $T_w=0.40xT_{aw}$ simulation until the neutral point located at x=8.46 in. with an amplitude of $9.95x10^{-7}$ is observed. Maximum amplitude for this case is 0.129 occurred at x=14.62 in. More cooling increased the maximum amplitude level to the same value of adiabatic case.

Finally, for the $T_w=0.20xT_{aw}$ simulation the maximum amplitude increased more than two times and reached 0.301 at the end of the computational domain x=19.9 in. Further cooling moved the neutral point to x=13.4 in. where the amplitude is $4.7x10^{-8}$.

In these simulations the neutral point was not discernable for the adiabatic wall and $T_w=0.75xT_{aw}$, but it appeared for $T_w=0.50xT_{aw}$ and cooler wall temperatures because of the stabilization of the first mode (Slow Wave) with wall cooling.

Transition locations computed for $T_w=T_{aw}$, $0.50xT_{aw}$, $0.40xT_{aw}$, and $0.20xT_{aw}$ wall temperature conditions forced with slow wave acoustic disturbances are 9.47, 9.67, 14.62, and 19.9 in. respectively. Transition location is delayed with wall cooling for the same slow wave frequency because of the stabilization of the first mode. However, the amplitudes of wall pressure fluctuations increased with wall cooling to larger values than those of the adiabatic case.

Figure 6.23 compares the unsteady wall pressure fluctuations for $T_w=T_{aw}$, $0.75xT_{aw}$, $0.50xT_{aw}$, $0.40xT_{aw}$, $0.30xT_{aw}$, and $0.20xT_{aw}$ wall temperature conditions in log scale. The delay of the transition locations and comparison of the amplitude levels can be easily seen in this figure

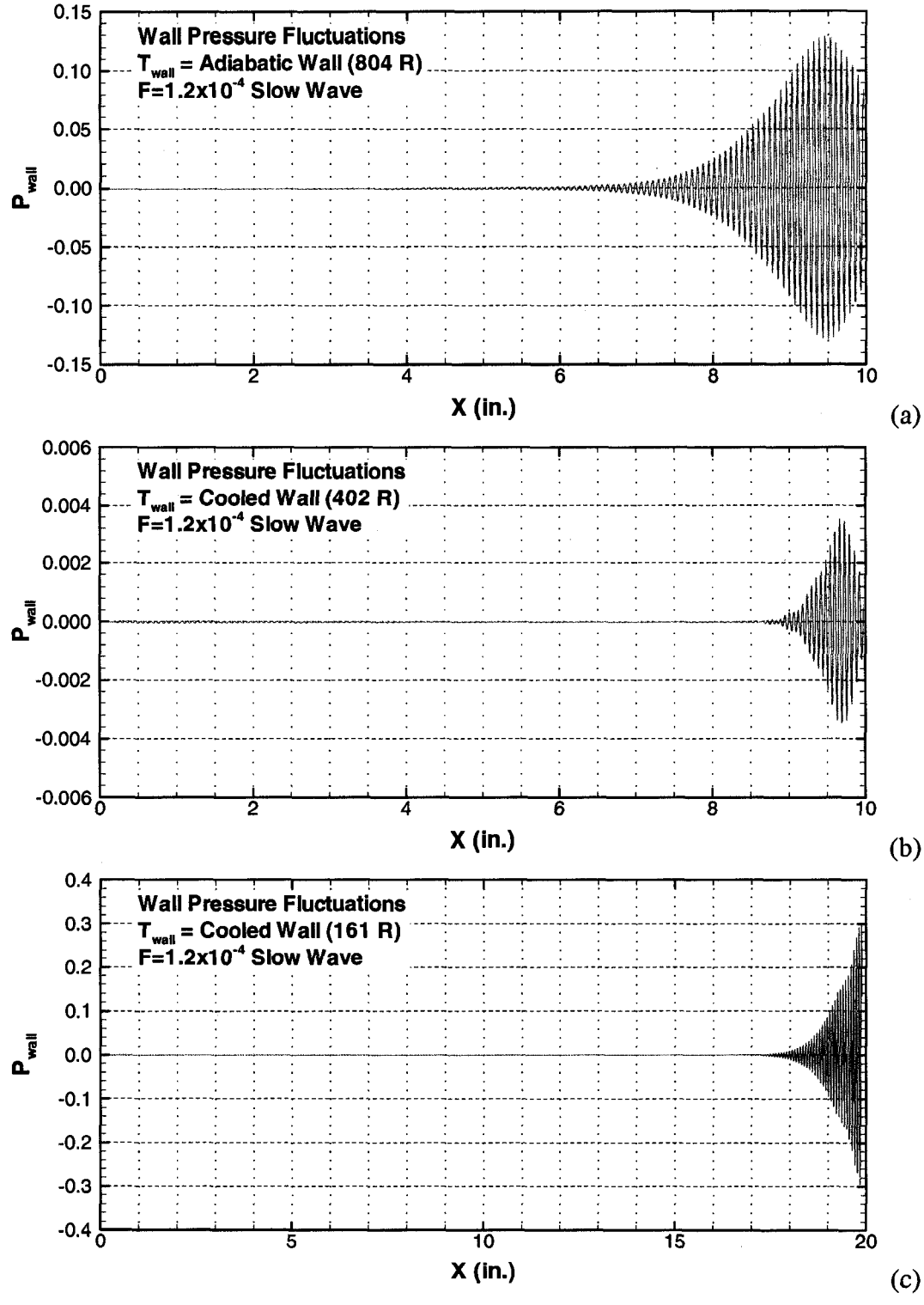

Figure 6.21 Pressure fluctuations on the wall under the effect of same forcing frequency F = 1.2x10^{-4}, (a) Adiabatic wall (T_{aw}), (b) T_w=T_{aw}x0.50, (c) T_w=T_{aw}x0.20.

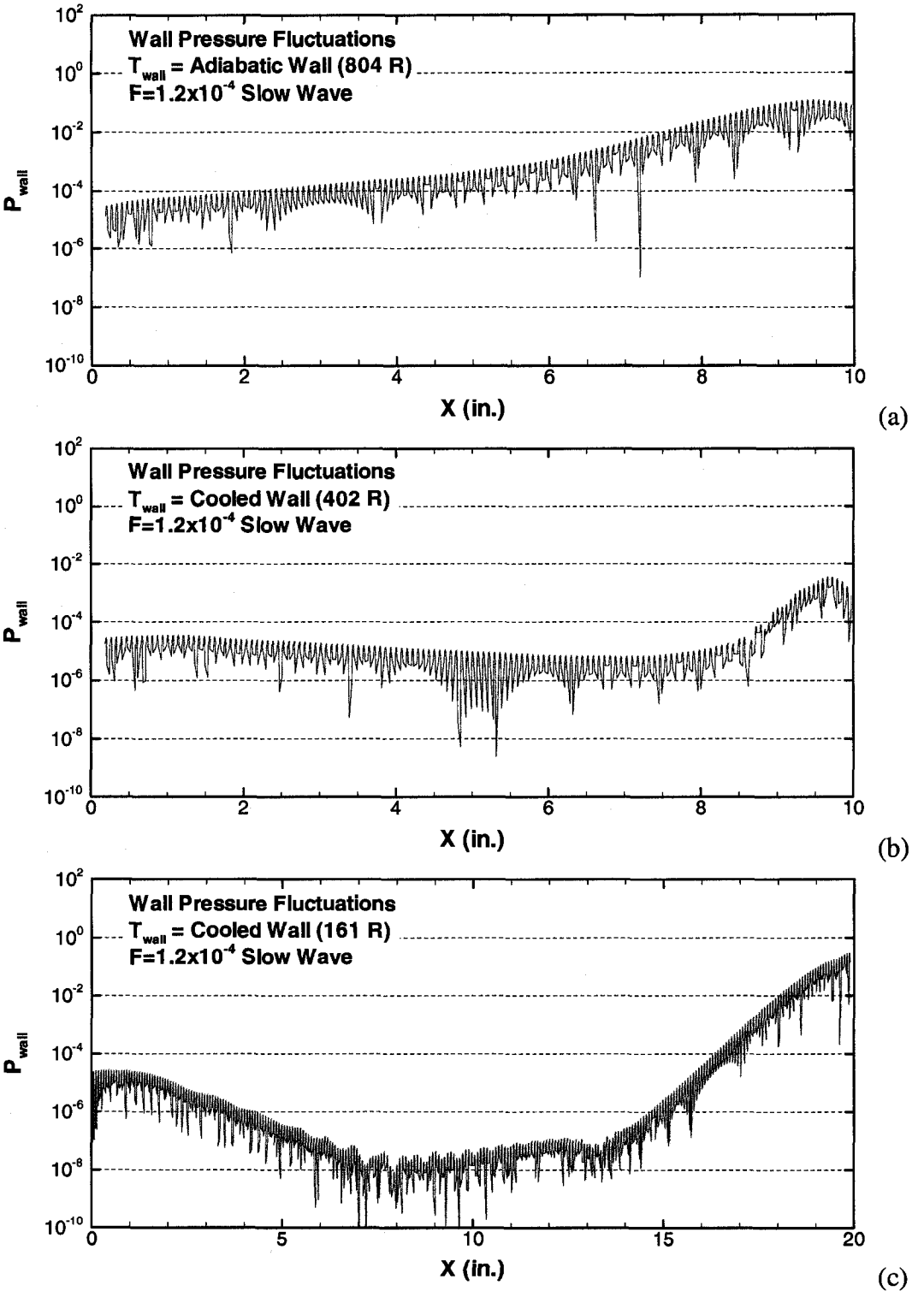

Figure 6.22 Pressure fluctuations on the wall under the effect of same forcing frequency $F = 1.2x10^{-4}$ in log scale, (a) Adiabatic wall (T_{aw}), (b) $T_w=T_{aw}x0.50$, (c) $T_w=T_{aw}x0.20$.

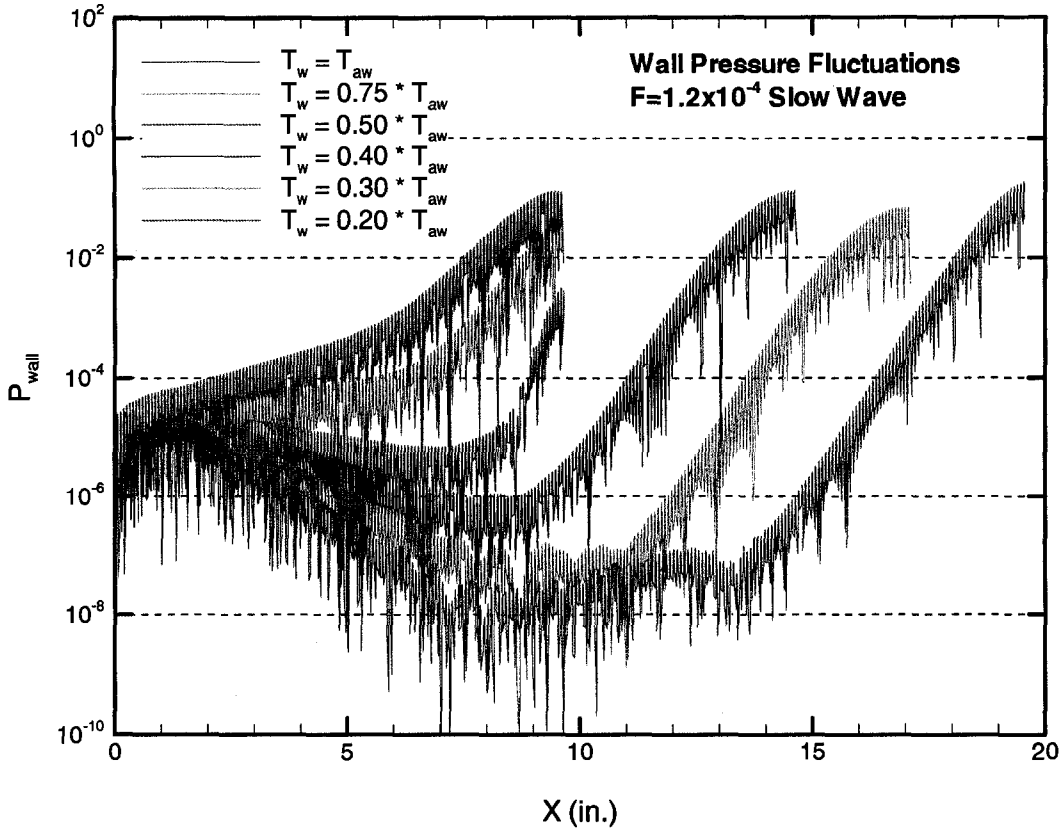

Figure 6.23 Comparison of wall pressure fluctuations under the same forcing frequency ($F=1.2x10^{-4}$) at different wall temperature conditions.

Figure 6.24 shows variation of phase speed (c_r) and eigenvalues (α_r, α_i) for the slow and fast acoustic disturbance waves for the non-dimensional frequency of $F=2x10^{-4}$ at the $T_w=0.20xT_{aw}$, wall temperature simulation. Figure 6.24 (a) and (b) have similar topological structure to Fedorov[46]'s cooled wall case where $T_w/T_{aw}=0.1$. There are three distinct regions in Figure 6.24 (a). Region one shows that the boundary layer modes are synchronized with acoustic waves in the leading edge. At region two a fast acoustic wave is synchronized with the waves of phase speed $c_r=1$, and in region three the fast wave is synchronized with the slow wave that leads to discrete spectrum branching. In this region the boundary layer is extremely receptive to acoustic disturbances. Figure 6.24 (b) shows growth rate branching of slow and fast acoustic waves.

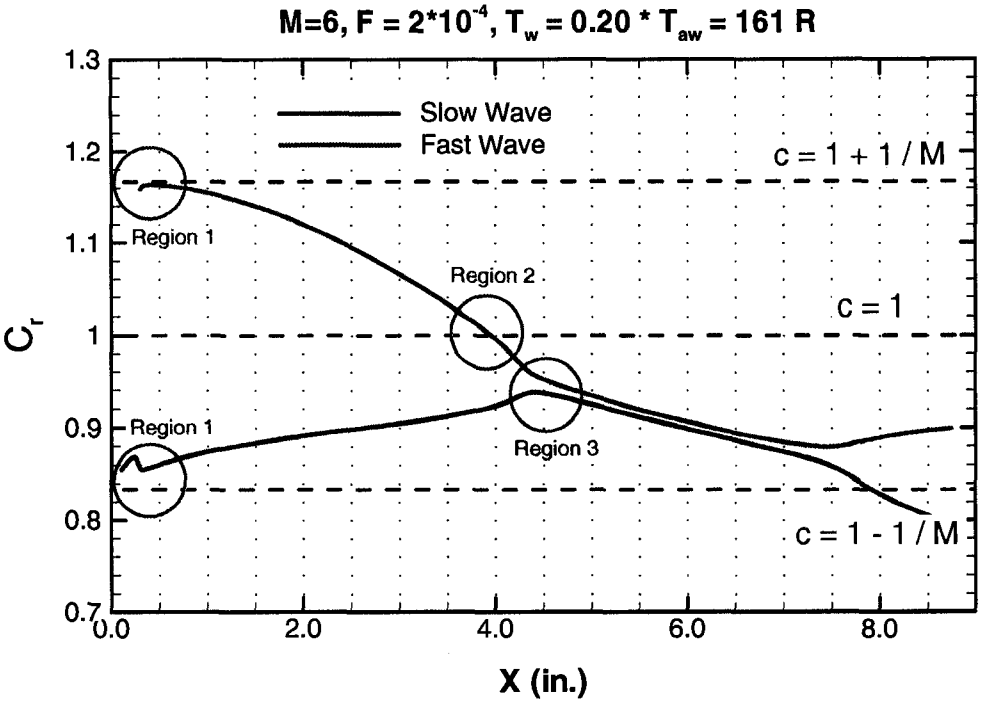

(a)

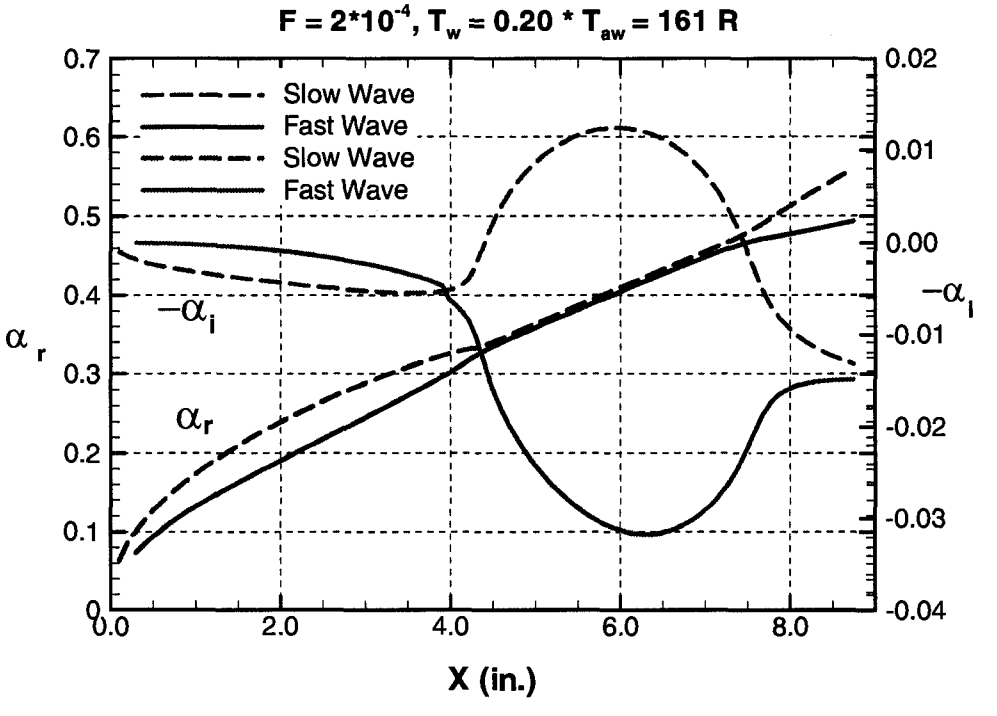

(b)

Figure 6.24 (a) Phase speed and (b) eigenvalues (α_r, α_i) for fast and slow modes for $F=2.0\times10^{-4}$.

Figure 6.25 compares the evolution of unsteady density fluctuations obtained from the simulations for a slow wave ($F=1.2x10^{-4}$) at a fixed time for adiabatic and cooled wall ($T_w=0.20xT_{aw}$) conditions. Figures 6.25 (a) and (b) clearly show that there is no entropy layer generated by small bluntness, and the disturbances excite the boundary layer up to the wall. These figures clearly show the disturbance evolution in the nose region. Acoustic disturbances pass the bow shock and directly enter the boundary layer. Figure 6.25 (b) shows that the boundary layer is thinner and the amplitude of the fluctuations inside the boundary layer is weaker for the cooled wall than for the adiabatic wall presented in Figure 6.25 (a).

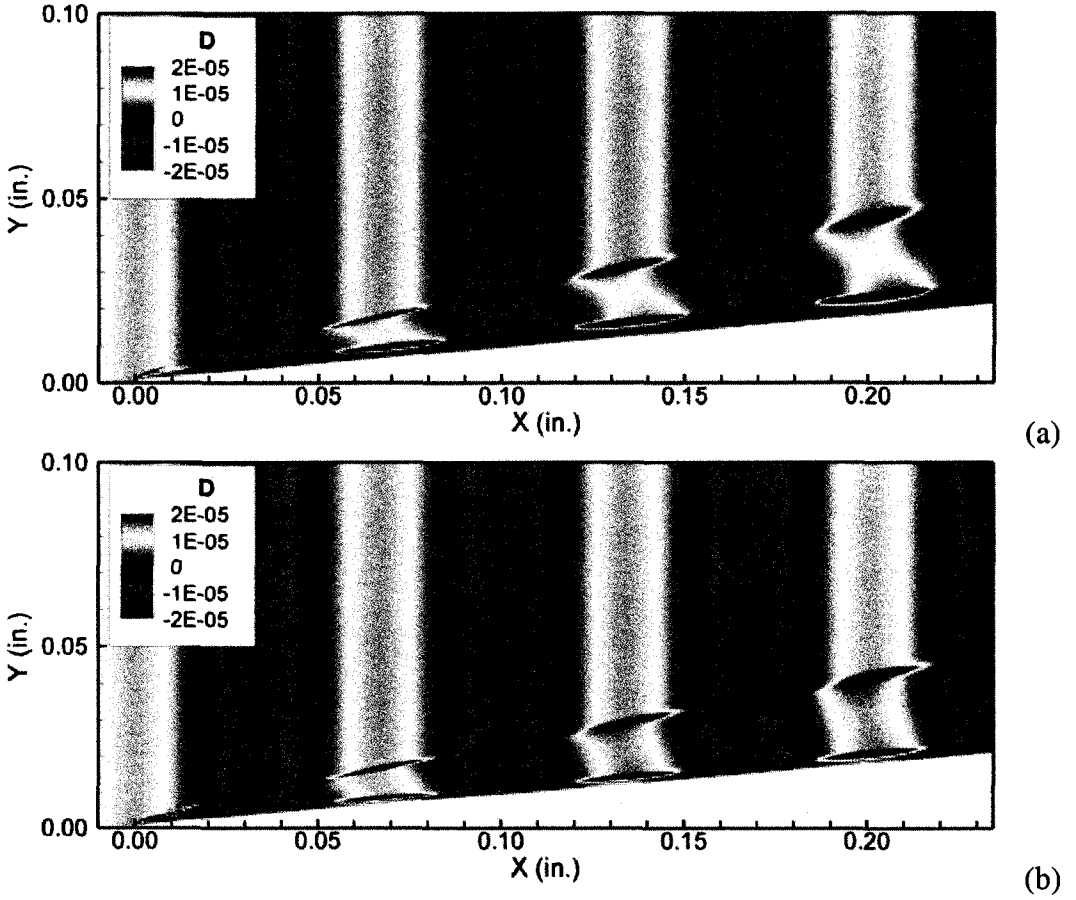

Figure 6.25 Contours of unsteady density fluctuations inside the boundary layer near the nose region. (a) Adiabatic wall ($T_w = T_{aw}$), (b) Cooled wall ($T_w = T_{aw}x0.20$)

Figures 6.26 and 6.27 show the propagation of density fluctuations inside the boundary layer from the leading edge to the end of the computational domain. In Figure 6.26 (a) disturbances interact with the bow shock in the nose region and directly enter the boundary layer. Then the disturbances generate a rope shape structure inside the boundary layer and on the oblique shock. The interaction is obvious between the density fluctuations on the oblique shock and boundary layer.

Figure 6.26 (b) shows the disturbance field from 0.3 in. to 2.0 in. In this figure four different zones are observed similar to previous studies.[22, 40, 52, 84, 85] First zone is the area outside the shock where acoustic disturbances propagate uniformly. In the second zone acoustic waves are transmitted through the shock layer. The third zone is the area between the shock and the boundary layer. This region consists of the transmitted external acoustic field and the disturbances radiated from the boundary layer. It is interesting to see that the third region is much quieter compared to the acoustic waves outside the shock layer. This implies that the acoustic waves are weakly transmitted through the shock. The fourth zone is the boundary layer where the boundary layer disturbances evolve. Figure 6.26 (c) clearly shows the decay of amplitudes of density fluctuation from the order of 10^{-5} to 10^{-8}, which corresponds to first mode stabilization. In Figure 6.27 (a) and (b) density fluctuations inside the boundary layer are not discernable, and the region between shock layer and the cone wall seems quiet. However, acoustic disturbances propagated from 4 in. to 16 in. (also look at Figure 6.22 (c)) in the order of 10^{-7} or below and then started to gain amplitude and became visible. This phenomenon shows the necessity of a high resolution grid and higher order accurate schemes. Figure

6.27 (c) shows destabilization of the second mode disturbances near the end of the computational domain.

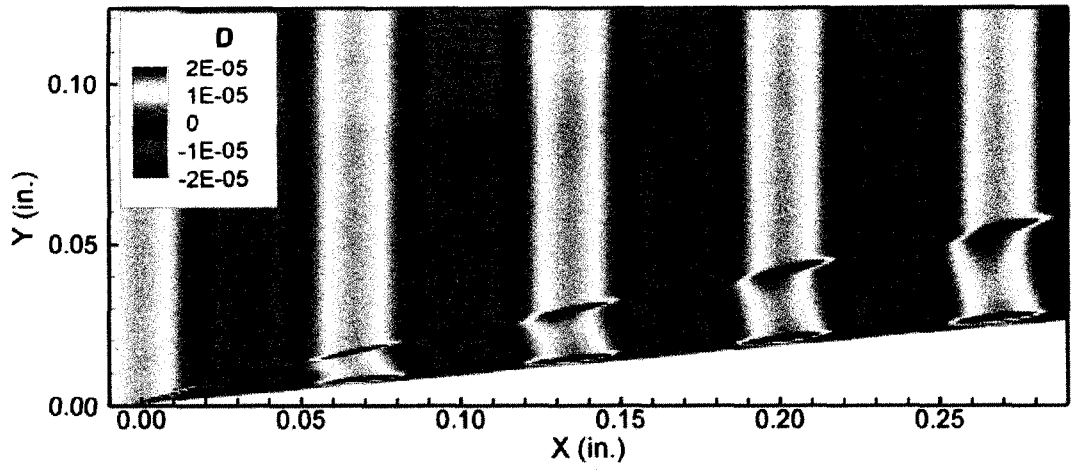

(a) x=[0.0-0.3]in

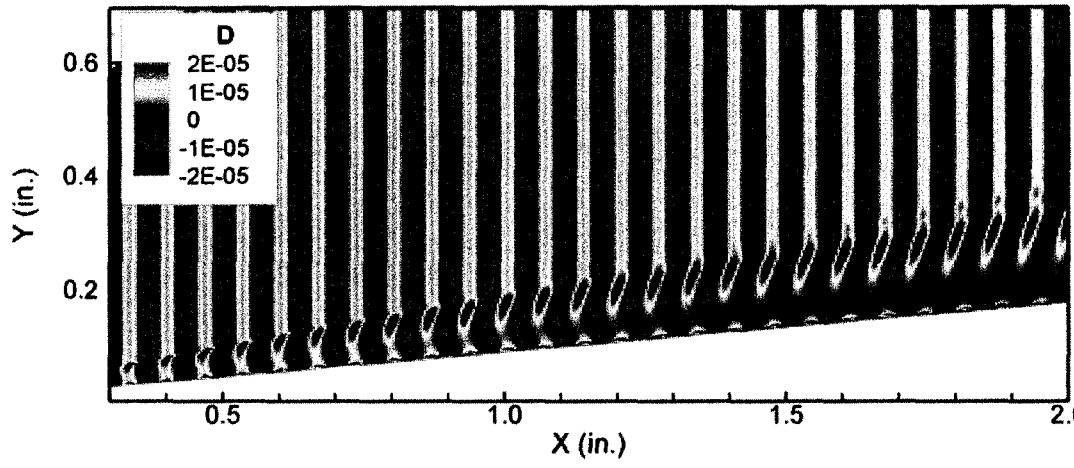

(b) x=[0.3-2.0]in

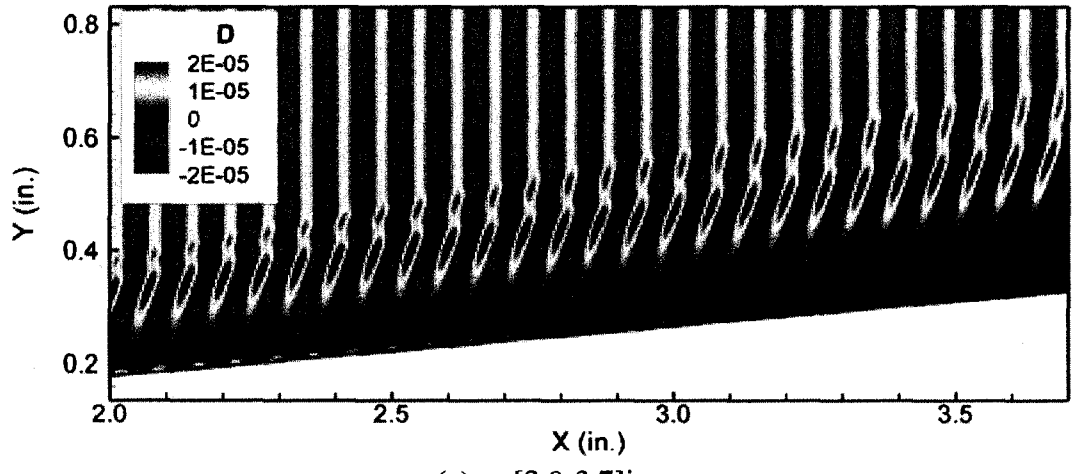

(c) x=[2.0-3.7]in

Figure 6.26 Contours of unsteady density fluctuations inside the boundary layer along the cooled cone wall ($T_w=T_{aw}$x0.2), (a) x=[0-0.3], (b) x=[0.3-2], and (c) x=[2-3.7]in.

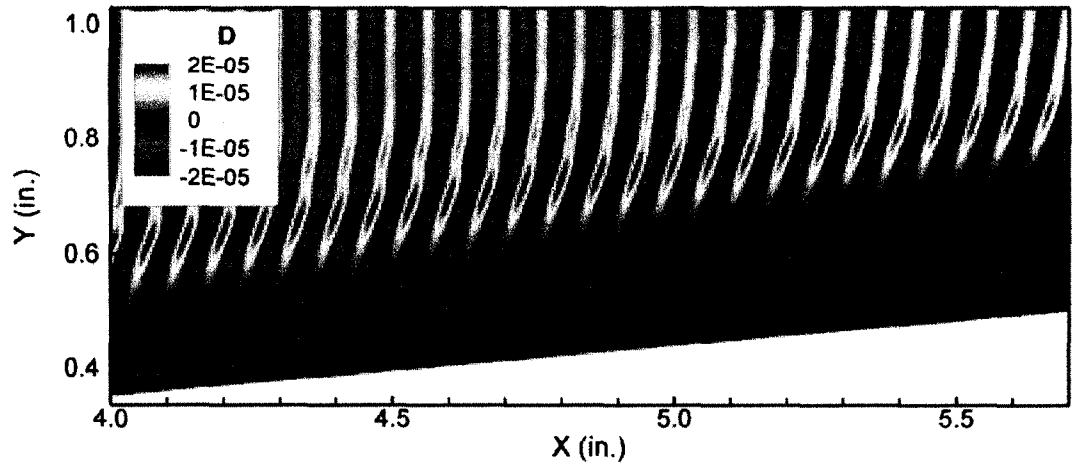

(a) x=[4.0-5.7]in

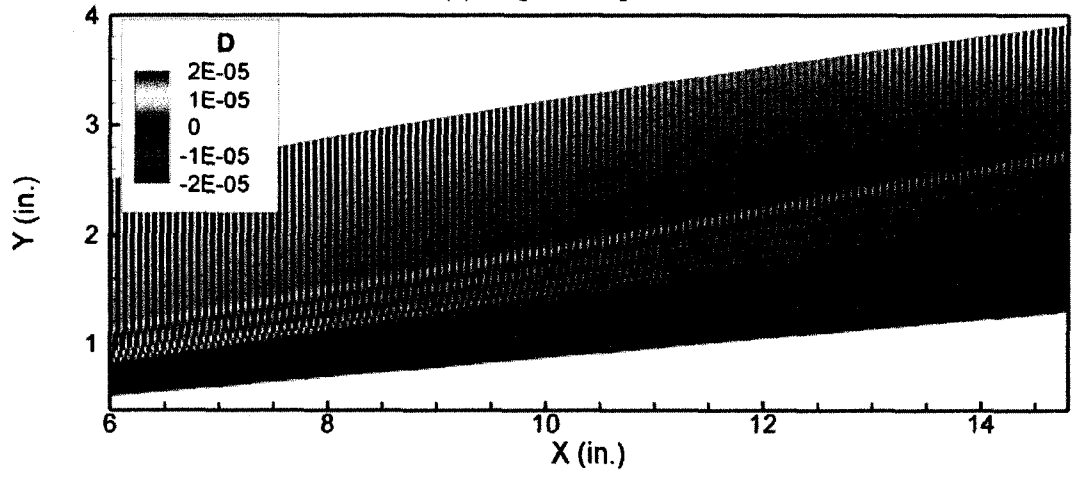

(b) x=[6.0-15.0]in

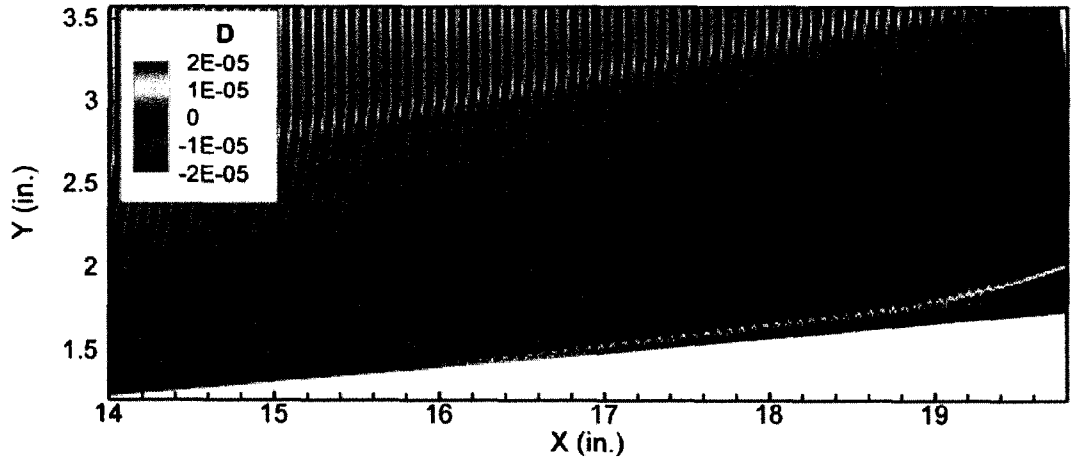

(c) x=[14.0-19.8]in

Figure 6.27 Contours of unsteady density fluctuations inside the boundary layer along the cooled cone wall ($T_w=T_{aw}$x0.2), (a) x=[4-5.7], (b) x=[6-15], and (c) x=[14-19.8] in.

6.6 Discussion and Conclusion

The receptivity and stability of hypersonic boundary layers over a blunt cone with a 5 degree half-angle with nose radius 0.001 in. are numerically investigated at a free stream Mach number of 6.0 and at a Reynolds number of 7.8×10^6/ft. Both steady and unsteady solutions are obtained by solving compressible Navier-Stokes equations using the 5^{th} order accurate Weighted Essentially Non-Oscillatory (WENO) scheme for space discretization and using a 3^{rd} order Total-Variation-Diminishing (TVD) Runge-Kutta scheme for time integration. Unsteady flow is forced using slow and fast acoustic disturbance waves with the most amplified disturbances calculated based on mean flow analyses and also forced with non-dimensional frequency of $F=1.2 \times 10^{-4}$. Computations are performed for different wall temperatures 804 (adiabatic wall), 603, 402, 322, 241, and 161 °R.

Table 6.2 summarizes computation parameters and the receptivity coefficients for the most amplified slow and fast mode acoustic disturbances at different wall temperature conditions. It is shown that the first mode of slow wave acoustic disturbances was stabilized by wall cooling. However, wall cooling also caused the destabilization of the second mode, and the transition location moved to upstream from x=19.1 in. for the adiabatic case to x=7.61 in. for the highly cooled wall case.

It is also interesting to observe that wall cooling did not affect the first mode of fast acoustic disturbance waves. The receptivity coefficient of the fast wave case is 50 times greater than of the slow wave case. We can conclude that the boundary layer is much more receptive to fast acoustic waves as compared to the slow wave.

Table 6.2 Computation parameters and receptivity coefficients for the most amplified frequencies at different wall temperatures.

$F \times 10^{-4}$	T_{wall}/T_{aw}	$(P_{wall})_{np}$	$C_{recpt.} = (P_{wall})_{np}/P_{ac}$	$x_{Tr.}(in.)$	$(P_{wall})_{Tr.}$
0.96^{S}	1.00	8.5×10^{-6}	4.23**,#	19.1	0.552
1.08^{S}	0.75	4.8×10^{-5}	2.39*,#	13.1	0.0734^{+}
1.32^{S}	0.50	6.2×10^{-6}	0.309*	10.7	0.0041^{+}
2.0^{S}	0.20	2.0×10^{-8}	0.010**	7.61	0.0002
2.0^{F}	0.20	1.0×10^{-6}	0.500**	7.59	0.0029

$T_\infty = 113.98$ °R, $^{*}P_{ac} = 2 \times 10^{-5}$, $^{**}P_{ac} = 2 \times 10^{-6}$. +These values divided by 10 to make the initial amplitudes in the same order. #In these simulation neutral point is not observed and amplitude values from x=1 in. is used.
S Slow wave, F Fast Wave.

The transition locations stayed almost the same for the adiabatic wall and cooled walls (603°R and 402°R) respectively for 9.475, 9.714 and 9.672 in. Transition locations increased dramatically for wall temperatures 322°R, 241°R and 161°R to 14.628, 17.013, and 19.906 in. This happened due to the stabilization of the first mode disturbances. However, amplitude of wall pressure fluctuations of the cooled wall case (T_w=161°R) increased 2.34 times that of the adiabatic wall case (T_w= T_{aw}=804°R). Table 6.3 summarizes the simulation parameters and gives the receptivity coefficients for the same slow wave disturbance frequency, F=1.2x10^{-4}, at different wall temperature conditions.

Because of the initial growth of the first mode in the adiabatic and cooled wall cases (T_w=0.75xT_{aw}) neutral points are not observed. Therefore, wall pressure fluctuations at 0.207 in. are used in the receptivity coefficient calculations. Neutral point locations moved downstream with wall cooling. Receptivity coefficients are 1.5225, 1.4613, 0.3246, 0.0497, 0.0059, and 0.0023 respectively for wall temperatures 804, 603, 402, 322, 241, and 161 °R.

Table 6.3 Computation parameters and receptivity coefficients for the same slow wave disturbance frequency at different wall temperatures.

T_{wall}(°R)	T_{wall}/T_{aw}	$x_{np.}(in.)$	$C_{recpt.} = (P_{wall})_{np}/P_{ac}$	$x_{Tr.}(in.)$	$(P_{wall})_{Tr.}$
804	1.00	0.207	1.5225#	9.475	0.129
603	0.75	0.207	1.4613#	9.714	0.046
402	0.50	6.965	0.3246	9.672	0.003
322	0.40	8.466	0.0497	14.628	0.129
241	0.30	10.964	0.0059	17.013	0.068
161	0.20	13.397	0.0023	19.906	0.301

$T_\infty = 113.98\,°R, P_{ac} = 2 \times 10^{-5}, Nose\ Radius\ R_n = 0.001\ in.$ # Neutral point is not observed for this case and amplitude from x=0.207 is used.

Wall cooling reduced receptivity coefficients and increased the transition Reynolds numbers for the same forcing frequency, F=1.2x10^{-4}. The receptivity coefficient for the adiabatic wall case is 1.5225, and it is much smaller in the order of 10^{-3} for highly cooled cones (241°R and 161°R). This raises some questions[85] about the transition process over a cone with small bluntness. If the receptivity coefficients are very small for the second modes, as was found in this chapter, how can the amplitude of the disturbances reaches such high values? Probably, non-zero acoustic incident angles may produce larger receptivity coefficients than the zero incident angle used in this work.

CHAPTER VII

7. CONCLUSIONS AND RECOMMENDATIONS

The receptivity mechanisms of hypersonic boundary layers to free stream acoustic disturbances are studied by using both linear stability theory (LST) and direct numerical simulations (DNS) over cones and wedges. A computational code is developed for numerical simulation of steady and unsteady hypersonic flow over cones by combining a fifth-order Weighted Essentially Non-Oscillatory (WENO) scheme with a third-order Total-Variation-Diminishing (TVD) Runge-Kutta method. Hypersonic boundary layer receptivity to freestream acoustic disturbances in slow and fast modes over 5-degree, half-angle blunt cones and wedges is numerically investigated. The free-stream Mach number is 6.0, and the unit Reynolds number is 7.8×10^6 /ft. Both the steady and unsteady solutions are obtained by solving the full Navier-Stokes equations in two-dimensional and axisymmetric coordinates.

Computations are performed in three steps. After the steady mean flow field is computed, linear stability analysis is performed to find the most amplified frequency and the unstable disturbance modes in different flow regions. Then, unsteady acoustic disturbances in slow or fast mode are introduced from the upper boundary of the computational domain with the most amplified frequency and time accurate computations performed to investigate the initial generation, interaction and evolution of instability waves inside the boundary layer. Since a very fine spatial grid is used to resolve the leading edge and boundary layer regions, these computations require a very small time

step. To reduce the runtime the code is parallelized with message passing interface (MPI) routines.

Receptivity computations showed that the acoustic disturbance waves propagated uniformly downstream and interacted with the bow shock and entered the boundary layer; then they generated the initial amplitude of the instability waves in the leading edge region.

Effects of the entropy layer due to nose bluntness to the receptivity process are studied. It is found that transition location moved downstream and was delayed by the increasing bluntness. Moreover, the role of the entropy layer in this process is revealed. Also, the effects of wall cooling to the receptivity process using slow and fast mode acoustic disturbances are studied. The effects of cooling on the first and second mode regions are investigated. It is found that the first mode is stabilized and the second mode is destabilized by wall cooling when the flow was forced by acoustic waves in slow mode.

Chapters 4-6 have their own detailed discussion and conclusion sections and here we will give the summary of those. Based on all the numerical simulations the following conclusions and recommendations for future research have been made.

7.1 Conclusions

The simulations for the comparison of the receptivity process over a cone and wedge revealed the following.

1. According to the unsteady simulations, instability waves are generated very close to the leading edge region.
2. The simulations for the cone showed that the first mode starts to grow starting from the leading edge (due to the nonparallel effects) before they grow exponentially due to the unstable second mode.
3. In the wedge simulations, the first mode disturbances decay first before they start to grow exponentially due to the second mode.
4. The receptivity coefficient of the instability waves generated by the slow acoustic wave is about 4 times that of the free stream acoustic wave's amplitude.
5. The amplitude of the instability waves generated by the slow mode acoustic disturbances is about 67 times larger than that for the fast mode. Therefore, forcing by slow mode is much more relevant in the transition process in hypersonic boundary layers.
6. The receptivity coefficient for the wedge is 0.8, which is 5 times smaller than that for the cone. This is due to the initial growth of the first mode in the cone case.
7. The above item shows that the slow mode is much more efficient in flows over a cone with small bluntness than a wedge with the same cross section.

Effects of the nose bluntness on the receptivity process are summarized as follows.

1. The results showed that bluntness has a strong stabilizing effect on the stability of the boundary layers. The transition Reynolds number increases

slowly up to a nose Reynolds number of 30,000 and then increases sharply at higher nose Reynolds numbers.

2. The transition Reynolds number for a cone at a nose Reynolds number of 65,000 is about 1.8 times larger than that for the Blasius boundary layer. This is due to the entropy layer that is generated near the leading edge. These layers persist for longer distances with increasing bluntness.
3. In the small bluntness case, the disturbances grow starting from the nose region and reach very large values, ~0.50, near the transition point. The growth of the first mode is much stronger for this case due to the non-parallel effects. The amplitude levels of the disturbances are much smaller, in the order of 10^{-4} in the larger bluntness cases.
4. There are no unstable first modes observed in the large bluntness cases, and the disturbances decay by two orders before they start to grow due to the second mode instability.
5. The receptivity coefficient at small bluntness r_0=0.001 in. is about 4.23, and it is much smaller, in the order of ~ 10^{-3}, in the larger bluntness cases.

Effects of the wall cooling on the receptivity process are summarized as follows.

1. It is shown that the first mode of slow wave acoustic disturbances is stabilized by wall cooling. However, wall cooling caused the destabilization of the second mode, and the transition location moved upstream from x=19.1 in. for adiabatic case to x=7.61 in. highly cooled wall case.
2. It is also interesting to note that wall cooling did not affect the first mode of fast acoustic disturbance waves. The receptivity coefficient of the fast wave

case is 50 times greater than that of the slow wave case. We can conclude that the boundary layer is much more receptive to fast acoustic waves as compared to the slow wave when wall cooling is applied.

3. For the same slow wave disturbance frequency, $F=1.2x10^{-4}$, at different wall temperature conditions the transition locations stayed almost the same for the adiabatic wall and cooled walls (603°R and 402°R) at 9.475, 9.714 and 9.672 in. Transition locations increased dramatically for wall temperatures 322°R, 241°R and 161°R to 14.628, 17.013, and 19.906 in. This is due to the stabilization of the first mode disturbances. However, the amplitude of wall pressure fluctuations of the cooled wall case (T_w=161°R) increased 2.34 times of the adiabatic wall case ($T_w = T_{aw}$=804°R).
4. Wall cooling reduced receptivity coefficients and increased the transition Reynolds numbers for the same forcing frequency, $F=1.2x10^{-4}$.

7.2 Recommendations for Future Research

Future work should be performed to investigate the following items.

1. The acoustic disturbance waves considered in this dissertation have zero incident angles. Non-zero acoustic incident angles may produce larger receptivity coefficients than the zero incident angle used in this work.
2. There may be other unstable modes in the entropy layer, as were observed in the experiments[54], other than the first-mode type instabilities that were considered in this work. Whether they exist and what role these waves play in

the transition process still has to be investigated using three-dimensional simulations.

3. Additional simulations for larger nose bluntness can be considered to capture the transition reversal phenomena.
4. In order to fully understand the instability mechanisms, vortical and wall induced disturbance waves should be considered over cones.

REFERENCES

[1]Schneider, S.P., "Hypersonic Laminar-Turbulent Transition on Circular Cones and Scramjet Forebodies," *Progress in Aerospace Sciences*, Vol. 40, 2004, pp. 1-50.

[2]Gollub, J., "Research in Fluid Dynamics: Meeting National Needs," Winter, 2006.

[3]Rufer, S. and Schneider, S.P., "Hot-Wire Measurements of Instability Waves on a Blunt Cone at Mach 6," 35th AIAA Fluid Dynamics Conference, Toronto, Canada, AIAA 2005-5137.

[4]Saric, W.S., Reed, H.L. and Kerschen, E.J., "Boundary Layer Receptivity to Freestream Disturbances," *Annu. Rev. Fluid Mech.*, Vol. 34, 2002, pp. 291-319.

[5]Dryden, H.L., "Transition from Laminar to Turbulent Flow," *High Speed Aerodynamics and Jet Propulsion Vol:V. Turbulent Flows and Heat Transfer*, edited by Lin, C.C.,Princeton University Press, 1959. pp. 3-74.

[6]Tani, I., "Boundary Layer Transition," *Annu. Rev. Fluid Mech.*, Vol. 1, 1969, pp. 169-196.

[7]Morkovin, M.V., "Critical Evaluation of Transition from Laminar to Turbulent Shear Layers with Emphasis on Hypersonically Travelling Bodies," AFFDL-TR-68-148, 1969.

[8]Reshotko, E., "Boundary Layer Stability and Transition," *Annu. Rev. Fluid Mech.*, Vol. 8, 1976, pp. 311-349.

[9]Reshotko, E., "Boundary Layer Instability, Transition and Control," 32nd Aerospace Sciences Meeting and Exhibit, Reno, NV, AIAA 1994-0001.

[10]Reshotko, E., "Transition Issues at Hypersonic Speeds," 44th AIAA Aerospace Sciences Meeting and Exhibit, Reno, NV, AIAA 2006-0707.

[11]Reshotko, E., "Progress, Accomplishments and Issues in Transition Research," 28th AIAA Fluid Dynamics Conference, Reno, NV, AIAA 1997-1815.

[12]Morkovin, M.V. and Reshotko, E., "Dialogue on Progress and Issues in Stability and Transition Research," *Laminar Turbulent Transition*, edited by Arnal, D. and Michel, R.,Springer-Verlag, 1990. pp. 3-29.

[13]Bayley, B.J., Orszag, S.A. and Herbert, T., "Instability Mechanisms in Shear-Flow Transition," *Annu. Rev. Fluid Mech.*, Vol. 20, 1988, pp. 359.

[14]Arnal, D. and Delery, J., "Laminar-Turbulent Transition and Shock Wave/Boundary Layer Interaction," NATO-RTO-EN-AVT-116-4, 2005.

[15]Saric, W.S., Muylaert, J. and Dujarrik, C., "Hypersonic Experimental and Computational Capability, Improvement and Validation," 1996.

[16]Saric, W.S., Reed, H.L. and White, E.B., "Stability and Transition of Three Dimensional Boundary Layers," *Annu. Rev. Fluid Mech.*, Vol. 35, 2003, pp. 413-440.

[17]Saric, W.S., White, E.B. and Reed, H.L., "Boundary Layer Receptivity to Freestream Disturbances and Its Role in Transition (Invited)," 30th AIAA Fluid Dynamics Conference, Norfolk, VA, AIAA 1999-3788.

[18]Reed, H.L. and Saric, W.S., "Stability of Three Dimensional Boundary Layers," *Annu. Rev. Fluid Mech.*, Vol. 21, 1989, pp. 235-284.

[19]Reed, H.L., Saric, W.S. and Arnal, D., "Linear Stability Theory Applied to Boundary Layers," *Annu. Rev. Fluid Mech.*, Vol. 28, 1996, pp. 389-428.

[20]Morkovin, M.V., Reshotko, E. and Herbert, T., "Transition in Open Systems - A Reassessment," *Bull. Am. Phys. Soc.*, Vol. 39, 1994, pp. 1882.

[21]Balakumar, P., "Transition in a Supersonic Boundary Layer Due to Acoustic Disturbances," 43rd AIAA Aerospace Sciences Meeting and Exhibit, Reno, NV, AIAA-2005-0096.

[22]Balakumar, P., "Stability of Supersonic Boundary Layers Over Blunt Wedges," 36th AIAA Fluid Dynamics Conference and Exhibit, San Francisco, Ca, AIAA-2006-3053.

[23]Shu, C.-W., "Essentially Non-Oscillatory and Weighted Essentially Non-Oscillatory Schemes for Hyperbolic Conservation Laws," NASA CR-97-206253, 1997.

[24]Atkins, H.L., "High-Order ENO Methods for The Unsteady Compressible Navier-Stokes Equations," 10th AIAA Computational Fluid Dynamics Conference, Honolulu, HI, AIAA-1991-1557.

[25]Balakumar, P., Zhao, H. and Atkins, H.L., "Stability of Hypersonic Boundary Layers over a Compression Corner," 42nd AIAA Fluid Dynamics Conference and Exhibit, St. Louis, Missouri, AIAA-2002-2848.

[26]Harten, A., Enquist, B., Osher, S. and Chakravarthy, S., "Uniformly High Order Essentially Non-Oscillatory Schemes," *Journal of Computational Physics*, Vol. 71, 1987, pp. 231-303.

[27]Shu, C.-W. and Osher, S., "Efficient Implementation of Essentially Non-Oscillatory Shock Capturing Schemes," *Journal of Computational Physics*, Vol. 77, 1988, pp. 439-471.

[28]Shu, C.-W. and Osher, S., "Efficient Implementation of Essentially Non-Oscillatory Shock Capturing Schemes II," *Journal of Computational Physics*, Vol. 83, 1989, pp. 32-78.

[29]Gottlieb, S. and Shu, C.-W., "Total Variation Diminishing Runge-Kutta Schemes," *Mathematics of Computation*, Vol. 67, 1998, pp. 73-85.

[30]Mair, W.A., "Experiments on Seperation of Boundary Layers on Probes in Front of Blunt-Nosed Bodies in a Supersonic Air Stream," *Philosophical Magasine*, Vol. 43 (342), 1952, pp. 695-734.

[31]Dyke, M.V., *An Album of Fluid Motion*, The Parabolic Press, Stanford, CA, 1982.

[32]Merzkirch, W., *Flow Visualization*, Academic Press, Orlando, 1987.

[33]Johnston, I.A., "Simulation of Flow around Hypersonic Blunt-Nosed Vehicles for the Calibration of Air Data System," PhD Dissertation, Mechanical Engineering, The University of Queensland, Australia, 1999.

[34]Ambrosio, A. and Wortman, A., "Stagnation Point Shock Detachment Distance for Flow around Spheres and Cylinders," *ARS Journal*, Vol. 32, 1962, pp. 281.

[35]Horvath, T.J., Berry, S.A., Hollis, B.R., Chang, C.-L. and Singer, B.A., "Boundary Layer Transition on Slender Cones in Conventional and Low Disturbance Mach 6 Wind Tunnels," 32nd AIAA Fluid Dynamics Conference, St. Louis, Missouri, AIAA 2002-2743.

[36]Billig, F.S., "Shock-Wave Shapes around Spherical and Cylindrical-Nosed Bodies," *Journal of Spacecraft*, Vol. 4 (6), 1967, pp. 822-823.

[37]Anderson, J.D., *Hypersonic and High Temperature Gas Dynamics*, 1st ed., McGraw-Hill, New York, 1989.

[38]Anderson, J.D., *Hypersonic and High Temperature Gas Dynamics*, 2nd ed., AIAA, Reston, VA, 2006.

[39]Kara, K., Balakumar, P. and Kandil, O.A., "High Order WENO Method for the Steady Compressible 2D & Axisymmetric Navier-Stokes Equations," AIAA Region I, YPSE-06, Baltimore, MD, Year.

[40]Kara, K., Balakumar, P. and Kandil, O.A., "Receptivity of Hypersonic Boundary Layers Due to Acoustic Disturbances over Blunt Cone," 45th Aerospace Sciences Meeting and Exhibit, Reno, NV, AIAA 2007-0945.

[41]Mack, L.M., "Linear Stability Theory and the Problem of Supersonic Boundary- Layer Transition," *AIAA Journal*, Vol. 13, 1975, pp. 278-289.

[42]Gaponov, S.A., "Interaction Between a Supersonic Boundary Layer and Acoustic Disturbances " *Fluid Dynamics*, Vol. 6, 1977, pp. 858-862.

[43]Gaponov, S.A. and Smorodsky, B.V., "Supersonic Boundary Layer Receptivity to Streamwise Acoustic Field," IUTAM Symposium, Sedona, AZ, 1999.

[44]Mack, L.M., "Boundary-Layer Stability Theory," Report 900-277 Rev. A, 1969.

[45]Fedorov, A.V. and Khokhlov, A.P., "Excitation of Unstable Modes in a Supersonic Boundary Layer," *Fluid Dynamics*, Vol. 9, 1991, pp. 456-467.

[46]Fedorov, A.V., "Prehistory of Instability in a Hypersonic Boundary Layer," *Theoret. Comput. Fluid Dynamics*, Vol. 14, 2001, pp. 359-375.

[47]Fedorov, A.V., "Receptivity of a High-Speed Boundary Layer to Acoustic Disturbances," *Journal of Fluid Mechanics*, Vol. 491, 2003, pp. 101-129.

[48]Ma, Y. and Zhong, X., "Receptivity of a Supersonic Boundary Layer over a Flat Plate. Part 1. Wave Structures and Interactions," *Journal of Fluid Mechanics*, Vol. 488, 2003, pp. 31-78.

[49]Ma, Y. and Zhong, X., "Receptivity of a Supersonic Boundary Layer over a Flat Plate. Part 2. Receptivity to Freestream Sound," *Journal of Fluid Mechanics*, Vol. 488, 2003, pp. 79-121.

[50]Ma, Y. and Zhong, X., "Receptivity of a Supersonic Boundary Layer over a Flat Plate. Part 3. Effects of Different Types of Freestream Disturbances," *Journal of Fluid Mechanics*, Vol. 532, 2005, pp. 63-109.

[51]Egorov, I.V., Fedorov, A.V. and Soudakov, V.G., "Receptivity of a Hypersonic Boundary Layer over a Flat Plate with a Porous Coating," *Journal of Fluid Mechanics*, Vol. 601, 2008, pp. 165-187.

[52]Malik, M.R. and Balakumar, P., "Receptivity of Supersonic Boundary Layers to Acoustic Disturbances " 35th AIAA Fluid Dynamics Conference and Exhibit, Toronto, Canada, AIAA-2005-5027.

[53]Malik, M.R. and Balakumar, P., "Acoustic Receptivity of Mach 4.5 Boundary Layer with Leading-Edge Bluntness," *Theoret. Comput. Fluid Dynamics*, Vol. 21 (5), 2007, pp. 323-342.

[54]Stetson, K.F., Thompson, E.R., Donaldson, J.C. and Siler, L.G., "Laminar Boundary Layer Stability Experiments on a Cone at Mach 8. Part II - Blunt Cone," 22nd Aerospace Sciences Meeting, Reno, NV, AIAA 1984-0006.

[55]Reshotko, E. and Khan, M.M.S., "Stability of the Laminar Boundary Layer on a Blunted Plate in Supersonic Flow," Laminar Turbulent Transition Symposium, Stuttgart, Germany, 1979.

[56]Malik, M.R., Spall, R.E. and Chang, C.-L., "Effect of Nose Bluntness on Boundary Layer Stability and Transition," 28th Aerospace Sciences Meeting, Reno, NV, AIAA 1990-0112.

[57]Hu, S.H. and Zhong, X., "Hypersonic Boundary Layer Stability over Blunt Leading Edges with Bow Shock Effects," 36th Aerospace and Sciences Meeting & Exhibit, Reno, NV, AIAA 1998-0433.

[58]Zhong, X., "Receptivity and Linear Stability of Stetson's Mach 8 Blunt Cone Stability Experiments," 32nd AIAA Fluid Dynamics Conference and Exibit, St. Louis, Missouri, AIAA 2002-2849.

[59]John, C.E., "Transition Studies on Blunted Bodies at Supersonic Speeds," 9th International Congress of Applied Mechanics Brussel, Sep. 5-13 1956.

[60]Stetson, K.F., "Nosetip Bluntness Effects on Cone Frustrum Boundary Layer Transition in Hypersonic Flow," 16th Fluid and Plasma Dynamics Conference, Danvers, MA, AIAA 1983-1763.

[61]Maslov, A.A., Shiplyuk, A.N., Sidorenko, A.A. and Arnal, D., "Leading-Edge Receptivity of a Hypersonic Boundary Layer on a Flat Plate," *Journal of Fluid Mechanics*, Vol. 426, 2001, pp. 73-94.

[62]Maslov, A.A., Mironov, S.G., Shiplyuk, A.N., Sidorenko, A.A., Buntin, D.A. and Aniskin, V.M., "Hypersonic Flow Stability Experiments," 40th Aerospace Sciences Meeting & Exhibit, Reno, NV, AIAA 2002-0153.

[63]Rufer, S. and Schneider, S.P., "Hot-Wire Measurements of Stability Waves on Cones at Mach 6," 36th AIAA Fluid Dynamics Conference and Exhibit, San Francisco, CA, AIAA 2006-3054.

[64]Schneider, S.P., "Hypersonic Laminar Instability on Round Cones Near Zero Angle of Attack," 39th Aerospace Sciences Meeting & Exibit, Reno, NV, AIAA 2001-0206.

[65]Potter, J.L., "Boundary Layer Transition on Supersonic Cones in an Aerobalistic Range," *AIAA Journal*, Vol. 13 (3), 1975, pp. 270-277.

[66]Rosenboom, I., Hein, S. and Dallmann, U., "Influence of Nose Bluntness on Boundary-Layer Instabilities in Hypersonic Cone Flows " 30th AIAA Fluid Dynamics Conference, Norfolk, VA, AIAA 1999-3591.

[67]Zhong, X., "Effects of Nose Bluntness on Hypersonic Boundary Layer Receptivity over a Blunt Cone," 35th AIAA Fluid Dynamics Conference and Exhibit, Toronto, Canada, AIAA 2005-5022.

[68]Lees, L., "The Stability of the Laminar Boundary Layer in a Compressible Fluid," NACA Report 876, 1947.

[69]Mack, L.M., "Boundary-Layer Stability Theory," AGARD-R-709, 1984.

[70]Demetriades, A., "New Experiments on Hypersonic Boundary Layer Stability Including Wall Temperature Effects," *Proceedings of the Heat Transfer and Fluid Mechanics Institute*, Vol. 26, 1978, pp. 39-54.

[71]Lysenko, V.I., Maslov, A.A. and Semenov, N.M., "Experimental Study of the Effect of Wall Heating on the Transition and Stability of Supersonic Boundary Layers," *Fluid Mechanics - Soviet Research*, Vol. 11 (6), 1982, pp. 32-43.

[72]Stetson, K.F., Thompson, E.R., Donaldson, J.C. and Siler, L.G., "Laminar Boundary Layer Stability Experiments on a Cone at Mach 8. Part 5 - Test with a Cooled Model," 20th Fluid Dynamics, Plasma Dynamics and Lasers Conference, Buffalo, NY, AIAA 1989-1895.

[73]Balakumar, P. and Malik, M.R., "Effects of Adverse Pressure Gradient and Wall Cooling Instability of Hypersonic Boundary Layers," HTC-9404, 1994.

[74]Maslov, A.A., Shiplyuk, A.N., Bountin, D.A. and Sidorenko, A.A., "Mach 6 Boundary-Layer Stability Experiments on Sharp and Blunted Cones," *Journal of Spacecrafts and Rockets*, Vol. 43 (1), 2006, pp. 71-76.

[75]Borg, M.P., Schneider, S.P. and Juliano, T.J., "Effect of Freestream Noise in Roughness-Induced Transition for the X-51A Forebody," 46th Aerospace and Sciences Meeting & Exhibit, Reno, NV, AIAA 2008-0592.

[76]Fedorov, A.V., Malmuth, N.D., Rasheed, A. and Hornung, H.G., "Stabilization of Hypersonic Boundary Layers by Porous Coatings," *AIAA Journal*, Vol. 39, 2001, pp. 605.

[77]Fedorov, A.V., "Receptivity of Hypersonic Boundary Layer to Wall Disturbances," *Theoret. Comput. Fluid Dynamics*, Vol. 15, 2002, pp. 231-254.

[78]Fedorov, A.V., Shiplyuk, A.N., Maslov, A.A., Burov, E.V. and Malmuth, N.D., "Stabilization of a Hypersonic Boundary Layer Using an Ultrasonically Absorptive Coating," *Journal of Fluid Mechanics*, Vol. 479, 2003, pp. 99-124.

[79]Tumin, A., "Receptivity of Compressible Boundary Layers to Three Dimensional Wall Perturbations," 44th Aerospace Sciences Meeting & Exhibit, Reno, NV, AIAA-2006-1110.

[80]Collis, S.S. and Lele, S.K., "Receptivity to Surface Roughness Near a Swept Leading Edge," *Journal of Fluid Mechanics*, Vol. 380, 1999, pp. 141-168.

[81]Zhong, X., "Leading-Edge Receptivity to Freestream Disturbance Waves for Hypersonic Flow over Parabola," *Journal of Fluid Mechanics*, Vol. 441, 2001, pp. 315-367.

[82]Zhong, X., "Receptivity of Mach 6 Flow over a Flared Cone to Freestream Disturbance," 42nd Aerospace Sciences Meeting and Exhibit, Reno, NV, AIAA 2004-0253.

[83]Balakumar, P., "Control of Supersonic Boundary Layers Using Steady Suction," 36th AIAA Fluid Dynamics Conference and Exhibit, San Francisco, Ca, AIAA-2006-3058.

[84]Balakumar, P., "Receptivity of Supersonic Boundary Layers To Acoustic Disturbances Over Blunt Cones," 37th AIAA Fluid Dynamics Conference and Exhibit, Miami, FL, AIAA-2007-4491.

[85]Kara, K., Balakumar, P. and Kandil, O.A., "Effects of Nose Bluntness on Stability of Hypersonic Boundary Layers over a Blunt Cone," 37th Fluid Dynamics Conference & Exhibit, Miami, FL, AIAA 2007-4492.

[86]Cebeci, T., *Stability and Transition: Theory and Application*, Horizons Publishing, Long Beach, 2004.

[87]Malik, M.R., Chang, S. and Hussaini, M.Y., "Accurate Numerical Solution of Compressible, Linear Stability Equations," *Journal of Applied Mathematics and Physics (ZAMP)*, Vol. 33, 1982, pp. 189-201.

[88]Cebeci, T. and Bradshaw, P., *Momentum Transfer in Boundary Layers*, Hemisphere Pub. Corp., Washington, 1977.

APPENDIX

LINEAR STABILITY THEORY (LST)

The following formulation of linear stability theory was given by Mack[44] (and more recently by Cebeci[86]). To derive the linear stability equations for a compressible flow we start with the Navier-Stokes equations (non dimensionalized by the parameters given in Section 2.2) for a perfect gas. Neglecting the body forces one can write they as

Continuity equation

$$\frac{\partial \rho}{\partial t}+\frac{\partial}{\partial x}(\rho u)+\frac{\partial}{\partial y}(\rho v)+\frac{\partial}{\partial z}(\rho w)=0 \tag{A.1}$$

Momentum equations

$$\rho\frac{Du}{Dt}=-\frac{\partial p}{\partial x}+\frac{1}{Re}\left\{\begin{array}{l}\frac{2}{3}\frac{\partial}{\partial x}\left[\mu\left(2\frac{\partial u}{\partial x}-\frac{\partial v}{\partial y}-\frac{\partial w}{\partial z}\right)\right]\\ +\frac{\partial}{\partial y}\left[\mu\left(\frac{\partial v}{\partial x}+\frac{\partial u}{\partial y}\right)\right]\\ +\frac{\partial}{\partial z}\left[\mu\left(\frac{\partial w}{\partial x}+\frac{\partial u}{\partial z}\right)\right]\end{array}\right\} \tag{A.2}$$

$$\rho\frac{Dv}{Dt}=-\frac{\partial p}{\partial y}+\frac{1}{Re}\left\{\begin{array}{l}\frac{\partial}{\partial x}\left[\mu\left(\frac{\partial u}{\partial y}+\frac{\partial v}{\partial x}\right)\right]\\ +\frac{2}{3}\frac{\partial}{\partial y}\left[\mu\left(2\frac{\partial v}{\partial y}-\frac{\partial u}{\partial x}-\frac{\partial w}{\partial z}\right)\right]\\ +\frac{\partial}{\partial z}\left[\mu\left(\frac{\partial w}{\partial y}+\frac{\partial v}{\partial z}\right)\right]\end{array}\right\} \tag{A.3}$$

$$\rho\frac{Dw}{Dt}=-\frac{\partial p}{\partial z}+\frac{1}{Re}\left\{\begin{array}{l}\frac{\partial}{\partial x}\left[\mu\left(\frac{\partial u}{\partial z}+\frac{\partial w}{\partial x}\right)\right]\\+\frac{\partial}{\partial y}\left[\mu\left(\frac{\partial v}{\partial z}+\frac{\partial w}{\partial y}\right)\right]\\+\frac{2}{3}\frac{\partial}{\partial z}\left[\mu\left(2\frac{\partial w}{\partial z}-\frac{\partial v}{\partial y}-\frac{\partial u}{\partial x}\right)\right]\end{array}\right\} \tag{A.4}$$

Energy equation

$$\begin{aligned}\rho\frac{DT}{Dt}=&\frac{\gamma}{Pr\,Re}\left[\frac{\partial}{\partial x}\left(\mu\frac{\partial T}{\partial x}\right)+\frac{\partial}{\partial y}\left(\mu\frac{\partial T}{\partial y}\right)+\frac{\partial}{\partial z}\left(\mu\frac{\partial T}{\partial z}\right)\right]\\&+\frac{\gamma(\gamma-1)M_\infty^2}{Re}\left\{\begin{array}{l}2\mu\left[\left(\frac{\partial u}{\partial x}\right)^2+\left(\frac{\partial v}{\partial y}\right)^2+\left(\frac{\partial w}{\partial z}\right)^2\right]\\-\frac{2}{3}\mu\left(\frac{\partial u}{\partial x}+\frac{\partial v}{\partial y}+\frac{\partial w}{\partial z}\right)^2\\+\mu\left[\left(\frac{\partial u}{\partial y}+\frac{\partial v}{\partial x}\right)^2+\left(\frac{\partial u}{\partial z}+\frac{\partial w}{\partial x}\right)^2+\left(\frac{\partial v}{\partial z}+\frac{\partial w}{\partial y}\right)^2\right]\end{array}\right\}\\&-\gamma(\gamma-1)M_\infty^2 p\left(\frac{\partial u}{\partial x}+\frac{\partial v}{\partial y}+\frac{\partial w}{\partial z}\right)\end{aligned} \tag{A.5}$$

State equation

$$p=\frac{\rho T}{\gamma M_\infty^2} \tag{A.6}$$

where

$$\frac{D}{Dt}=\frac{\partial(\,)}{\partial t}+u\frac{\partial(\,)}{\partial x}+v\frac{\partial(\,)}{\partial y}+w\frac{\partial(\,)}{\partial z} \tag{A.7}$$

and assume that the velocity components u, v, and w, pressure p, temperature T, density ρ, represent the instantaneous components of the flow properties in Equations (A.1) to

(A.6) and divide them into a mean term and a fluctuating term so that the instantaneous flow properties can be expressed as

$$\begin{aligned} u &= \bar{U} + u' & T &= \bar{T} + T' & \mu &= \bar{\mu} + \mu' \\ v &= \bar{V} + v' & p &= \bar{p} + p' & \rho &= \bar{\rho} + \rho' \\ w &= \bar{W} + w' \end{aligned} \tag{A.8}$$

where the symbol '-' represents the mean flow quantities, and '`' stands for the disturbance quantities. The viscosity is a function only of temperature. We have the following equations.

$$\begin{aligned} \mu' &= \frac{\partial \bar{\mu}}{\partial \bar{T}} T' \\ \frac{\partial \mu}{\partial x_i} &= \frac{\partial^2 \bar{\mu}}{\partial \bar{T}^2} \frac{\partial T}{\partial x_i} T' + \frac{\partial \bar{\mu}}{\partial \bar{T}} \frac{\partial T'}{\partial x_i} \\ \frac{\partial \bar{\mu}}{\partial x_i} &= \frac{\partial \bar{\mu}}{\partial \bar{T}} \frac{\partial T}{\partial x_i} \end{aligned} \tag{A.9}$$

First one can substitute Equation (A.8) into Equations (A.1)-(A.6) and cancel out the mean flow terms assuming that they satisfy the Navier-Stokes equations for steady laminar flow. Since disturbance quantities are small, their squares and products can be neglected. They are, however, still complicated and can be further simplified by assuming the flow is parallel, and we can write them as follows.

$$\bar{u} = \bar{u}_{(y)}, \quad \bar{w} = \bar{w}_{(y)}, \quad \bar{\rho} = \bar{\rho}_{(y)}, \quad \bar{T} = \bar{T}_{(y)}, \quad \bar{v} = 0 \tag{A.10}$$

Dropping the over-bars on mean flow variables for convenience allows the nondimensional linearized disturbance equations to be written as

$$\frac{\partial \rho'}{\partial t} + \rho \left(\frac{\partial u'}{\partial x} + \frac{\partial v'}{\partial y} + \frac{\partial w'}{\partial z} \right) + u \frac{\partial \rho'}{\partial x} + v' \frac{\partial \rho}{\partial y} + w \frac{\partial \rho'}{\partial z} = 0 \tag{A.11}$$

$$\rho\left(\frac{\partial u'}{\partial t}+u\frac{\partial u'}{\partial x}+v'\frac{du}{dy}+w\frac{\partial u'}{\partial z}\right)=-\frac{1}{\gamma M_e^2}\frac{\partial p'}{\partial x}$$
$$+\frac{1}{R}\left\{\begin{array}{l}2\mu\frac{\partial^2 u'}{\partial x^2}+\mu\left(\frac{\partial^2 u'}{\partial y^2}+\frac{\partial^2 u'}{\partial z^2}+\frac{\partial^2 v'}{\partial x\partial y}+\frac{\partial^2 w'}{\partial x\partial z}\right)+\frac{2}{3}(\lambda-\mu)\left(\frac{\partial^2 u'}{\partial x^2}+\frac{\partial^2 v'}{\partial x\partial y}+\frac{\partial^2 w'}{\partial x\partial z}\right)\\+\frac{d\mu}{dT}\frac{dT}{dy}\left(\frac{\partial u'}{\partial y}+\frac{\partial v'}{\partial x}\right)+\frac{d\mu}{dT}\left(\frac{\partial^2 u}{\partial y^2}T'+\frac{\partial u}{\partial y}\frac{\partial T'}{\partial y}\right)+\frac{d^2\mu}{dT^2}\frac{dT}{dy}\frac{du}{dy}T'\end{array}\right\} \quad \text{(A.12)}$$

$$\rho\left(\frac{\partial v'}{\partial t}+u\frac{\partial v'}{\partial x}+w\frac{\partial v'}{\partial z}\right)=-\frac{1}{\gamma M_e^2}\frac{\partial p'}{\partial y}$$
$$+\frac{1}{R}\left\{\begin{array}{l}2\mu\frac{\partial^2 v'}{\partial y^2}+\mu\left(\frac{\partial^2 v'}{\partial x^2}+\frac{\partial^2 v'}{\partial z^2}+\frac{\partial^2 u'}{\partial x\partial y}+\frac{\partial^2 w'}{\partial y\partial z}\right)+\frac{2}{3}(\lambda-\mu)\left(\frac{\partial^2 u'}{\partial x\partial y}+\frac{\partial^2 v'}{\partial y^2}+\frac{\partial^2 w'}{\partial y\partial z}\right)\\+\frac{d\mu}{dT}\left(2\frac{dT}{dy}\frac{\partial v'}{\partial y}+\frac{du}{dy}\frac{\partial T'}{\partial x}+\frac{dw}{dy}\frac{\partial T'}{\partial z}\right)+\frac{2}{3}\left(\frac{d\lambda}{dy}-\frac{d\mu}{dy}\right)\frac{dT}{dy}\left(\frac{\partial u'}{\partial x}+\frac{\partial v'}{\partial y}+\frac{\partial w'}{\partial z}\right)\end{array}\right\} \quad \text{(A.13)}$$

$$\rho\left(\frac{\partial w'}{\partial t}+u\frac{\partial w'}{\partial x}+v'\frac{dw}{dy}+w\frac{\partial w'}{\partial z}\right)=-\frac{1}{\gamma M_e^2}\frac{\partial p'}{\partial z}$$
$$+\frac{1}{R}\left\{\begin{array}{l}2\mu\frac{\partial^2 w'}{\partial z^2}+\mu\left(\frac{\partial^2 w'}{\partial x^2}+\frac{\partial^2 w'}{\partial y^2}+\frac{\partial^2 v'}{\partial y\partial z}+\frac{\partial^2 u'}{\partial x\partial z}\right)+\frac{2}{3}(\lambda-\mu)\left(\frac{\partial^2 w'}{\partial z^2}+\frac{\partial^2 v'}{\partial y\partial z}+\frac{\partial^2 u'}{\partial x\partial z}\right)\\+\frac{d\mu}{dT}\frac{dT}{dy}\left(\frac{\partial w'}{\partial y}+\frac{\partial v'}{\partial z}\right)+\frac{d\mu}{dT}\left(\frac{\partial^2 w}{\partial y^2}T'+\frac{\partial w}{\partial y}\frac{\partial T'}{\partial y}\right)+\frac{d^2\mu}{dT^2}\frac{dT}{dy}\frac{dw}{dy}T'\end{array}\right\} \quad \text{(A.14)}$$

$$\rho\left(\frac{\partial T'}{\partial t}+u\frac{\partial T'}{\partial x}+v'\frac{dT}{dy}+w\frac{\partial T'}{\partial z}\right)=-(\gamma-1)p\left(\frac{\partial u'}{\partial x}+\frac{\partial v'}{\partial y}+\frac{\partial w'}{\partial z}\right)$$
$$+\frac{\gamma\mu}{P_r R}\left[\left(\frac{\partial^2 T'}{\partial x^2}+\frac{\partial^2 T'}{\partial y^2}+\frac{\partial^2 T'}{\partial z^2}\right)+\frac{1}{k}\frac{dk}{dT}\frac{d^2T}{dy^2}T'+\frac{2}{k}\frac{dk}{dT}\frac{dT}{dy}\frac{\partial T'}{\partial y}+\frac{1}{k}\frac{d^2k}{dT^2}\left(\frac{dT}{dy}\right)^2T'\right] \quad \text{(A.15)}$$
$$\frac{\gamma(\gamma-1)M_e^2}{R}\left[2\mu\frac{du}{dy}\left(\frac{\partial u'}{\partial y}+\frac{\partial v'}{\partial x}\right)+2\mu\frac{dw}{dy}\left(\frac{\partial v'}{\partial z}+\frac{\partial w'}{\partial y}\right)+\frac{d\mu}{dT}\left(\frac{du}{dy}\right)^2T'+\frac{d\mu}{dT}\left(\frac{dw}{dy}\right)^2T'\right]$$

$$p'=\rho' T+\rho T' \quad \text{(A.16)}$$

Equations (A.11) to (A.16) form a set of coupled partial differential equations whose solutions describe how disturbances originate near the surface, $y=0$, and spread out through the boundary layer. One can assume that the small disturbance is a sinusoidal travelling wave and write the three-dimensional disturbances

$$\begin{bmatrix} u' \\ v' \\ w' \\ \rho' \\ p' \\ T' \end{bmatrix}_{(x,y,z,t)} = \begin{bmatrix} \hat{u} \\ \hat{v} \\ \hat{w} \\ \hat{\rho} \\ \hat{p} \\ \hat{T} \end{bmatrix}_{(y)} e^{i(\alpha x+\beta z-\omega t)} \tag{A.17}$$

where $\hat{u},\hat{v},\hat{w},\hat{\rho},\hat{p},\hat{T}$ are the complex amplitude functions of the flow variables u',v',w',ρ',p',T' respectively. α and β are the dimensionless wave numbers $2\pi L/\lambda_x$ and $2\pi L/\lambda_z$, where λ_x and λ_z are the wavelengths in streamwise and spanwise directions respectively, and ω is the dimensionless frequency.

After substituting Equation (A.17) back into Equations (A.11) to (A.16) we can get eight first order differential equations written in matrix form as follows

$$\frac{d\hat{q}}{dy} = A\hat{q} \tag{A.18}$$

where A is an 8x8 coefficient matrix, and the non-zero elements are

$$a_{1,2} = 1$$

$$a_{2,1} = \frac{iR}{\mu T}(\alpha U - \omega) + (\alpha^2 + \beta^2)$$

$$a_{2,2} = -\frac{1}{\mu}\frac{d\mu}{dT}\frac{dT}{dy}$$

$$a_{2,3} = \frac{1}{\mu}\left(\frac{R}{T}\frac{du}{dy} - i\alpha\frac{d\mu}{dT}\frac{dT}{dy}\right) - \frac{i\alpha}{3T}\frac{dT}{dy}$$

$$a_{2,4} = \frac{i\alpha R}{\mu\gamma M^2} - \frac{\alpha}{3}(\alpha u - \omega)$$

$$a_{2,5} = \frac{\alpha}{3T}(\alpha u - \omega) - \frac{1}{\mu}\left(\frac{d\mu}{dT}\frac{d^2u}{dy^2} + \frac{d^2\mu}{dT^2}\frac{dT}{dy}\frac{du}{dy}\right)$$

$$a_{2,6} = -\frac{1}{\mu}\frac{d\mu}{dT}\frac{du}{dy}$$

$$a_{3,1} = -i\alpha$$

$$a_{3,3} = \frac{1}{T}\frac{dT}{dy}$$

$$a_{3,4} = -i(\alpha u - \omega)$$

$$a_{3,5} = \frac{i(\alpha u - \omega)}{T}$$

$$a_{3,7} = -i\beta$$

$$a_{4,1} = -\frac{i\alpha}{L}\left[\frac{4\mu}{3T}\frac{dT}{dy} + 2\frac{d\mu}{dT}\frac{dT}{dy}\right]$$

$$L = \frac{R}{\gamma M^2} + \frac{4}{3}i\mu(\alpha u - \omega)$$

$$a_{4,2} = -\frac{i\alpha\mu}{L}$$

$$a_{4,3} = \frac{1}{L}\left[\frac{4}{3T}\left(\mu\frac{d^2T}{dy^2} + \frac{d\mu}{dT}\left(\frac{dT}{dx}\right)^2\right) - i\frac{R}{T}(\alpha u - \omega) - \mu(\alpha^2 + \beta^2)\right]$$

$$a_{4,4} = -\frac{4i}{3L}\left[\mu\left((\alpha u - \omega)\frac{1}{T}\frac{dT}{dy} + \alpha\frac{du}{dy}\right) + \frac{d\mu}{dT}\frac{dT}{dy}(\alpha u - \omega)\right]$$

$$a_{4,5} = \frac{4}{3}\frac{i}{LT}\left[\alpha\mu\frac{du}{dy} + \frac{d\mu}{dT}\frac{dT}{dy}(\alpha u - \omega)\right] + \frac{i\alpha}{L}\frac{d\mu}{dT}\frac{du}{dy}$$

$$a_{4,7} = -\frac{i\beta}{L}\left[\frac{4\mu}{3T} + 2\frac{d\mu}{dT}\right]\frac{dT}{dy}$$

$$a_{4,8} = -\frac{i\beta\mu}{L}$$

$$a_{5,6} = 1$$

$$a_{6,2} = 2(1-\gamma)M^2 P_r\frac{du}{dy}$$

$$a_{6,3} = \frac{P_r R}{\mu T}\frac{dT}{dy} - 2i(\gamma - 1)\alpha M^2 P_r\frac{du}{dy}$$

$$a_{6,4} = \frac{iP_r R}{\gamma\mu}(1-\gamma)(\alpha u - \omega)$$

$$a_{6,5} = \frac{iP_r R}{\mu T}(\alpha u - \omega) + (\alpha^2 + \beta^2) - \frac{1}{\mu}\left[\frac{d\mu}{dT}\frac{d^2T}{dy^2} + \frac{d^2\mu}{dT^2}\left(\frac{dT}{dy}\right)^2\right]$$
$$-\frac{(\gamma-1)P_r M^2}{\mu}\frac{d\mu}{dT}\left(\frac{du}{dy}\right)^2$$

$$a_{6,6} = -\frac{2}{\mu}\frac{d\mu}{dT}\frac{dT}{dy}$$

$$a_{7,8} = 1$$

$$a_{8,3} = -i\beta\left(\frac{1}{3T}\frac{dT}{dy} + \frac{1}{\mu}\frac{d\mu}{dT}\frac{dT}{dy}\right)$$

$$a_{8,4} = \beta\left[-\frac{1}{3}(\alpha u - \omega) + \frac{iR}{\mu\gamma M^2}\right]$$

$$a_{8,5} = \frac{\beta}{3T}(\alpha u - \omega)$$

$$a_{8,7} = \frac{iR}{\mu T}(\alpha u - \omega) + (\alpha^2 + \beta^2)$$

$$a_{8,8} = -\frac{1}{\mu}\frac{d\mu}{dT}\frac{dT}{dy}$$

In Equation (A.18) $\hat{q}$ is

$$\hat{q} = \left[\hat{u},\ \frac{d\hat{u}}{dy},\ \hat{v},\ \frac{d\hat{v}}{dy},\ \hat{T},\ \frac{d\hat{T}}{dy},\ \hat{w},\ \hat{p}\right]^T$$

The boundary conditions are

$$\hat{u} = \hat{v} = \hat{w} = \hat{T} = 0,\ at\ y = 0 \tag{A.19}$$

and

$$\hat{u}, \hat{v}, \hat{w}, \hat{T} \to 0, as\ y \to \infty \tag{A.20}$$

The first order differential equations derived above along with the homogenous boundary conditions are actually an eigenvalue problem that can be written as follows.

$$F_{(\alpha,\beta,\omega,R)} = 0 \tag{A.21}$$

For a given Reynolds number, if any pair of three variables α, β, and ω is known, one can find the third variable from the above equation.

The eigenvalue problem can be solved using the boundary value method (BVM). Malik, Chuang and Hussani[87]developed a fourth order accurate two-point compact difference scheme based on BVM using the Euler-Maclaurin formula:

$$\Psi^k - \Psi^{k-1} = \frac{h_k}{2}\left(\frac{d\Psi^k}{dy} + \frac{d\Psi^{k-1}}{dy}\right) - \frac{h_k^2}{12}\left(\frac{d^2\Psi^k}{dy^2} - \frac{d^2\Psi^{k-1}}{dy^2}\right) + O\left(h_k^5\right) \qquad \text{(A.22)}$$

where $\Psi^k = \Psi_{(y_k)}$ and $h_k = y_k - y_{k-1}, k = 1,2,...,N$.

In order to apply this scheme to Equation (A.18), one can write

$$\Psi = \{\hat{q}_i\}, \qquad \frac{d\Psi}{dy} = \left\{\sum_{j=1}^{8} a_{ij}\hat{q}_j\right\}, \qquad \frac{d^2\Psi}{dy^2} = \left\{\sum_{j=1}^{8} b_{ij}\hat{q}_j\right\} \qquad \text{(A.23)}$$

where

$$b_{ij} = \frac{da_{ij}}{dy} + \sum_{l=1}^{8} a_{il}a_{lj} \qquad \text{(A.24)}$$

Substituting the above equations into Equation (A.22), we get

$$\hat{q}_i^k - \frac{h_k}{2}\sum_{j=1}^{8} a_{ij}^k\hat{q}_j^k + \frac{h_k^2}{12}\sum_{j=1}^{8} b_{ij}^k\hat{q}_j^k - \left[\hat{q}_i^{k-1} - \frac{h_k}{2}\sum_{j=1}^{8} a_{ij}^{k-1}\hat{q}_j^{k-1} + \frac{h_k^2}{12}\sum_{j=1}^{8} b_{ij}^{k-1}\hat{q}_j^{k-1}\right] = 0 \qquad \text{(A.25)}$$

Following the procedure given by Cebeci and Bradshaw[88] the above equation system along with the boundary conditions given in Equations (A.19) and (A.20), can be written in block tridiagonal form as follows.

$$A_k\hat{q}^{k-1} + B_k\hat{q}^k + C_k\hat{q}^{k+1} = RHS, \quad k = 1,2,...,N \qquad \text{(A.26)}$$

where A_k, B_k, and C_k are 8x8 matrices and *RHS* is an 8x1 null matrix.

Nonhomogenous boundary conditions are imposed at the wall to avoid a trivial solution. The boundary condition $\hat{q}_1^1 = 0$ is replaced by $\hat{q}_8^1 = 0$, which is equivalent to normalizing the eigenfunction by the value of the pressure perturbations at the wall. Now Equation (A.26) is nonhomogenous and a non-trivial solution can be obtained for a guessed eigenvalue. For example, $\omega = \omega_0$ if α and β are given. Newton's method is used to iterate on ω such that the missing boundary condition $\hat{q}_1^1 = 0$ satisfied. Thus, when a solution, $\hat{q}$, is obtained for ω_0, the correction, $\Delta\omega$, is determined from the following equation.

$$\hat{q}_1^1 + \frac{\partial \hat{q}_1^1}{\partial \omega}\Delta\omega = 0 \tag{A.27}$$

where $\hat{q}_1^1$ is known from the solution $\hat{q}$ just obtained; $\partial\hat{q}_1^1/\partial\omega$ is obtained by solving

$$\frac{\partial \hat{q}_1^1}{\partial \omega} = \frac{\hat{q}_1^1\Big|_{\omega+\delta\omega} - \hat{q}_1^1\Big|_{\omega}}{\delta\omega} \tag{A.28}$$

one can use the same strategy to obtain $\hat{q}_1^1\Big|_{\omega+\delta\omega}$.

We can also obtain α and β based on the same method described above if the other two variables are known.

VITA

Kursat KARA
Aerospace Engineering Department
Old Dominion University
Norfolk, VA 23529

Educational Background

Ph.D.	: December 2008, Old Dominion University, Norfolk VA USA
Major	: Aerospace Engineering
Dissertation	: Hypersonic Boundary Layer Receptivity to Acoustic Disturbances over Cones.
M.Sc.	: May 2003, Istanbul Technical University, Istanbul TURKEY
Major	: Aeronautical Engineering
Thesis	: Simulation and Analysis of 3-D Separated Flow around Sphere and Circular Cylinder.
B.Sc.	: June 1999, Istanbul Technical University, Istanbul TURKEY
Major	: Aeronautical Engineering
Thesis	: Comparison of Source and Doublet Panel Methods for 2-D Airfoils.

Major Publications

1. **K. Kara**, P. Balakumar, O. A. Kandil, Effects of Wall Cooling on Hypersonic Boundary Layers Receptivity over a Cone, 38th AIAA Fluid Dynamics Conference and Exhibit, Seattle, WA, AIAA 2008-3734.
2. **K. Kara**, P. Balakumar, O. A. Kandil, Effects of Nose Bluntness on Stability of Hypersonic Boundary Layers over a Blunt Cone, 37th AIAA Fluid Dynamics Conference and Exhibit, Miami, FL, AIAA 2007-4492.
3. **K. Kara**, P. Balakumar, O. A. Kandil, Receptivity of Hypersonic Boundary Layers Due To Acoustic Disturbances over Blunt Cone, 45th AIAA Aerospace Sciences Meeting and Exhibit, Reno, NV, AIAA 2007-0945.
4. **K. Kara**, P. Balakumar, O. A. Kandil, High Order WENO Method for the Steady Compressible 2D and Axisymmetric Navier-Stokes Equations. YPSE-06, Johns Hopkins University, Baltimore, MD, 2006.
5. W. A. Mokhtar, X. D. Zheng, I. Koc, **K. Kara**, Aerodynamics and Flow Control of Flapping Wings. 44th AIAA Aerospace Sciences Meeting and Exhibit, Reno, NV, AIAA 2006-1059.